DEVELOPMENT OF PLASTICIZED METHYLCELLULOSE-POTATO STARCH BLEND BASED POLYMER ELECTROLYTES FOR PROTONIC CELL AND SUPERCAPACITOR APPLICATIONS

MUHAMAD HAFIZ BIN HAMSAN

INSTITUTE FOR ADVANCED STUDIES
UNIVERSITY OF MALAYA
KUALA LUMPUR

2020

DEVELOPMENT OF PLASTICIZED METHYLCELLULOSE-POTATO STARCH BLEND BASED POLYMER ELECTROLYTES FOR PROTONIC CELL AND SUPERCAPACITOR APPLICATIONS

MUHAMAD HAFIZ BIN HAMSAN

THESIS SUBMITTED IN FULFILMENT OF THE REQUIREMENTS FOR THE DEGREE OF DOCTORAL PHILOSOPHY

INSTITUTE FOR ADVANCED STUDIES
UNIVERSITY OF MALAYA
KUALA LUMPUR

2020

UNIVERSITY OF MALAYA
ORIGINAL LITERARY WORK DECLARATION

Name of Candidate: **Muhamad Hafiz Bin Hamsan**

Matric No: **HVA170008**

Name of Degree: **Doctor of Philosophy (Ph.D)**

Title of Project Paper/Research Report/Dissertation/Thesis ("this Work"):

Development of Plasticized Methylcellulose-Potato Starch Blend Based Polymer Electrolytes for Protonic Cell and Supercapacitor Applications

Field of Study: **Physic (Materials Physics)**

I do solemnly and sincerely declare that:

(1) I am the sole author/writer of this Work;
(2) This Work is original;
(3) Any use of any work in which copyright exists was done by way of fair dealing and for permitted purposes and any excerpt or extract from, or reference to or reproduction of any copyright work has been disclosed expressly and sufficiently and the title of the Work and its authorship have been acknowledged in this Work;
(4) I do not have any actual knowledge nor do I ought reasonably to know that the making of this work constitutes an infringement of any copyright work;
(5) I hereby assign all and every rights in the copyright to this Work to the University of Malaya ("UM"), who henceforth shall be owner of the copyright in this Work and that any reproduction or use in any form or by any means whatsoever is prohibited without the written consent of UM having been first had and obtained;
(6) I am fully aware that if in the course of making this Work I have infringed any copyright whether intentionally or otherwise, I may be subject to legal action or any other action as may be determined by UM.

Candidate's Signature Date:

Subscribed and solemnly declared before,

Witness's Signature Date:

Name:

Designation:

DEVELOPMENT OF PLASTICIZED METHYLCELLULOSE-POTATO STARCH BLEND BASED POLYMER ELECTROLYTES FOR PROTONIC CELL AND SUPERCAPACITOR APPLICATIONS

ABSTRACT

In the current work, the preparation of the polymer electrolyte (PE) systems consists of methylcellulose-potato starch polymer matrix, ammonium nitrate (NH_4NO_3) as ionic source and glycerol as plasticizer are done by solution cast technique. X-ray diffraction (XRD) has shown that blend with 60 wt.% methylcellulose and 40 wt.% potato starch possesses the lowest degree of crystallinity. The possible interactions within the PE are verified using Fourier transform infrared (FTIR) spectroscopy. As the concentration of NH_4NO_3 is at 30 wt.%, the conductivity is optimized up to $(4.37 \pm 0.16) \times 10^{-5}$ S cm^{-1} and then maximized to $(1.26 \pm 0.1) \times 10^{-3}$ S cm^{-1} with the assist of 40 wt.% glycerol. The conductivity is found to be affected by the ionic mobility (μ), diffusivity (D) and number density (n). The addition of glycerol has changed the conductivity-temperature relation from Arrhenius to Vogel-Fulcher-Tammann rule. PE in this work is discovered to obey the non-Debye behavior via dielectric study. From transference number measurement (TNM), ions are considered as the dominant charge carrier and the cation transference number (t_c) for the highest conducting electrolyte (C4) is 0.40. Thermogravimetric analysis (TGA) portrays thermal stability up to 150 °C for the plasticized electrolyte. XRD, differential scanning calorimetry (DSC) and field emission scanning electron microscopy (FESEM) have strengthened the conductivity patterns. C4 is electrochemically stable up to 1.88 V. Galvanostatic charge-discharge measurement of the EDLC has been supported with cyclic voltammetry (CV) analysis. The protonic cells are discharged at various temperatures and constant currents. The rechargeability has been tested at 1 and 4 mA for 15 cycles.

Keywords: polymer electrolytes, polymer blend, starch, methylcellulose, protonic cell

PEMBANGUNAN ELEKTROLIT POLIMER BERASASKAN CAMPURAN POLIMER METIL SELULOSA-KANJI KENTANG BAGI APLIKASI BATERI PROTON DAN SUPERKAPASITOR

ABSTRAK

Dalam kerja ini, penyediaan elektrolit polimer yang mengandungi perumah polimer metil selulosa-kanji kentang, ammonium nitrat (NH_4NO_3) sebagai sumber ion dan gliserol sebagai pemplastik telah dilaksanakan melalui teknik penuangan larutan. Pembelauan sinar-X (XRD) menunjukkan bahawa campuran polimer dengan 60% metil selulosa dan 40% kanji kentang mempunyai tahap kristal yang paling rendah. Sebarang interaksi di dalam elektrolit telah dibuktikan dengan spektroskopi inframerah transformasi Fourier (FTIR). Pada tahap 30% berat NH_4NO_3, kekonduksian telah dioptimumkan sehingga $(4.37 \pm 0.16) \times 10^{-5}$ S cm^{-1} dan dimaksimumkan sehingga $(1.26 \pm 0.1) \times 10^{-3}$ S cm^{-1} dengan 40% berat gliserol. Kekonduksian didapati terjejas dengan mobiliti, kekenyapan dan kepadatan ionik. Penambahan gliserol telah mengubah hubungan kekonduksian-suhu dari peraturan Arrhenius ke Vogel-Fulcher-Tammann. Elektrolit di dalam kerja ini didapati mengikut teori bukan Debye melalui kajian dielekrik. Dari pengukuran nombor pemindahan (TNM) ion, ion dianggap sebagai pembawa cas utama dan pemindahan kation untuk elektrolit yang mempunyai kekonduksian tertinggi adalah 0.4. Analisa gravimetri terma (TGA) menggambarkan kestabilan haba adalah sehingga 150 °C untuk elektrolit berplastik. XRD, pengimbas kalometri pembezaan (DSC) dan pengimbas mikroskopi elektron (FESEM) telah menguatkan lagi corak kekonduksian. Elektrolit C4 adalah stabil sehingga 1.88 V. Pengukuran cas-nyahcas galvanostat untuk EDLC telah disokong oleh kitaran voltametri (CV). Bateri proton telah dinyahcas pada pelbagai suhu dan arus malar. Tahap cas-nyahcas bateri proton telah dicuba menggunakan 1 dan 4 mA untuk 15 kitaran.

Kata kunci: elektrolit polimer, campuran polimer, kanji, metil selulosa, bateri proton

ACKNOWLEDGEMENTS

I feel grateful to have my supervisor, Assoc. Prof. Dr. Mohd Fakhrul Zamani bin Abdul Kadir, for his encouragement and guidance to ace this work. I thank him for his advice and idea which allowed me to move forward in this work. I wish to express my appreciation to my co-supervisor, Dr. Muhammad Fadhlullah Bin Abd. Shukur, for sharing his scientific knowledge and experience.

I wish to state my greatest gratitude to my family, loved one and friends for their endless support that enabled me to finish my PhD journey with a healthy and stable mind. I would like to thank all my laboratory partners from Advanced Materials Laboratory, for their care, cooperation, friendship and encouragement.

Not to forget, University of Malaya for the financial support as well as staffs from University of Malaya for helping me with stuff related or unrelated to my PhD journey. I also thank Centre for Foundation Studies in Science, University of Malaya for giving me the opportunity to be a lab demonstrator and gained some knowledge to be a lecturer in the future. Last but not least, I would like to thank Malaysian Ministry of Education for the scholarship awarded.

TABLE OF CONTENTS

LIST OF FIGURES

LIST OF TABLES

LIST OF SYMBOLS

A	:	Area of electrolyte-electrode interface
A_{am}	:	Area of amorphous region
A_s	:	Summation of area
C	:	Capacitance
C_s	:	Specific capacitance
C_o	:	Vacuum capacitance
D	:	Diffusion coefficient
d	:	Thickness of electrolyte
d_i	:	Interplanar spacing
e	:	Electronic charge
emf	:	Electromotive force
E_a	:	Activation energy
E_d	:	Energy density
E_p	:	Pseudo-activation energy
f	:	frequency
i	:	Constant current
I	:	Current
I_{ss}	:	Steady state current
J	:	Current density
k	:	Inverse of capacitance
k_B	:	Boltzmann constant
m	:	Mass
n	:	Ionic number density
n_r	:	Reflection order
p	:	Deviation of plot
P_d	:	Power density
Q	:	Discharge capacity
Q_{spe}	:	Specific discharge capacity
r	:	Internal resistance
R	:	Bulk resistance
R_c	:	Charge transfer resistance
R_{es}	:	Equivalent series resistance
R_{load}	:	Load resistance

s_{dis}	:	Slope of discharge
T	:	Absolute temperature
t	:	Relaxation time
t_c	:	Cation transference number
t_{ch}	:	Charge time
t_d	:	Discharge time
t_e	:	Electronic transference number
$t_{plateau}$	:	Time of plateau region
T_g	:	Glass transition temperature
t_i	:	Ionic transference number
T_o	:	Ideal glass transition temperature
x_1	:	Fraction of the polymer
V_{drop}	:	Voltage drop
V_{oc}	:	Open circuit potential
V_{xy}	:	Terminal voltage from point x to y
Z_i	:	Imaginary part of impedance
Z_r	:	Real part of impedace
λ	:	Wavelength
μ	:	Ionic mobility
θ	:	Angle
τ	:	Inverse of angular frequency
η	:	Cycling efficiency
χ_{crys}	:	Degree of crystallinity
ω	:	Angular frequency
σ	:	Ionic conductivity
σ_o	:	Pre-exponential factor
ε_i	:	Dielectric loss
ε_r	:	Dielectric constant
ε_o	:	Vacuum permittivity

LIST OF ABBREVIATIONS

A-N	:	Arof Noor
CPE	:	Constant phase element
CV	:	Cyclic voltammetry
DEC	:	Diethyl carbonate
DMC	:	Dimethyl carbonate
DSC	:	Differential Scanning Calorimetry
EC	:	Ethylene carbonate
EDLC	:	Electrochemical double-layer capacitor
ES	:	Ethylene sulphite
FESEM	:	Field emission scanning electron microscopy
ESR	:	Equivalent series resistance
FTIR	:	Fourier transform infrared spectrocopy
H^+	:	Hydrogen ion
HFP	:	Hexafluoropropylene
KIO_4	:	Potassium periodate
Li^+	:	Lithium ion
$LiBF_4$	:	Lithium tetrafluoroborate
$LiCF_3SO_3$	:	Lithium triflate
$LiClO_4$	:	Lithium perchlorate
$LiCoO_2$	:	Lithium cobalt oxide
LiI	:	Lithium iodide
$LiMn_2O_4$	:	Lithium manganese oxide
$LiMn_3NiO_8$	:	Lithium manganese nickel oxide
LSV	:	Linear sweep voltammetry
$LiPF_6$	:	Lithium hexafluorophospate
MC	:	Methylcellulose
Mg^{2+}	:	Magnesium ion
$Mg(NO_3)_2$	:	Magnesium nitrate
MnO_2	:	Manganese (IV) oxide
MOF	:	Metal-organic framework
NH_4^+	:	Ammonium ion
$NH_4CH_3CO_2$	:	Ammonium acetate
NH_4Br	:	Ammonium bromide

$NH_4CF_3SO_3$	:	Ammonium triflate
NH_4Cl	:	Ammonium chloride
NH_4ClO_4	:	Ammonium perchlorate
NH_4F	:	Ammonium fluoride
NH_4I	:	Ammonium iodide
NH_4NO_3	:	Ammonium nitrate
$(NH_4)_3PO_4$	:	Ammonium phosphate
NH_4SCN	:	Ammonium thiocyanate
$NH_4SO_3CF_3$	:	Ammonium trifluoromethane sulfonate
Na^+	:	Sodium ion
$NaClO_4$	:	Sodium perchlorate
NaI	:	Sodium iodide
$NaNO_3$	:	Sodium nitrate
NaOH	:	Sodium hydroxide
NaTf	:	Sodium triflate
OH	:	Hydroxyl
PC	:	Polyethylene carbonate
PCL	:	Poly-ε-caprolactone
PE	:	Polymer electrolyte
PEG	:	Polyethylene glycol
PEMA	:	Polyethyl methacrylate
PEO	:	Polyethylene oxide
PMMA	:	Polymethyl methacrylate
PS	:	Potato starch
PVA	:	Polyvinyl alcohol
PVA	:	Polyvinyl chloride
PVDF	:	Polyvinylidene fluoride
PVP	:	Polyvinyl pyrrolidone
SEI	:	Solid electrolyte interface
SiO_2	:	Silicon dioxide
SS	:	Stainless steel
TGA	:	Thermogravimetric Analysis
TiO_2	:	Titanium dioxide
TNM	:	Transference number measurement
V_2O_3	:	Vanadium (III) oxide

V_2O_5	:	Vanadium (IV) oxide
wt%	:	Weight percentage
XRD	:	X-ray diffraction
$ZnSO_4.7H_2O$	:	Zinc sulphate
ZrO_2	:	Zirconium dioxide

CHAPTER 1: INTRODUCTION

1.1 Research Background

Material that is able to conduct ions with the presence of salt in a polymer is called polymer electrolyte (PE) (Aziz, Woo, Kadir & Ahmed, 2018). The study of PE was started by Peter V. Wright in 1975. Wright first demonstrated a PE system with poly-ethylene oxide (PEO) as the polymer matrix doped with potassium and sodium salts (Armand, 1994). The significance of Wright's work was not realized by solid state community until 1978. The research spurred a massive amount of attention worldwide as other solid state chemists suggested the employment of alkali metal based solid PE in the fabrication of lithium-ion batteries (Armand, Chabagno & Duclot, 1979). The year 1980 is the second decade in the growth of PE study. The development of micro- and portable-electronics has been the main attention in this decade. The ionic conductivity was then found to be preferable in the amorphous nature (Berthier, Gorecki, Minier, Armand, Chabagno & Rigaud, 1983).

At the early development of PE, synthetic polymers such as polyethylene (Ma et al., 2018), polymethyl methacrylate (Vodrak et al., 2001), polyester (Manaresi et al., 1993), polyamide (Yu, Xiong, You, Dong & Yao, 2008), polyurethane (Su'ait et al., 2014) and polysulfone (Lufrano, Staili, Arico & Antonucci, 2008) were used as polymer host. In recent year time, Samsung; a famous telephone brand, faced a problem of devices explosion due to batteries which injured the user (Cheng, Jeong & Dou, 2016). Furthermore, the environmental waste from synthetic polymers has become one of the major problems cause by polymer industry (Maitz, 2015). As a safer alternative, biopolymers from natural renewable sources which possess interesting characteristics such as abundance in nature, environmentally friendly, non-toxic, economical and

biodegradable were employed (Du, Hu, Singh, Tsai, Lin & Ko, 2017). Biopolymers can be used in PE preparation (Subban & Arof, 2004; Majid & Arof, 2005).

Polymer blending is an excellent method to improve the ionic conductivity of the electrolyte (Arunkumar, Babu, Usha & Kalainathan, 2017). Polymer blend is a mixture of at least two polymers. Polymer blend method creates an opportunity in finding new materials which possess the characteristic that could not be achieved by single polymer (Muthuvinayagam & Gopinathan, 2015). The structure stability or mechanical properties of the material also can be improved by blending different polymers (Tamilselvi & Hema, 2014). Plasticization is another technique to maximize the ionic conductivity. The low conductivity value of the free-plasticizer PE is usually due to rigidity of the polymer chains which lower the mobility of the chain for ions transportation. The addition of plasticizer can improve the flexibility of the polymer chain which indirectly enhances the conductivity of the electrolyte (Simari, Lufrano, Coppola & Nicotera, 2018).

The properties of an electrolyte such as ionic conductivity, thermal stability, potential stability and amorphousness are strongly dependent on type of ionic provider used. Generally, lithium ion, Li^+, hydrogen ion, H^+, sodium, Na^+ and magnesium ion, Mg^{2+} are used in PEs studies (Noor, Majid & Arof, 2013; Yuan & Quesnel, 2016: Na, Wei, Yu & Taohai, 2017; Bingbing, et al., 2018). These ions have been reported in several electrical energy storage technologies such as supercapacitors (Taghavikish et al., 2018), batteries (Subba et al., 2006; Masashi, Shufeng, Rika, Shunichi & Li 2017), solar cells (Chuan-Pei, Chun-Ting, & Kuo-Chuan, 2017) and fuel cells (Michaela, 2018). The employment of PEs as electrode separator in these devices is due to rapid ionic

migration, compatibility and excellent electrodes insulation (Ng, Wong, Chew & Osman, 2011; Braun, Uhlmann, Weiss, Weber & Ivers-Tiffee, 2018).

In this work, methylcellulose (MC)-potato starch (PS) blend based biopolymers are used as the polymer host. Several tests are conducted to identify the most suitable composition for the polymer blend. H^+ ions are provided by the impregnation of ammonium nitrate (NH_4NO_3) salts into the low conductive polymer blend host. Plasticization of the PE is done via the addition of glycerol. Several characterization techniques are conducted to determine the most conductive sample. Plasticized electrolyte of optimum conductivity is used to assemble the supercapacitors and protonic cells. These devices are characterized to check their stability and the performances.

1.2 Objectives of the Thesis

The objectives of the present work can be expressed as follows:

- To prepare proton conducting methylcellulose-potato starch based solid biodegradable polymer electrolytes containing different amounts of ammonium nitrate salt.
- To study the characteristic of the PE using several analysis.
- To improve the conductivity of the electrolytes with the addition of glycerol as plasticizer.
- To investigate the performance of the fabricated energy devices.

1.3 Scope of the Thesis

A total of ten chapters are presented in this thesis. Chapter 1 explains the primary scope and main objectives of this research in brief. Chapter 2 provides the related previous and current topics regarding the studies of PE. The details of the electrolytes preparation and characterization techniques such as XRD and impedance analysis are described in Chapter 3. The characterizations of the assembled protonic cells and supercapacitor are also provided in this chapter. The characterizations of polymer blend host confirmation are included in Chapter 4. Chapter 5 provides the crystallinity and interaction among the functional groups of the polymer blend host with the salt and plasticizer via FTIR analysis. The information on PE's conductivity, transference number and dielectric behavior are discussed in Chapter 6. The studies on thermal properties and surface morphology of the PE are provided in Chapter 7. The application of PE as electrode separator in the supercapacitor and protonic cells assembly is discussed in Chapter 8. More explanations and summaries on the presented outcomes of this study can be found in Chapter 9. Chapter 10 includes the conclusion of the thesis and few suggestions for future improvements.

CHAPTER 2: LITERATURE REVIEW

2.1 Introduction

Electrical energy storage devices attract many researchers due to its interesting features such as wide thermal stability range, leakage free and flexible. Furthermore, in recent time demand on electrical devices such as mobile phones, tablets, laptop and cameras has been increased. The most popular demands are high batteries efficiency, light weight, safe and flexible. Various types of storing energy media are used such as chemical, kinetic, thermal and electric. Supercapacitors (Tripathi & Singh, 2018) and protonic cells (Nyuk & Isa, 2017) are well recognized for its surface charge storage and chemically stored energy, respectively. These energy storage devices need to be further explored to achieve the current demands. The idea of polymer-based energy storage technologies has developed interest among the researchers due to the possibilities of constructing environmentally friendly and flexible devices (Ravi, Kumar, Mohan & Rao, 2014; Li, Wang, Yang & Holze, 2015).

In a device, electrolyte plays a role as a medium for negatively charged species (anion) and positively charged species (cation) to migrate towards electrodes (Pozyczka, Marzantowicz, Dygas & Krok, 2017). Electrolytes must possess a conductivity value of ~ 10^{-4} S cm^{-1} in order to be useful as electrode separator in electrochemical devices (Simonetti, Carewsk, Maresca, De Francesco & Appetecchi, 2017). High conductivity value of liquid-based electrolyte makes it preferable in the energy storage study (Qi, Juner, Lei, Xueqian & Yingying, 2016). However, the leakage of electrolyte can cause corrosion on the electrodes and other compartment of the devices (Feng, He & Zhou, 2016; Dyartanti, Purwanto, Widiasa & Susanto, 2018). The safety issue of a device can be eliminated by replacing liquid electrolyte with polymer electrolyte (PE). Inexpensive

cost and flexible packaging of devices can be achieved with the presence of PE (Lee, Yanilmaz, Toprakci, Fu & Zhang, 2014).

2.2 Polymer Electrolytes (PE)

PEs are produced by dissolution of inorganic salt in a polar polymer host. PE acts as the conductor of ion and anode/cathode separator in the application of electrochemical energy devices to avoid them from touching (Taghavikish et al., 2018). The selection of PEs in various modern devices, such as supercapacitor, electrochromic technologies, batteries and sensors, are verified by examining their morphology, electrical properties, thermal properties and structure through various kinds of characterizations (Aziz & Abidin, 2015). PE gains so many attentions due to its dimensional stability, easy to prepare, shape versatility as well as safe in handling and electrochemical stability (Bingbing et al., 2018).

There are two types of PE; salt-polymer complex and plasticized polymer electrolyte (Muldoon, Bucur, Boaretto, Gregory & Di Noto, 2015). Salt-polymer complex can be obtained by doping polar polymer matrix with inorganic salt where metal ions from the salt form a coordinating bond or dative bond with oxygen or nitrogen functional group from the polymer (Rivas, Maureira, Guzman & Mondaca, 2009; Winter & Schubert, 2016). The inclusion of low molecular weight compounds into the polymer matrix can form plasticized polymer electrolyte (Stephan, Kumar, Kulandainathan & Lakshmi, 2009). Properties like compatible, flexible and able to form thin film medium make PE one of the best choice in current energy storage devices as well as excellent alternative to liquid electrolyte due to no leakage problem, thermally stable and easy to fabricate (Lin, Ito & Yokohama, 2018). The examples of PE are tabulated in Table 2.1.

Table 2.1: Polymer electrolyte studies.

Polymer Electrolyte	Conductivity (S cm^{-1})	Reference
PEO-NH_4F	1.11×10^{-6}	Kumar & Sekhon, 2002
PVA-$Mg(NO_3)_2$	7.36×10^{-7}	Polu & Kumar, 2013
PVP-KCl	1.00×10^{-5}	Rani, Raja, Sharma & Rao, 2013
PMMA-$NaBF_4$	1.03×10^{-6}	Yuan & Quesnel, 2016
PMMA-LiI	1.30×10^{-6}	Dzulkurnain, Rani, Ahmad & Mohamed, 2018

2.3 Biodegradable Polymers

Biopolymers can be extracted from natural renewable sources. Biopolymers possess interesting characteristics such as harmless, abundance in nature, environmentally friendly and economical (Aziz, Abdullah, Rasheed & Ahmed, 2017; Mostafa, Farag, Abo-dief & Tayeb, 2018; Muthukrishnan et al., 2018). Biodegradable characteristic of biopolymer makes it an excellent alternative to non-biodegradable synthetic polymers. Non-biodegradable synthetic polymers like polystyrene (Rohan et al., 2014), polymethyl methacrylate (Li, Wong, Dou, Zhang & Ng, 2018) and polyamide (Yu, Xiong, You, Dong & Yao, 2008) are expensive. Biopolymers are widely used in various kind of industry such as medical (Park, Lih, Park, Joung & Han, 2017), textile (Younes, 2017), cosmetic (Rebelo, Fernandes & Fangueiro, 2017) and food packaging (Othman, 2014) industries. Biopolymers also have been studied in PEs applications which can be illustrated in Table 2.2.

Table 2.2: Biopolymer-based polymer electrolytes.

Polymer electrolytes	Conductivity (S cm^{-1})	Reference
Carrageenan-NaOH	5.30×10^{-7}	Mobarak, Ramli, Ahmad & Rahman, 2012
Chitosan-NH_4Br	4.38×10^{-7}	Shukur et al., 2013b
Polyactides-LiI-PEG	4.16×10^{-6}	Tan, Ahmad & Anuar, 2014
Pectin-ammonium bis(trifluoromethylsulfonyl)imide	1.43×10^{-6}	Mendes, Esperanca, Medeiros, Pawlicka & Silva, 2017
Alginate-NH_4Br	$\sim 10^{-5}$	Fuzlin, Rasali & Samsudin, 2018

2.4 Methylcellulose Based Polymer Electrolytes

Methylcellulose (MC) is obtained from the modification of cellulose. The process includes the reaction between methyl chloride or dimethyl sulfate with alkali based cellulose (Filho et al., 2007). As shown in Figure 2.1, the structure of MC composed of methoxy and hydroxyl groups. The glycosidic linkage (β-1,4) is a bond which connect the glucose rings to form cellulose (Biswal & Singh, 2004). These functional groups contain oxygen atom which has lone pair electrons that provides the polymer chain the ability to conduct ions. MC can be dissolved in water and form transparent film (Nik Aziz, Idris & Isa, 2010). MC is broadly used in many different industrial sectors, such as mineral processing, paints, food, cloth and medical (Frinkenstadt, 2005). MC also has been incorporated as polymer host in polymer electrolyte studies due to its excellent mechanical, electrical and thermal stability. Several examples of studies on MC based polymer electrolytes are listed in Table 2.3.

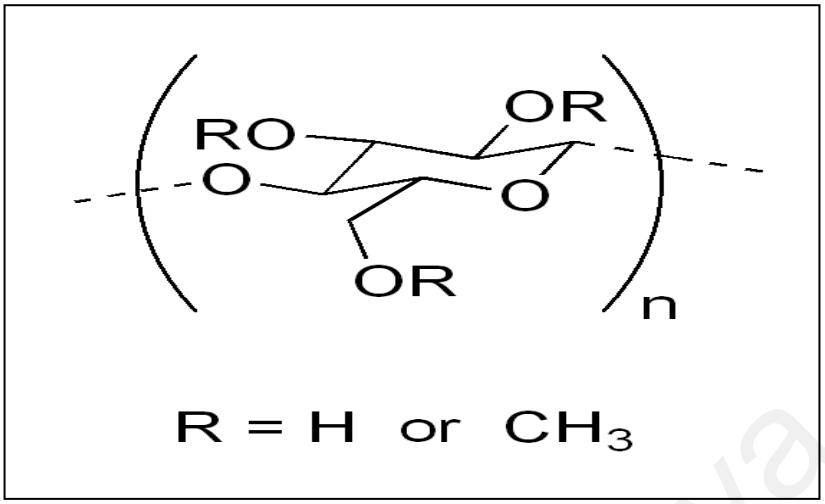

Figure 2.1: Structure of methylcellulose (Desbrieres et al., 2000).

Table 2.3: Polymer electrolytes with methylcellulose as the polymer host.

Polymer electrolytes	Conductivity (S cm^{-1})	Reference
MC-NH_4NO_3	2.10×10^{-6}	Shuhaimi, Teo, Majid & Arof, 2010
MC-NH_4F	6.40×10^{-7}	Nik Aziz et al., 2010
MC-$LiCF_3SO_3$	2.13×105^{-7}	Sahli & Ali, 2012
MC-NaI	2.70×10^{-5}	Farghali & Ahmad, 2015
MC-$Ca(NO_3)_2$	2.21×10^{-7}	Nurhaziqah et al., 2018

2.5 Starch Based Polymer Electrolytes

Figure 2.2 shows that starch is a polymeric carbohydrate that composed of branched amylopectin with structural formula of α-1,6-D-glucopyranoside and poly-α-1,4-D-glucopyranoside while linear amylose with structural formula of poly-α-1,4-D-glucopyranoside (Teramoto, Motoyama, Mosomiya & Shibata, 2003; Follain, Joly, Dole & Bliard, 2005). The oxygen from hydroxyl group and glycosidic linkage in the

structure of starch contain lone pair electrons which assists the conduction of charge carriers. The double helices arrangement of amylopectin reduces the mobility of polymer chain. Hence, starch with high amylose content is highly amorphous and preferable to be employed as polymer host in electrolytes (Chartterjee, Kulshrestha & Gupta, 2015). Table 2.4 shows the various types of starch and their amylose content. Starch is a cheap renewable green-resource that has been used in various industries such as textiles, coating in paper, adhesives, binders and absorbants (Biswas, Willet, Gordon, Finkenstadt & Cheng, 2006). Several reported works that used starch as polymer host in their electrolyte systems are tabulated in Table 2.5.

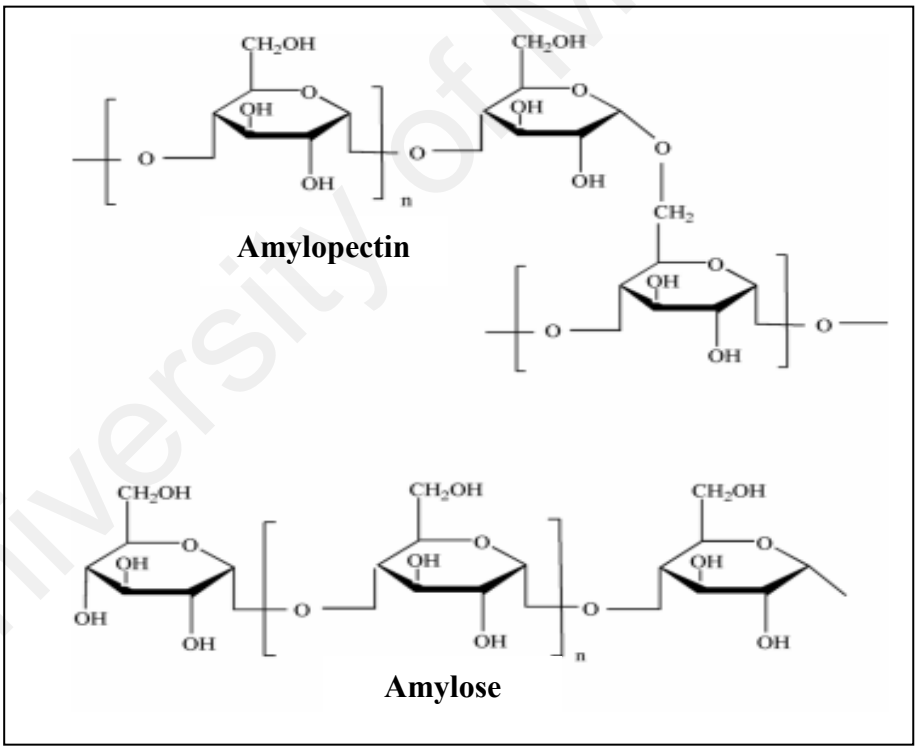

Figure 2.2: Structure of starch (Ismail, Irani & Ahmad, 2013).

Table 2.4: Various starch sources with their amylose content.

Starch	Amylose content (%)	Reference
Potato	31	Singh, Singh & Sodhi, 2002; Jansky & Fajardo, 2016; Zhao, Andersson & Andersson, 2018
Corn	28	Singh, Singh & Sodhi, 2002 Liu, Yu, Xie & Chen, 2006
Cassava	19.5	Oladunmoye, Aworh, Maziya-Dixon, Erukainure & Elemo, 2014
Tapioca	17	Nuwamanya, Baguma, Emmambux & Rubaihayo, 2010
Rice	8.7 -19.9	Park, Ibanez & Shoemaker, 2007

Table 2.5: Polymer electrolytes with starch as the polymer host.

Polymer electrolytes	Conductivity (S cm^{-1})	Reference
Starch-NH_4NO_3	2.83×10^{-5}	Khiar & Arof, 2010
Starch-$LiPF_6$	$\sim 10^{-7}$	Ramesh, Liew & Arof, 2011
Starch-$Mg(CH_3O_2)_2$	2.60×10^{-6}	Shukur, Ithnin & Kadir, 2016
Starch-LiOAc	1.48×10^{-5}	Shukur et al., 2014a
Starch-$NaClO_4$	7.19×10^{-6}	Tiwari, Srivastava & Srisvastava, 2013

2.6 Binary Polymer Blend

Polymer blending is an easy technique to increase conductivity where two or more polymers are combined together. Polymer blend method creates an opportunity in finding new materials which possess the characteristic that could not be achieved by single polymer (Muthuvinayagam & Gopinathan, 2015). Furthermore, the structure stability or mechanical properties of the material also can be improved by blending different polymers (Tamilselvi & Hema, 2014). On the other hand, polymer blend has good potential in electrochemical devices application, ease of preparation and the physical properties can be controlled (Kadir, Majid & Arof, 2010). Ions hopping or exchange processes are more efficient in polymer blend due to more sites created with the presence of two or more polymers. Consequently, strengthen the ionic conductivity of the electrolyte (Yusof, Shukur, Illias & Kadir, 2014). Table 2.6 shows the examples of conductivity improvement via polymer blending technique.

Table 2.6: Polymer electrolytes with blend polymer host.

Polymer blend electrolyte	Conductivity (S cm^{-1})	Reference
Starch-NH_4Br Starch-chitosan-NH_4Br	5.57×10^{-5} 9.72×10^{-5}	Shukur & Kadir, 2015; Shukur et al., 2013b
Chitosan-NH_4Br Chitosan-starch-NH_4Br	4.38×10^{-7} 9.72×10^{-5}	Shukur et al., 2013a; Shukur et al., 2013b
Chitosan-NH_4I Chitosan-PVA-NH_4I	3.73×10^{-7} 1.77×10^{-6}	Buraidah et al., 2009; Buraidah & Arof, 2011
Corn Starch-NH_4NO_3 Starch-chitosan-NH_4NO_3	2.83×10^{-5} 3.89×10^{-5}	Khiar & Arof, 2010; Khiar & Arof, 2011

2.6.1 Cellulose-Starch Blend

Starch is famous of its brittleness, poor mechanical strength and poor long-term stability (Kampeerapappun, Aht-ong, Pentrakoon & Srikulkit, 2007; Lu, Xiao & Xu, 2009). Starch films are also known to have a several disadvantages such as gel syneresis, retrodegradation and brittle in shear force (Donatell, Barbara, Romano, Cristian & Alessandro, 2003). However, these issues can be solved by blending starch with other polymers (Miyamoto, Yamane, Seguchi & Okajima, 2009; Ramly, Isa & Khiar, 2011; Mendes et al., 2016).

Abd El-Kader and Ragab (2013) reported that the ionic mobility and transference number can be improved by mixing MC and maize starch which leads to conductivity enhancement. As reported by Babu, Bera, Kumari, Mandal and Saxena (2014), the enhancement in tensile strength of starch/cellulose blend film is attributed to the reaction of amylopectin crosslinking of the starch. Miyamoto, Yamane, Seguchi & Okajima (2009) reported that cellulose and starch were miscible and formed a porous structure which is good for ionic conductivity.

2.7 Proton Provider

PEs with proton as the charge carriers have been known for their compatibility with electrochemical devices (Deraman, Mohamed & Subhan, 2013; Rani, Mohamed & Isa, 2016). Typically, there are two proton providers for polymer electrolyte application which are inorganic acids and ammonium salts. Common strong inorganic acids used are sulfuric acid (H_2SO_4) and phosphoric acid (H_3PO_4) (Prajapati, Roshan & Gupta; 2010; Yan et al., 2011). However, a phenomenon of chemical degradation occurs when inorganic acid complexes with a polymer which made them incompatible for practical applications (Gao & Lian, 2014). Hence, ammonium salts are preferable as proton

provider in polymer electrolyte application (Majid & Arof, 2005; Nik Aziz et al., 2010; Deraman et al., 2013; Shukur & Kadir, 2015; Salleh et al., 2016). Examples of proton based polymer electrolyte systems are listed in Table 2.7.

Table 2.7: Examples of proton based polymer electrolytes.

Polymer electrolyte	Conductivity (S cm^{-1})	Reference
Chitosan acetate - NH_4NO_3	2.35×10^{-5}	Majid & Arof, 2005
PVC-$NH_4CF_3SO_3$	$\sim 10^{-7}$	Deraman et al., 2013
Starch-NH_4PF_6	1.52×10^{-5}	Mishra & Rai, 2013
PVDF-NH_4F	1.17×10^{-7}	Kumar, Sharma, Dhiman & Pathak, 2016

2.7.1 Protonic Conduction

It is well known that in proton-based PE or proton batteries, hydrogen ions (H^+) are the conducting species (Devi, Chitra, Selvasekarapandian, Premalatha, Monisha & Saranya, 2017). Hashmi, Kumar, Maurya and Chandra (1990) stated that H^+ is the conducting species in PEO-NH_4ClO_4. H^+ ions are also reported as charge carriers in proton-based polyethylene succinate polymer electrolyte (Srivastava & Chandra, 2000). In ammonium salt-based PE, NH_4^+ cation possesses four hydrogen ions in tetrahedral structure. One of these H^+ ions has the weakest bond with the nitrogen atom which can be separated in the presence of electric field (Anuar, Zainal, Mohamed & Subban, 2012; Lim, Sadakiyo & Kitagawa, 2019). H^+ ion is migrated from one coordinating site to

another and creates vacancy for next H^+ ion to migrate. This migration process is well known as Grotthuss mechanism (Agnom, 1995).

2.8 Relation Between Conductivity and Temperature

In PE, ions migrate from coordinating site of polymer's functional groups to another coordinating site. With the presence of enough thermal energy, ions are able to undergo conduction process from one electrode to another electrode. The magnitude of conductivity is typically affected by the concentration of salt, amorphousness and temperature (Bruce & Vincent, 1993). Ratner (1987) reported that the most crucial property of PE is the relationship between ionic conductivity and temperature. The study on ionic conductivity versus temperature is done to observe the type of ionic conduction and the stability of ionic migration at elevated temperature. There are two types of conductivity-temperature relation theory which are Arrhenius theory and Vogel-Fulcher-Tammann (VFT) theory.

2.8.1 Arrhenius Theory

The relation of ionic conductivity (σ) and temperature by Arrhenius theory can be explained from the following equation:

$$\sigma = \sigma_o \exp\left(-E_a \left(k_B T\right)^{-1}\right) \tag{2.1}$$

Here σ_o stands for factor of pre-exponential, E_a is the activation energy, k_B is Boltzmann constant while T is the thermodynamic temperature. Arrhenius theory can be assumed if

the linearity (linear, $R^2 \sim 1$) is observed in conductivity-temperature relation (Osman Ghazali, Othman & Isa, 2012). Ions are assumed to jump from neighboring vacant sites to another due to thermal activation (Singh et al., 2016). As observed in Figure 2.3, Su'ait et al. (2014) reported that the plot of log σ against 1000/T for polyurethane-LiI system is linear, which is in agreement with Arrhenius theory.

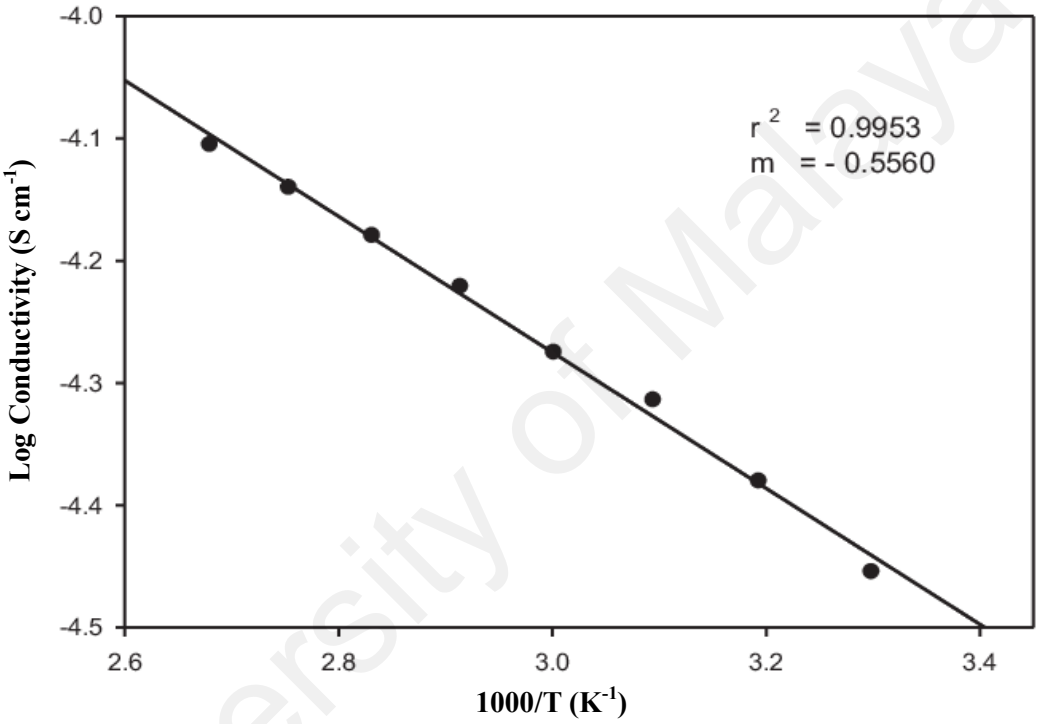

Figure 2.3: Conductivity-temperature dependence for polyurethane-LiI (Su'ait et al., 2014).

2.8.2 Vogel-Fulcher-Tammann (VFT) Theory

The VFT theory can be applied using the following equation:

$$\sigma = \sigma_o T^{-\frac{1}{2}} \exp\left(-\frac{E_p}{k_B(T - T_o)}\right) \tag{2.2}$$

where the pseudo-activation energy is denoted as E_p and T_o stands for the ideal glass transition temperature usually 50 K lesser than the glass transition temperature (T_g) (Diederichsen, Buss & McCloskey, 2017).

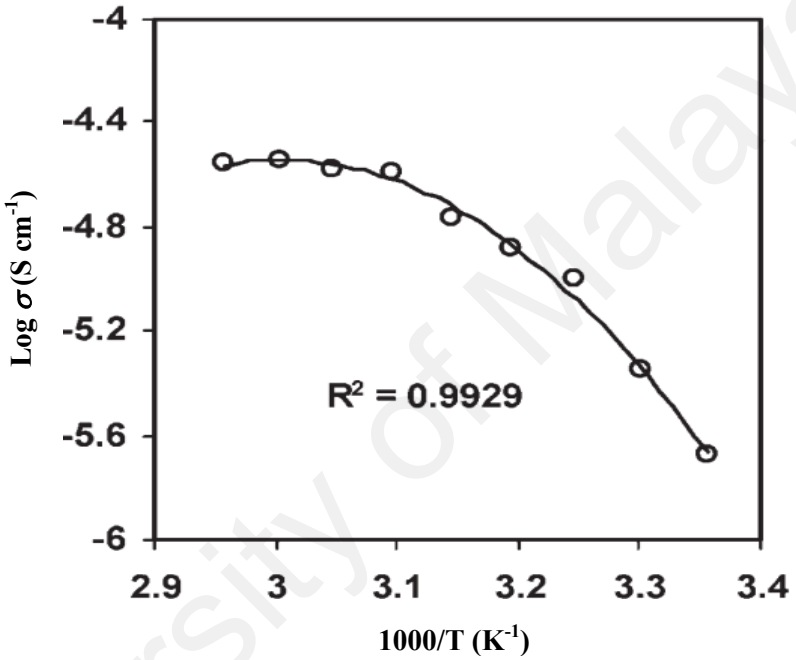

Figure 2.4: Conductivity-temperature dependence for MC-NH_4NO_3 (Shuhaimi, Majid & Arof, 2010).

Typically, VFT theory can be used when the conductivity-temperature relation is non-linear (polynomial, $R^2 \sim 1$). VFT theorize that the migration of mobile ions is mainly due to the polymer chain's movement (Alves, Sentanin, Sabadini, Pawlicka & Silva, 2016). As observed in Figure 2.4, the plot of log σ against 1000/T for MC-NH_4NO_3 system possessed non-linear conductivity-temperature relation which reported by Shuhaimi, Majid and Arof (2010).

2.9 Addition of Plasticizer (Glycerol)

To develop a good electrochemical device, the electrolyte must possess at least a conductivity value of ~ 10^{-4} S cm^{-1} (Kadir, 2010). The low conductivity of a polymer electrolyte is due to the rigidity of the polymer chains which slower the ion mobility. Plasticization is a method to strengthen the conductivity value by the inclusion of additives or plasticizer (Perďochová et al., 2017). Hence, the existence of plasticizer can improve the flexibility of the polymer chain indirectly enhance the conductivity of the electrolyte (Naimi et al., 2018). The presence of plasticizer in salt-polymer complex can reduce the glass transition temperature, T_g and improve the amorphousness of the polymer (Matthew, Karthika, Ulaganathan & Rajendran, 2015). Polymer electrolytes with different plasticizers are listed in Table 2.8.

Table 2.8: Plasticized polymer electrolytes.

Polymer electrolyte	Conductivity (S cm^{-1})	Reference
PEO/chitosan-NH_4NO_3-ES	~ 10^{-4}	Kadir, Abdul, Teo, Majid & Arof, 2009
MC-NH_4NO_3-PEG	1.14×10^{-4}	Shuhaimi, Alias, Kufian, Majid & Arof, 2010
PCL-NH_4SCN-EC	3.80×10^{-5}	Woo, Majid & Arof, 2013
PVdF-HFP-PMMA-$LiClO_4$-PC-DEC	2.83×10^{-4}	Gobel & Kanchan, 2016
PVdF-HFP -$LiBF_4$-EC-PC	8.1×10^{-4}	Song, Wang, Tang, Muchakayala & Ma, 2017

As seen in Figure 2.5, glycerol possesses multihydroxyl moiety structure which can serve as alternative path for charge carriers to migrate in the polymer electrolytes (Chai & Isa, 2016).

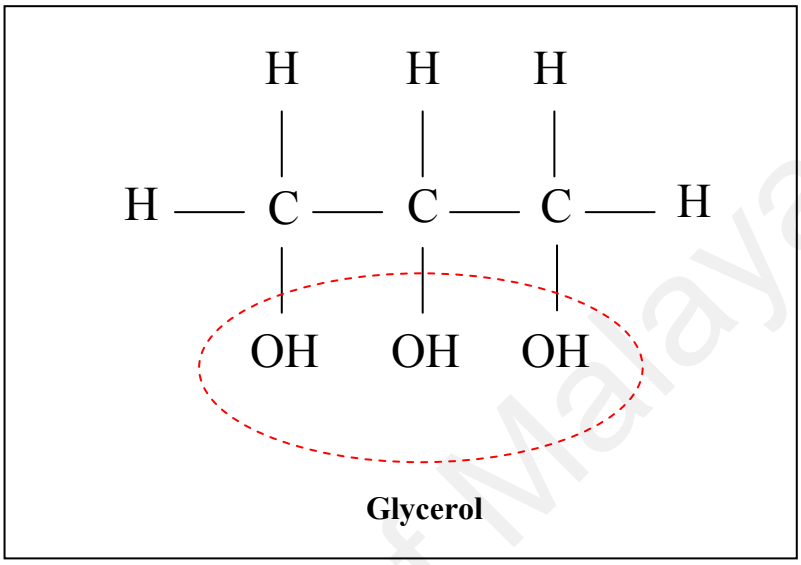

Figure 2.5: Structure of glycerol (Balqis, Khaizura, Russly & Hanani, 2017).

Glycerol ($C_3H_8O_3$) is harmless to both human and environment (Pradima, Kulkarni & Archna, 2016). Unique characteristics of glycerol which have small melting point at ~18 °C and high boiling point at 290 °C can avoid it from becoming solid or vapor at room temperature. The solidification or vaporization of a material at room temperature can limit the mobility of ions (Isahak, Ismail, Yarmo, Jahim & Salimon, 2010). The attraction between polymer chains can be reduced due to high dielectric constant (ε) of glycerol which is 42.5. High value of ε also can aid in the process of salt dissociation which increase more free ions (Shukur & Kadir, 2015).

2.10 Protonic-Based Energy Devices

Nowadays, renewable polymer electrolyte based energy storage devices are popular topics due to global concerns towards efficient and safer energy providers. Due to safe and high ionic conductivity, PE can be considered as an important component in electrical energy storage technologies. The incorporation of PE is one of the ways to eliminate the electrode's degradation (Mohamad, 2005). As stated in the literature, PE has been chosen in modern devices study due to durability, high performance, cost-effectiveness, mechanical flexibility and portability (Jung et al., 2017). Proton-based (H^+) polymer electrolytes have attracted attention of many researchers for alternative of lithium ion-based energy storage technologies (Aziz, Karim, Qadir & Zafar, 2018).

2.10.1 Supercapacitor

Supercapacitor is one of the substitutes to the conventional rechargeable batteries (Tripathi & Kumar, 2018). Supercapacitors are divided into three kinds depending on the mechanism of charge storage: (1) pseudocapacitors, (2) electrochemical double-layer capacitor (EDLC) and (3) hybrid capacitors **(**Wang, Song & Xia, 2016). In pseudocapacitors energy is stored through the chemical reaction between electrode material and electrolyte which is known as Faradic redox reactions (Sellam & Hashmi, 2013). In EDLC, energy is electrostatically stored due to charge accumulation at the surface of the electrode (Krishnan, Jayaraman, Balasubramanian & Mani, 2018). Hybrid capacitors possess the combination of EDLC and pseudocapacitor energy storage processes (Sun et al., 2017).

EDLC is a vital provider of power in modern daily life such as memory back-up, communication devices and electric transportations (Zhang, Xu, Harrison, Fyson & Southee, 2016). EDLC possesses long lifetimes, high power density and similar carbon-

based electrodes. A range of active materials have been employed in the electrode of EDLC e.g. carbon aerogel (Yang et al., 2016), graphite (Andres, Dahlstrom, Blomquist, Norgen & Olin, 2018), manganese oxide (Subramanian, Zhu & Wei, 2008), carbon nanofiber (Tran & Kalra, 2013) and activated carbon (Zhao et al., 2018). Among these active materials, activated carbon is an ideal material to be employed in EDLC application due to its high specific surface area, reasonable price and excellent conductivity (Xu et al., 2017). Proton-based EDLCs with activated carbon electrodes are listed in Table 2.9.

Table 2.9: Proton-based EDLC with activated carbon electrodes.

Polymer electrolyte	Active materials	Reference
MC-NH_4NO_3- PEG	Activated Carbon	Shuhaimi, Teo, Woo, Majid & Arof, 2012
Chitosan-starch-NH_4I-glycerol	Activated Carbon	Yusof, Majid, Kasmani, Illias & Kadir, 2014
PCL-NH_4SCN	Activated Carbon	Woo, Liew, Majid & Arof, 2014
Chitosan-Starch-NH_4Cl-glycerol	Activated Carbon	Shukur & Kadir, 2015
PVA-$NH_4CH_3CO_2$	Activated Carbon	Liew, Ramesh & Arof, 2016

2.10.2 Protonic Cell

H^+ or proton conducting polymer electrolytes have been discovered as an alternative for lithium ion (Li^+) in the fabrication of electrochemical cells (Nyuk & Isa, 2018). Typically lithium-based polymer electrolyte possesses electrochemical stability up to 5 V (Li et al., 2017) while protonic-based polymer electrolyte decomposed at ~ 1 to 2 V (Rani, Mohamed & Isa, 2016). Even so, due to safety awareness and low cost of materials, protonic cell can be a good alternative to lithium ion cell (Mainar et al.,

2018). Other than that, ionic radius of Li^+ (0.90×10^{-10} m) is larger than H^+ (0.84×10^{-15} m). Hence, it is easier for H^+ to intercalate into electrode materials compared to Li^+ (Wongsaenmai, Ananta & Yimnirun, 2012; Mishra, 2013; Antognini et al., 2013).

Generally, cathode materials for protonic cells includes lead oxide (Chen, Ma & Kong, 2013), vanadium (III) oxide (V_2O_3) (Morales, Petkova, Cruz & Caballero, 2006), vanadium (IV) oxide (V_2O_5) (Wang et al., 2015) and manganese (IV) oxide (MnO_2) (Dose & Donne, 2014). MnO_2 has been concluded as a better active material for cathode in protonic cell application by Bansod, Bhoga, Singh and Tiwari (2007), they also tested other cathode materials. As reported by Alias, Chee and Mohamad (2017), MnO_2-based protonic cell possesses larger value of capacity and open circuit potential (V_{oc}) compared to V_2O_5-based protonic cell because during discharge V_2O_5 experience structural alteration. Well known materials for anode which are mixture of zinc (Zn) and zinc sulfate ($ZnSO_4.7H_2O$). $ZnSO_4.7H_2O$ is the provider of H^+ charge-discharge process of the cell (Mishra, Pundir & Rai, 2014). Table 2.10 shows several examples of protonic cell studies.

Table 2.10: Protonic cells studies.

Polymer electrolyte	Anode|cathode	Reference
PVA-chitosan-NH_4NO_3-EC	Zn+ $ZnSO_4.7H_2O$|MnO_2	Kadir, 2010
CMC-NH_4Br	Zn+ $ZnSO_4.7H_2O$|MnO_2	Samsudin, Lai & Isa, 2014
PMMA-NH_4SCN-PC	Zn+ $ZnSO_4.7H_2O$|MnO_2	Mishra et al., 2014
Chitosan-Starch-NH_4Cl-glycerol	Zn+ $ZnSO_4.7H_2O$|MnO_2	Shukur & Kadir, 2015
Chitosan-$NH_4CH_3CO_2$	Zn+ $ZnSO_4.7H_2O$|MnO_2	Alias et al., 2017

2.11 Summary

Background and literature review of related theories and materials have been explained in this chapter. The discussions regarding supercapacitor and protonic cells have been included. The crucial information has also provided which will be used later in the results section. With all the information obtained and listed in this chapter, it is expected that MC-PS-NH_4NO_3-glycerol can be employed as ionic conductor in the supercapacitor and protonic cells.

CHAPTER 3: RESEARCH METHODOLGY

3.1 Introduction

In this study, methylcellulose (MC)-potato starch (PS) blend was used as the polymer matrix, NH_4NO_3 as the source of ions and glycerol as the plasticizer. Three systems have been prepared which is polymer blend, polymer blend-salt (salted) and polymer blend-salt-plasticizer (plasticized) via solution cast technique. The degree of crystallinity obtained from X-ray diffraction (XRD) analysis was done to confirm the most suitable ratio of MC-PS to serve as the host. In order to check the compatibility of the blend, the blend with the most suitable ratio has been tested using Fourier transform infrared (FTIR), field emission scanning electron microscopy (FESEM), thermogravimetric analysis (TGA) and differential scanning calorimetry (DSC).

In salted system, the blend host was infused with NH_4NO_3. Glycerol was included in the highest conducting salted electrolyte to strengthen the conductivity. The polymer electrolytes were examined via various methods e.g. FTIR, FESEM and impedance spectroscopy. Transference number measurement (TNM) and comparative cyclic voltammetry (CV) studies were used to prove the protonic conduction. The electrochemical stability of the most conducting electrolyte was tested using linear sweep voltammetry (LSV). The electrolyte was utilized in two electrochemical devices applications; electrochemical double-layer capacitor (EDLC) and protonic cell. The EDLC was tested using galvanostatic charge-discharge (GCD) and CV techniques while the protonic cell was characterized via GCD and open circuit potential (V_{oc}).

3.2 Preparation of Samples

3.2.1 Methycellulose-Potato Starch Blend System

PS (Sigma-Aldrich) (*x* wt.%) was added in 1% acetic acid (SYSTERM) (100 mL) at 80 °C for 20 minutes. As the PS solution cooled to room temperature, (100- *x*) wt.% of MC (Sigma-Aldrich) was included. The solutions were poured into Petri dishes and allowed to dry at room temperature (25 °C, Relative humidity ~ 50%) for few days. The dried samples were placed in a dessicator containing silica gel prior to further use. The composition and labeling of various MC-PS starch blends are presented in Table 3.1.

Table 3.1: Composition and labeling of polymer blend.

MC : PS composition (wt.%)	MC (g)	PS (g)	Label
100 : 0	1.0	0	A10
90 : 10	0.9	0.1	A9
80 : 20	0.8	0.2	A8
70 : 30	0.7	0.3	A7
60 : 40	0.6	0.4	A6
50 : 50	0.5	0.5	A5
40 : 60	0.4	0.6	A4
30 : 70	0.3	0.7	A3
20 : 80	0.2	0.8	A2
10 : 90	0.1	0.9	A1
0 : 100	0	1.0	A0

The formed MC-PS film can be observed in Figure 3.1. MC-PS film possesses a rigid and transparent physical appearance.

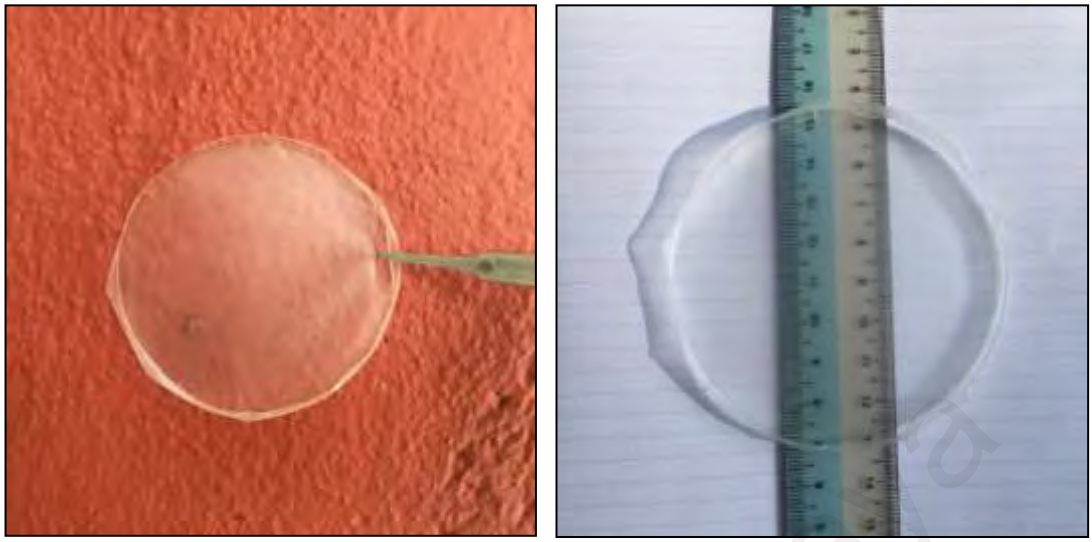

Figure 3.1: Stiff and transparent MC-PS blend film.

3.2.2 Methycellulose-Potato Starch-NH_4NO_3 System

A total of 0.40 g PS was stirred in 1% acetic acid (100 mL) for 20 minutes at 80 °C. When the starch solution cooled to room temperature, 0.60 g MC was mixed together in the solution. NH_4NO_3 (SYSTERM) were added to the solutions varying from 5 wt.% to 40 wt.%. The homogenous solutions were dried at room temperature in a Petri plates for few days. The dried samples were placed in a dessicator containing silica gel prior to further use. The composition and labelling of electrolytes in salted system are listed in Table 3.2.

Table 3.2: Composition and labeling of salted electrolytes.

MC : PS : NH_4NO_3 composition (wt.%)	**MC (g)**	**PS (g)**	**NH_4NO_3 (g)**	**Label**
60 : 40 : 0	0.6	0.4	0.000	A6
57 : 38 : 5	0.6	0.4	0.053	B1
54 : 36 : 10	0.6	0.4	0.111	B2

Table 3.2, continued

MC : PS : NH_4NO_3 composition (wt.%)	MC (g)	PS (g)	NH_4NO_3 (g)	Label
51 : 34 : 15	0.6	0.4	0.177	B3
48 : 32 : 20	0.6	0.4	0.250	B4
45 : 30 : 25	0.6	0.4	0.333	B5
42 : 28 : 30	0.6	0.4	0.429	B6
40 : 26 : 35	0.6	0.4	0.538	B7
36 : 24 : 40	0.6	0.4	0.667	B8

The physical characteristic of MC-PS-NH_4NO_3 is shown in Figure 3.2.

Figure 3.2: Flexible and transparent MC-PS-NH_4NO_3 blend film.

3.2.3 Methycellulose-Potato Starch-NH_4NO_3-Glycerol System

The plasticized electrolytes were prepared by mixing 0.60 g MC with 0.40 g PS in 1% acetic acid (100 mL) at 80 °C. Then 30 wt.% or 0.43 g of NH_4NO_3 was included in the blend solution. The plasticization was done by varying the concentration of glycerol from 10 wt.% to 50 wt.%. The dissolved solutions were placed in Petri dishes for few

days. The dried samples were placed in a dessicator containing silica gel prior to further use. The composition and labeling for the plasticized electrolytes was tabulated in Table 3.3.

Table 3.3: Composition and labeling of plasticized electrolytes.

MC : PS : NH_4NO_3 : Glycerol composition (wt.%)	MC (g)	PS (g)	NH_4NO_3 (g)	Glycerol (g)	Label
42 : 28 : 30 : 0	0.6	0.4	0.429	0.000	B6
38 : 25 : 27 : 10	0.6	0.4	0.429	0.158	C1
34 : 22 : 24 : 20	0.6	0.4	0.429	0.357	C2
29 : 20 : 21 : 30	0.6	0.4	0.429	0.612	C3
25 : 17 : 18 : 40	0.6	0.4	0.429	0.953	C4
21 : 14 : 15 : 50	0.6	0.4	0.429	1.430	C5

The physical characteristic of MC-PS-NH_4NO_3-glycerol is demonstrated in Figure 3.3.

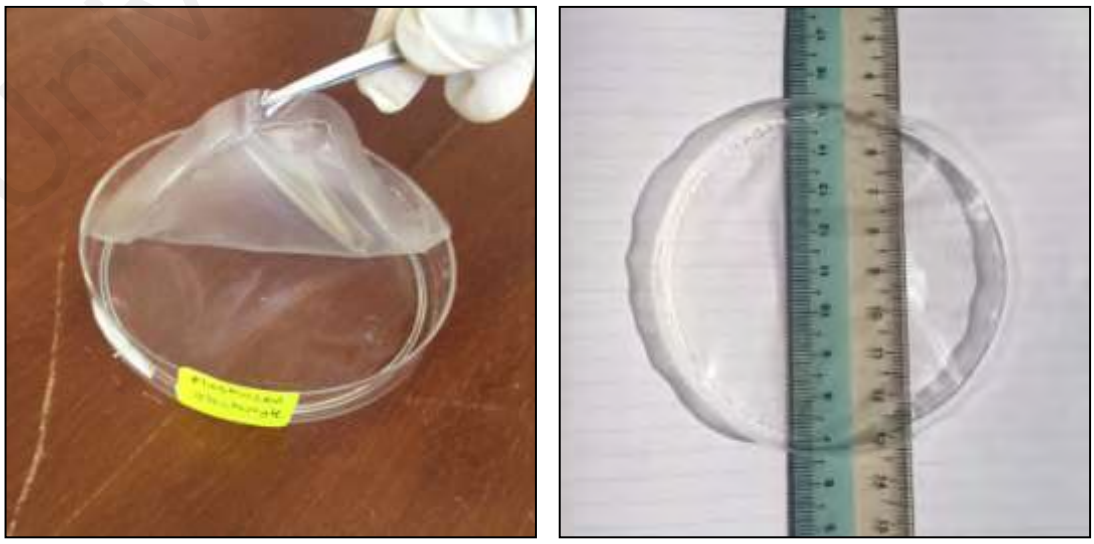

Figure 3.3: Flexible and transparent MC-PS-NH_4NO_3-glycerol blend film.

3.3 Characterization of Electrolytes

3.3.1 Fourier Transform Infrared (FTIR) Analysis

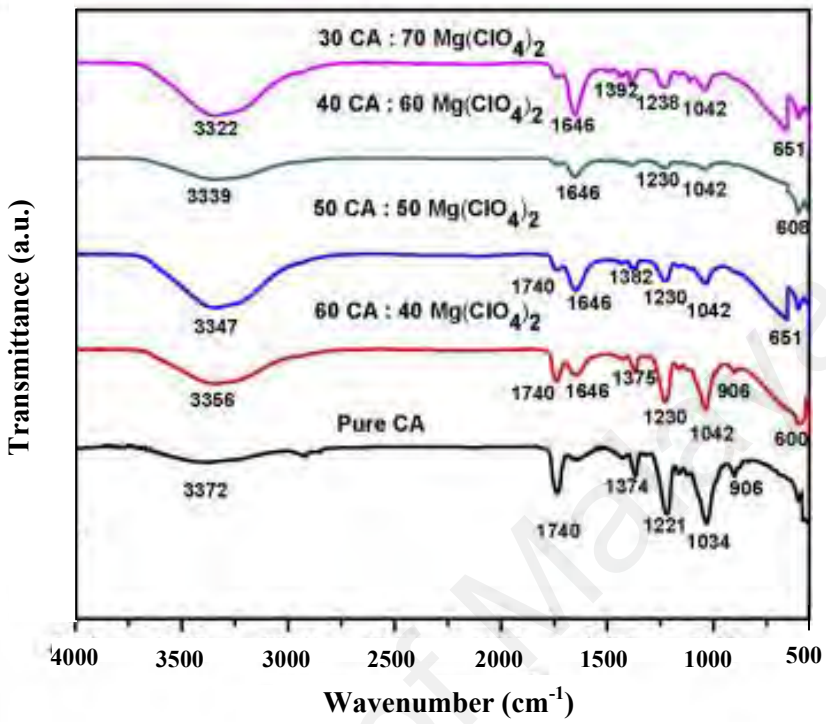

Figure 3.4: (a) FTIR spectra for cellulose acetate-$Mg(ClO_4)_2$ system (Mahalakshmi et al., 2019).

FTIR analysis was used to confirm the coordination of cation of salt at the functional groups of the polymer electrolyte. Molecule in the electrolyte experiences spectroscopic transition from lower to upper vibrational energy level as infrared is absorbed. Different molecules and atoms are vibrating at different frequencies, thus the changes in the peak position and intensity in an infrared spectrum indicates the polymer-salt interaction (Kuo et al., 2013). Spotlight 400 Perkin-Elmer spectrometer was employed to obtain the infrared spectra for the electrolytes. The infrared spectra were recorded in the transmission mode from 450 to 4000 cm^{-1} at 1 cm^{-1} resolution. The FTIR was done at room temperature. Deconvolution method was used to extract any overlapping peaks. Correction of baseline and curve fitting was implemented via Gaussian-Lorentzian mixed mode.

Figure 3.4 shows the FTIR for cellulose acetate (CA)-magnesium perchlorate ($Mg(ClO_4)_2$ polymer electrolyte system (Mahalakshmi et al., 2019). Different functional groups possess different wavenumber. It is noticeable that the peak of pure CA shifted to lower wavenumber which signifies the bonding of polymer chain and salt. The authors explained the phenomenon of salt recombination and recrystallization via FTIR results.

3.3.2 X-Ray Diffraction (XRD)

The amorphousness of the polymer electrolytes was identified using XRD analysis. In XRD method, an X-ray light with wavelength, λ, pass through the material at various angles, θ. Constructive interferences and diffracted ray produced from the interaction between material and the incident rays can be explained from the following Bragg's condition:

$$n_r\lambda = (2d_i)\sin\theta \tag{3.1}$$

where θ stands for Bragg's angle or the angle between the planes and incident beam, λ is the wavelength, n stands for reflection order and d is interplanar spacing. Siemens D5000 X-ray diffractometer was employed with 2θ from 5° to 80° at 0.1° resolution. Figure 3.5 depicts the example of XRD patterns for polyacrylonitrile (PAN)-NH_4Br electrolyte system (Sikkanthar et al., 2014). The authors stated that the concentration of salt influenced the amorphousness of the polymer electrolytes.

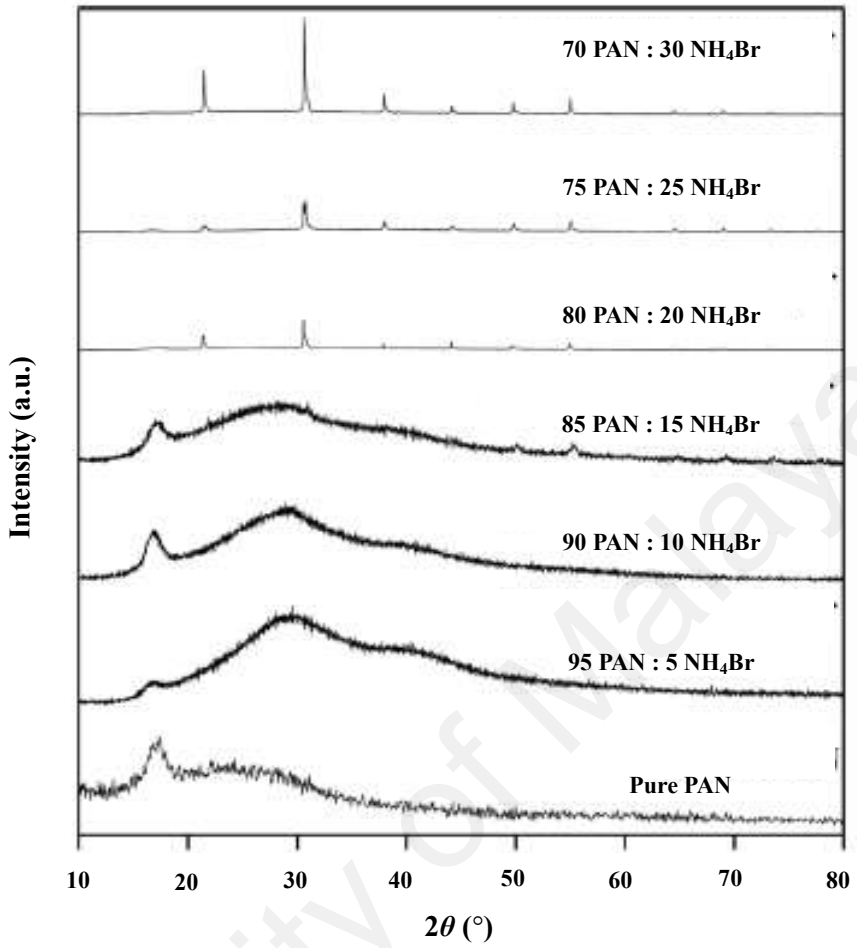

Figure 3.5: XRD pattern for PAN-NH_4Br system (Sikkanthar et al., 2014).

3.3.3 Field Emission Scanning Electron Microscopy (FESEM)

In FESEM, an electron beam projected to a surface of a material where the beam interacts with the molecules and create different signal that can be detected. These signals possess the information regarding the surface morphology and topography. In this work, the miscibility of the blend was studied by analyzing the FESEM image of the cross-section of the blend sample. For salted and plasticized electrolytes, FESEM was employed to examine the morphological changes of electrolyte surface and relate it with the trend of conductivity. Hitachi SU8220 scanning electron microscope was used to conduct FESEM with ×1k and ×1.5k magnification for the cross section and surface

of the polymer electrolytes, respectively. Figure 3.6 shows the surface of PMMA-$Mg(CF_3SO_3)_2$ electrolytes. The surface of the electrolyte becomes well dispersed with the impregnation of salt. This phenomenon inferring that the polymer electrolyte has become more amorphous. When more than 20 wt.% of $Mg(CF_3SO_3)_2$ was added, solid crystalline particles appear on the surface indicating the recrystallization of the salt (Zainol et al., 2013).

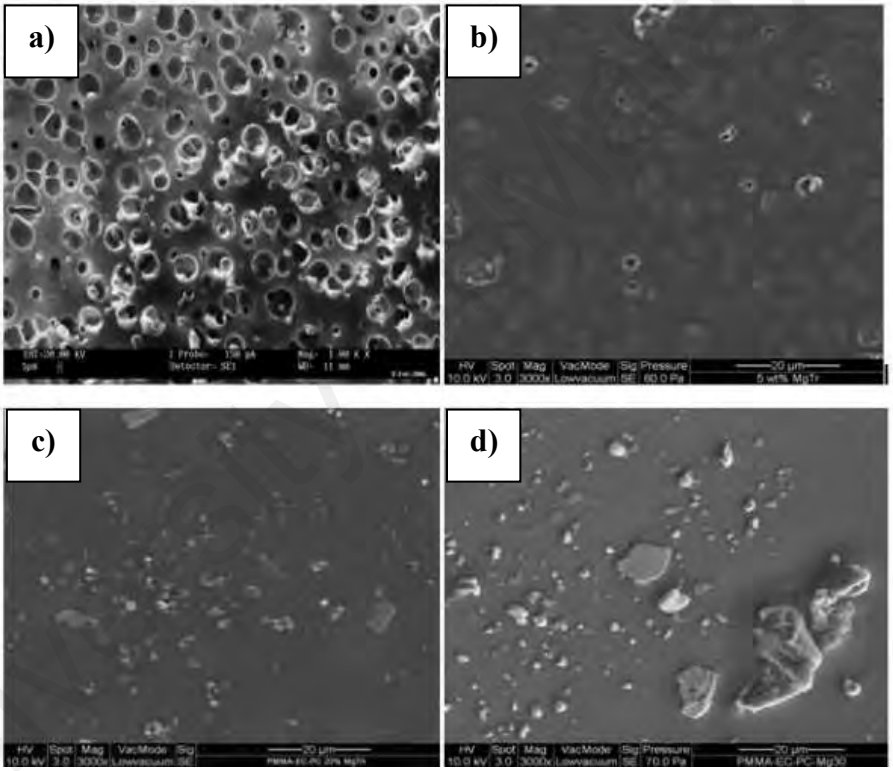

Figure 3.6: FESEM micrographs for pure PMMA with (a) 0 wt.%, (b) 5 wt.%, (c) 20 wt.% and 30 wt.% $Mg(CF_3SO_3)_2$ (Zainol et al., 2013).

3.3.4 Thermogravimetric Analysis (TGA)

Degradation temperature and water content information of the electrolyte can be studied using TGA analysis. Different material will decompose at different temperature. Furthermore the impregnation of salt into a polymer matrix also will change the value

of decompose temperature. In TGA measurement, a constant flow of heat is applied through a material in a controlled environment and the changes in material's weight were recorded. In this work, STA 6000 Perkin Elmer was used at a heating rate of 20 °C min^{-1} from 25 to 700 °C. Figure 3.7 illustrates the TGA thermograms for pure dextran (Azmeera, Adhikary & Krishnamoorthi, 2012). The authors reported that the decomposition below 100 °C is due to water and dextran decomposes at 300 °C.

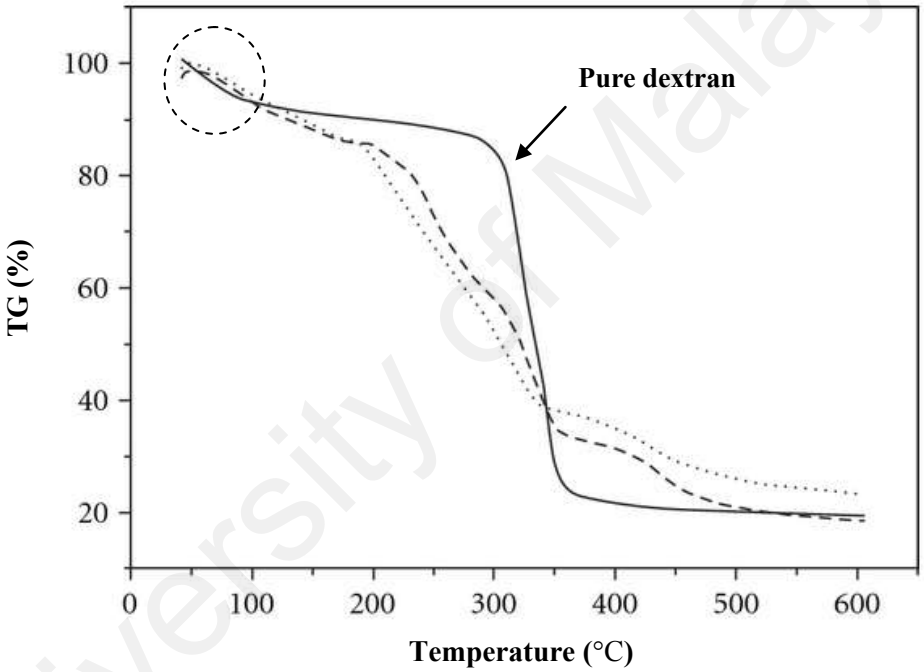

Figure 3.7: TGA thermograms of dextran (Azmeera, Adhikary & Krishnamoorthi, 2012).

3.3.5 Differential Scanning Calorimetry (DSC)

In polymer blend studies, the miscibility of the polymers can be determined via the analysis of glass transition temperature, T_g. Ionic conduction is more efficient in amorphous region where the transportation is dependent on polymer's segmental motion. Lower value of T_g portrays the enhancement of segmental motion (Sikkanthar

et al., 2014). The sample was placed in a sealed aluminum crucible. TA Instruments Q200 was used with operating temperature from −80 to 120 °C at 10 °C min^{-1} of cooling/heating rate. A total of 50 mL min^{-1} of nitrogen flow was used in this experiment. Figure 3.8 shows the DSC curve for PEMA-$NH_4SO_3CF_3$ with the addition of butyl-trimethyl ammonium bis(trifluoromethylsulfonyl)imide (BMATFSI). T_g can be observed when there is a change of gradient in heat flow. The addition of BMATFSI reduces the value of T_g indicates the polymer has become more flexible and the increase in ionic conductivity (Anuar, Subban & Mohamed, 2012).

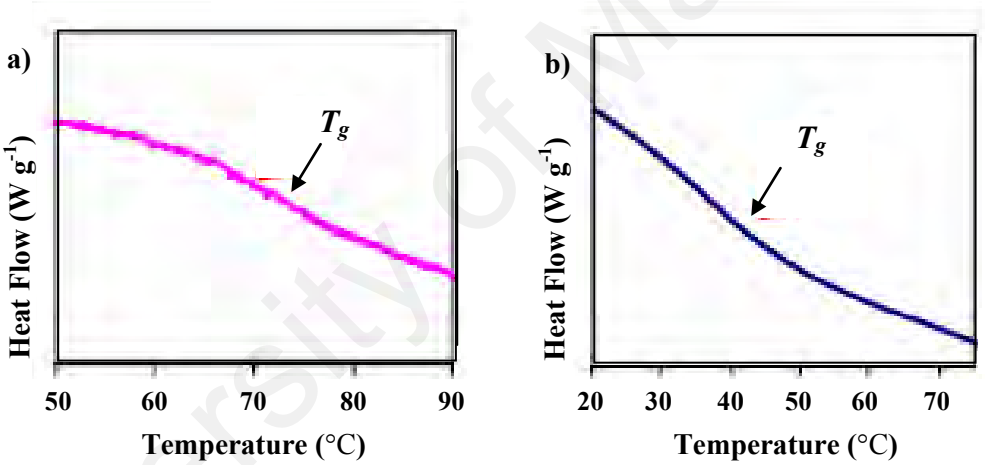

Figure 3.8: DSC of (a) salted and (b) plasticized electrolyte (Anuar et al., 2012).

3.3.6 Impedance Spectroscopy

One of the most crucial characteristics of an electrolyte that need to be determined is the ionic conductivity. Electrolyte with high conductivity can improve the performance of energy devices. Suitable size of electrolyte films were prepared and placed in between two stainless steel of a holder as shown in Figure 3.9.

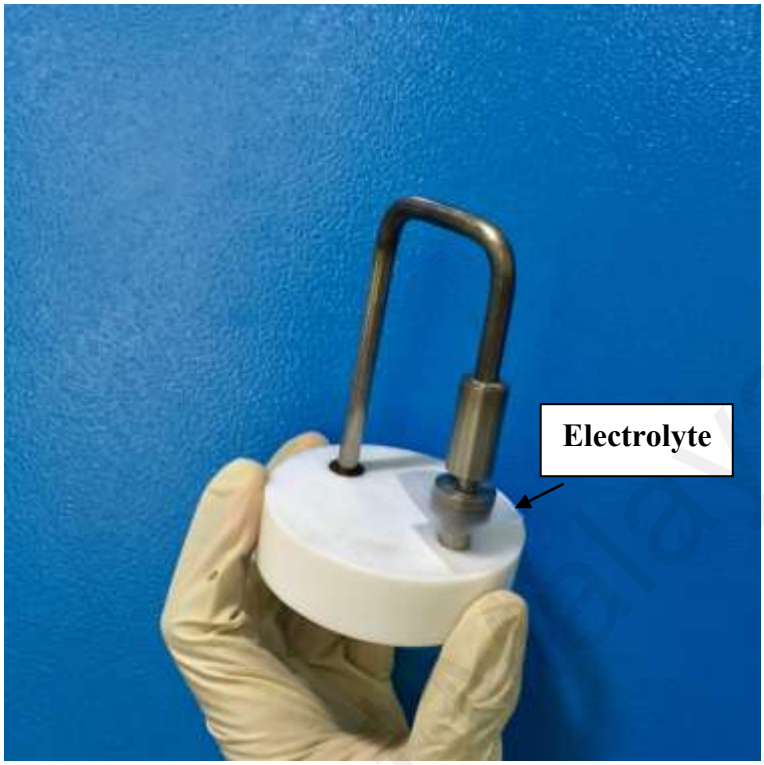

Figure 3.9: Electrolyte film in between stainless steel of a conductivity holder.

Impedance spectroscopy was conducted using HIOKI 3532–50 LCR HiTESTER. The impedance measurements were done in the frequencies of 50 Hz to 5 MHz at 298 K to 343 K. The conductivity, σ of the electrolyte with thickness d was calculated via the following equation:

$$\sigma = d \times (R_b A)^{-1} \tag{3.2}$$

From impedance analysis, Nyquist plot was generated where the value of R_b can be extracted. Nyquist plot for pristine PVA film at room temperature can be observed in Figure 3.10. The interception between semicircle and the adjacent line is where the value of R_b is located (Selvasekarapandian, Hema, Kawamura, Kamishima & Baskaran,

2010). Area of the stainless steel surface is given as A which is 2.01 cm^2. The thickness of the electrolyte was determined using Mitutoyo electronic micrometer gauge. Results from EIS were used to analyze dielectric and modulus behavior.

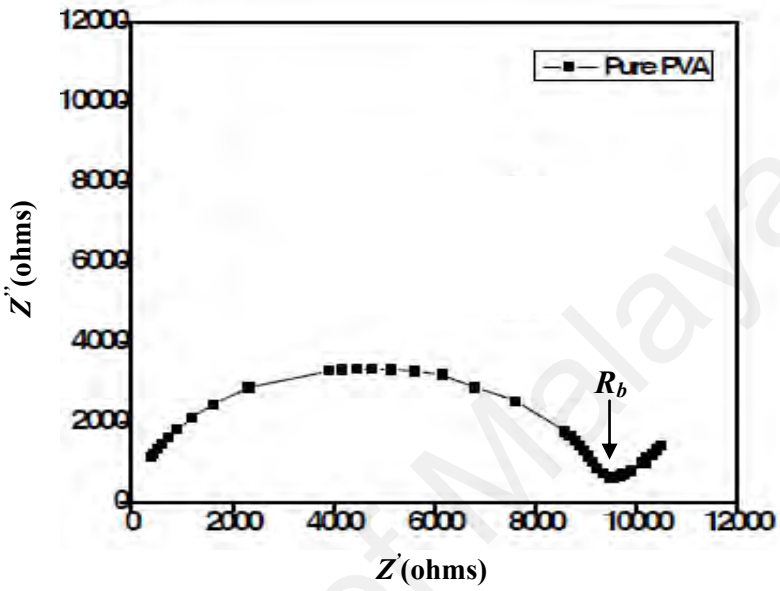

Figure 3.10: Pure PVA film Nyquist plot (Selvasekarapandian et al., 2010).

3.3.7 Transference Number Analysis

It is well known that transference number analysis has been used by many researchers to identify the conducting species in an electrical conductor. From this analysis, transference number for ion (t_i) and electron (t_e) can be discovered. V&A Instrument DP3003 digital dc power source was incorporated for this analysis. DC polarization method by Wagner and Wagner (1957) was employed where a constant potential of 0.2 V was subjected to the cell with arrangement of stainless steel (SS)|electrolyte|SS.

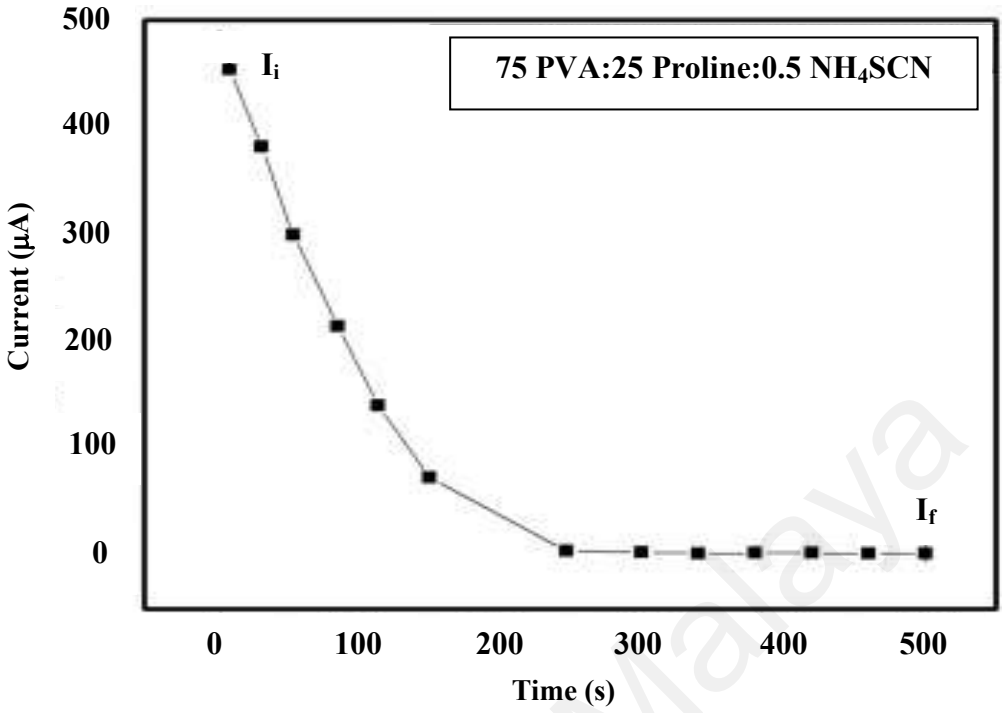

Figure 3.11: Polarization of PVA-proline-NH_4SCN (Hemalatha, Alagar, Selvasekarapandian, Sundaresan & Moniha, 2019).

Figure 3.11 shows the polarization of PVA-proline-NH_4SCN system (Hemalatha et al., 2019). They have found that $t_i > t_e$ thus they concluded that the main conducting species PVA-proline-NH_4SCN electrolyte system were ions. The highest conducting electrolyte in this study acts as the electrodes separator for the protonic cell. Thus, cation contribution to the overall conduction must be determined. A simple method by Watanabe, Nagano, Sanui and Ogata (1988) was employed to identify the cation transference number (t_c). In order to focus the contribution of cation, the use of anion blocking electrode is compulsory. In this work manganese (IV) oxide (MnO_2) (Sigma-Aldrich) was used as the electrode instead of SS. The composition of the electrode was MnO_2 (0.44 g), activated carbon (0.04 g) from Kuraray and polytetrafluoroethylene (PTFE) (0.08 g) as a binder. These materials were combined using ball miller for 10

minutes. The mixed powder was pressed via hydraulic press for ~ 20 minutes. The arrangement for the cell was MnO_2|electrolyte|MnO_2.

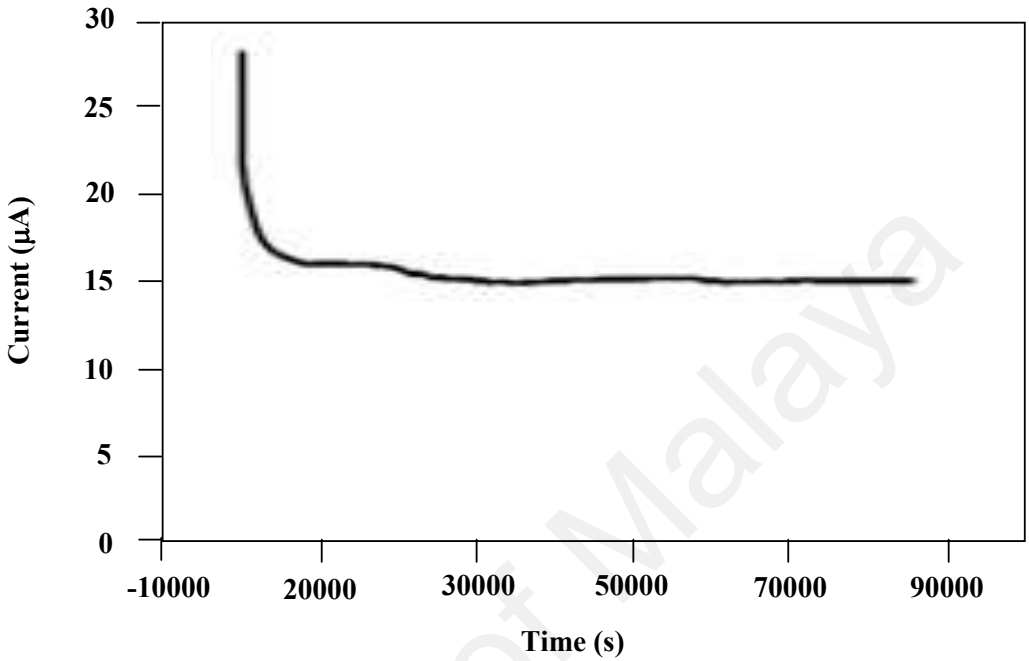

Figure 3.12: Polarization of MnO_2|electrolyte|MnO_2 at 0.2 V (Woo, Majid & Arof, 2011).

Figure 3.12 shows the polarization of PCL-NH_4SCN system with MnO_2 electrodes (Woo et al., 2011). The authors reported that t_c of 0.21 and stated that ion association may affected the transference number but still gives a good understanding towards the process of ionic conduction.

3.3.8 Linear Sweep Voltammetry

The limit of operating voltage for an electrolyte must be checked before employing it in electrical energy devices. Digi-IVY DY2300 potentiostat was used in linear sweep voltammetry (LSV) analysis. The working, reference and counter electrodes used were

stainless steel (SS). Current at working electrode is monitored as the potential is swept linearly in time between reference and working electrode. The arrangement of the cell for LSV analysis was SS|electrolyte|SS. The cell was subjected to a scan rate of 1 mV s^{-1} from 0 to 2.20 V. The measurement was varied from room temperature to 343 K.

Figure 3.13 shows LSV plot for PVC-$NH_4CF_3SO_3$-BATS electrolyte. Deraman, Mohamed and Subban (2013) reported that there was no obvious change in current from 0 V to 1.10 V indicating that PVC-$NH_4CF_3SO_3$-BATS electrolyte can be used up to operating voltage of 1.10 V with room temperature conductivity of 1.56×10^{-4} S cm^{-1}. The electrolyte was employed in the construction of protonic cells by the authors. The decomposition voltage of an electrolyte must be at least 1 V for protonic energy storage devices.

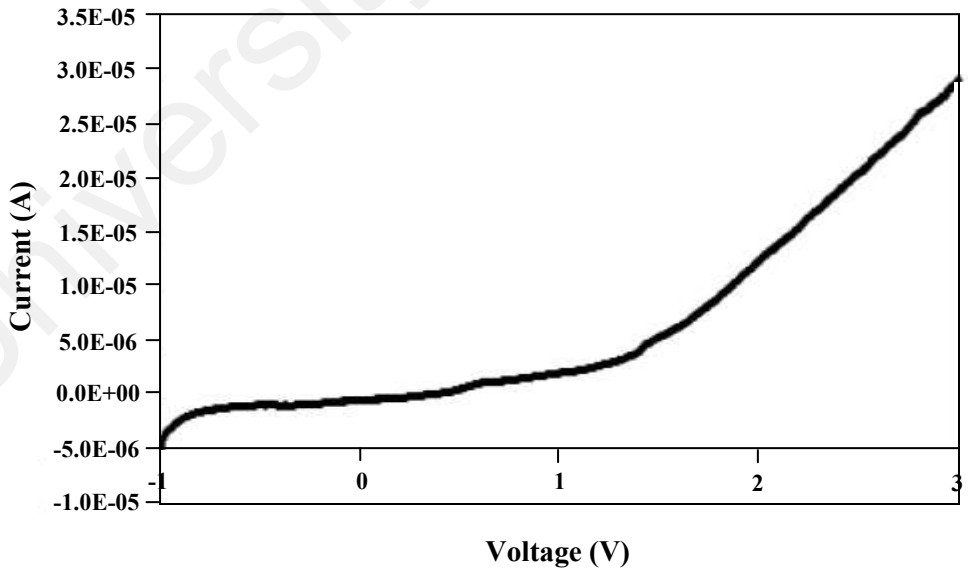

Figure 3.13: LSV PVC-$NH_4CF_3SO_3$-BATS (Deraman et al., 2013).

3.3.9 Cyclic Voltammetry

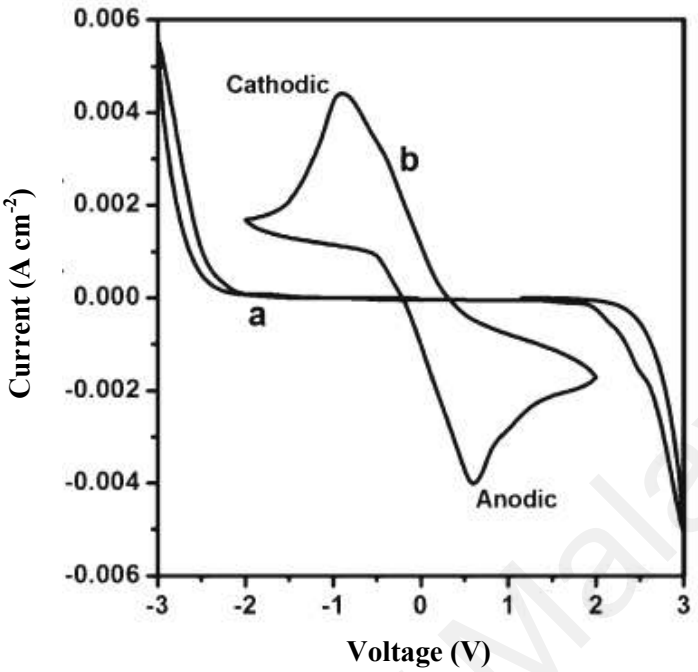

Figure 3.14: CV for (a) SS|PVdF-HFP/PVP-BMImHSO$_4$|SS and (b) cell Zn|PVdF-HFP/PVP-BMImHSO$_4$|Zn (Mishra, Hashm & Rai, 2014).

One of the techniques to check the occurence of protonic conduction is through comparative cyclic voltammetry (CV) measurement. Digi-IVY DY2300 potentiostat was used to conduct CV. The chosen scan rate for CV was 5 mV s^{-1}. Zinc|$ZnSO_4.7H_2O$ and stainless steel electrodes were employed as reversible and blocking electrodes, respectively. Figure 3.14 shows the cyclic voltammetry for protonic-based PVdF-HFP/PVP electrolyte with different electrodes at a scan rate of 5 mV s^{-1}. Mishra et al. (2014) reported that the appearance of anodic and cathodic peaks proves the protonic conduction.

3.4 Construction and Characterization of Supercapacitor

3.4.1 Preparation of Electrodes

Figure 3.15 shows the illustration of the fabricated EDLC in this work.

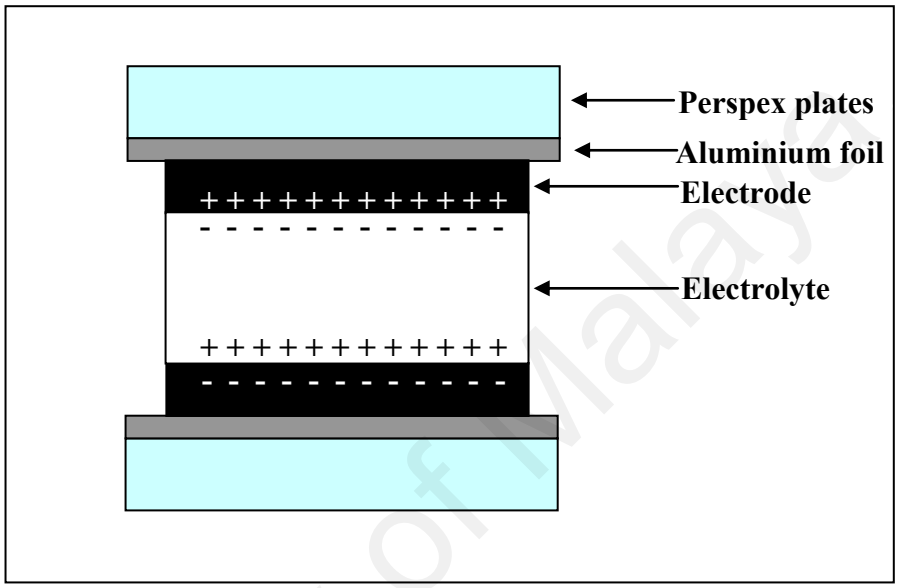

Figure 3.15: Illustration of the fabricated EDLC.

The electrodes for the EDLC consisted of polyvinylidene fluoride (PVdF) (12.5 wt.%) as the binder, carbon black (6.25 wt.%) as the electronic conductor and activated carbon (81.25 wt.%) as the active material. These three powders were mixed using ball miller for 10 minutes. The solvent used to dissolve these powders was 30 mL of N-methyl pyrrolidone from EMPLURA. The electrode solution was then coated on aluminium foil using doctor blade. The coated aluminium foil was dried in an oven at ~ 60 °C. The thickness of the electrode is 25 mm. The dried electrodes were placed in a dessicator.

3.4.2 Characterization of Supercapacitor

The fabricated EDLC was tested using two characterizations which are charge-discharge measurement and cyclic voltammetry. Neware battery cycler was used to run galvanostatic charge-discharge (GCD) measurement. The EDLC was charged to 0.85 V and discharged to 0 V for 1000 complete cycles. The EDLC was exposed to a current density of 0.2 mA cm^{-2}.

Specific capacitance (C_s), cycling efficiency (η), equivalent series resistance (R_{es}), power density (P_d) and energy density (E_d) are the important characteristics of the EDLC. These crucial characteristics will be discussed in Chapter 8. Figure 3.16 depicts the GCD curves for MC-NH_4NO_3-PEG electrolyte. Shuhaimi (2011) stated that the small voltage drop before discharge part is due to internal resistance and the R_{es} of the EDLC were 109.1 and 122.4 Ω at 0.22 and 1.39 mA cm^{-2}, respectively.

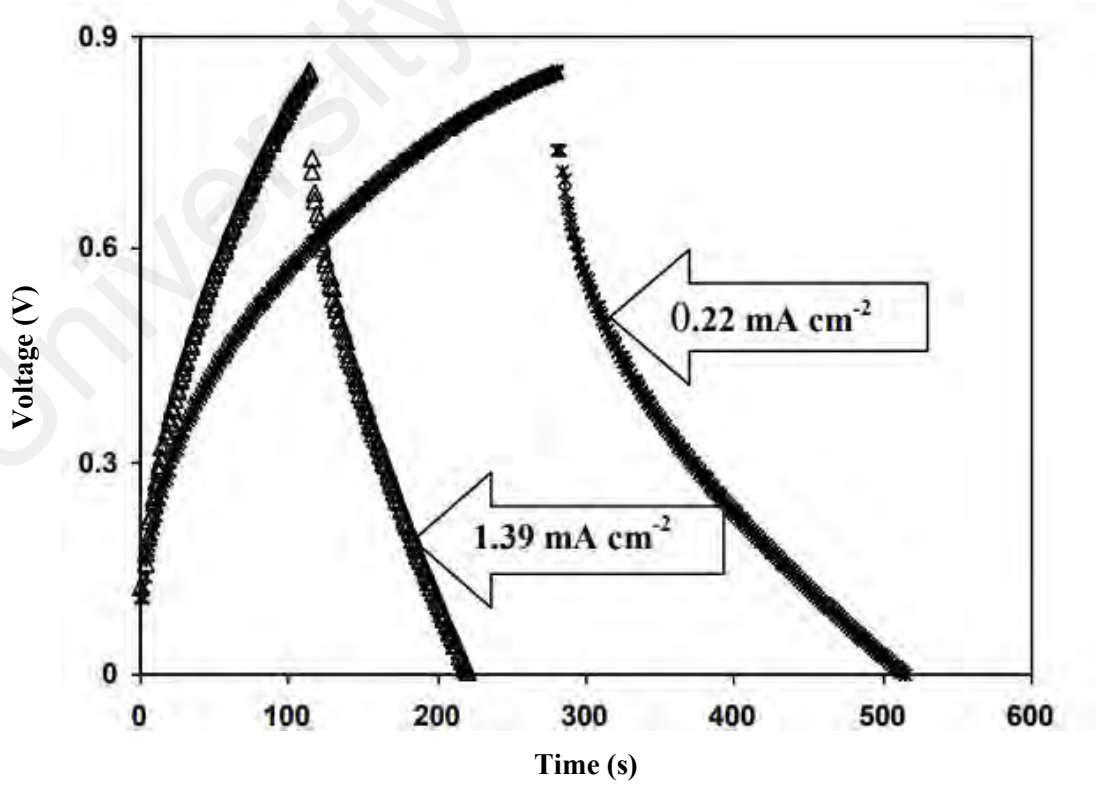

Figure 3.16: Charged-discharged for EDLC with MC-NH_4NO_3-PEG electrolyte (Shuhaimi, 2011).

One of the purposes of CV for EDLC was to confirm the value of C_s obtained from GCD (Teoh, Lim, Liew, Ramesh & Ramesh, 2015). Potential for the EDLC was set from 0 to 0.85 V via Digi-IVY DY2300 potentiostat with various scan rate e. g. 2, 5, 10, and 20 mV s^{-1}. CV also can portray the double-layer behavior when there are no peaks appeared in the CV plot which can be observed in Figure 3.17. Liew (2015) reported that no occurrence of redox reaction and the shape of CV curves are not rectangular enough is due to porous morphology of carbon electrodes and internal resistance.

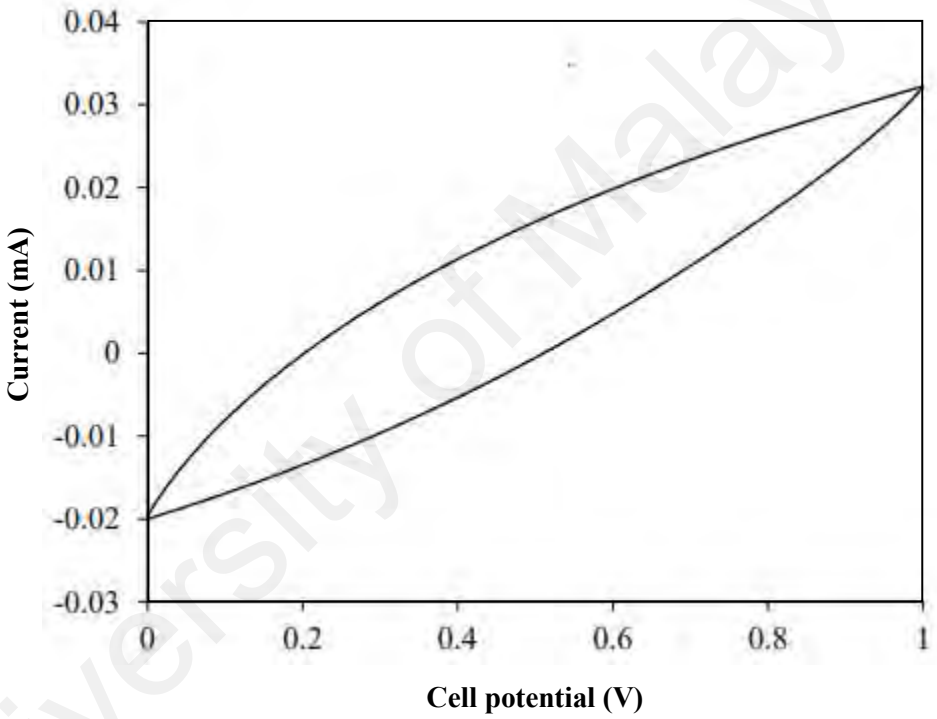

Figure 3.17: CV for PVA-$NH_4CH_3CO_2$ based EDLC (Liew, 2015).

3.5 Construction and Characterization of Protonic Cell

3.5.1 Preparation of Electrodes

Figure 3.18 depicts the illustration of the fabricated protonic cell. In this work, the cathode consisted of 0.88 g of MnO_2, 0.08 g of carbon black and 0.02g of PTFE while the anode consisted of 0.62 g of zinc, 0.30 g of $ZnSO_4.7H_2O$, 0.04 g of carbon black and 0.04 g of PTFE. These zinc-based and MnO_2-based electrodes were mixed separately

via ball miller for 10 minutes. In order to form electrode pellets, the mixture was pressed with hydraulic press for 20 minutes at 5 metric ton. As shown in Figure 3.15, the arrangement of the protonic cell was MnO_2|electrolyte|Zinc.

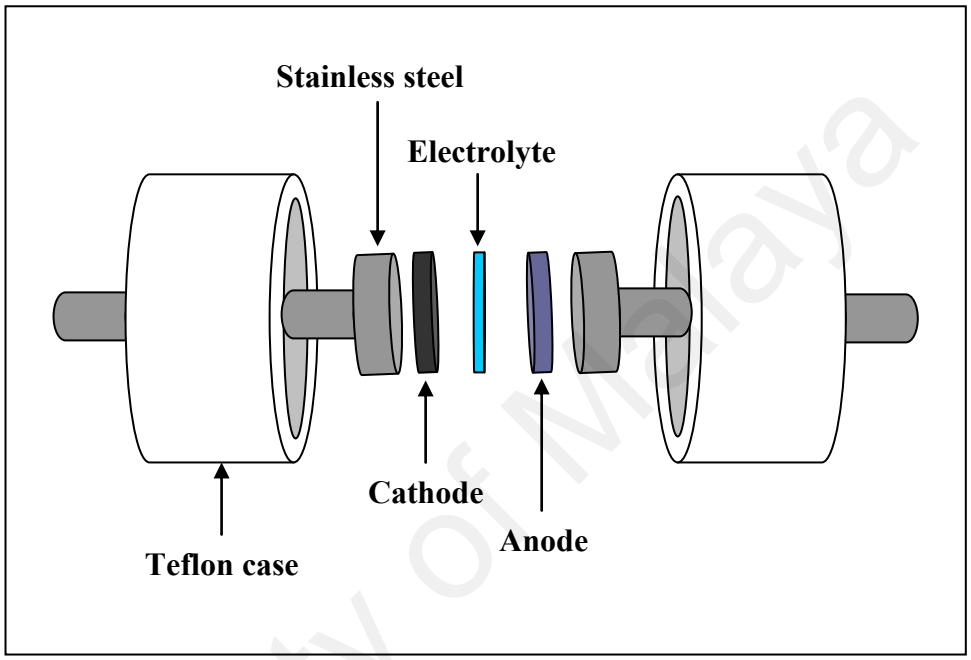

Figure 3.18: Illustration of the fabricated protonic cell.

3.5.2 Characterization of Protonic Cell

The most common characteristic of a cell or battery is open circuit potential (V_{oc}). When a cell is not subjected with any load, electric field or external circuit, there is a potential difference among the terminals of the cell denoted as V_{oc} (Dai, Peng, Chae & Chen, 2015). Figure 3.19 show example of V_{oc} for CMC-NH_4Br based protonic cell. Material used by Samsudin and Isa (2015) for anode and cathode were zinc and MnO_2, respectively. The authors reported that the V_{oc} of the protonic cell was initially at ~ 1.6 V and stabilized at 1.48 V for 24 hours. In this study, V_{oc} of the fabricated

protonic cell was tested for 24 hours via Neware battery cycler. The V_{oc} was tested at different temperature.

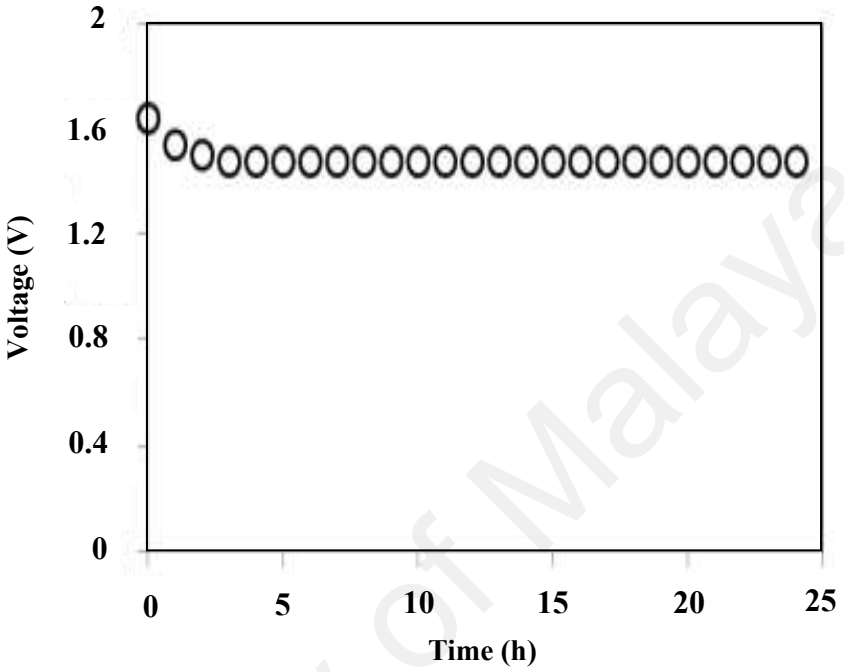

Figure 3.19: Open circuit potential for CMC-NH_4Br (Samsudin & Isa, 2015).

A battery cycler (Neware) was used to study the discharge characteristic of the protonic cell. The protonic cell was charged and discharged at constant currents of 1 mA, 2 mA, 3 mA and 4 mA. The discharge characteristic of the fabricated protonic cell also was performed at different temperature at constant current of 3 mA. Figure 3.20 shows the discharge profile for protonic cell at different temperature at 0.03 mA (Nyuk & Isa, 2017). The authors reported that the discharge capacity increases as the temperature increases. The author then concluded that the increase in temperature created more ions to be involved in intercalation/deintercalation process.

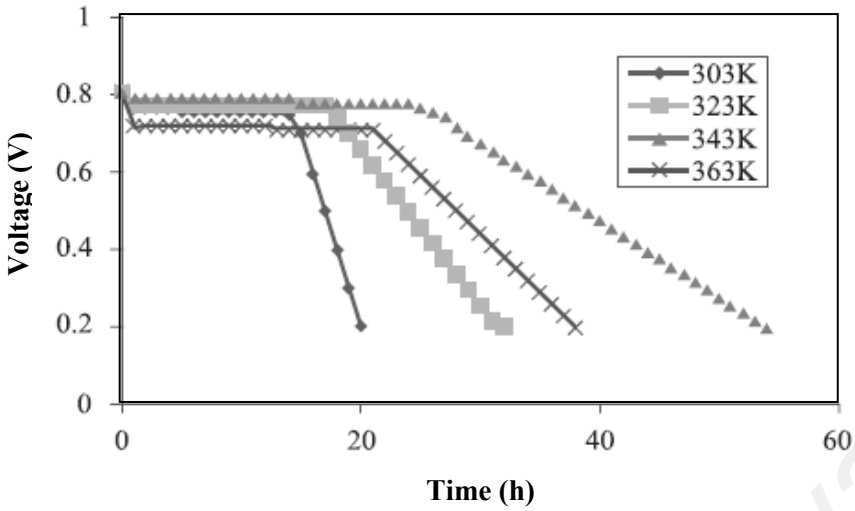

Figure 3.20: Discharge profile at elevated temperature.

Other characteristics for the protonic cell are relation between current and potential or called as *I-V* characteristic. Second characteristic is relation between current density and power density or called as *J-P* characteristic. These two characteristics were identified via current draining from 1.6 µA to 65 mA. *I-V* characteristic and *J-P* characteristic were tested at elevated temperature from 298 K to 343 K. Figure 3.21 shows the *I-V* characteristic and *J-P* characteristic at elevated temperature for protonic cell with chitosan–NH_4NO_3–EC electrolyte (Ng & Mohamad, 2008).

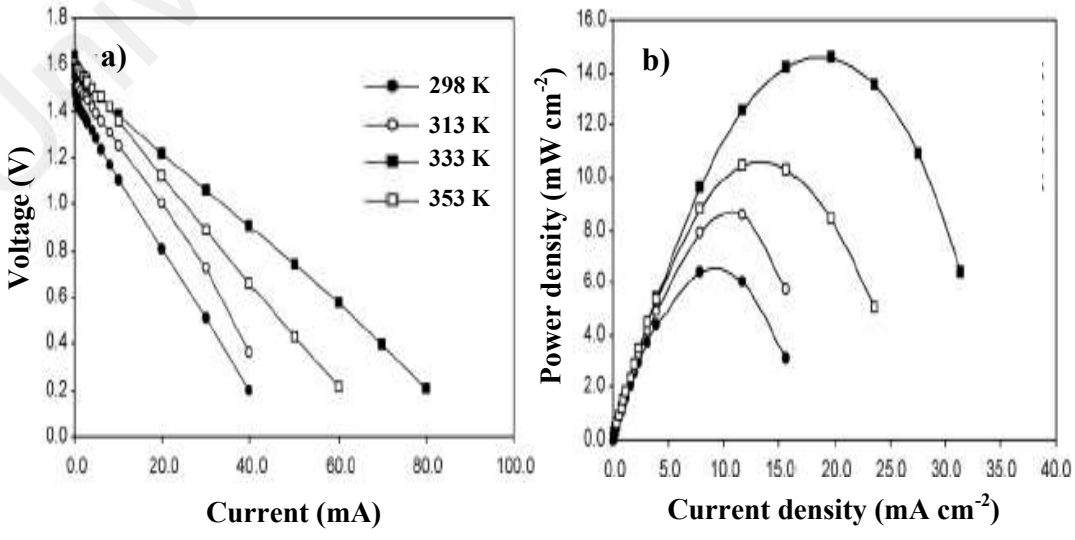

Figure 3.21: (a) Current-potential and (b) current density–power density curves of protonic cells at 298, 313, 333 and 353K

The rechargeability of the protonic cell is the most crucial properties in order to be useful in modern electrical gadgets. The ability to discharge and charge the protonic cell was tested using Neware battery cycler with fast and slow constant current which is 4 mA and 1 mA, respectively. The protonic cell in this work was tested from 1 V to 1.5 V for 15 cycles. Figure 3.22 shows the polymer blend based rechargeable protonic cell (Mishra et al., 2014). The authors tested the battery at constant current of 50 μA from 1 V to 1.6 V for 10 cycles. They also concluded that the poor charge-discharge ability is due to structural modification of cathode.

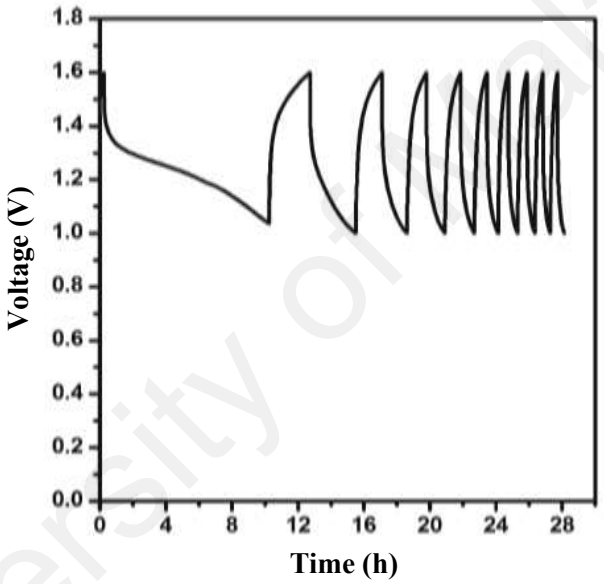

Figure 3.22: Charge-discharge for the protonic cell (Mishra et al., 2014).

3.6 Summary

This part of the thesis has explained the preparation of MC-PS polymer electrolytes. Various techniques have been used to characterize the electrolyte as listed in this chapter. Electrolyte with the highest conductivity value has been incorporated in the construction of the supercapacitor and protonic cell. Outcomes from the characterizations performed using the method listed in this chapter will be further explained in next chapters.

CHAPTER 4: CHARACTERIZATIONS OF POLYMER BLEND HOST

4.1 Introduction

It is well known that the blend of two or more polymers allowed researchers to develop new polymer electrolytes (PEs). Polymer blending possesses a simple fabrication method and inexpensive (Rudziah, Mohamed & Ahmad, 2013). The most crucial parameter in polymer blend studies is the miscibility of the polymers. Good miscibility between the polymers portrays a good intermolecular interaction (Aid, Eddhahak, Ortega, Froelich & Tcharkhtchi, 2017). Hana, Shia and Jin (2013) stated that the ratio of the polymer components affected the amorphousness of polymer blend. According to El-Hadi (2019), the amorphousness of poly(L-lactic acid) increases as the concentration of poly(DL-lactic acid) increases from 25 to 50 wt.%. Report by Abdelrazek, Hezma, El-khodary and Elzayat (2016) illustrates that the intensity of crystalline peaks of polycaprolactone decreases with the increase in the amount of polymethyl methacrylate.

Excellent intermolecular interaction between starch and cellulose has been reported by Babu et al. (2014) where the tensile strength of starch increases with the addition of cellulose. Rodriguez, Flores, Martinez, Castillo and Espinoza (2015) reported that an increase in thermal stability of cellulose-starch blend via thermogravimetric analysis (TGA). Hence, it is crucial to identify the suitable amount of methylcellulose (MC) and potato starch (PS) to serve as a good polymer host. In this work, MC-PS blend has been tested with several characterizations i.e. XRD, FESEM, TGA and DSC.

4.2 XRD Analysis

The ionic conduction is preferable in the amorphous region of the electrolyte. Thus the suitable ratio of the polymer components can be identified via XRD analysis. MC is known of its film-forming properties while starch possesses a brittle film structure (Kathe & Kathpalia, 2017). Bourtoom and Chinnan (2008) stated that the flexibility, miscibility and crystallinity of a polymer blend are affected by the ratio of the chosen polymers.

One of the methods to observe the changes in crystalline peaks in a polymer electrolyte is deconvolution method. The raw results from XRD analysis may possess overlapping peaks which is difficult to be analyzed. Typically, amorphous part possesses broad and wide peaks while crystalline part has small, narrow and sharp peaks (Terinte, Ibbett & Schuster, 2011). The degree of crystallinity (χ_{crys}) of each sample can be identified using the following equation:

$$\chi_{crys} = (A_s - A_{am}) \times A_s^{-1} \times 100\% \quad (4.1)$$

The summation of crystalline and amorphous part area is denoted as A_s while area of amorphous part is given as $A_{am.}$ These areas are determined via Origin 8.5 software.

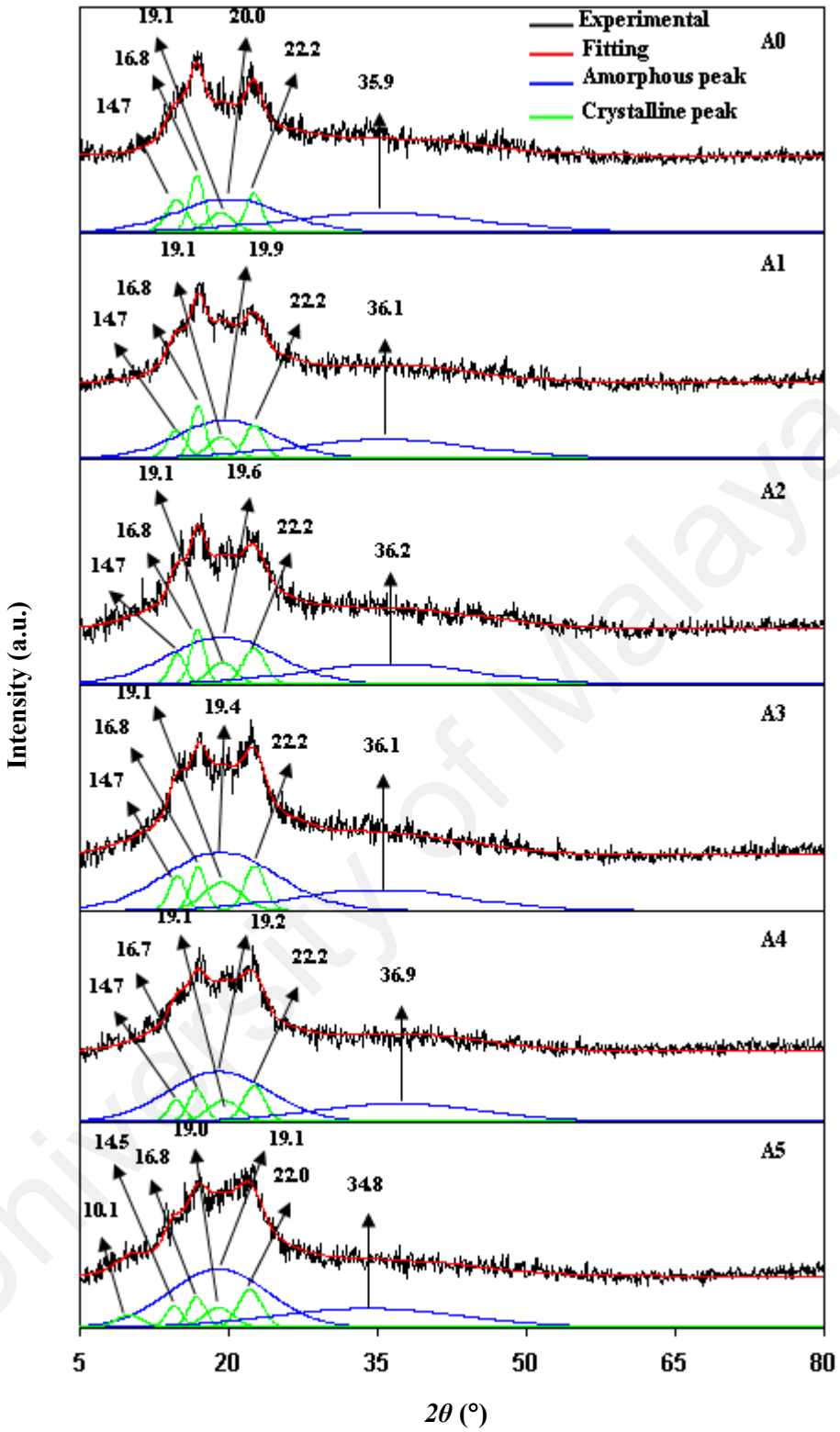

Figure 4.1: A0 to A5 polymer blend's deconvoluted XRD patterns.

The deconvoluted XRD patterns for A0, A1, A2, A3, A4 and A5 blend are shown in Figure 4.1. XRD pattern of A0 (PS film) possesses two amorphous peaks at $2\theta = 20.0°$

and 35.9°. Four crystalline peaks appeared at 2θ = 14.7°, 16.8°, 19.1° and 22.2° in XRD pattern of A0 with notations (Miller indices) of [120], [121], [103] and [113], respectively, (Singh, Ali, Somashekar & Mukherjee, 2006; Rubio, Flanagan, Gilbery & Gidley, 2008). These result is comparable to the one reported by Amran, Manan & Kadir (2016). The presence of both amorphous and crystalline part is an evidence of a semicrystalline material (Shukur, 2015). The addition of MC reduces the intensity of the crystalline peaks as observed in XRD pattern of A1. As the concentration of MC increases, the intensity of all crystalline peaks reduces as depicted in XRD pattern of A4. The XRD patterns for A1, A2, A3 and A4 have similar pattern with A0 due to high concentration of starch. As 50 wt.% of MC (A5) is blended, a new crystalline peak appeared at 2θ = 10.1°, which belongs to MC.

Figure 4.2 displays the deconvoluted XRD patterns for A6, A7, A8, A9 and A10. As 60 wt.% of MC (A6) is added, all five crystalline peaks at 2θ = 10.1°, 14.4°, 16.8°, 19.2° and 22.1° have been suppressed. Furthermore, the intensity of crystalline peaks for A6 is smaller compared to A0, A1, A2, A3, A4 and A5 which indicates that A6 possesses less crystalline structure. It is noticeable that the intensity of the crystalline peaks increase as the 70 wt.% of MC (A7) is added. In addition, two peaks can be monitored at 2θ = 8.0° and 10.3° which are attributed to MC. The crystalline peaks continue to increase as more MC is included. The XRD pattern for A10 (pure MC film) has crystalline peaks at 2θ = 8.3° [040], 10.2° [001], 16.3° [101], 19.8° [112] and 22.0° [002] (Nishida & Takahashi, 2008; Liu, Zhong, Chang, Li & Wu, 2010). This result is almost similar to the one reported by Salleh et al. (2016). It is also noticeable that XRD patterns of A7, A8 and A9 is almost similar to XRD pattern of A10 due to high concentration of MC.

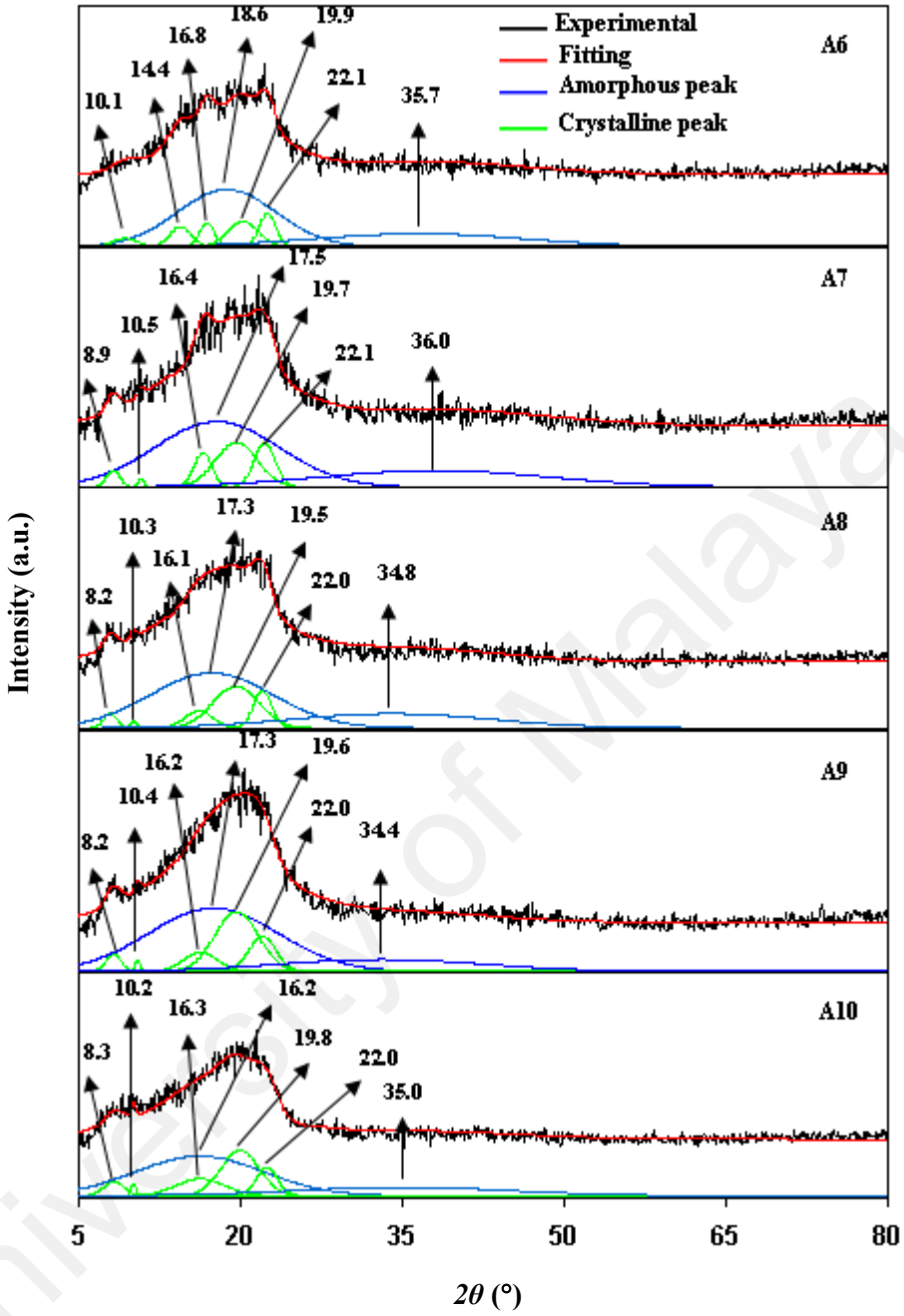

Figure 4.2: A6 to A10 polymer blend's deconvoluted XRD patterns.

From the deconvoluted XRD results, A6 has the smallest and less intense crystalline peaks compared to other ratio. From the deconvoluted XRD patterns, the value of χ_{crys} for all ratio have been identified and listed in Table 4.1.

Table 4.1: Degree of crystallinity versus methylcellulose-potato starch ratio.

Polymer blend	Degree of crystallinity (χ_{crys})
A0	26.56
A1	25.92
A2	24.90
A3	24.13
A4	23.05
A5	22.15
A6	**21.22**
A7	23.25
A8	26.03
A9	29.64
A10	32.89

Table 4.1 shows that A6 blend achieves the lowest degree of crystallinity of 21.22. This indicates that A6 is the most amorphous polymer blend in this study. The reduction in degree of crystallinity could be due to the interaction between functional groups of PS and MC (Mathew & Abraham, 2008). The interaction among polymers functional groups will be further discussed in the next chapter. Starch film undergoes crystallization when stored for a long time. Tora, Jimenez, Talens and Chiralt (2014) reported that the addition of cellulose to starch inhibit crystallization of starch film and reduce the degree of crystallinity. Abd El-Kader and Ragab (2013) reported that by blending maize starch with MC have reduced the degree of crystallinity of the polymer blend. Hence in this work, 60 wt.% MC-40 wt.% PS has been chosen as the polymer host for further analysis.

4.3 FESEM

In polymer blend system, miscibility test is one of the crucial parts. One of the ways to study the miscibility is by studying the cross-section of the polymer blend via FESEM images. Figure 4.3 demonstrates the cross-section for A0 (pure starch film). It can be seen that the cross section of pure starch film has rough, wrinkled and structural discontinuity. Yusof et al. (2016) reported that starch film possesses shrinkage like structure with a lot of discontinuity. The result of cross section for pure starch film by Halal et al. (2015) showed a structure with micro-cracks. Muscat, Adhikari, Adhikari and Chaudhary (2012) stated that starch film is extremely brittle while handling it after cast process. FESEM image of cross section of starch film in this work is consistent with reports from literature.

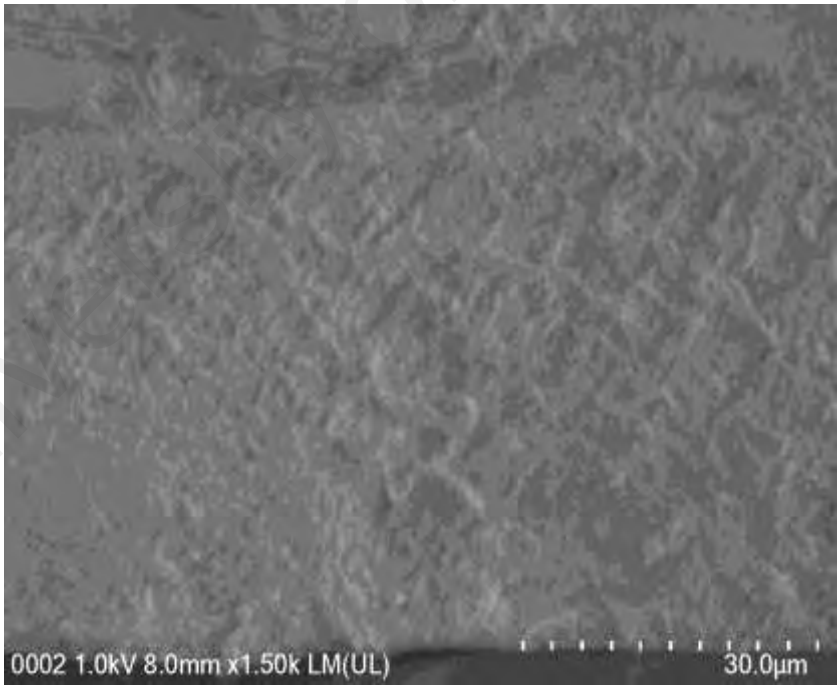

Figure 4.3: Cross-section image for A0 (pure starch film).

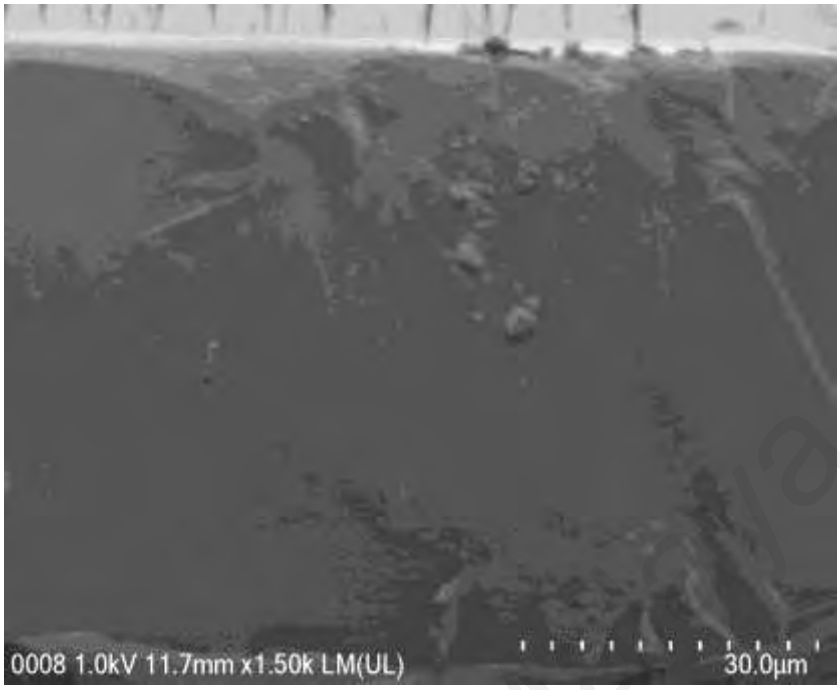

Figure 4.4: Cross-section image for A10 (pure MC film).

Figure 4.4 shows the cross-section image of A10 (MC film). In contrast with starch film, MC is famous of its smooth and high structural continuity. Tongdeesoon, Mauer, Wongruong, Sriburi and Rachtanap (2011) reported cross-section of MC with dense and smooth structure. Moura and Azeredo (2012) reported in book chapter where cellulose has a smooth cross-section. As reported by Noronha, de Carvalho, Lino and Barreto (2014) MC film holds a compact and smooth cross-section structure. These results from other studies harmonized with the cross-section of A10 film.

Figure 4.5 depicts the FESEM image for cross-section of A6 blend film. It is noticeable that as MC is blend with starch the structural continuity enhances for A6 blend. The improvement of rough A0 cross-section structure can be seen in A6 blend where A6 has a smoother, denser and higher structural integrity. In addition, there is no observable separation of phase in A6 cross-section. Tongdeesoon et al. (2011) reported

that the inclusion of cellulose into starch solution lead to a smoother cross-section structure. Miyamoto et al. (2009) reported that starch is miscible with cellulose via FESEM analysis. As stated by Babu et al. (2014), the structural integrity of starch improved with the addition of MC as the mechanical strength of the blend is higher compared to the single polymer. Hence, via cross-section study of the blend, it is proven that PS is miscible with MC. Confirmation on the miscibility of PS and MC will be further explained in differential scanning calorimetry (DSC) analyis section.

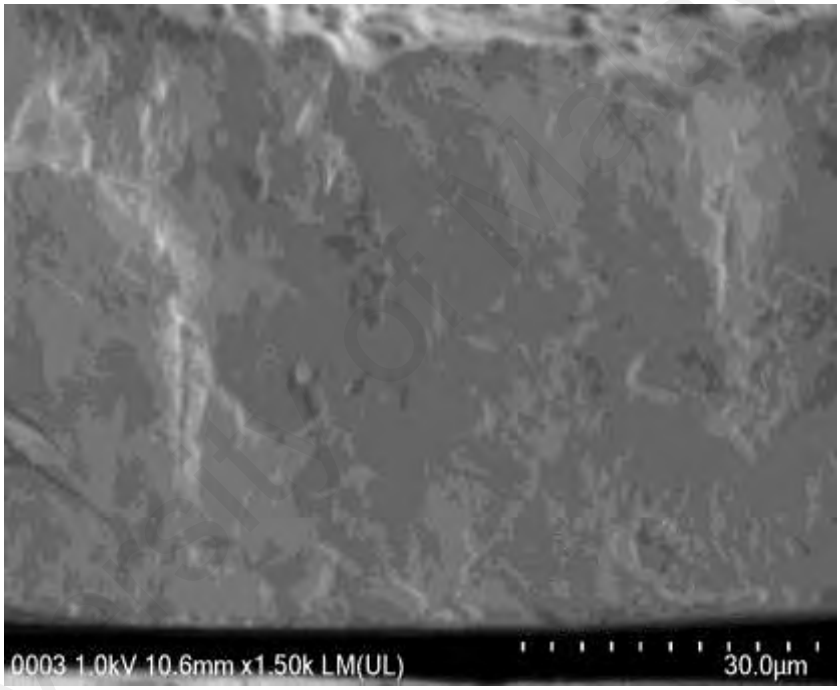

Figure 4.5: Cross-section image for A6 blend film.

Figure 4.6 portrays the surface image of A0 (PS film) where the surface is smooth. Azli, Manan and Kadir (2017) reported PS film with fair and smooth surface image. Nafchi, Alias, Mahmud and Robal (2012) also reported a smooth surface for pure PS film. Hence result from this study is consistent with other studies.

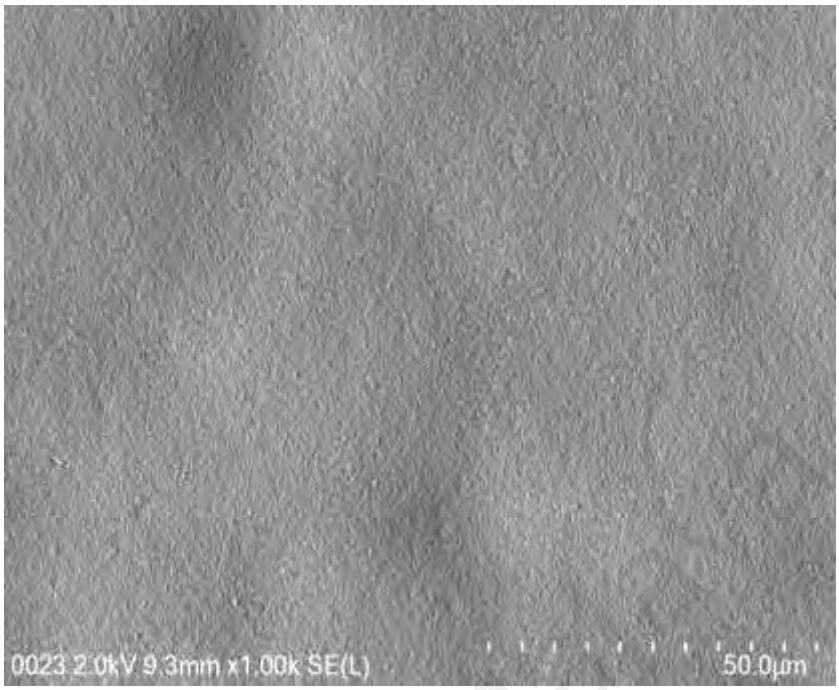

Figure 4.6: Surface image for A0 (PS film).

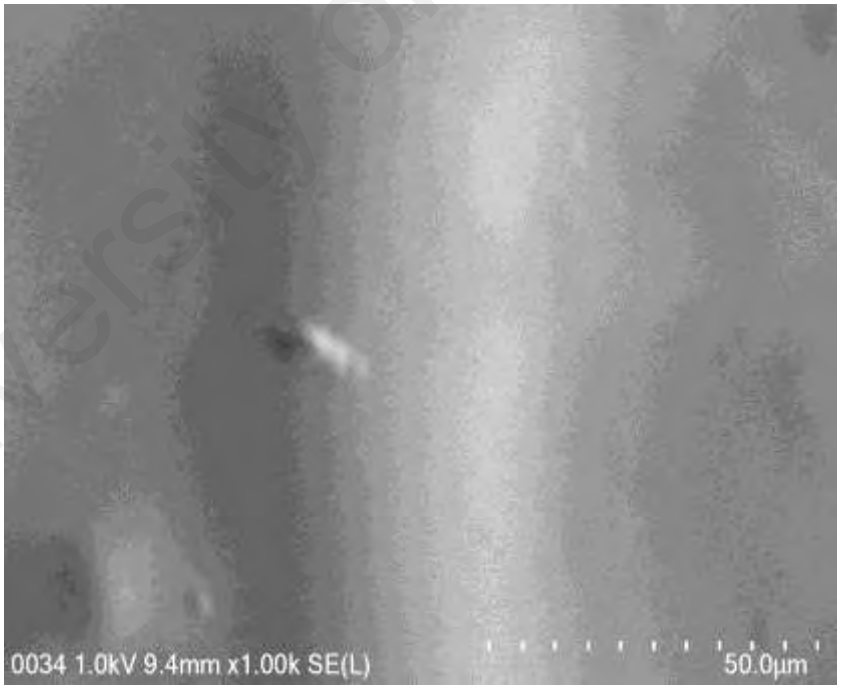

Figure 4.7: Surface image for A10 (MC film).

Surface for A10 (MC film) can be observed in Figure 4.7. A10 blend possesses smooth and homogeneous surface. As reported by Salleh et al. (2016), MC film's

surface showed no phase separation. Nemazifard, Kavoosi, Marzban and Ezedi (2017) reported MC film with compact and smooth surface morphology. Hence the result in this study is consistent with other studies.

Figure 4.8 shows the surface of A6 blend film. The surface of A6 blend has turned to a denser structure with the presence of spherical structure. The small spherical structure can be assumed as a space or room which later on will be filled by salt for ionic migration. Moura and Azeredo (2012) stated that there is a presence of spaces or voids in MC-based blend. As stated in the work by Arya and Sharma (2018), the change in the surface's morphology signifies the reduction of crystallinity. As referred in XRD section the crystallinity of A6 film is much lower than A0 and A10 films.

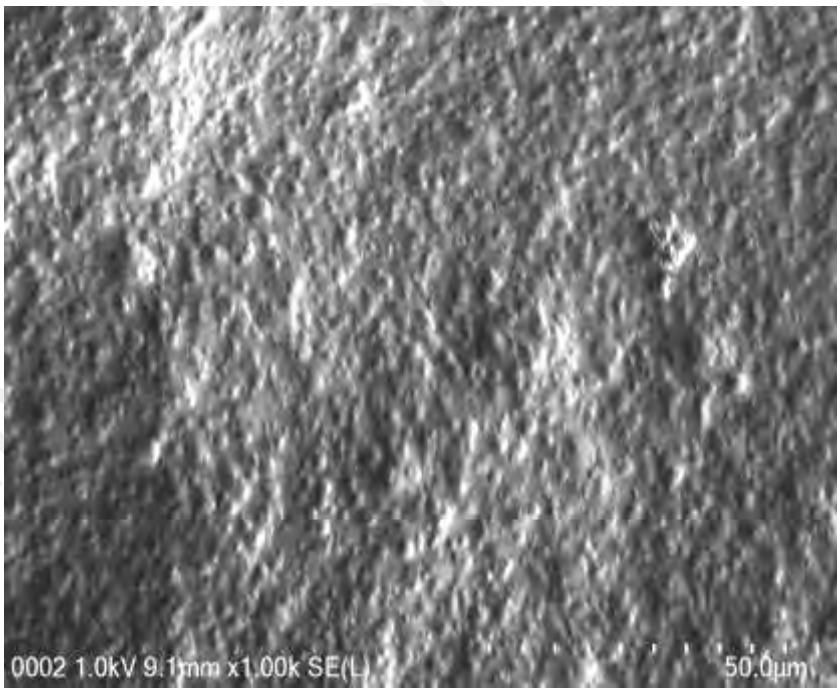

Figure 4.8: Surface image for A6 blend film.

4.4 TGA

In polymer blend studies, thermal stability is one of the crucial criteria need to be identify. Thermal stability can be determined via TGA measurement (Tuan et al., 2018). Figure 4.9 shows the TGA curves for A0, A6 and A10.

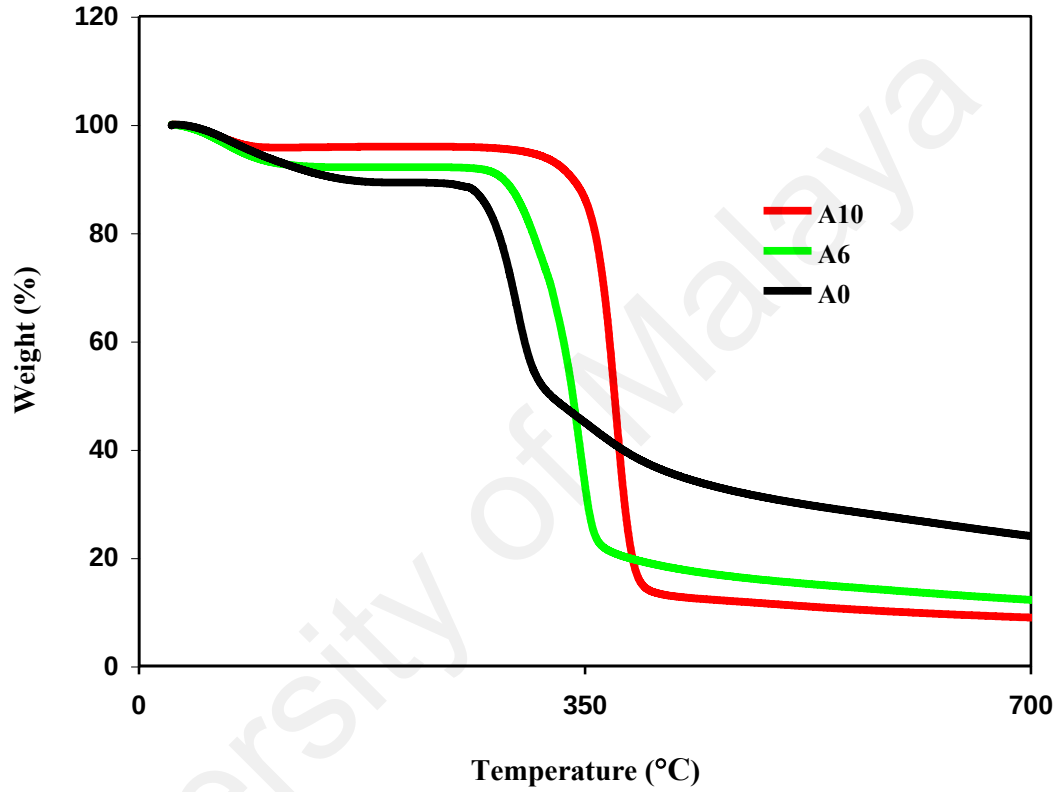

Figure 4.9: TGA curves for the polymer blends.

In Figure 4.9, it is noticeable that the first degradation stage in each polymer blend occurs up to ~150 °C. This first stage of degradation is due to the loss of water weight as the polymers naturally possess hydroscopic behaviour (Rajendran, Sivakumar & Subadevi, 2004). A0 film starts to decompose at 252 °C. Altayan, Darouich and Karabet (2017) reported that PS possesses decomposition temperature in between 250 °C to 300 °C. Ramesh, Shanti and Morris (2012) claimed that the weight loss of starch is due to detachment of amylopectin and amylose from the polymer chain and developing cross-linked structure. While for A10 the degradation begins at 315 °C. Liebeck,

Hidalgo, Roth, Popescu and Boker (2017) reported that MC decomposition temperature is in the range of 280 °C to 450 °C. MC undergoes decarboxylation from 200 °C to 400 °C (Samsudin, Lai & Isa, 2014). By blending PS and MC, the decomposition of the polymer blend (A6) is located at 280 °C. It is also observable in Figure 4.9 that A0 undergoes 35% weight loss while A10 ~ 80% weight loss. By blending the polymers, the weight loss for A6 is ~ 53% which is lower than A10. This result verifies the fact that blending MC and PS improves the thermal stability of PS based film.

4.5 DSC

In order to support miscibility result from FESEM analysis, DSC analysis has been conducted for the polymer blends. The value of glass transition temperature (T_g) is extracted from the heat capacity transition midpoint. The heat capacity transition is from glassy condition to rubbery (Lau & Mi, 2002). The polymer blend is considered an immiscible system if two transition appears. Miscible polymer blend system only shows a single value of T_g (Chiou et al., 2014). Figure 4.10 shows the DSC curves for A0, A6 and A10 films. The T_g for A0 and A10 are located at 164.8 °C and 118.0 °C, respectively. These values are comparable with other reports on starch and MC (Gomez-Carracedo, Alvarez-Lorenzo, Gomez-Amoza & Concheiro, 2003; Graaf, Karman & Janssen, 2003). The T_g for A6 film is located at 132.7 °C where it is positioned between T_g of A0 and A10. Single value of T_g verifies that PS and MC are miscible which harmonized FESEM result where no phase separation appears in the cross-section of the A6 blend.

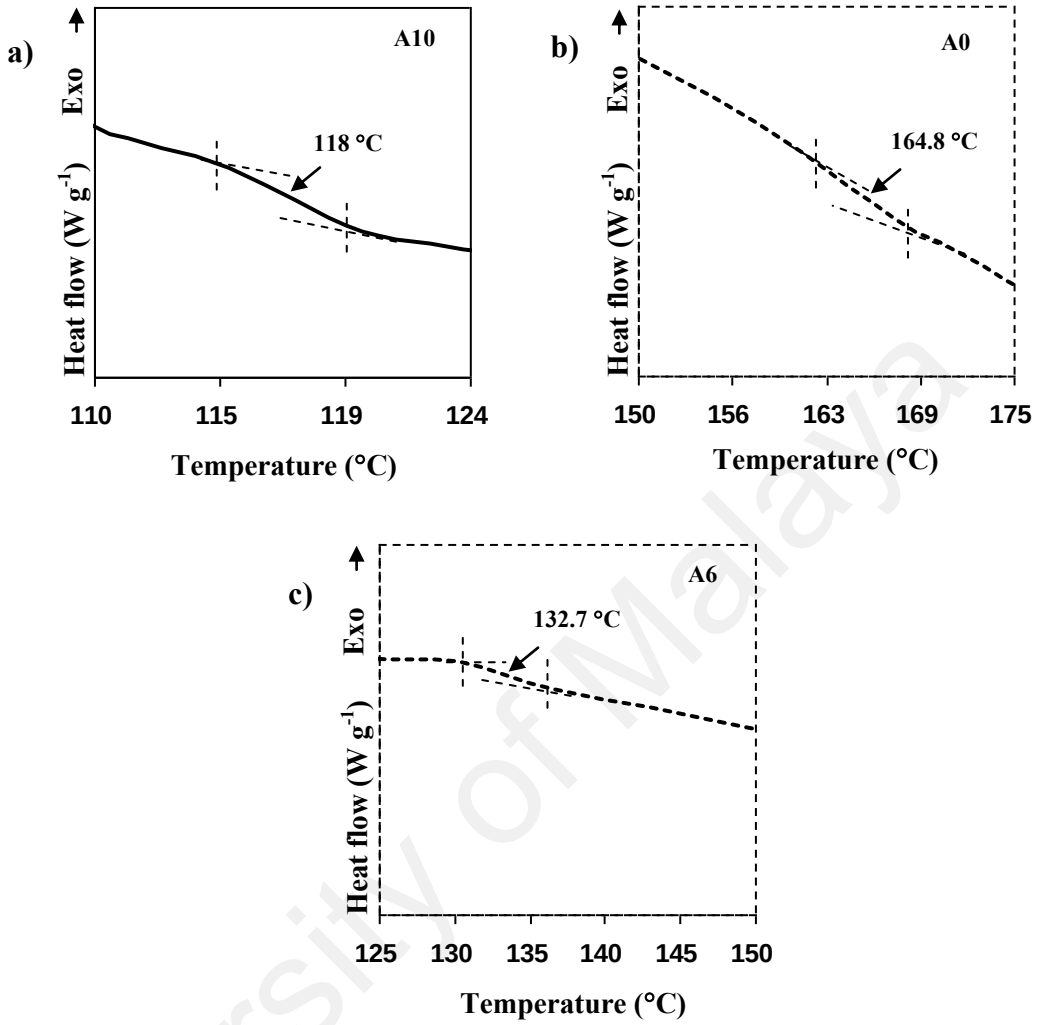

Figure 4.10: DSC curves for the polymer blends.

In order to confirm the value of T_g for the polymer blend, Fox equation has been incorporated. Fox equation is used to estimate the value of T_g for binary polymer blend. Fox equation can be expressed as (Senna, El-Shahat & El-Naggar, 2011):

$$\frac{1}{T_g} = \frac{x_1}{T_{g1}} + \frac{x_2}{T_{g2}} \tag{4.2}$$

Here x_1 and x_2 are the fraction of the individual polymers. T_g is the transition temperature from glassy to rubbery state for the polymer blend while $T_{g1,}$ and T_{g2} for the

individual polymers, respectively. The value of T_g predicted from Fox equation is 133.1 °C. The experimental T_g value of A6 blend (132.7 °C) is ~ 0.3 % lower than theoretical value. The deviation of experimental T_g value is due to intermolecular interaction between polymers (Nyamweya & Hoag, 2000; Mujaheddin, Jagadish, Sheshappa & Guru, 2012). Since the value of T_g from experimental and theoretical is almost identical, the value of T_g for A6 in this work is reliable.

4.6 Summary

The most amorphous MC-PS blend is found to be the blend of 60 wt.% MC and 40 wt.% PS which has been confirmed via XRD analysis. From FESEM analysis, it is confirmed that MC is miscible with PS where homogenous film is formed. By blending PS and MC, the polymer weight loss due to temperature has been decreased as shown in the TGA curves. From TGA, the decomposition temperature for PS has been improved with the presence of MC. The miscibility of MC and PS is further verified via DSC analysis where only single value of T_g has appeared. The value of T_g for 60 wt.% MC-40 wt.% PS blend also has been confirmed via Fox equation. Hence, polymer blend with 60 wt.% MC and 40 wt.% PS has been selected as the polymer matrix to be tested with addition of salt and plasticizer.

CHAPTER 5: STRUCTURAL PROPERTIES OF THE POLYMER ELECTROLYTE

5.1 Introduction

This chapter covers the interactions among the materials and crystallinity of the electrolyte via FTIR and XRD analysis, respectively. Results from XRD analysis will be deconvoluted in order to determine the changes in area of the crystalline and amorphous peaks as NH_4NO_3 and glycerol are included to the polymeric network. The areas obtained from deconvolution method are used to calculate the degree of cystallinity of each sample. The changes in peak's shape, position and intensity can be considered as an interaction as different materials are added into the polymers. Furthermore, the complexations among the materials of the electrolyte are preferable to occur in the amorphous regions (Alghunaim, 2016). Mathew, Karthika, Ulaganathan and Rajendran (2015) stated that ionic migration in a polymer electrolyte system take place usually in the region of amorphous. The existence of ionic interaction with polymers can be evidenced by FTIR analysis. It is well known that the complexation among polymers and salts are between their oxygen-containing functional groups with charge carriers (Ahmad & Isa, 2015). Shuhaimi (2011) reported that cations from NH_4NO_3 have interacted with lone pair electron of methylcellulose (MC) via FTIR analysis. According to Jesintha, Radha and Hemalatha (2017) the addition of NH_4NO_3 into the potato starch (PS) film has shifted the oxygen-containing functional groups band e.g. hydroxyl (OH) and linkage (C-O-C) band regions. Premalatha, Vijaya, Selvalakshmi and Monisha (2015) reported ammonium thiocyanate (NH_4SCN) interacted with PVA-PVP blend in the OH and C-O-C band regions. The occurrence of salt re-crystallization can be detected in FTIR analysis. Other than that, the position, shape and intensity of the vibrational modes of band regions in polymer matrix depend on the number of ions (Pandey, Joshi & Ghosh, 2017).

5.2 XRD studies

5.2.1 XRD patterns of Methylcellulose-Potato Starch-NH_4NO_3

Figure 5.1 shows the XRD pattern of the electrolyte at various concentrations of NH_4NO_3 and pure NH_4NO_3 from 5° to 80°.

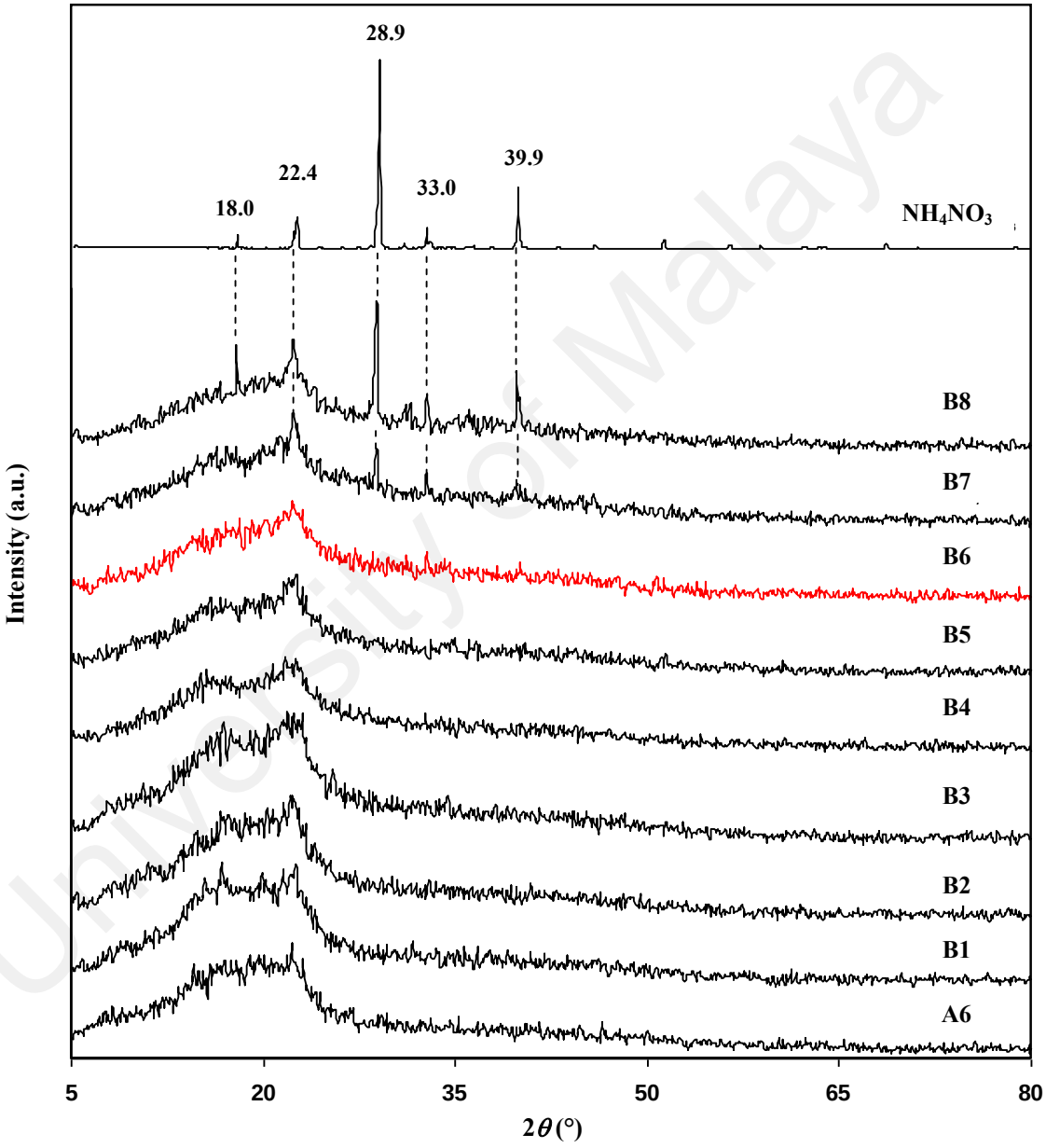

Figure 5.1: XRD plot for salted electrolytes.

Based on Figure 5.1, the crystalline peaks for pure NH_4NO_3 appear at 2θ of 18.0°, 22.4°, 28.9°, 33.0° and 39.9°. This result is comparable with the one reported by Kento, Hiroki and Atsumi (2016). In order to obtain more accurate result, deconvolution method has been used for salted electrolytes to take out any possible overlapping peaks.

The deconvoluted XRD patterns for the selected salted electrolytes are depicted in Figure 5.2. B2 has almost similar crystalline peaks as A6 blend (Figure 4.2) but with lower intensity. The intensity of these five crystalline peaks has been reduced for B4 and B5. The crystalline peak at 10.0° (in B5 XRD) disappears in the XRD pattern of B6. There are no crystalline peaks of NH_4NO_3 in the XRD patterns of B2, B4, B5 and B6 indicating to a proper dissociation of salt in the polymeric network (Noor, Ahmad, Rahman & Talib, 2010). The presence of NH_4NO_3 peaks at 2θ = 28.8°, 32.9° and 39.9° in XRD pattern of B7. This portrays the recrystallization of excess salt which decrease the free charge carriers (Amran et al., 2016).

The degree of crystallinity (χ_{crys}) of each salted electrolytes is tabulated in Table 5.1. The χ_{crys} decreases as the concentration of NH_4NO_3 increases. The χ_{crys} of B6 is the lowest with χ_{crys} = 13.46. Danielle et al. (2016) stated that ionic conduction is suitable in amorphous region. The conductivity trend from Figure 6.6 is harmonized with the pattern of χ_{crys} where the increment in χ_{crys} leads to decrement in conductivity value.

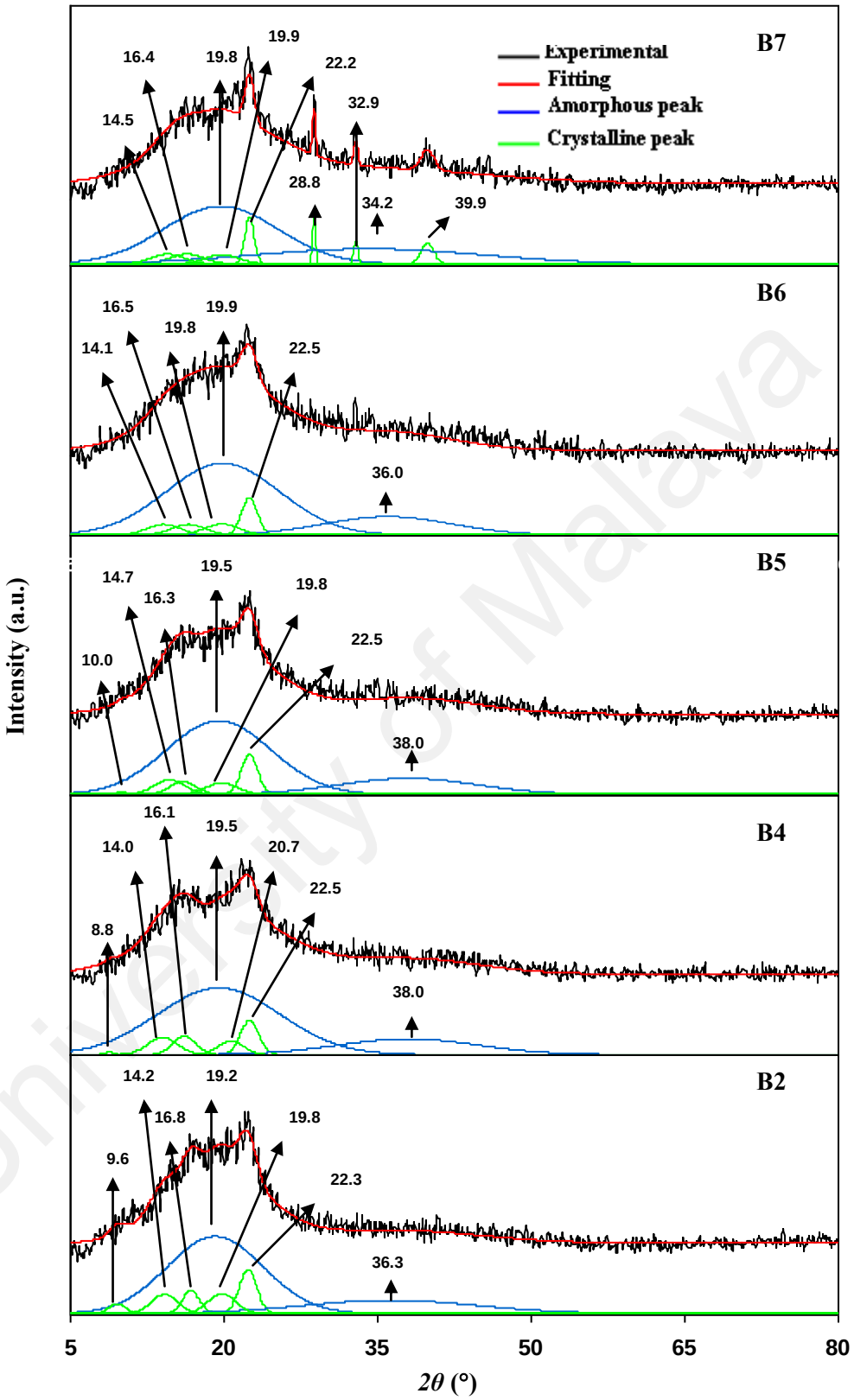

Figure 5.2: Deconvoluted XRD patterns for salted electrolytes.

Table 5.1: Degree of crystallinity for salted electrolytes.

Electrolyte	Degree of crystallinity (χ_{crys})
A6	21.22
B1	20.13
B2	19.71
B3	19.04
B4	17.12
B5	16.04
B6	13.46
B7	15.96
B8	18.72

5.2.2 XRD patterns of Methylcellulose-Potato Starch-NH_4NO_3-Glycerol

Figure 5.3 reveals the XRD patterns for plasticized electrolytes. The intensity of peaks located at 2θ = 16.0° and 22.0° in XRD pattern of B6 has been suppressed with addition of 10 wt.% glycerol and further reduce as 40 wt.% glycerol is incorporated. It is also detectable that no sharp peaks correspond to the crystalline peaks of NH_4NO_3. This indicates that salt is well dissolved in the polymeric network as glycerol is added. However, deconvolution need to be done in order to determine the changes in the area of each crystalline and amorphous peak as well as the value of χ_{crys} for plasticized electrolytes.

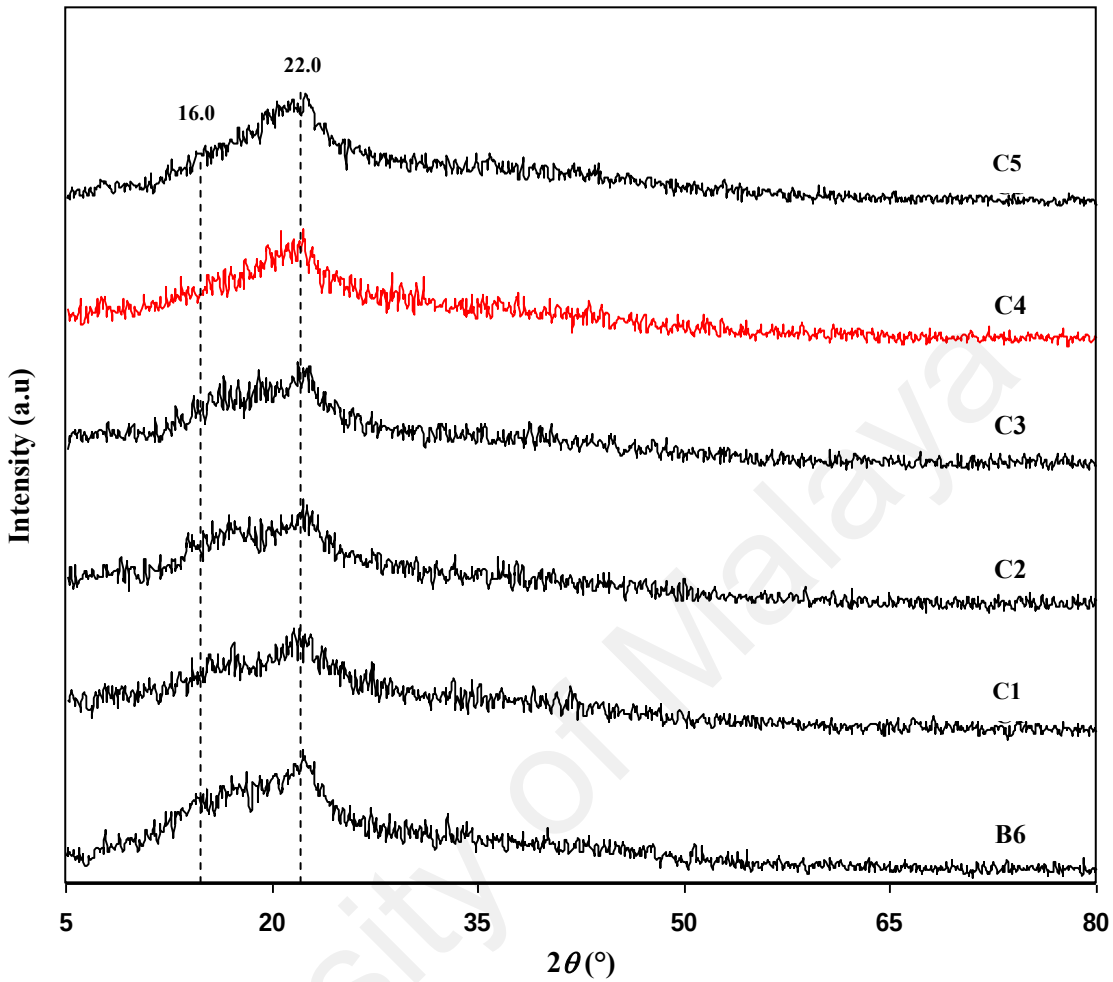

Figure 5.3: XRD plot for plasticized electrolytes.

Figure 5.4 shows the deconvoluted XRD pattern for plasticized electrolytes where the peaks at 2θ = 14.1°, 16.5°, 19.8° and 22.5° have become smaller with the addition of 10 wt.% glycerol. As 30 wt.% glycerol is included, peak at 2θ = 13.0° in C1 disappears. These three crystalline peaks are further suppressed with 40 wt.% glycerol indicating an increase in amorphousness (Shukur, 2015; Amran et al., 2016). Excess amount of glycerol can hinder the ion-polymer interaction that leads to the increment of crystalline peak's intensity which can be seen in C5 deconvoluted XRD pattern.

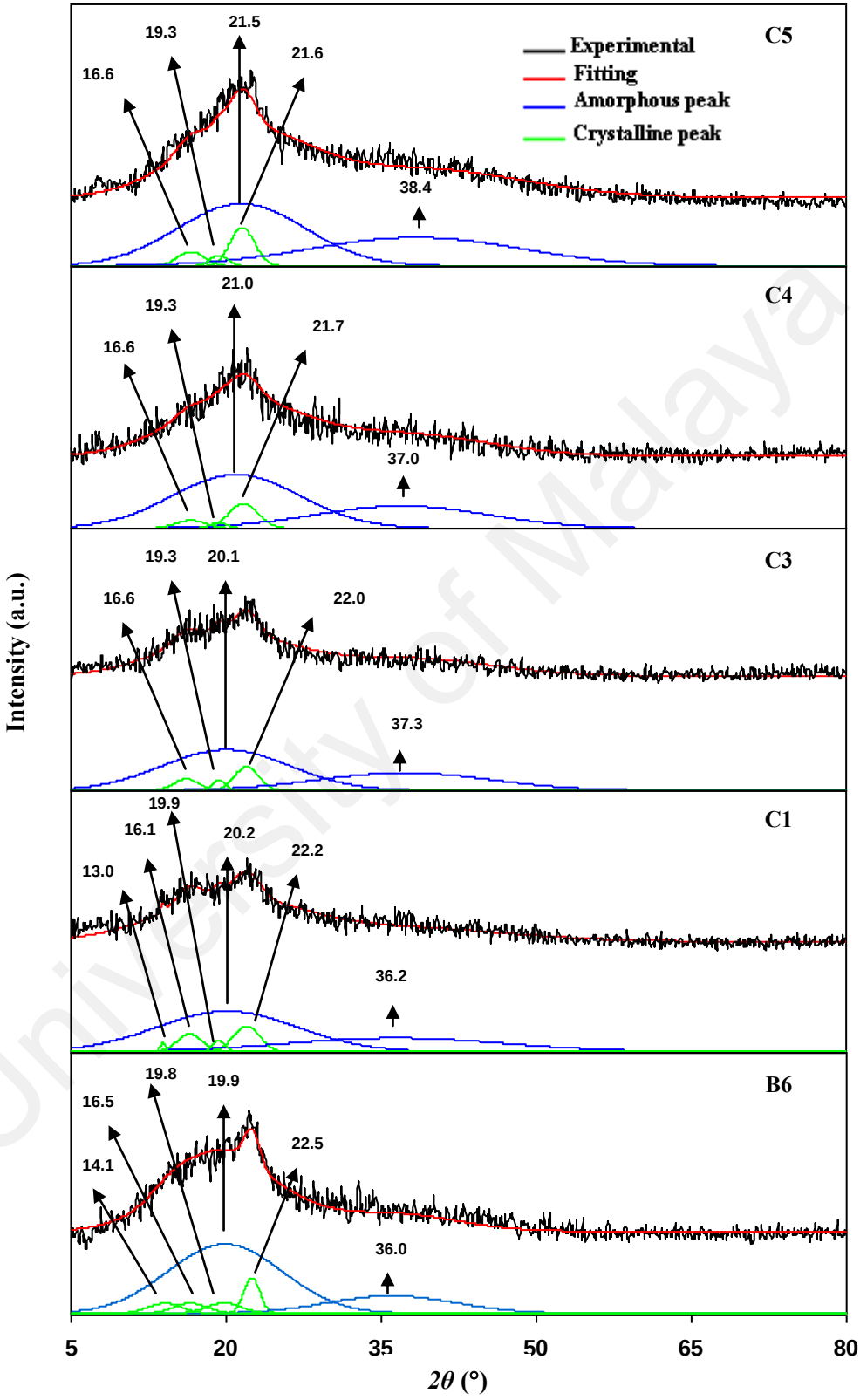

Figure 5.4: Deconvoluted XRD patterns for plasticized electrolytes.

The values of χ_{crys} for plasticized electrolytes are presented in Table 5.2. The value of χ_{crys} for B6 has been reduced from 13.46 to 12.84 with the inclusion of 10 wt.% glycerol and continue to decrease to 10.93 with 30 wt.% glycerol content. The highest conducting electrolyte in this study, C4, has the smallest value of χ_{crys} meaning that C4 is the most amorphous electrolyte. Hydroxyl-rich structure of glycerol helps MC-PS polymer structure to contain the salt, hence improve the amorphousness of the electrolytes (Chai & Isa, 2016). The trend of conductivity for plasticized electrolyte in Figure 6.7 in Chapter 6 is consistent with the χ_{crys} pattern.

Table 5.2: Degree of crystallinity for plasticized electrolytes.

Electrolytes	Degree of crystallinity (χ_{crys})
B6	13.46
C1	12.84
C2	11.86
C3	10.93
C4	8.86
C5	10.39

5.3 FTIR Studies

The pattern of conductivity values for the electrolyte can be strengthened using results from FTIR analysis. FTIR analysis in this work is focused on OH, C-O-C linkage and methoxy (OCH_3) band regions. Tables 5.3 and 5.4 list the vibrational modes for MC and PS, respectively.

Table 5.3: Vibrational modes for MC with their corresponding wavenumbers.

Wavenumber (cm^{-1})	Assignation	Reference
3400	O-H stretching	Shuhaimi, 2011
2800-2860	Methoxy, methyl ether $O-CH_3$, C-H stretching	Coates, 2006
1580-1700	Water molecule bending	Shuhaimi, 2011
1374	C-H bending	Filho et al., 2007
1111	Anhydroglucose ring, C-O stretching	Filho et al., 2007; Vieira et al., 2012
890-940	Glycosidic linkages, C-O-C	Filho et al., 2007; Synytsya & Novak, 2014
400-700	Characteristic of cellulose	Filho et al., 2007

Table 5.4: Vibrational modes for PS with their corresponding wavenumbers.

Wavenumber (cm^{-1})	Assignation	Reference
3284	O-H stretching	Amran et al., 2016
2800-3000	$C-H_2$ deformation	Kizil, Irudayaraj & Seetharaman, 2002
1374	Water molecule bending	Kizil et al., 2007
1162	Anhydroglucose ring, C-O stretching	Sechi & Marques, 2017
926	Glycosidic linkages, C-O-C	Shukur, 2015; Kizil et al., 2002
537, 581, 627, 711	Ring skeletal modes	Kizil et al., 2007

5.3.1 Methylcellulose Film

Figure 5.5 depicts the FTIR plot for A10 film at band regions of 3000-3600 cm^{-1} and 920-960 cm^{-1}.

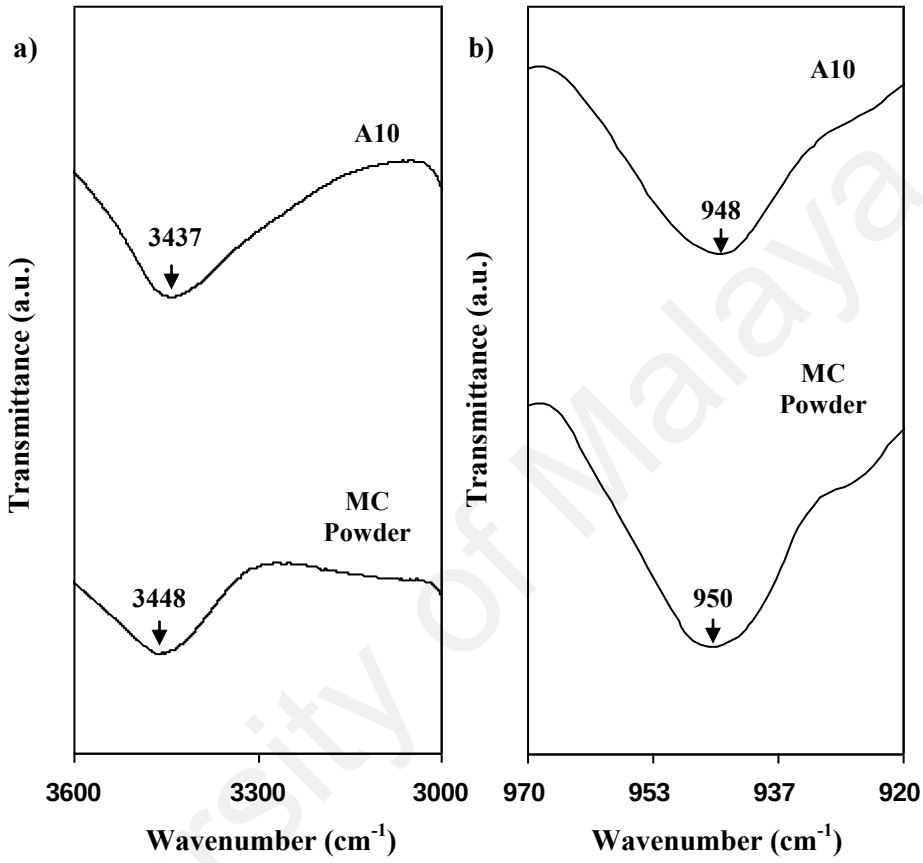

Figure 5.5: FTIR plot for A10 film and MC powder at a) 3000-3600 cm^{-1} and b) 920-960 cm^{-1} band regions.

As observed in Figure 5.5(a), the region from 3000 to 3600 cm^{-1} corresponds to hydroxyl (OH) band region for A10 and pure MC powder. OH band peak of A10 and MC powder is centered at 3437 cm^{-1} and 3448 cm^{-1}, respectively. Yusof (2017) reported that dissolving starch in acetic acid has shifted the OH peak which is consistent with the present results. Increase in intensity of OH peaks indicates the existent of OH functional groups (Teoh, 2012). Figure 5.5(b) represents the region of glycosidic linkages (C-O-C)

which is located at 950 cm^{-1} for MC powder and 948 cm^{-1} for A10 film which is comparable to other cellulose study (Synytsya & Novak, 2014). The shift signifies that acetic acid has been interacted with oxygen of C-O-C linkages.

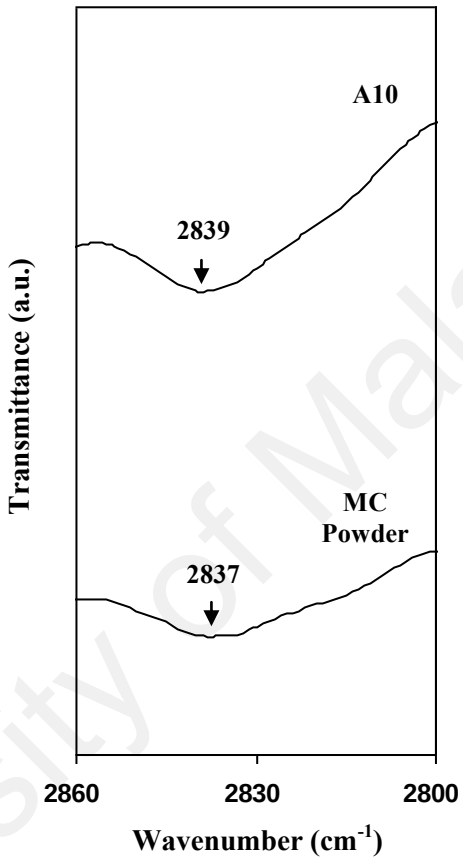

Figure 5.6: FTIR plot for A10 film and MC powder at 2800-2860 cm^{-1} band regions.

Figure 5.6 shows the FTIR band regions for A10 film and MC powder at 2800-2860 cm^{-1} (methoxy, OCH_3). OCH_3 functional group may contribute to the ion conduction due to the existence of lone pair electron at the oxygen atoms. OCH_3 band region for MC powder is positioned at 2837 cm^{-1}. The interaction of acetic acid and MC is further confirmed as the peak move to 2839 cm^{-1}. Coates (2006) stated that methoxy band region is located in the range of 2800 to 2860 cm^{-1}.

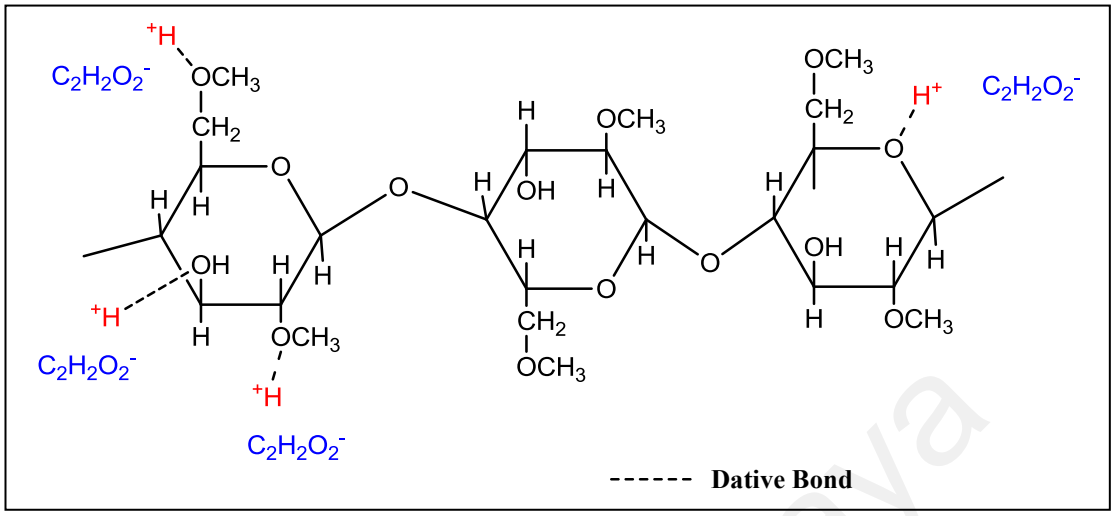

Figure 5.7: Illustration for the possible interactions between MC and acetic acid.

Figure 5.7 shows the possible interactions among MC's oxygen-containing functional groups with H^+ ion of acetic acid. Ions can form a dative bond with free lone pair electrons.

5.3.2 Potato Starch Film

Figure 5.8 represents the FTIR band regions of OH and glycosidic linkages for A0 film and pure PS powder. OH peak for PS powder has shifted from 3194 cm^{-1} to 3288 cm^{-1}. Furthermore the intensity of OH peak for A0 increases as PS is dissolved in acetic acid. The changes in peak's intensity and position indicate the interaction between acetic acid and OH groups of PS (Bokobza, 2018).

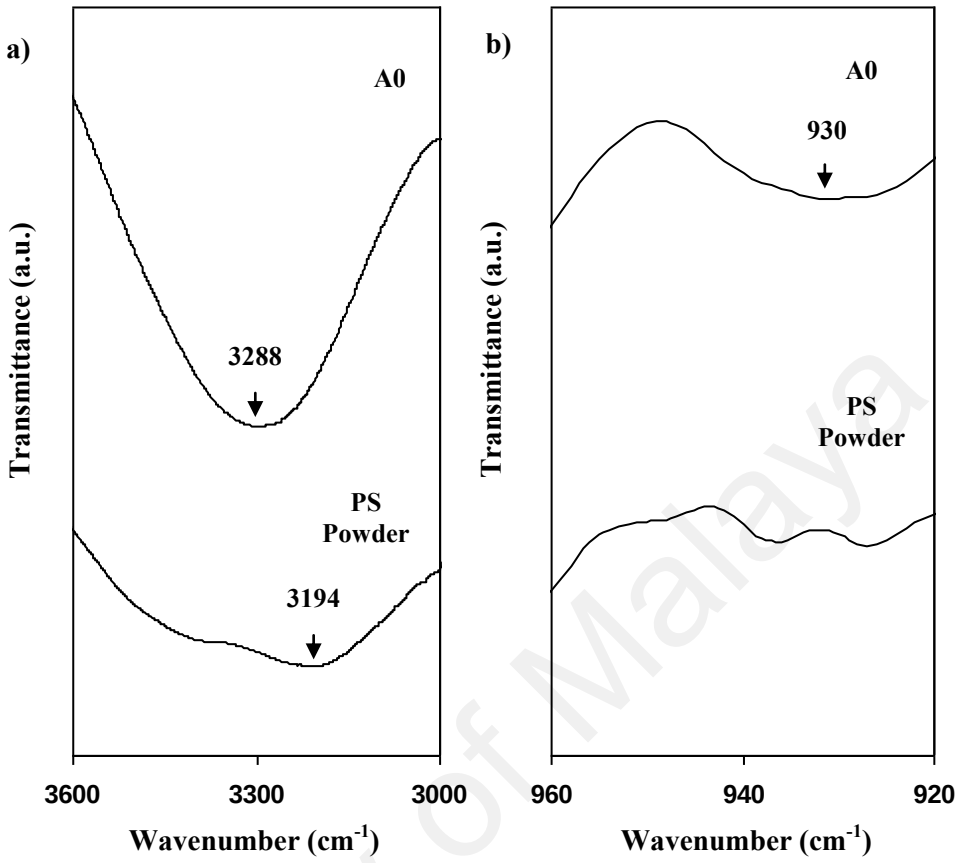

Figure 5.8: FTIR plot for A0 film and PS powder at a) 3000-3600 cm^{-1} and b) 920-960 cm^{-1} band regions.

Figure 5.8(b) reveals that the shape and intensity of C-O-C from glycosidic linkage band region for PS powder changed with the presence of acetic acid. C-O-C band region for A0 film is centered at 930 cm^{-1}. Shukur (2015) reported a value of 926 cm^{-1} for starch glycosidic linkages band via FTIR analysis. The possible interactions of PS and acetic acid based on Figure 5.8 are depicted in Figure 5.9. H^+ ions are expected to interact with C-O-C from glycosidic bond as well as OH functional groups.

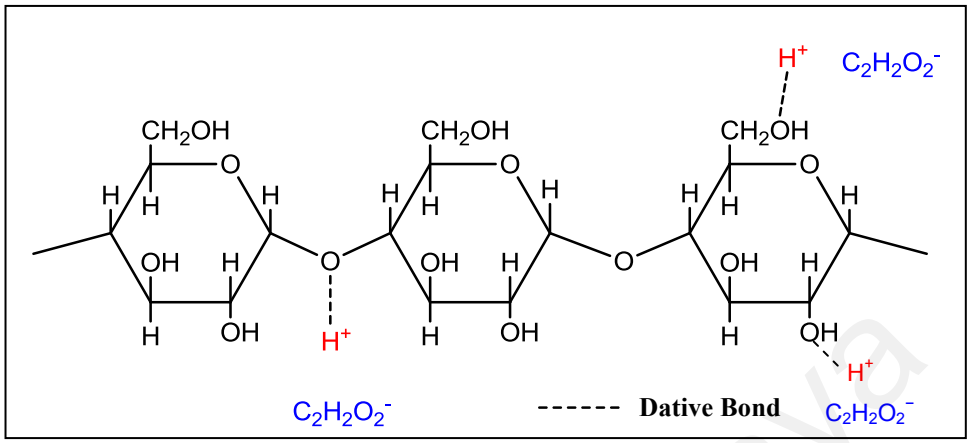

Figure 5.9: Illustration for the possible interactions between PS and acetic acid.

5.3.3 Methylcellulose-Potato Starch Film

It is well known that the interactions between polymers in polymer blending are by hydrogen bond (Kuo, 2008). Yusof (2017) verifies the hydrogen bonding between chitosan and starch from the shifting of OH peak and other oxygen-containing functional groups. Figure 5.10(a) illustrates the OH band region for A10, A6 and A0 films. A10 and A0 films possess OH peaks at 3437 cm^{-1} and 3288 cm^{-1}, respectively. Shuhaimi (2011) reported that MC film's OH peak is centered at 3440 cm^{-1} while Amran et al. (2016) reported that PS film's OH peak is located at 3284 cm^{-1}. As MC is blend with PS the OH peak is observed at 3428 cm^{-1} (A6). The changes in spectral peaks of polymer blend portray the chemical reaction of the polymers (Ashori & Bahrami, 2014). The shape of OH peak for A6 is almost similar to A10 which is due to high weight percentage of MC in the blend.

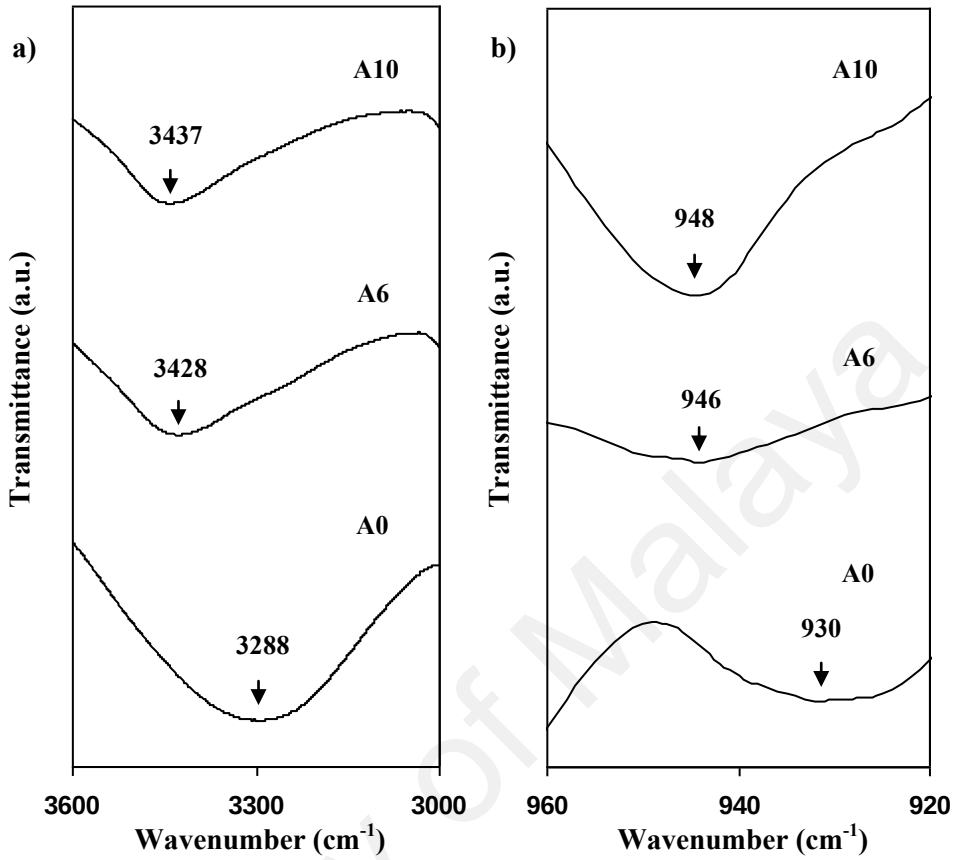

Figure 5.10: FTIR plot for A10, A6 and A0 films at a) 3000-3600 cm^{-1} and b) 920-960 cm^{-1} band regions.

. Figure 5.10(b) shows the peaks correspond to glycosidic linkage. A6 film's peak is located at 946 cm^{-1} which located in between A10 and A0. This phenomenon suggests a good miscibility between PS and MC where the interaction is due to hydrogen bonding. As reported by Shukur (2015), the glycosidic linkages peak shifted as chitosan and starch is blended. The author also stated that hydrogen bonding improves the miscibility of the polymers.

From Figure 5.11, it can be observed that no peak of OCH_3 in starch due to the absence of OCH_3 functional group in the structure of starch. The peak of OCH_3 for A10

shifted from 2839 to 2840 cm^{-1}. This signifies that oxygen atom in OCH_3 groups have interacted with PS.

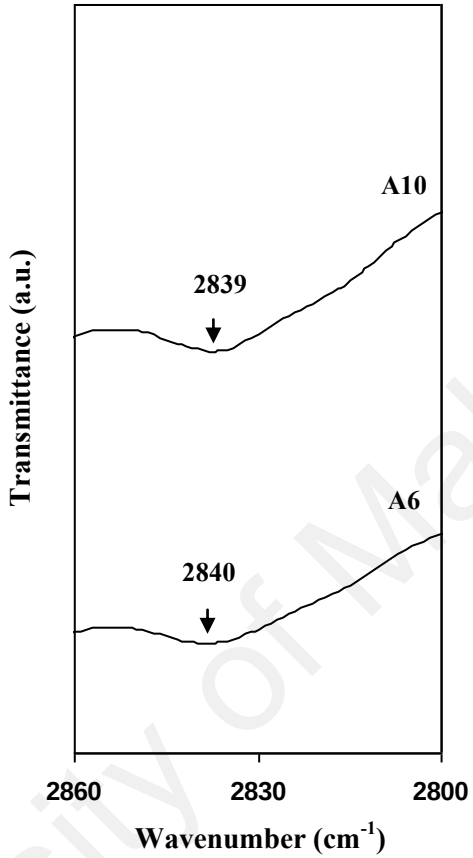

Figure 5.11: FTIR plot for A10, A6 and A0 films at 2800-2860 cm^{-1} band regions.

The illustration for possible MC-PS blend interaction is shown in Figure 5.12. It is preferable for potato starch to mix with MC in amylose structure compared to branched amylopectin. Hence, in MC-PS blend, the interaction happens via hydrogen bonding among the amylose of PS and MC atom (Mathew & Abraham, 2008).

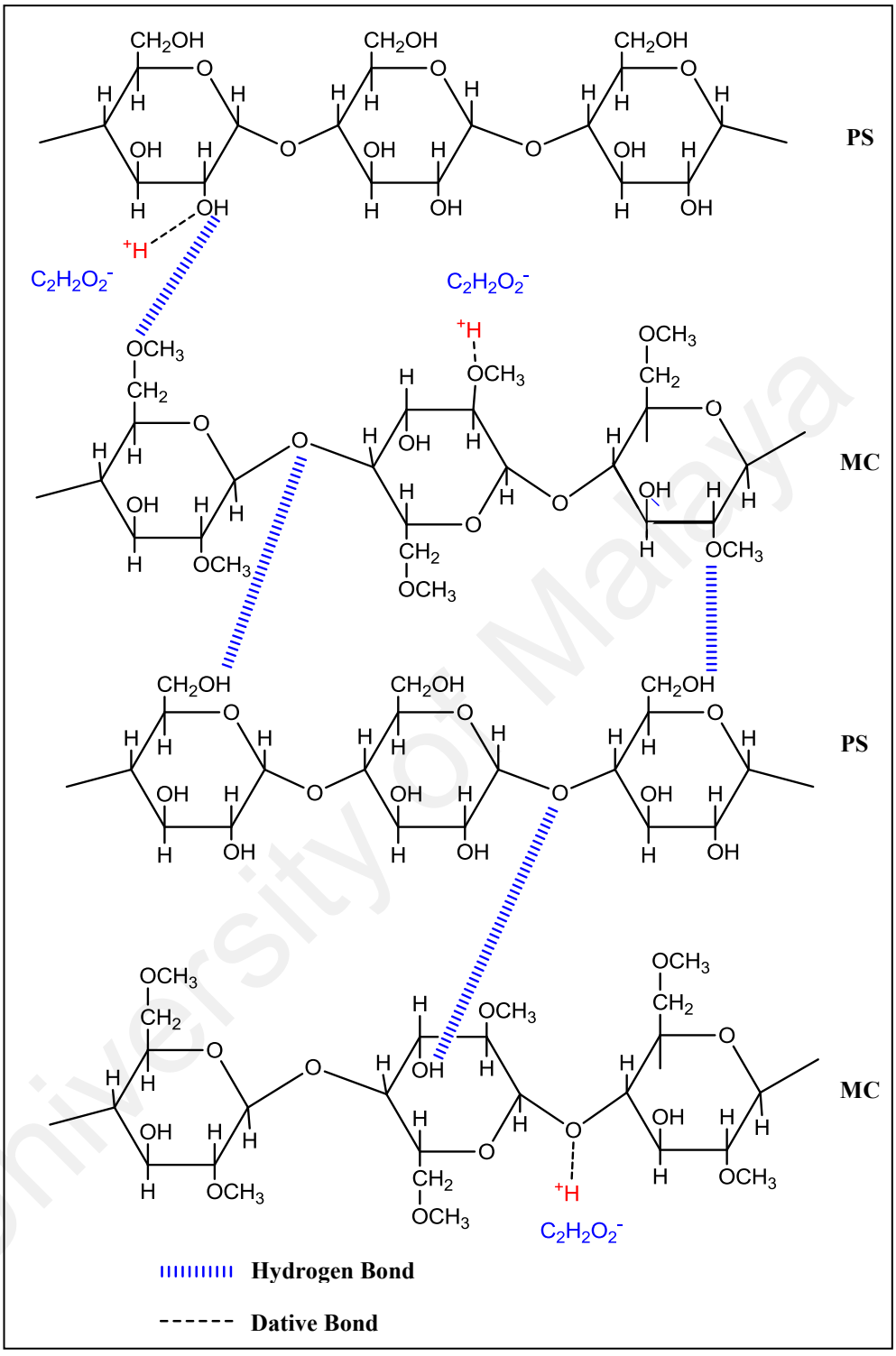

Figure 5.12: Illustration of possible interactions between methylcellulose and potato starch.

5.3.4 Methylcellulose-Potato Starch-NH_4NO_3

Figure 5.13 shows the FTIR plots for the selected salted electrolytes at OH and glycosidic linkages.

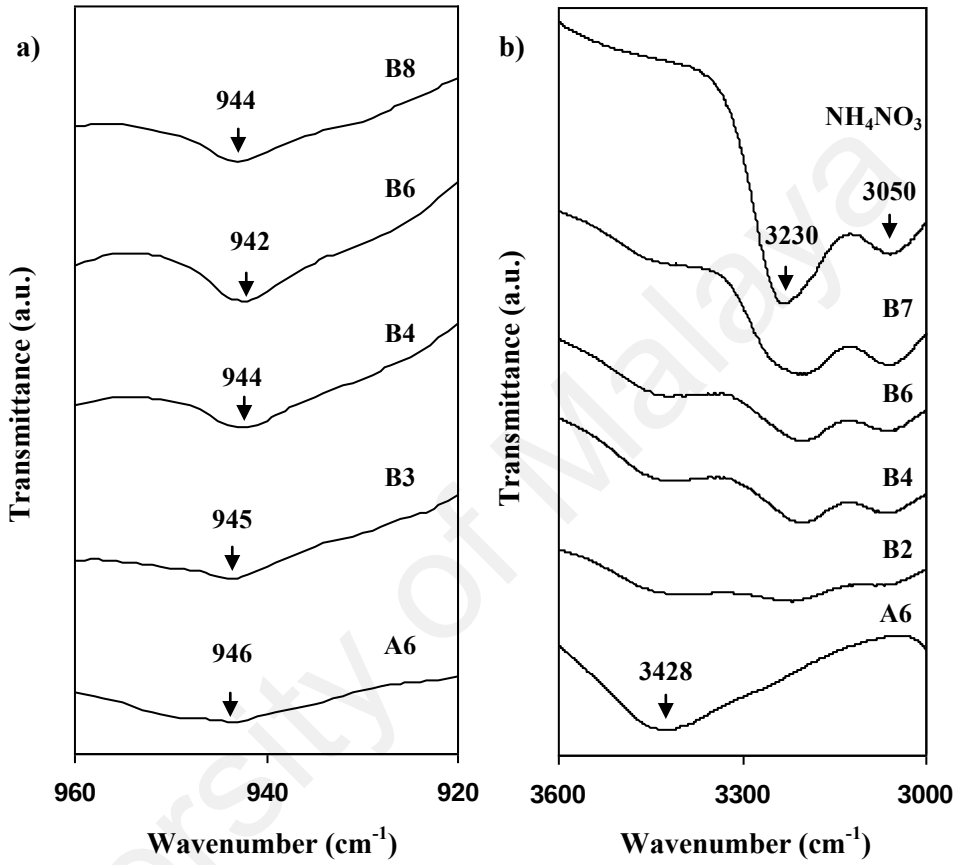

Figure 5.13: FTIR for salted electrolytes at a) 920-960 cm^{-1} and b) 3000-3600 cm^{-1}.

As shown in Figure 5.13(a), the glycosidic band of A6 at 946 cm^{-1} is noticed to shift to 945 cm^{-1} as 15 wt.% of NH_4NO_3 is included to the polymer blend. The peak shifted to a lower wavenumber of 942 cm^{-1} for B6 electrolyte. The shift of the peaks signifies that cations from NH_4NO_3 undergo complexation at oxygen atoms of the C-O-C linkages. In B8, the peak shifted back to higher wavenumber (944 cm^{-1}) due to the decrement of ion's number density which lessen the salt-oxygen atom interaction (Amran et al., 2016). In addition, the peak's shape has become sharper as the addition of

salt increases. Sim, Majid and Arof (2012) stated that the alteration of peak's wavenumber, shape and intensity indicate the interaction of salt and polymers.

FTIR of OH band region for selected salted electrolytes can be observed in Figure 5.13(b). A6 blend possesses broad OH peak that centered at 3428 cm^{-1}. It is noticeable that the inclusion of 10 wt.% of NH_4NO_3 (B2) resulting in appearance of two additional peaks. By referring to Kadir, Aspanut, Majid and Arof (2011), these two peaks correspond to asymmetry vibration ($v_{as}(NH_4^+)$) and symmetry vibration ($v_s(NH_4^+)$). The authors also reported that these two peaks are situated at 3222 and 3055 cm^{-1}, respectively, which proves cation-polymers interaction. The intensity of these two peaks increases with increasing concentration of NH_4NO_3. The variation of shape is considered as overlapping of OH band, $v_{as}(NH_4^+)$ and $v_s(NH_4^+)$ peaks which can be separated via deconvolution method which depicted in Figure 5.14. OH peak for B2 electrolyte is located at 3424 cm^{-1} and shifted to 3415 cm^{-1} for B6. This indicates the ionic interaction at OH groups of the polymers. The peak is observed to change back to higher wavenumber of 3420 cm^{-1} for B7 electrolyte. This situation explains the occurrence of neutral ion pairs that decrease the interaction of cation and OH groups (Mason, Hu & Frech, 2010; Ashworth, Matthews, Welton & Hunt, 2016).

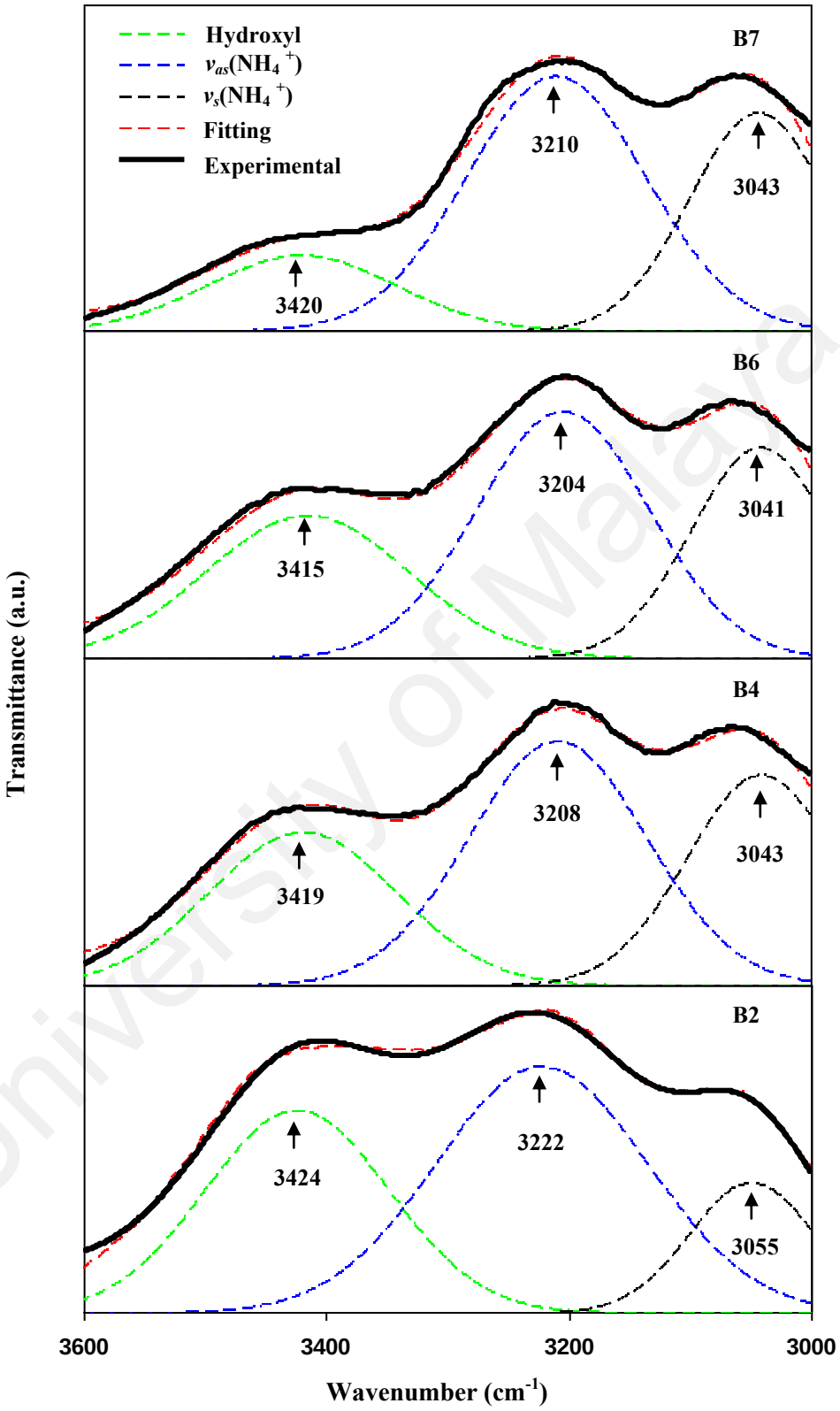

Figure 5.14: Deconvoluted FTIR for selected salted electrolytes at 3000-3600 cm^{-1}.

Figure 5.15 shows the FTIR spectra for the selected salted electrolytes at OCH_3 band regions.

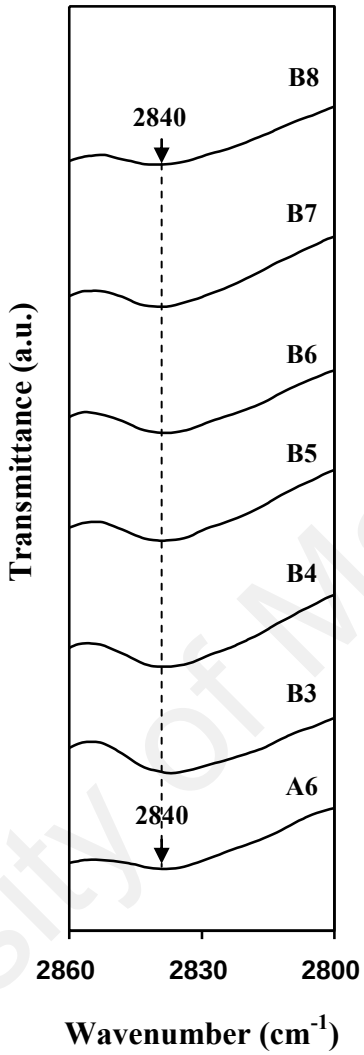

Figure 5.15: FTIR for the selected salted electrolytes at 2800-2860 cm^{-1}.

The peak of OCH_3 for A6 film also does not undergo any obvious changes of wave number or intensity as depicted in Figure 5.15. Hence, it can be concluded that there is no interaction between cation from NH_4NO_3 and oxygen atoms of methoxy groups of the polymer blend.

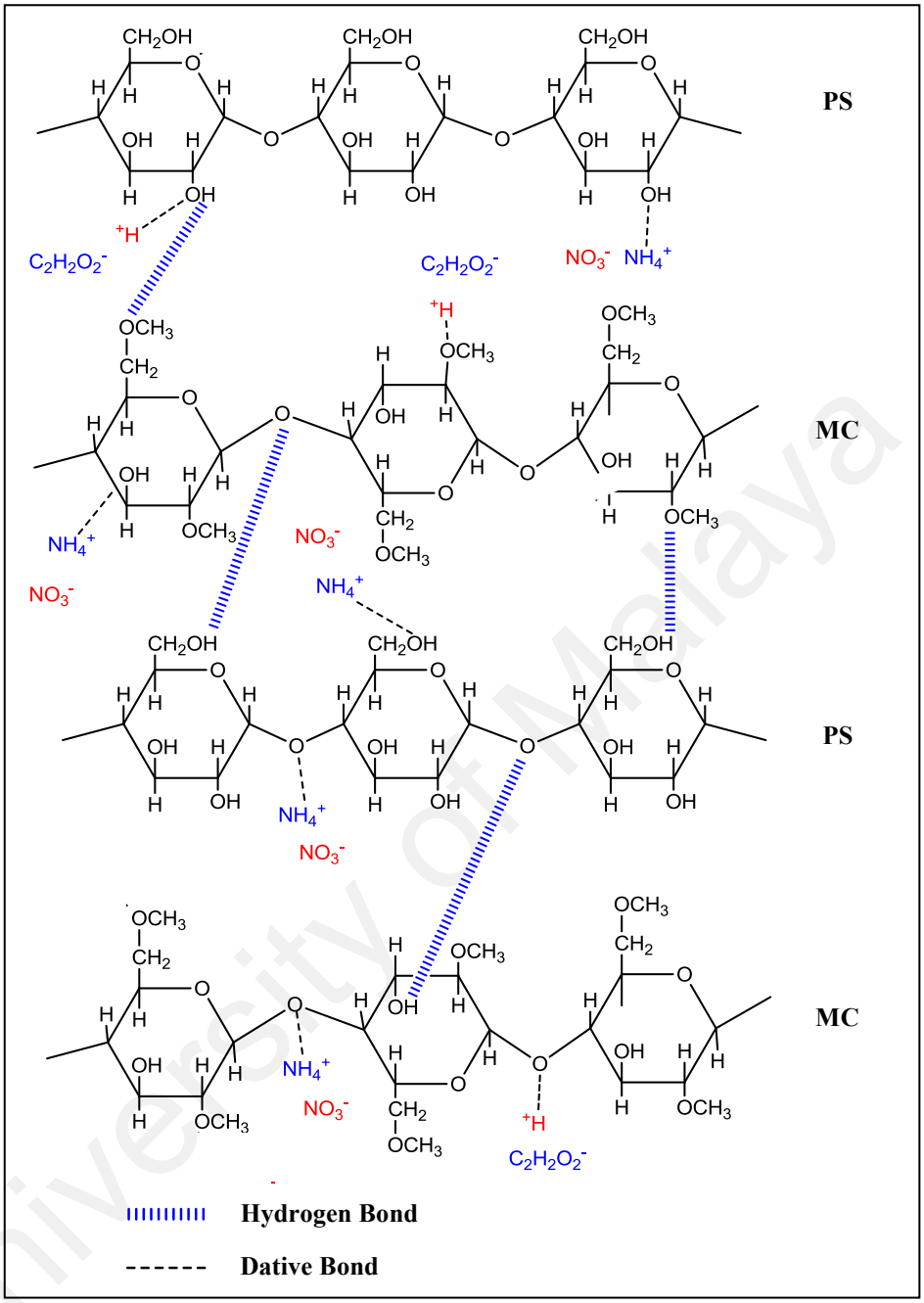

Figure 5.16: Illustration of possible interaction between methylcellulose, potato starch and NH_4NO_3.

The illustration of interaction between MC-PS starch blend with NH_4NO_3 is presented in Figure 5.16. Ions from NH_4NO_3 form complexation with MC-PS polymeric network through dative bond.

5.3.5 Methylcellulose-Potato Starch-Glycerol

Figure 5.17 show the FTIR spectra for MC-PS blend with various concentrations of glycerol at OH and glycosidic linkage band regions.

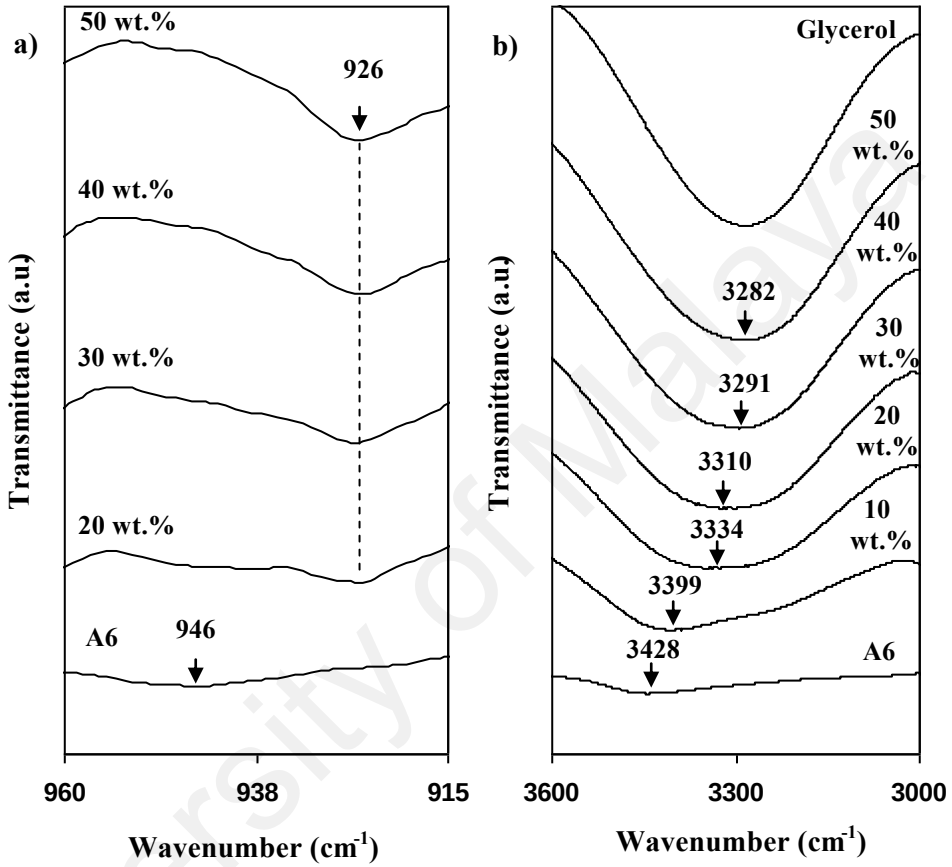

Figure 5.17: FTIR for MC-PS blend with various concentration of glycerol at a) 915-960 cm^{-1} and b) 3000-3600 cm^{-1}.

As observed in Figure 5.17(a), glycosidic linkage peak for A6 film at 946 cm^{-1} has shifted to a lower wavenumber of 926 with the inclusion of glycerol. Furthermore, with impregnation of glycerol up to 40 wt.% has increased the intensity of the peak. This condition proves the interaction of polymers and glycerol at glycosidic linkage regions.

Figure 5.17(b) shows OH peak at 3428 cm^{-1} for A6 film that has shifted to 3399, 3334, 3310, 3292 and 3282 cm^{-1} as 10, 20, 30, 40 and 50 wt.% are added, respectively.

Hence, from Figure 5.17(a) and Figure 5.17(b), it is assumed that the interaction between glycerol and polymers is preferable at OH regions rather than glycosidic regions. The schematic diagram of glycerol-polymers interactions can be observed in Figure 5.18.

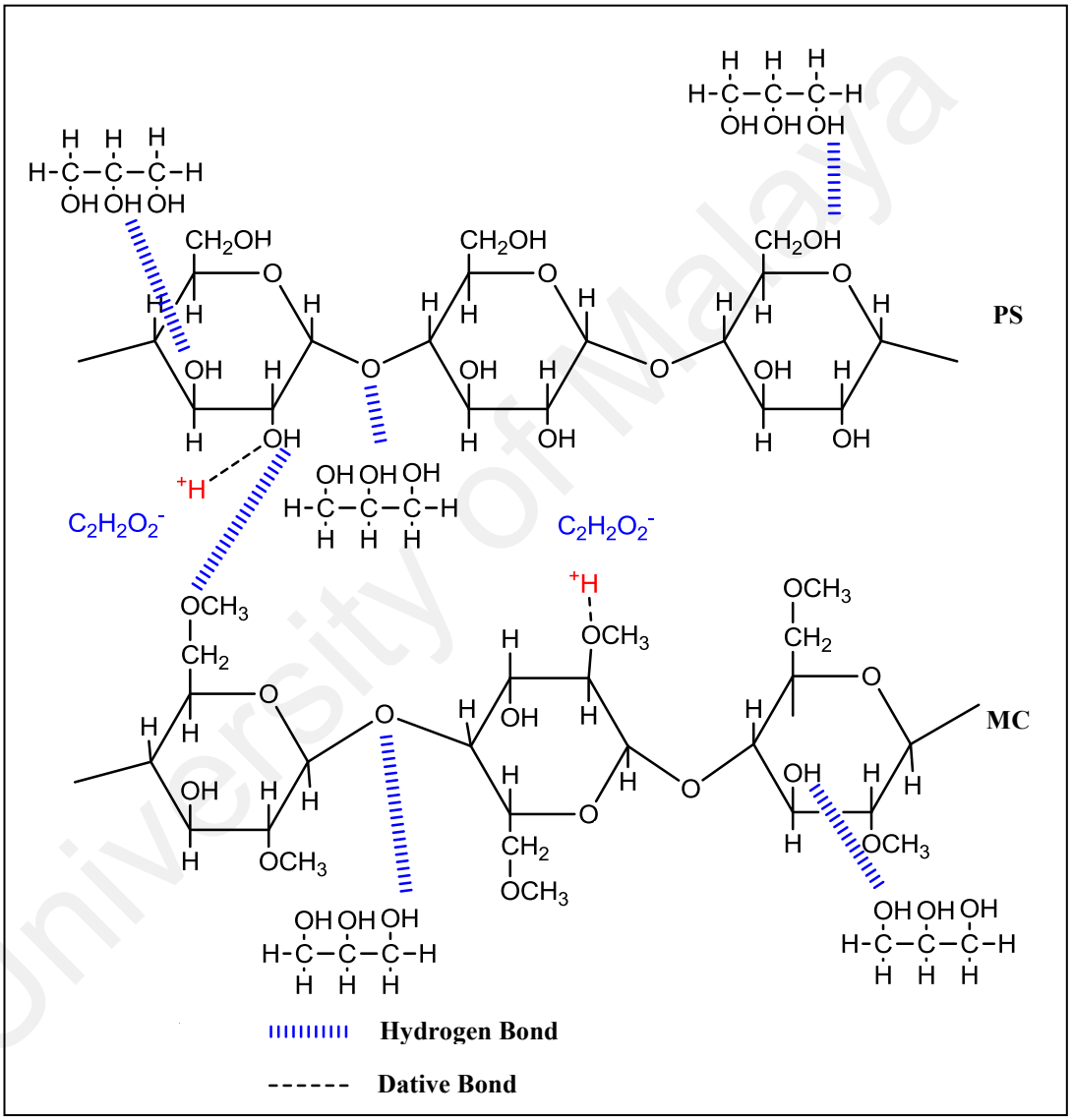

Figure 5.18: Illustration of possible interactions between methylcellulose, potato starch and glycerol.

5.3.6 Glycerol-NH_4NO_3

The purpose of plasticizer addition is to maximize the dissociation of salt which will enhance ionic conductivity, thus the interaction between glycerol and NH_4NO_3 has to be determined. The tested region is OH region due to high number of OH groups in glycerol structure. Figure 5.19 depicts the FTIR spectra of pure glycerol with addition of various NH_4NO_3 concentrations.

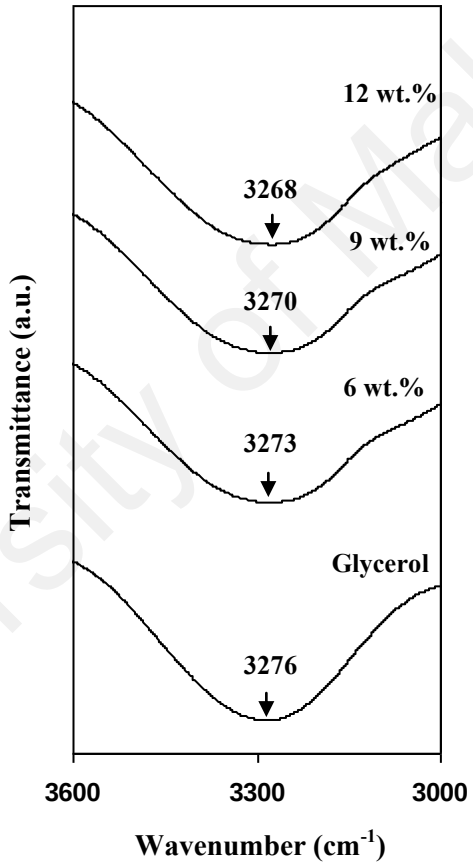

Figure 5.19: FTIR of glycerol with various concentrations of NH_4NO_3.

The broad peak of hydroxyl for glycerol is centered at 3276 cm^{-1} as observed in Figure 5.19. Shukur (2015) reported that OH peak for pure glycerol is centered at 3286 cm^{-1} which is almost consistent with this study. As 6 wt.% of NH_4NO_3 is added, the peak has changed to 3273 cm^{-1} and continue to shift to 3268 cm^{-1} with 12 wt.%.

The shift of OH peak describes that NH_4^+ has interacted with oxygen atoms of glycerol which can be referred in Figure 5.20. Glycerol is well known of possessing a rich-hydroxyl moiety structure that can form hydrogen bonding with oxygen and hydrogen atoms of the polysaccharide chains (Balakrishna, Gopi, Sreekala & Thomas, 2018).

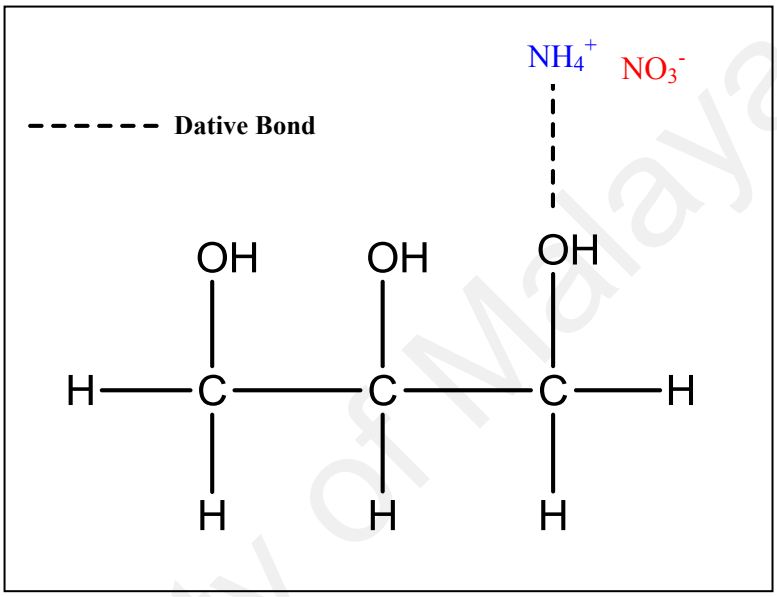

Figure 5.20: Illustration of possible interactions between glycerol and NH_4NO_3.

5.3.7 Methylcellulose-Potato Starch-NH_4NO_3-Glycerol

FTIR spectra for the sample with various concentration of glycerol are shown in Figure 5.21. The band region of glycosidic linkages and OH are observed to determine if more ions are interacted with the polymer as the glycerol is added.

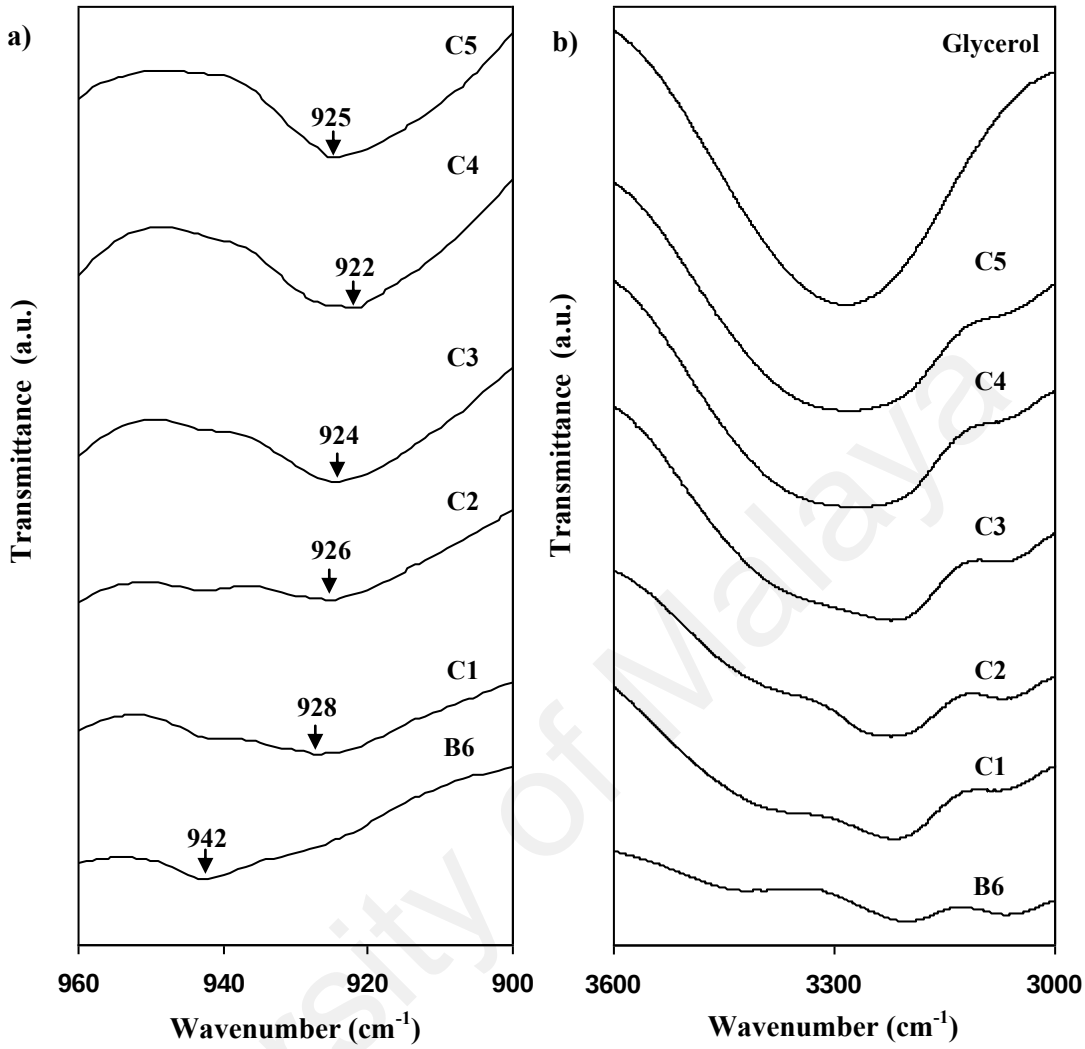

Figure 5.21: FTIR for selected plasticized electrolytes at a) 920-960 cm^{-1} and b) 3000-3600 cm^{-1}.

The glycosidic linkage peak for B6 electrolyte is observed at 942 cm^{-1} as depicted in Figure 5.21(a). Inclusion of 10 wt.% glycerol has shifted the peak to 928 cm^{-1} and 40 wt.% at 922 cm^{-1}. The presence of glycerol initiates more dissociation of ions to occur, thus more ions are free to interact with lone pair electrons at the oxygen atoms of the glycosidic linkage (Rasali & Samsudin, 2018).

Figure 5.21(b) reveals that in the region of 3000 to 3600 cm^{-1} there are three peaks appear for plasticized electrolyte. This is due to the overlapping between OH peak with $v_{as}(NH_4^+)$ and $v_s(NH_4^+)$ peaks which need to be deconvoluted. The presence of $v_{as}(NH_4^+)$ and $v_s(NH_4^+)$ peaks is one of the evidences of cations-polymers complexations (Kadir, Majid & Arof, 2010).

The deconvoluted version of 3000-3600 cm^{-1} band region for plasticized electrolytes is shown in Figure 5.22. B6 possesses OH peak at 3415 cm^{-1} which changed to 3408 cm^{-1} with incorporation of 10 wt.% of glycerol (C1). The peak continues to shift to 3352 cm^{-1} and 3352 cm^{-1} when 20 wt.% (C2), 30 wt.% glycerol (C3), respectively, are added to the salted electrolyte. The OH peak optimized at a lower wavenumber for the highest conducting electrolyte (C4) at 3328 cm^{-1}. The shifting of peak's wavenumber signifies that more free ions have interacted with oxygen of OH moiety in the polymeric network.

As more than 40 wt.% of glycerol is added, OH peak is observed to shift back to 3330 cm^{-1}. This situation signifies that less cations-OH interaction as the concentration of glycerol exceeded 40 wt.%. High concentration of plasticizer promotes the development of self-link between plasticizer, resulting ions recombination that leads to decrement in ionic number density (Shukur & Kadir, 2015; Rasali, Muzakir & Samsudin, 2017). The reduction of free ion can reduce the ionic conductivity. This condition will be further discussed in conductivity and transport analysis in Chapter 6.

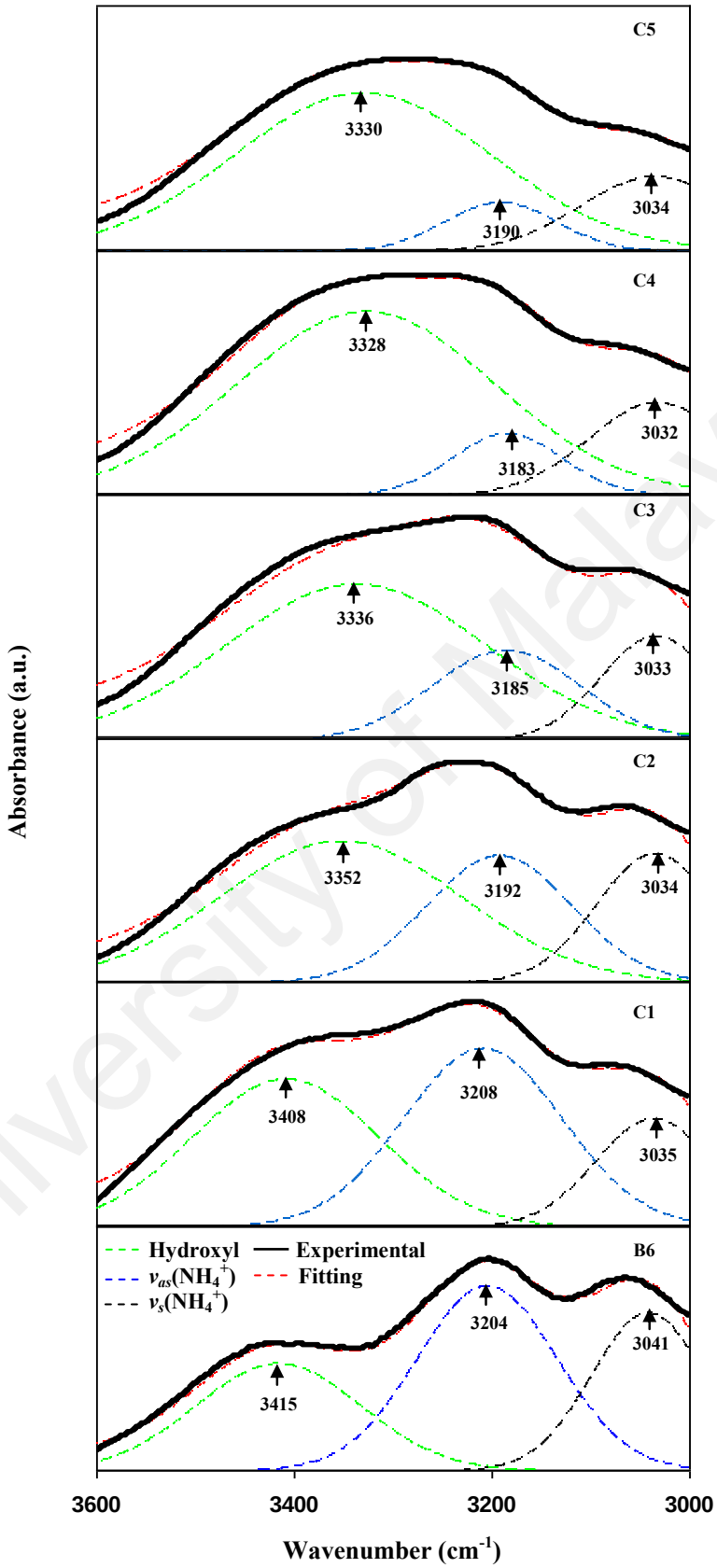

Figure 5.22: Deconvoluted FTIR for plasticized electrolytes at 3000-3600 cm^{-1}.

Figure 5.23 shows the schematic illustration of any possible interaction between MC, PS, NH_4NO_3 and glycerol.

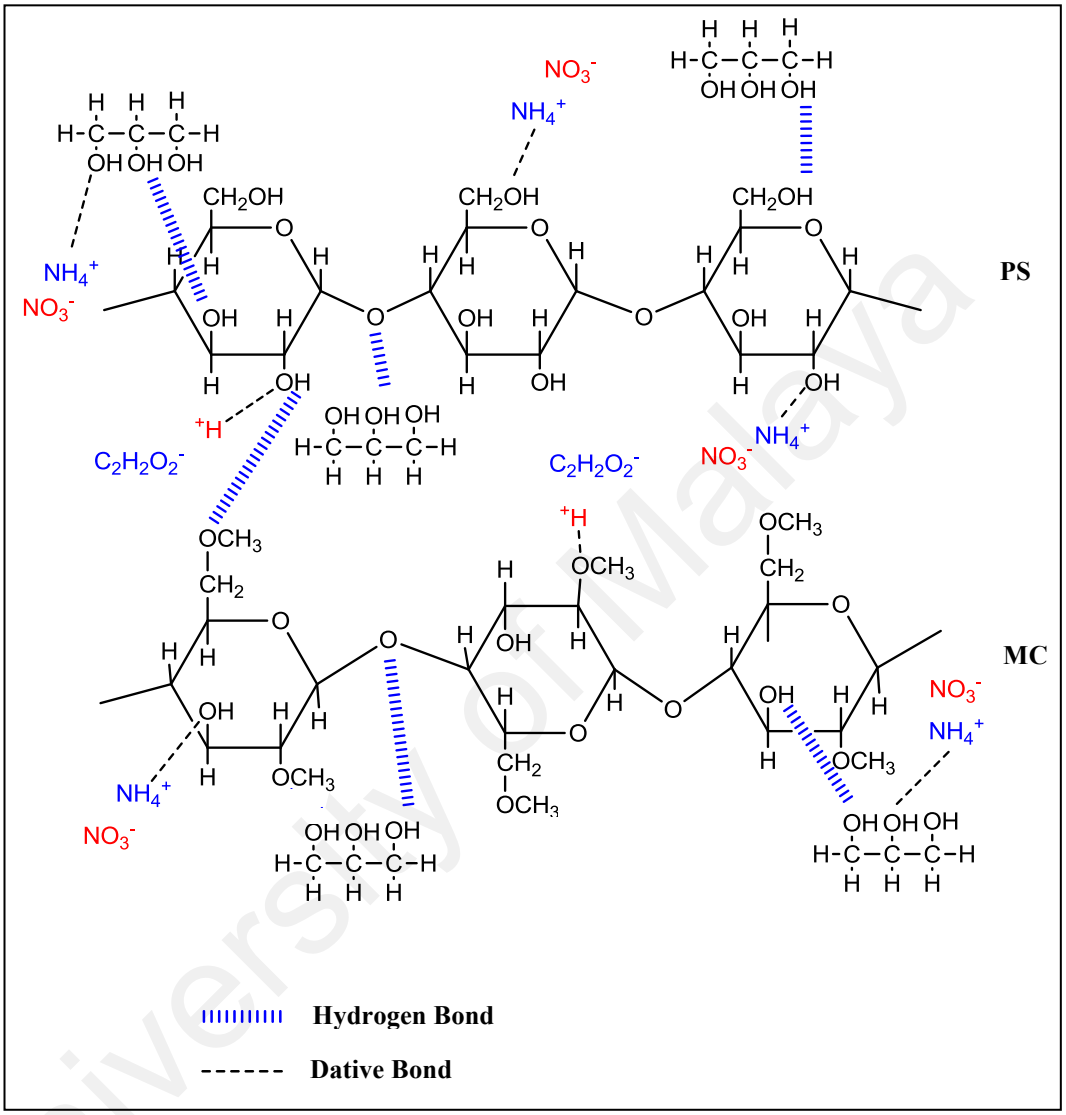

Figure 5.23: Illustration of possible interactions between methylcellulose, potato starch, NH_4NO_3 and glycerol.

The interactions occur at OH and glycosidic linkages. No interactions detected at OCH_3 functional group with the addition of glycerol to MC-PS-NH_4NO_3 system. Hence the ionic conductivity is expected to be enhanced with the inclusion of glycerol. Bin-Dahman, Rahaman, Khastgir and Al-Harthi (2017) stated that glycerol's high

dielectric constant lessen the cation-anion electrostatic force which in turn will offer more mobile charge carriers.

5.4 Summary

. From XRD analysis, it is found that the inclusion of 30 wt.% NH_4NO_3 provides the most amorphous sample for salted electrolytes. The amorphousness of the electrolyte is further enhanced with the presence of 40 wt.% glycerol. C4 is proven as the electrolyte with the highest percentage of amorphous phase via deconvolution method, where C4 possesses the lowest value of degree of crystallinity. From FTIR analysis on MC-PS with acetic acid, it is found that the interaction occurs at OH and glycosidic linkages. For MC the interaction also happen at methoxy groups. By blending 60 wt.% MC with 40 wt.% PS, the changes in position of OH, glycosidic linkages and C-O-C peaks can be assumed as development of hydrogen bonding between MC and PS. As NH_4NO_3 is included to the MC-PS matrix, cation is detected to form complexation with OH and glycosidic linkages. No interaction observed for methoxy groups. MC-PS-glycerol shows interactions at OH and glycosidic band regions. Glycerol-NH_4NO_3 interaction also has been verified as the addition of NH_4NO_3 to the pure glycerol has shifted the OH peak of glycerol. The changes in peak's shape, position and intensity confirms the interaction among MC, PS, NH_4NO_3 and glycerol. Hence, glycerol is considered to serve as alternative pathway for ions migrations.

CHAPTER 6: ELECTRICAL PROPERTIES OF THE POLYMER ELECTROLYTE

6.1 Introduction

Based on the XRD results in Chapter 4, the blend composition of 60 wt.% methylcellulose (MC)-40 wt.% potato starch (PS) is chosen as the polymer host for the electrolyte due to its high amorphous nature. From FESEM and DSC results in Chapter 4, it is found that MC and PS are miscible with no phase separation. Thus NH_4NO_3 salt is added to MC-PS blend to provide ions for the conduction process. The effect of salt concentration to the conductivity and other electrical properties is explained in details in this chapter. Those parameters are further analyzed on addition of various concentration of glycerol.

An EIS based method as proposed by Arof, Amirudin, Yusof and Noor (2014) has been utilized to study the transport properties i.e. ionic mobility and diffusion coefficient of MC-PS-NH_4NO_3 (salted electrolyte) and MC-PS-NH_4NO_3-glycerol (plasticized electrolyte) at room and elevated temperatures. Vogel-Fulcher-Tammann (VFT) theory for conductivity-temperature behaviour can be observed as glycerol is added to MC-PS-NH_4NO_3.

The main charge carriers are analyzed using ionic and protonic transference number analysis. Comparative cyclic voltammtery (CV) is used to verify the existence of protonic conduction in MC-PS-NH_4NO_3-glycerol system. Two cells are fabricated for this CV analysis which are Zn + $ZnSO_4.H_2O$|C4|Zn + $ZnSO_4.H_2O$ and stainless steel (SS)|C4|SS.

6.2 Impedance Analysis

Nyquist graph for B1, B2, B3 and B4 at room temperature are shown in Figure 6.1.

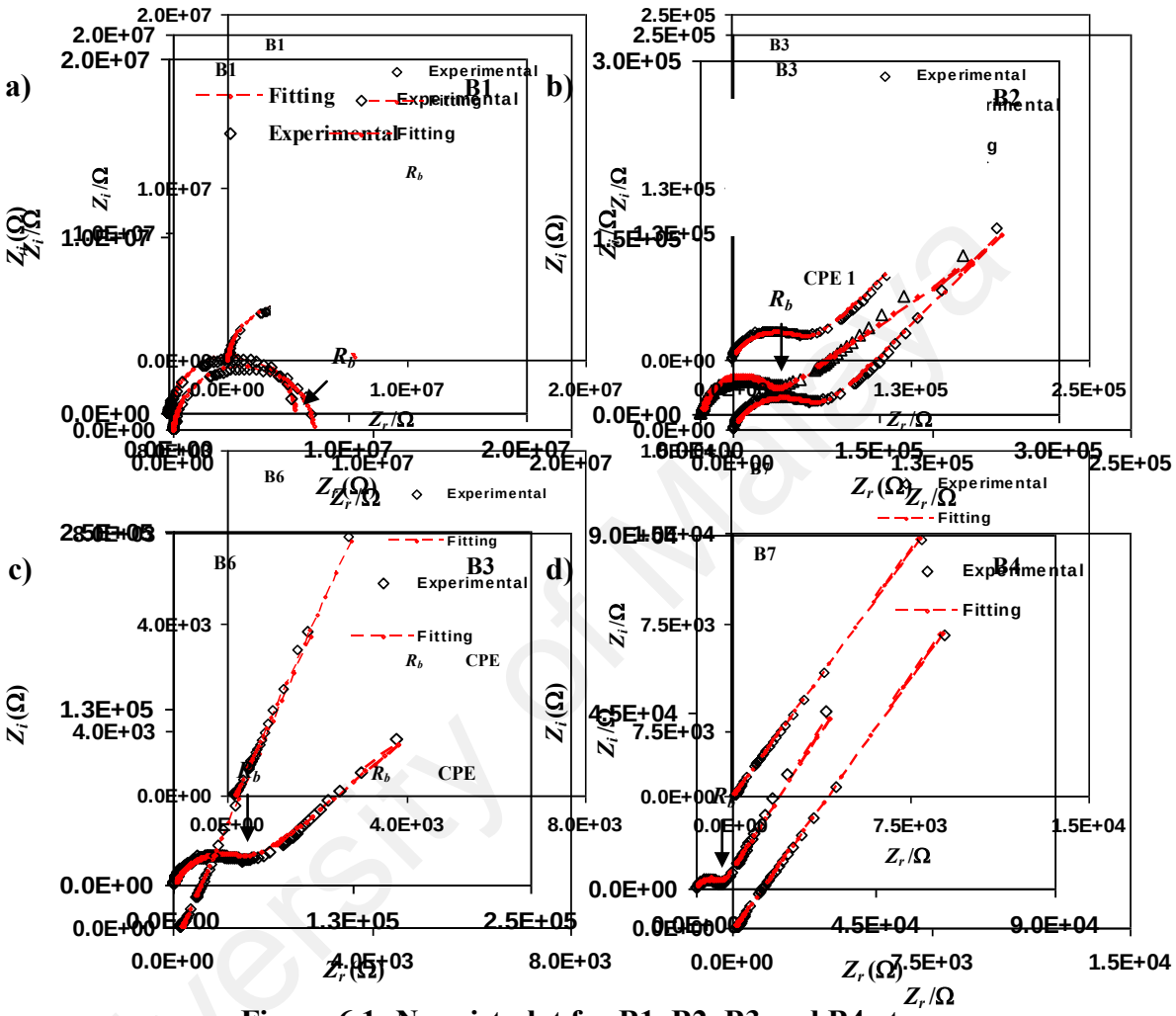

Figure 6.1: Nyquist plot for B1, B2, B3 and B4 at room temperature.

B1 (Figure 6.1(a)) has only a semicircle where the bulk resistance (R_b) can be taken from the interception of the semicircle with real axis (horizontal axis). As 10 wt.% NH_4NO_3 (Figure 6.1(b)) is added, the plot is a combination of spike and semicircle. R_b for this kind of plot is taken from the interception of the semicircle and the spike. The spike at low frequency portrays the polarization effect while the semicircle at higher frequency region is due to migration of ions in the bulk of electrolyte (Samsudin,

Khairul & Isa, 2012). It is noticeable that the semicircle for B3 and B4 has become lessened. This indicates that more ions are available as the concentration of NH_4NO_3 increased for ionic migration from one electrode to another (Kartha, 2013).

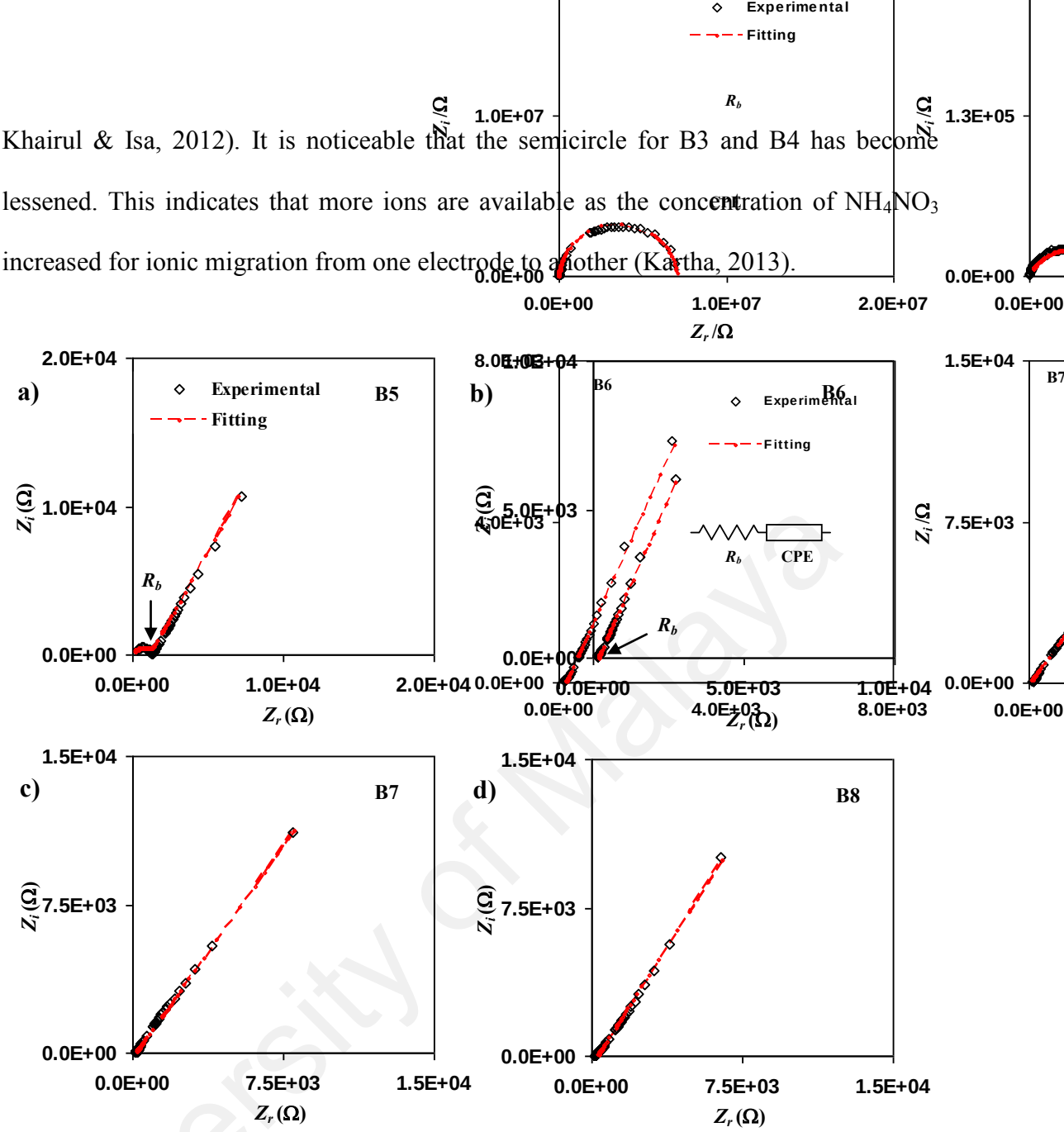

Figure 6.2: Nyquist plot for B5, B6, B7 and B8 at room temperature.

From Figure 6.2, the addition of 30 wt.% NH_4NO_3 (B6) shows the disappearance of semicircle part. R_b is extracted from the meeting point of the spike with the horizontal axis. The disappearance of semicircle part indicates that resistive parts of the polymer are dominant (Shukur, 2015). This situation also indicates that the number density of ion has been enhanced. The value of R_b increases for B7 and B8 meaning that salt has been recrystallized (Selvasekarapandian, Baskaran & Hema, 2005; Yulianti, Deswita,

Sudaryanto & Mashadi, 2019). This suggested that B7 and B8 have lower conductivity value compared to B6 electrolyte.

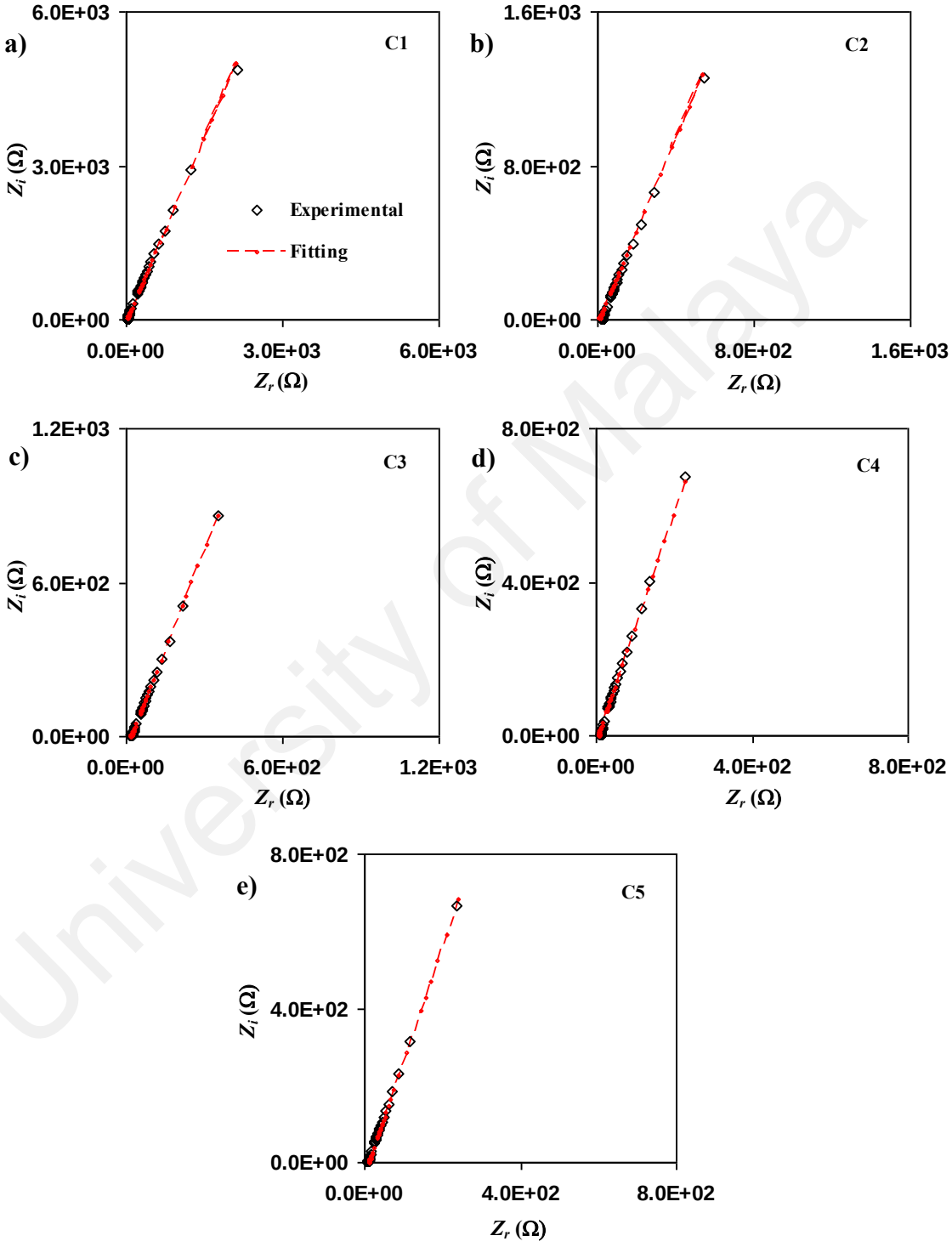

Figure 6.3: Nyquist plot for C1, C2, C3, C4 and C5 at room temperature.

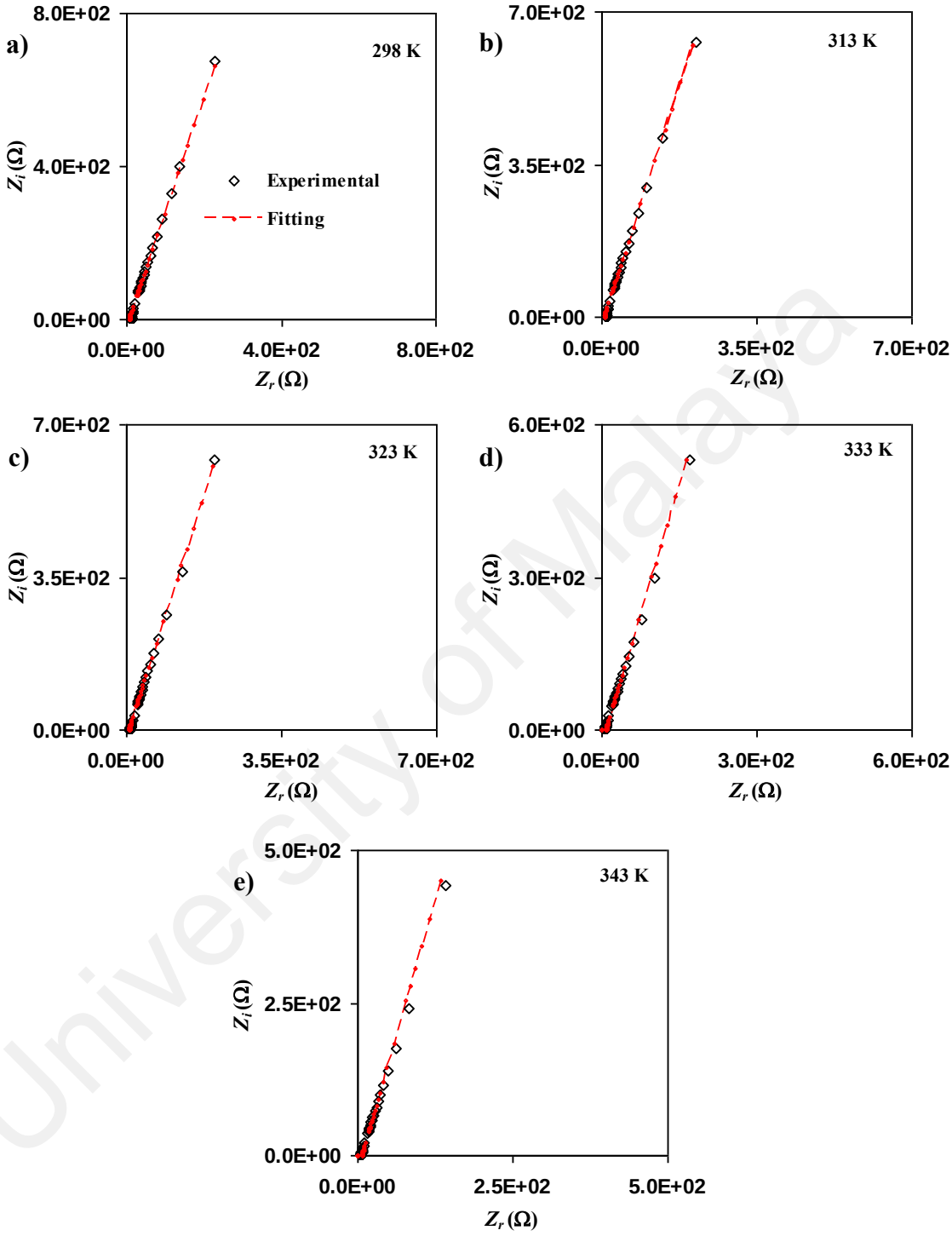

Figure 6.4: Nyquist plot for C4 at various temperatures.

Figure 6.3 depicts the Nyquist plots of certain plasticized electrolytes. It is noticeable that all samples possess only tilted line. R_b is observed to decrease as 10 wt.% of

glycerol is added and further reduces when 20, 30 and 40 wt.% of glycerol are included. Plasticizer promotes the increase in mobility of charge carriers which in turn increase the value of ionic conductivity (Selvasekarapandian et al., 2005; Ahmed, Jalal, Tahir, Mohamad & Abdullah, 2019). C5 possesses higher value of R_b compared to C4 which signifies that C5 has lower ionic conductivity compared to C4.

C4 electrolyte has been chosen to be used in impedance analysis at different temperatures as depicted in Figure 6.4. The value of R_b decreases with the increase in temperature. It is known that temperature affect the salt dissociation and the segmental motion of the polymer (Yao et al., 2019). The conductivity of the electrolyte is expected to increase as the temperature increases which will be discussed in the next section.

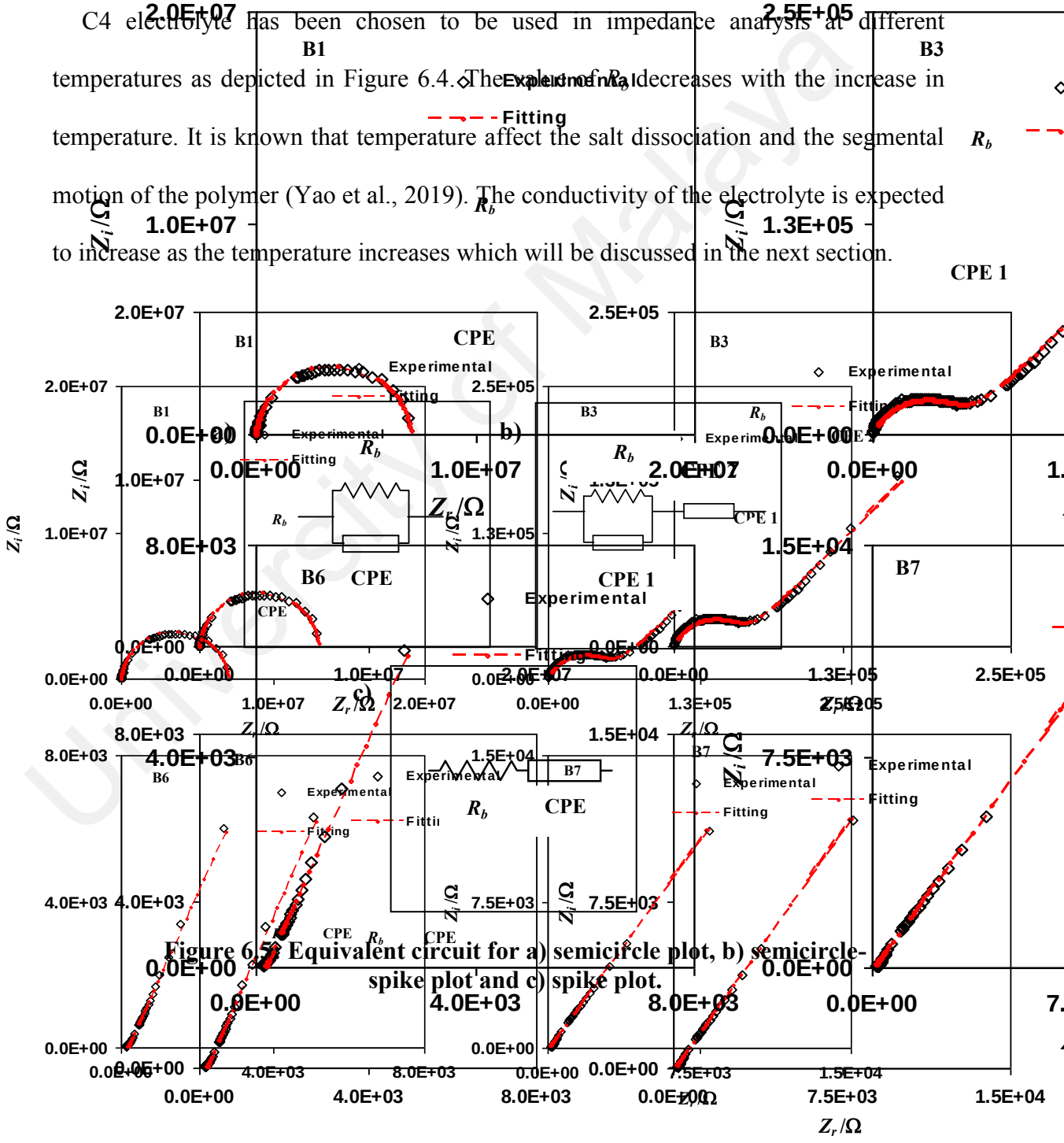

Figure 6.5: Equivalent circuit for a) semicircle plot, b) semicircle-spike plot and c) spike plot.

The equivalent electrical circuit illustration is utilized as its offers simple and clear picture of the system. The equivalent circuit for semicircle, semicircle-spike and spike plots can be seen in Figure 6.5(a), (b) and (c), respectively. The inhomogeneity of the electrolyte characterized the electrolyte as an "imperfect capacitor" which is called as constant phase element (CPE). CPE is given as (Qian et al., 2001; Adam et al., 2019):

$$Z_{CPE} = \frac{1}{C\omega^{p}}\left[\cos\left(\frac{\pi p}{2}\right) - i\sin\left(\frac{\pi p}{2}\right)\right] \tag{6.1}$$

where p is associated with the plot's deviation from the axis. Z_i and Z_r are the indicators of the imaginary and real parts of the impedance, respectively. C stands for capacitance for CPE and ω is the radial frequency.

The impedance plot which consists of only semicircle can be interpreted as a combination of CPE and R_b with parallel arrangement (Figure 6.5(a)) and can be expressed as:

$$Z_r = \frac{R_b C\omega^{p}\cos\left(\frac{\pi p}{2}\right) + R_b}{2R_b C\omega^{p}\cos\left(\frac{\pi p}{2}\right) + {R_b}^2 C^2\omega^{2p} + 1} \tag{6.2}$$

$$Z_i = \frac{{R_b}^2 C\omega^{p}\cos\left(\frac{\pi p}{2}\right)}{R_b C\omega^{p}\cos\left(\frac{\pi p}{2}\right) + {R_b}^2 C^2\omega^{2p} + 1} \tag{6.3}$$

For impedance plot with spike and semicircle, the equivalent circuit can be observed in Figure 6.5(b) and can be expressed via the following equations:

$$Z_r = \frac{R_b C_1 \omega^{p1} \cos\left(\frac{\pi p_1}{2}\right) + R_b}{2R_b C_1 \omega^{p} \cos\left(\frac{\pi p}{2}\right) + {R_b}^2 C^{\,2} \omega^{2p} + 1} + \frac{\cos\left(\frac{\pi p_2}{2}\right)}{C_2 \omega^{p2}} \tag{6.4}$$

$$Z_i = \frac{R_b C_1 \omega^{p1} \sin\left(\frac{\pi p_1}{2}\right)}{2R_b C_1 \omega^{p} \cos\left(\frac{\pi p}{2}\right) + {R_b}^2 C^{\,2} \omega^{2p} + 1} + \frac{\sin\left(\frac{\pi p_2}{2}\right)}{C_2 \omega^{p2}} \tag{6.5}$$

where p_2 and p_1 are the deviation of spike from the horizontal axis and deviation semicircle from vertical axis, respectively. Capacitance at high and low frequency are denoted as C_1 and C_2, respectively.

Impedance plot with a spike has an equivalent circuit of series combination between R_b and CPE as shown in Figure 6.5(c). This type of impedance can be expressed as:

$$Z_r = \frac{\cos\left(\frac{\pi p}{2}\right)}{C\omega^{p}} + R_b \tag{6.6}$$

$$Z_i = \frac{\sin\left(\frac{\pi p}{2}\right)}{C\omega^{p}} \tag{6.7}$$

Circuit elements for salted electrolytes have been calculated and listed in Table 6.1.

Table 6.1: Room temperature circuit elements for salted electrolytes.

Electrolyte	p_1 (rad)	p_2 (rad)	C_1(F)	C_2(F)
B1	0.94	-	1.79×10^{-11}	-
B2	1.00	0.38	1.92×10^{-11}	4.76×10^{-7}
B3	0.80	0.45	1.54×10^{-9}	4.83×10^{-7}
B4	0.80	0.64	3.85×10^{-9}	4.88×10^{-7}
B5	0.71	0.68	5.26×10^{-8}	1.64×10^{-6}
B6	-	0.73	-	2.22×10^{-6}
B7	-	0.61	-	2.17×10^{-6}
B8	-	0.64	-	2.13×10^{-6}

Based on Table 6.1, the value of C is higher at low frequency compared to high frequency. This phenomenon harmonized with the following equation:

$$C = \frac{A\varepsilon_o\varepsilon_r}{d} \tag{6.8}$$

here the thickness of the electrolyte is denoted as d while the indicator for contact area is given as A. ε_r and ε_o stand for dielectric constant and vacuum's permittivity, respectively. The value of ε_r is low at high frequency which in turn giving a low value of C (Hema et al., 2009; Kumar & Rao, 2019). The information on dielectric will be further explained in dielectric section. The value of C is noticed to increase as more salt is included. This signifies that more ions are created at high concentration giving a high value of C.

Table 6.2: Room temperature circuit elements for plasticized electrolytes.

Electrolyte	p_1(rad)	C(F)
C1	0.74	2.53×10^{-6}
C2	0.75	9.71×10^{-6}
C3	0.77	1.32×10^{-5}
C4	0.80	1.48×10^{-5}
C5	0.79	1.45×10^{-5}

Table 6.2 lists the room temperature circuit elements for plasticized electrolyte. The addition of glycerol enhances the value of *C*. Inclusion of glycerol increase the number of ions in the electrolyte. Thus more ions are available for electrode polarization which resulting in the enhancement of *C* (Salanne et al., 2016).

Table 6.3: High temperature circuit elements for C4 electrolyte.

Temperature (K)	p_1(rad)	C_1(F)
298	0.80	1.48×10^{-5}
313	0.80	1.52×10^{-5}
323	0.81	1.54×10^{-5}
333	0.82	1.67×10^{-5}
343	0.83	1.85×10^{-5}

Table 6.3 shows the variation of C4's circuit element at 298, 313, 323, 333 and 343 K. The enhancement of *C* at higher temperature is due to development of more free charge carriers at high temperature. Shuhaimi et al. (2012) reported that the increase in *C* value with increasing temperature implies that the electrolyte is suitable to be incorporated in electrochemical device technologies.

6.3 Conductivity at Room Temperature

Figure 6.8 depicts the influence of NH_4NO_3 of room temperature ionic conductivity of the electrolyte.

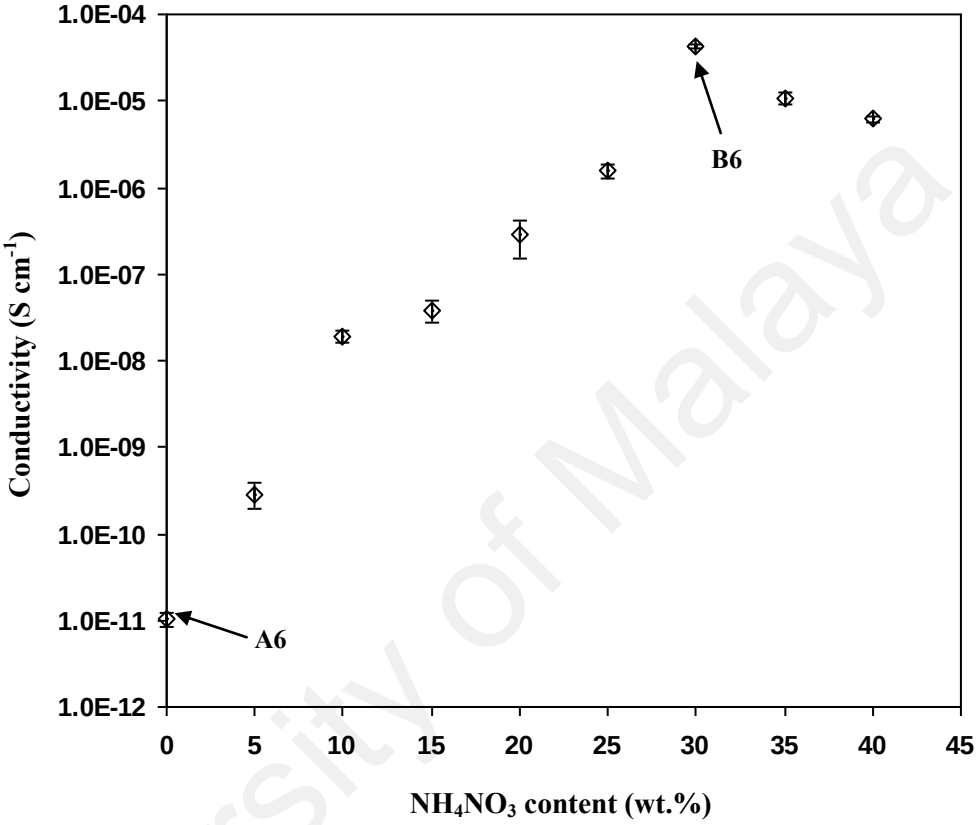

Figure 6.6: Room temperature conductivity of salted electrolytes.

Referring to Figure 6.6, A6 blend possesses a conductivity value of $1.04 \pm 0.19 \times 10^{-11}$ S cm^{-1}. Low conductivity of the polymer blend is due to low amount of free ions with absence of salt. The addition of 5 wt.% of NH_4NO_3 enhances the conductivity to $(2.89 \pm 0.91) \times 10^{-10}$ S cm^{-1}. As 20 wt.% of NH_4NO_3, the conductivity value is observed to enhance to $(1.44 \pm 2.80) \times 10^{-7}$ S cm^{-1}. The conductivity is maximized at $(4.35 \pm 0.16) \times 10^{-5}$ S cm^{-1} with the addition of 30 wt.% NH_4NO_3. Ahmed et al. (2019) stated that the improvement of ionic conductivity is attributed to increment of free charge carriers. The conductivity of the highest conducting MC-PS-NH_4NO_3

system in this study is higher than the single polymer systems i.e. MC-NH_4NO_3 (Shuhaimi et al., 2010) and starch-NH_4NO_3 (Khiar & Arof, 2010). The conductivity of electrolytes with polymer blend host is expected to have higher conductivity than the electrolyte with single polymer host due to extra active sites in polymer blend (Yusof et al., 2014). The conductivity is observed to decrease as 35 and 40 wt.% NH_4NO_3 are added to the polymer blend. Excess salt promotes the development of ion aggregates, triplets and pairs which reduce the mobility and amount of free ions (Salman, Abdullah, Hanna & Aziz, 2018; Jian et al., 2018).

The effect of glycerol on the room temperature conductivity is portrayed in Figure 6.7.

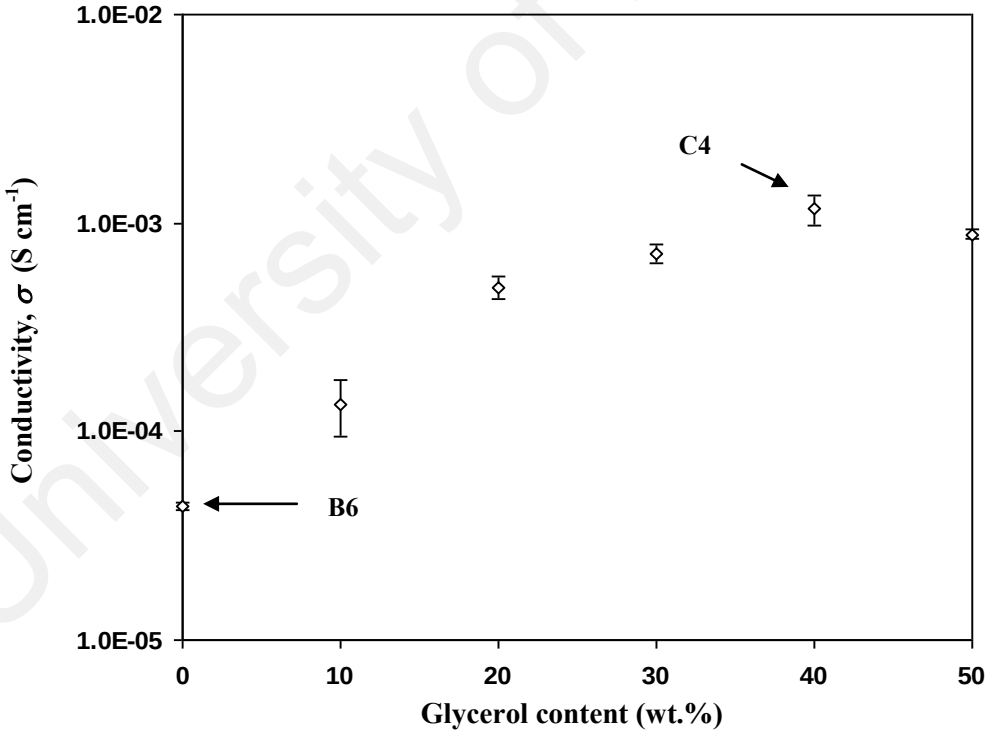

Figure 6.7: Room temperature conductivity of plasticized electrolytes.

The conductivity increases from $(4.37 \pm 0.16) \times 10^{-5}$ to $(4.47 \pm 0.41) \times 10^{-4}$ S cm^{-1} as 20 wt.% glycerol is added to the MC-PS-NH_4NO_3. The

maximum conductivity of (1.26 ± 0.1) × 10^{-3} S cm^{-1} is obtained at 40 wt.% glycerol. The increase in conductivity illustrates the effect of plasticization where different pathway for ion migration is provided by glycerol as well as improves the dissociation of ions. Thus enhances the ionic conductivity (Gondaliya, Kanchan & Sharma, 2013). Sekhar, Kumar and Sharma (2012) stated that it is easy for plasticizer molecules to migrate through the polymer host due to its small size which in turn reduces the polymer-polymer cohesive force. The reduction of conductivity at higher concentration of glycerol is due to development of plasticizer-plasticizer linkages which cause recrystalization of salt thus decreases the conductivity (Johan & Ting, 2011).

6.4 Temperature Dependent Conductivity of the Polymer Electrolyte

Figure 6.8 shows the effect of temperature on the conductivity of the electrolytes in salted system.

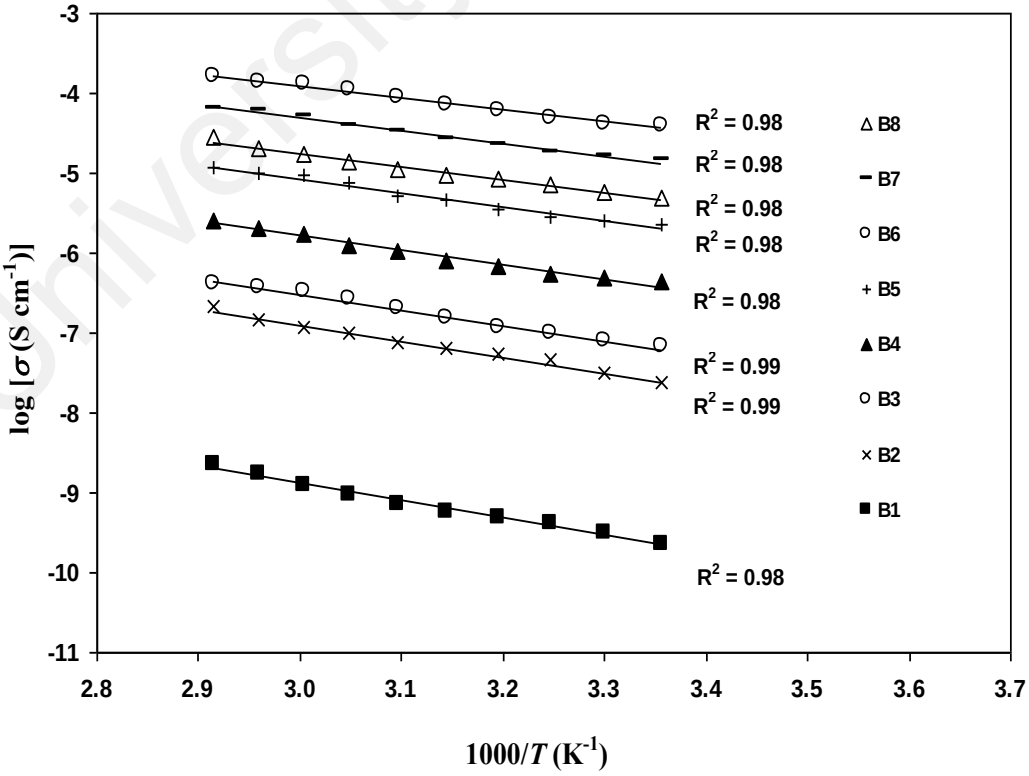

Figure 6.8: The conductivity of electrolyte in salted at various temperature.

It is observed that all electrolytes portray linear conductivity-temperature plot. This result shows that the ions are thermally activated for migration process thus obeying Arrhenius theory. This theory also suggests that a polymer chain does not undergo any phase transition with the inclusion of salt (Lim, Teoh, Ng, Liew & Ramesh, 2017). Temperature-ionic conductivity relation that obeys Arrhenius theory has been reported for many NH_4NO_3-based polymer electrolyte systems e.g. starch-NH_4NO_3 (Khiar, & Arof, 2010), Chitosan/PVA-NH_4NO_3 (Kadir, 2010), MC-NH_4NO_3 (Shuhaimi, 2010) and MC-PVA-NH_4NO_3 (Abdullah, Aziz & Rasheed, 2018). According to Equation (2.1), the value of activation energy (E_a) is taken from the plot in Figure 6.10 and listed in Table 6.4. Highest conducting electrolyte (B6) has the lowest E_a of 0.30 eV. As the concentration of NH_4NO_3 and temperature increases the number density of charge carriers increases thus decreases the barrier of energy for ionic migration (Gohel & Kachan, 2018). The effect of temperature and salt addition on ionic number density will be further analyzed in transport analysis section.

Table 6.4: The value of E_a for salted electrolytes.

Electrolyte	E_a (eV)
B1	0.43
B2	0.40
B3	0.39
B4	0.36
B5	0.35
B6	0.30
B7	0.32
B8	0.33

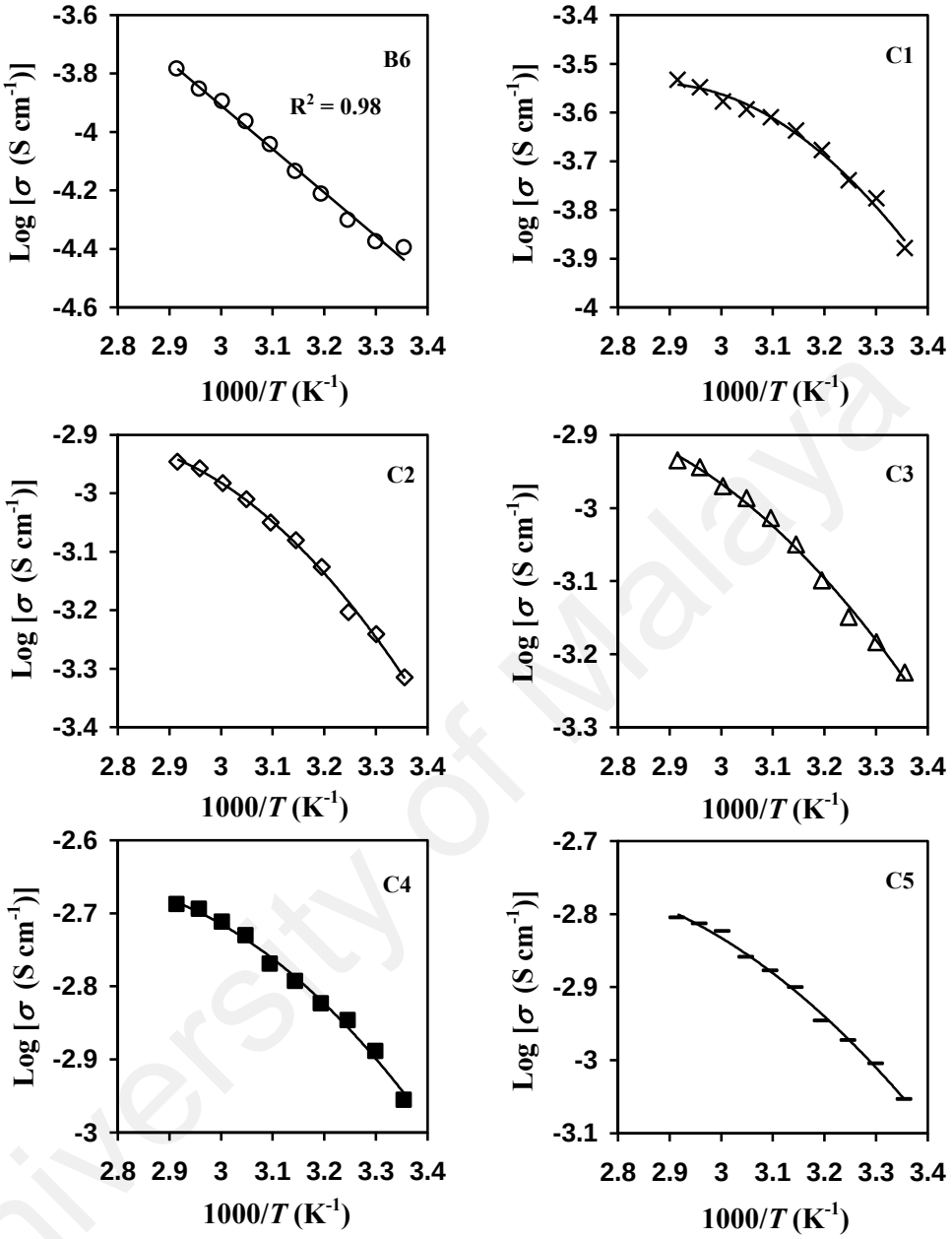

Figure 6.9: The conductivity of electrolyte in salted at various temperature.

Temperature-conductivity relation for electrolytes in plasticized system is illustrated in Figure 6.9. It can be observed that the plasticized electrolytes possess non-linear conductivity-temperature relation. This type of behavior obeys VFT model of conduction mechanism. VFT model stated that the movement of polymers chain is dominant in the process of ionic conduction (Alves, Sentanin, Sabadini, Pawlicka &

Silva, 2016). The changes from Arrhenius to VFT with the inclusion of glycerol have been reported in other works (Andrade, Raphael & Pawlicka, 2009; Mattos et al., 2012; Alves et al., 2016).

By employing Equation (2.2), VFT graph for plasticized electrolytes is plotted as shown in Figure 6.10. The value of pseudo-activation energy (E_p) is tabulated in Table 6.5.

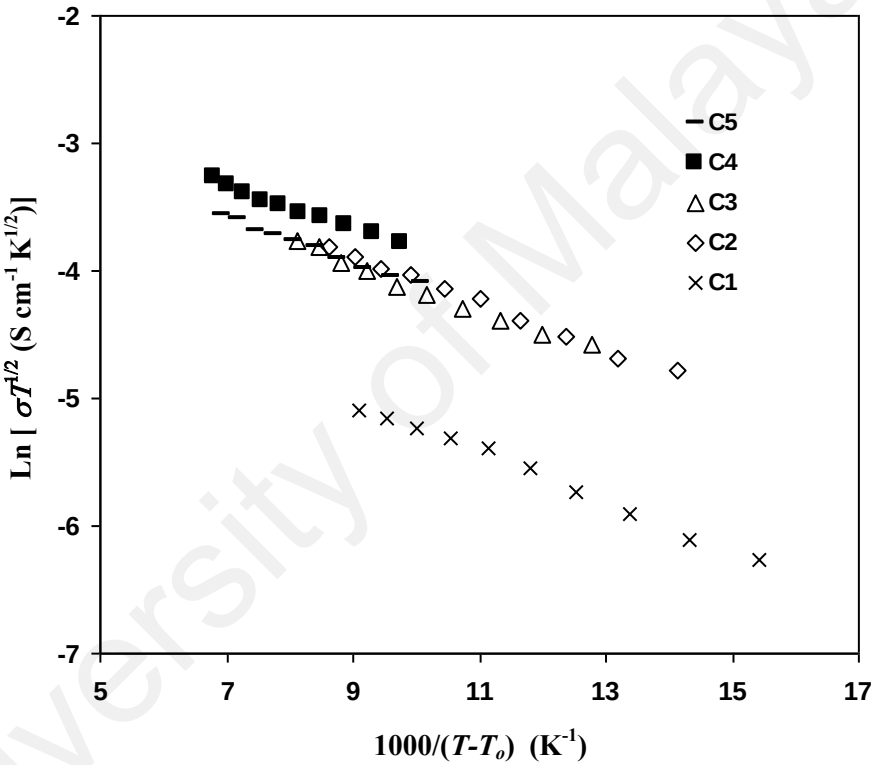

Figure 6.10: VFT plot for plasticized electrolytes.

Based on Table 6.5, the value of E_p reduces with the increment of glycerol content. The value of R^2 for the plot in Figure 6.10 is from 0.98 to 0.99 when T_g values from DSC results are used. Hence results from DSC and VFT analysis are reliable. C4 electrolyte achieves the lowest E_p of 13.0 meV which is comparable to plasticized proton-based electrolyte reported by Liew, Ramesh and Arof (2016).

The energy barrier of ionic migration process and polymer-polymer cohesive force has been decreased by the addition of plasticizer (Alves & Silva, 2014). This situation decreases the value of E_p. Surplus amount of glycerol in the electrolyte obstructs the interaction between lone pair electrons of oxygen atoms with cations. Cations have to compete with plasticizer molecule to accommodate the vacant sites at the polymer host which cause ion aggregation and increase the activation energy (Shukur, Ithnin & Kadir, 2016).

Table 6.5: VFT parameters for plasticized electrolytes.

Electrolytes	Glass transition temperature, T_g (°C)	Glass transition temperature, T_g (K)	Ideal glass transition temperature, T_o (K)	Pseudo-activation energy, E_p (meV)
C1	10.2	283.2	233.2	16.8
C2	4.2	277.2	227.2	15.6
C3	-3.3	269.7	219.7	15.4
C4	-27.5	245.5	195.5	13.9
C5	-24.2	248.8	198.8	15.2

6.5 Ionic Transport Study

It is crucial to identify the value of number density (n) and mobility (μ) of ions since the conductivity is depending on these two parameters as in the following equation:

$$\sigma = ne\mu \tag{6.9}$$

here e is the electronic charge.

Arof-Noor (A-N) method is employed to study the transport properties of the electrolytes (Arof et al., 2014). A-N method enables us to determine the transport properties employing impedance analysis. The value of μ is expressed as:

$$\mu = eD/kT \tag{6.10}$$

where diffusion coefficient (D) for impedance plots with combination of semicircle and spike can be described as:

$$D = \left(Ak_2\varepsilon_r\varepsilon_o\right)^2/\tau_2 \tag{6.11}$$

Here A is the contact area while the indicators for dielectric constant and vacuum permittivity are given as ε_r and ε_o, respectively. k_2 can be extracted from impedance where k_2 is inverse of C_2 while τ_2 is taken from the minimum of Z_i. Fadzallah, Noor, Careem and Arof (2016) stated that the value of ε_r should be taken at where log ε_r is constant.

For impedance plots with only spike the value of D can be determined from:

$$D = D_o \exp\left\{-0.0297[\ln D_o]^2 - 1.4348[\ln D_o] - 14.504\right\} \tag{6.12}$$

$$D_o = \left(4k^4d^2\right)\times\left(R_b{}^4\omega_m^3\right)^{-1} \tag{6.13}$$

where ω_m stands for angular frequency associated with minimum Z_i while d represents the electrolyte's thickness. k is the inverse of C from the impedance fitting.

In Figures 6.1 and 6.2, the Nyquist plot of B2, B3, B4 and B5 consist of a semicircle and tilted spike. Hence, Equation (6.11) is used to calculate the value of D. Furthermore, according to Equation (6.11), $\log \varepsilon_r$ vs $\log f$ must be plotted to identify the constant value of ε_r. Based on Figure 6.11, ε_r is obtained at $\log \varepsilon_r > 5.5$.

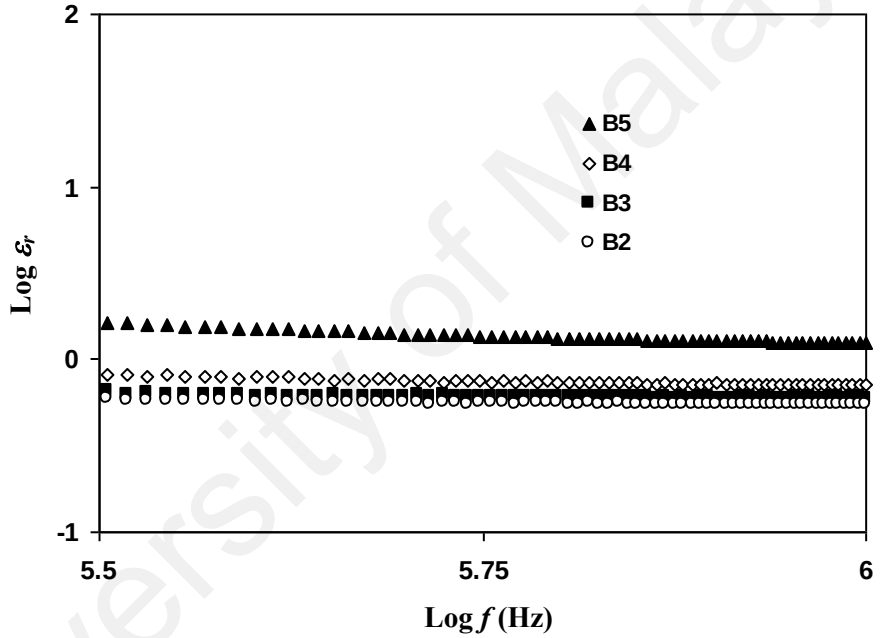

Figure 6.11: log ε_r vs log f for B2, B3, B4 and B5.

The values of k_2, ε_r and τ_2 for B2, B3, B4 and B5 are tabulated in Table 6.6. These parameters are used to calculate D, μ.and n via Equation (6.11), (6.10) and (6.9), respectively.

Table 6.6: The values of k_2, ε_r and τ_2 for B2, B3, B4 and B5 at room temperature.

Electrolyte	k_2 (F^{-1})	ε_r	τ_2 (s)
B2	2.10×10^6	0.55	1.77×10^{-5}
B3	2.07×10^6	0.60	1.22×10^{-5}
B4	2.05×10^6	0.71	2.65×10^{-6}
B5	6.11×10^5	1.24	2.31×10^{-7}

The impedance plot of B6, B7 and B8 consist of only spike with absence of semicircle hence the value of k and ω_m are listed in Table 6.7. Based on these values we can calculate D, μ and n via Equations (6.12), (6.10) and (6.9), respectively. The trend of D, μ.and n is expected to harmonize with the conductivity trend.

Table 6.7: The values of k and ω_m for B6, B7 and B8 at room temperature.

Electrolyte	k (F^{-1})	ω_m (rad s^{-1})
B6	4.50×10^5	9.42×10^6
B7	4.60×10^5	5.84×10^6
B8	4.70×10^5	1.01×10^7

Figure 6.12 shows the transport parameters for salted electrolyte at room temperature. In Figure 6.12(a), the value of D increases from 2.50×10^{-9} cm^2 s^{-1} to 6.00×10^{-7} cm^2 s^{-1} as the concentration of NH_4NO_3 increases from 10 wt.% to 30 wt.%. As 35 and 40 wt.% NH_4NO_3 are added the value of D drops to 2.48×10^{-7} cm^2 s^{-1} and 1.52×10^{-7} cm^2 s^{-1}, respectively.

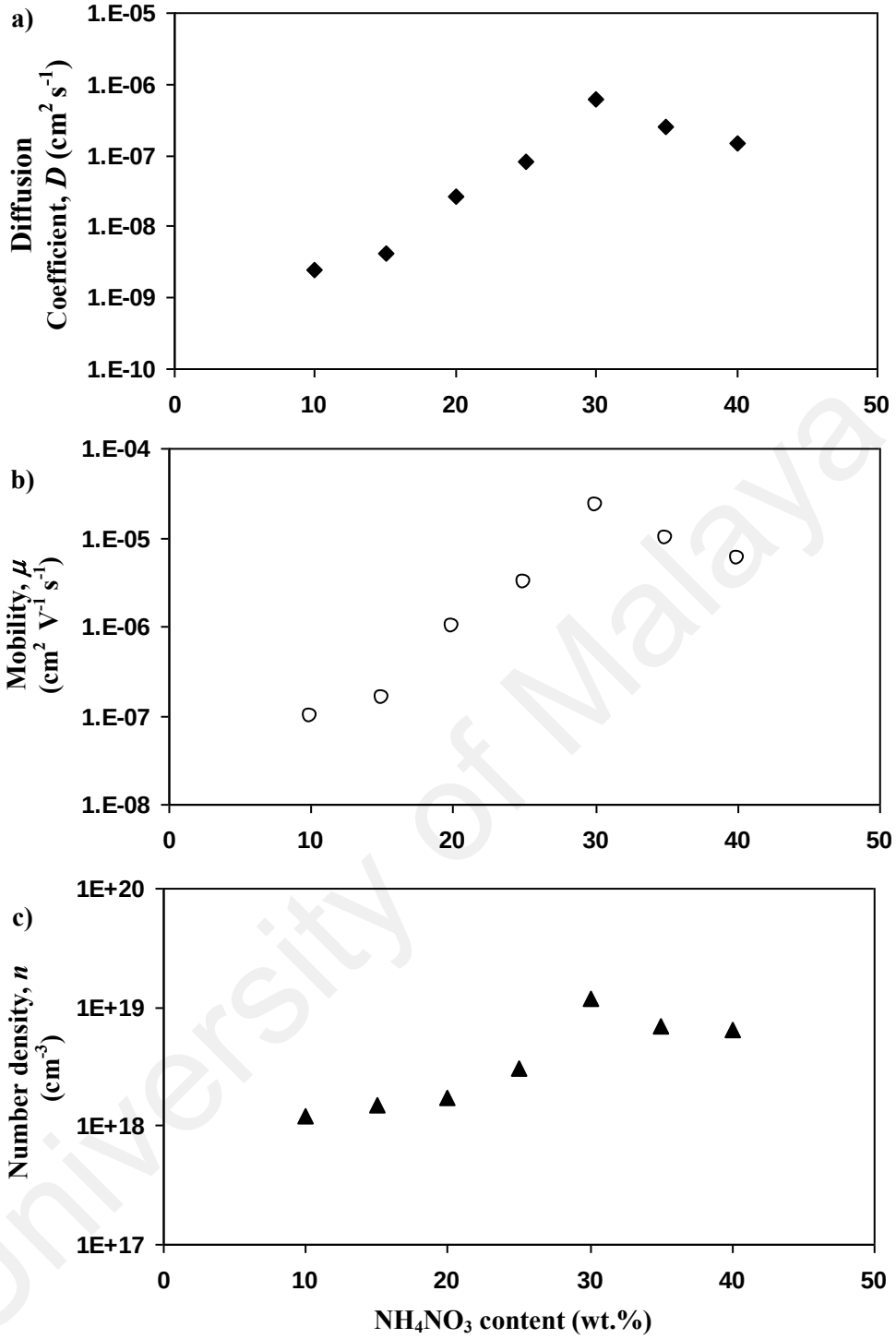

Figure 6.12: Graph of (a) *D*, (b) μ and (c) *n* for salted electrolytes at room temperature.

Similar trend is observed for μ as depicted Figure 6.12(b), where the highest conducting salted electrolyte with 30 wt.% NH_4NO_3 possesses the highest μ (2.34×10^{-5} cm^2 V^{-1} s^{-1}). The value of *n* in Figure 6.12(c) obtains the maximum value of

1.17×10^{19} cm^{-3} at 30 wt.% NH_4NO_3. As concentration of NH_4NO_3 exceeds 30 wt.%, the value of n is started to decrease. Hence the trend of ionic conductivity at room temperature for salted electrolyte harmonized with the trend of D, μ and n. It can be inferred that at high salt content, the reduction in those transport parameters is due to close distance between cations and anions which reduces the number density of ion as well as ionic conductivity (Ahmad & Isa, 2015).

As observed in Figure 6.3, all plasticized electrolytes possess impedance plot with just a tilted spike. Hence, the value of k and ω_m are listed in Table 6.8.

Table 6.8: The values of k and ω_m for plasticized electrolyte at room temperature.

Electrolyte	k (F^{-1})	ω_m (rad s^{-1})
C1	3.95×10^5	6.28×10^6
C2	1.03×10^5	4.40×10^6
C3	7.60×10^4	1.88×10^6
C4	6.75×10^4	1.10×10^6
C5	6.90×10^4	1.11×10^6

Figure 6.13 portrays the transport parameters for plasticized electrolyte at room temperature. The values of D, μ and n optimize at 8.33×10^{-6} cm^2 s^{-1}, 3.24×10^{-4} cm^2 V^{-1} s^{-1} and 2.15×10^{19} cm^{-3}, respectively, with the incorporation of 40 wt.% glycerol. The addition of glycerol enhances the flexibility of the polymer backbone thus increasing the value of D and μ. Furthermore, glycerol assists ion dissociation which increases the value of n (Nagraj, Sasidharan, David & Sambandam, 2017). However, excess plasticizer blocks the pathway for ionic conduction that reduces the ionic mobility and diffusivity. Limited space in the electrolyte also promotes ion

recombinations thus decreases the ionic number density (Shamsuddin, Noor, Albinsson, Mellander & Arof, 2017).

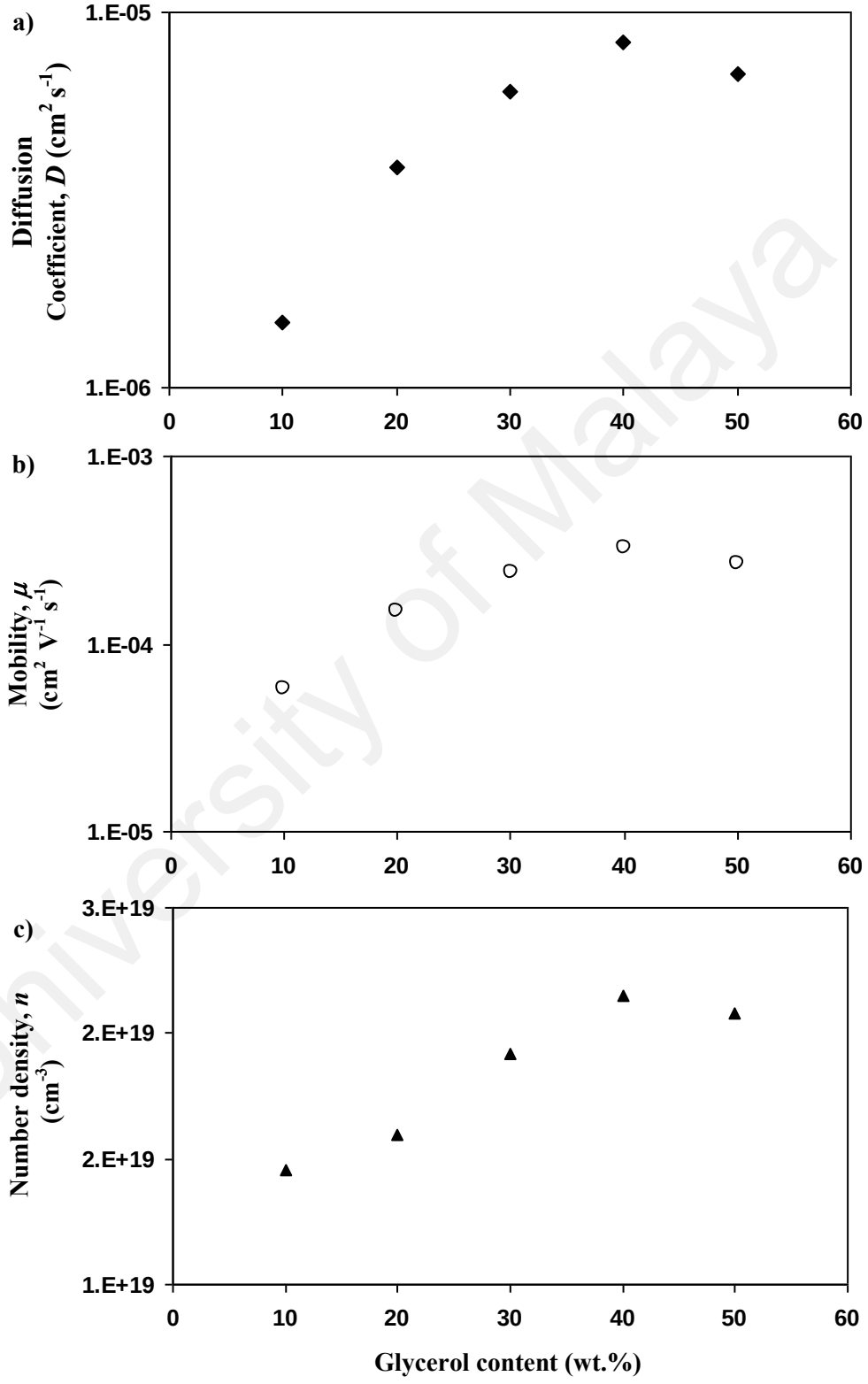

Figure 6.13: Graph of (a) *D*, (b) μ and (c) *n* for plasticized electrolytes at room temperature.

As observed in Figure 6.4, the impedance plot for C4 electrolyte at high temperature shows just a tilted spike with absence of semicircle. Thus Equations (6.12) and (6.13) have been used. The value of k and ω_m are tabulated in Table 6.9. The trend of D, μ.and n is expected to increase as the value of conductivity for C4 electrolyte increased at elevated temperature in Figure 6.9.

Table 6.9: The values of k and ω_m for C4 at high temperature.

Temperature (K)	k (F^{-1})	ω_m (rad s^{-1})
298	6.75×10^4	1.10×10^6
313	6.60×10^4	1.08×10^6
323	6.50×10^4	1.07×10^6
333	6.00×10^4	1.05×10^6
343	5.40×10^4	1.00×10^6

Figure 6.14 reveals the transport parameters for C4 at various temperatures. Figure 6.14(a) shows that the value of D enhances from 8.33×10^{-6} cm^2 s^{-1} to 1.63×10^{-5} cm^2 s^{-1} as the temperature varies from 298 K to 343 K. The same pattern for μ is obtained where the maximum value is observed at 5.53×10^{-4} cm^2 V^{-1} s^{-1} in Figure 6.14(b). From Figure 6.14(c), it is noticeable that the value of n enhances from 2.15×10^{19} cm^{-3} to 3.44×10^{19} cm^{-1}. The polymer segment vibrates at high temperature resulting to increase in free volume. This volume allows ion pairs to dissociate and form free ions which indirectly improve the ionic diffusivity and mobility (Noor, 2016; Aziz et al., 2018).

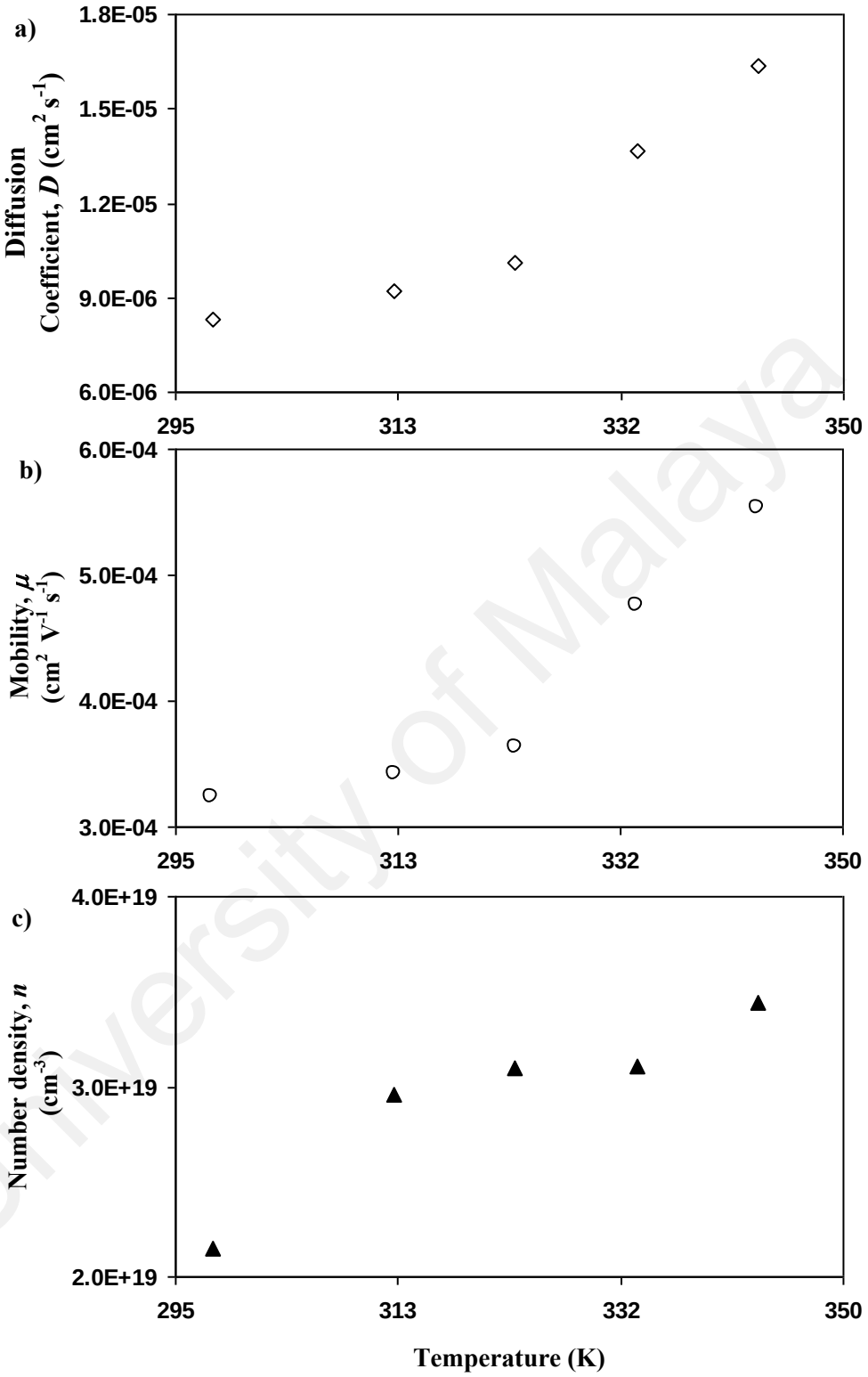

Figure 6.14: Graph of (a) *D*, (b) μ and (c) *n* for C4 electrolytes at various temperatures.

6.6 Transference Number Analysis

There are two types of crucial transference number analysis for polymer electrolyte i.e. ionic transference number and cation transference number. Ionic transference number analysis has been conducted to investigate the contribution of electrons and ions in the electrolyte by sandwiching the electrolyte with two blocking stainless steel (SS). It is important to know the contribution of cation to the conductivity since it can affect the protonic cell performance. Hence cation transference number has been carried out using non-blocking manganese oxide (MnO_2) electrodes.

6.6.1 Ionic Transference Number

Figure 6.15 depicts the polarization current against time for C4 at 0.20 V.

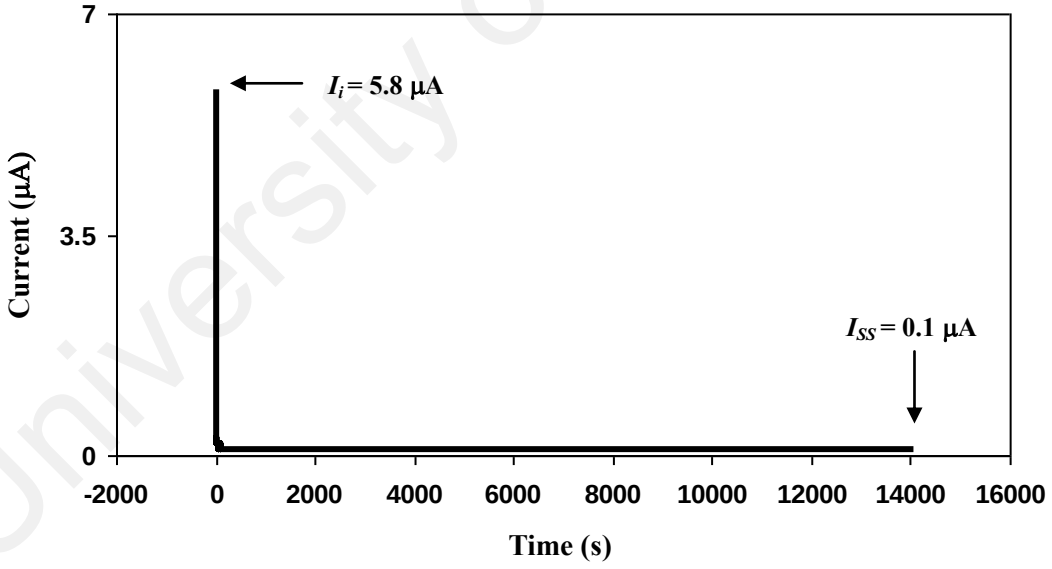

Figure 6.15: Plot of ionic transference number for SS|C4|SS.

The current starts at 5.8 μA and drastically drop to 0.1 μA. The drastic decrement of current is simply because only electrons can pass through stainless steel. This is a characteristic of ionic conductor. The current for non-ionic conductor will not reduce with time (Yap, 2012; Fong et al., 2019). As the conduction of ions achieves

equilibrium, steady-state can be observed. Constant current is an indicator for ionic conductors (Woo et al., 2013; Choi, Yang, Kim & Chung, 2019).

The value of electron transference number (t_e) can be obtained by dividing I_{ss} with I_i. Hence, if the value of t_e is known, the value of ionic transference number (t_i) can be calculated using:

$$t_i = 1 - t_e \tag{6.14}$$

From Equation (6.14), the values of t_e and t_i for C4 electrolyte are 0.02 and 0.98, respectively. Vijaya et al. (2013) reported that the highest conducting protonic-based polymer electrolyte possesses t_i of 0.97. The highest conducting sample of starch-chitosan-NH_4Cl-glycerol system has t_i of 0.98 (Shukur & Kadir, 2015). Yusof (2017) reported that NH_4I based biopolymer electrolyte has a conductivity of $\sim 10^{-3}$ S cm^{-1} and t_i of 0.99. These results are comparable with the current result in this study.

6.6.2 Cation Transference Number

In an electrolyte material, the dissolved ions carry different amount of electric current since mobility of ions has a great influence on the amount of current (Rigo et al. 2019). It is crucial to identify cation transference number (t_c) because in protonic cells only the positive charged ions involve in intercalation-deintercalation process (Xu, 2014). A method by Watanabe et al. (1988) is suggested that t_c is given as:

$$t_c = \frac{R_b}{\frac{\Delta V}{I_{ss}} - R_c} \tag{6.15}$$

here R_c and R_b are the charge transfer resistance and bulk resistance, respectively, while ΔV is the bias voltage. Figure 6.16 shows the impedance plot for MnO_2|C4| MnO_2. The values of $(R_b + R_c)$ and R_b are found to be 7150 Ω and 355 Ω, respectively.

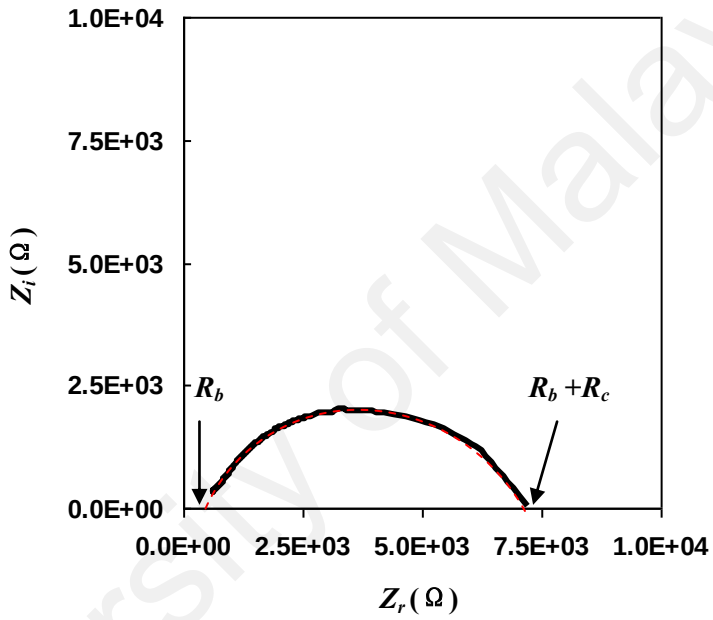

Figure 6.16: Impedance plot for cell with arrangement of MnO_2|C4|MnO_2.

Figure 6.17 reveals the polarization of MnO_2|C4|MnO_2 cell against time at 0.20 V. The value of I_{ss} is observed at 26.0 μA. The value of t_c is identified to be 0.40. Various values of t_c have been reported by other studies from 0.21 to 0.46 (Woo et al., 2011; Kufian et al., 2012: Shukur et al., 2015). Yusof et al. (2017) reported t_c value of 0.40 via Watanabe method for chitosan-starch-NH_4Cl-glycerol system which comparable to result in this study. This proves the existent of protonic conduction. Transference

number may affected by association of charge carriers but it still gives an idea of ionic transport process (Watanabe et al., 1988; Arya & Sharma, 2018).

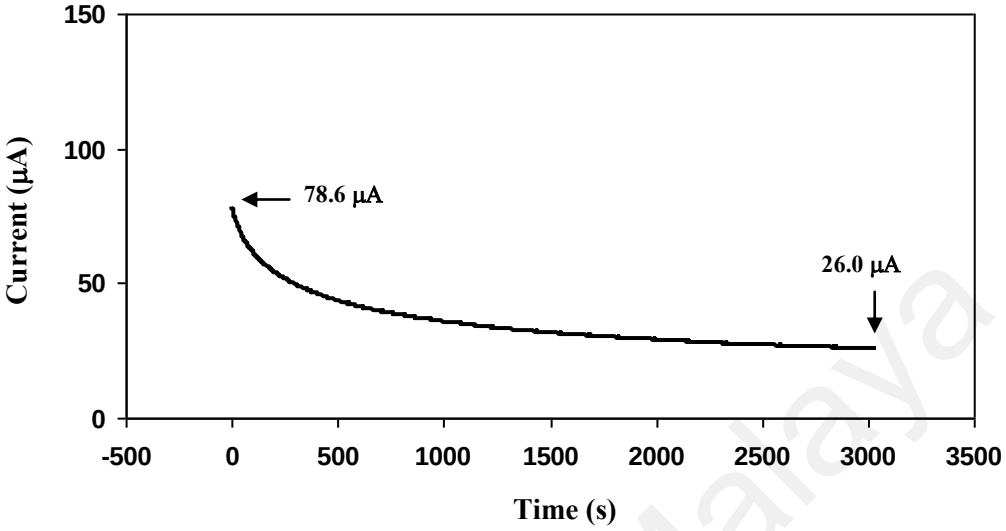

Figure 6.17: Plot of cation transference number for MnO_2|C4|MnO_2.

6.6.3 Comparative Cyclic Voltammetry Analysis

In order to verify the protonic conduction throughout the electrolyte, comparative cyclic voltammetry (CV) analysis has been carried out (Munichandraiah, Scanlon, Marsh, Kumar & Sircar, 1995; Kumar & Hashmi, 2010; Basha & Rao, 2018). A pellet consisting of zinc and $ZnSO_4.7H_2O$ mixture has been used as the anode in protonic cells. This mixture is known as the source of H^+ as referred in the following equation (Kadir, 2010; Samsudin et al., 2014; Alias et al., 2017):

$$Zn + ZnSO_4.7H_2O \rightleftarrows Zn^{2+} + 2e^- + ZnSO_4 + 7H^+ + 7OH^- \quad (6.16)$$

Two cells are fabricated to differentiate the resulting current. The arrangements of the cells are given as:

Cell A: SS|C4|SS

Cell B: Zn + $ZnSO_4 \cdot 7H_2O$ |C4 | Zn + $ZnSO_4 \cdot 7H_2O$

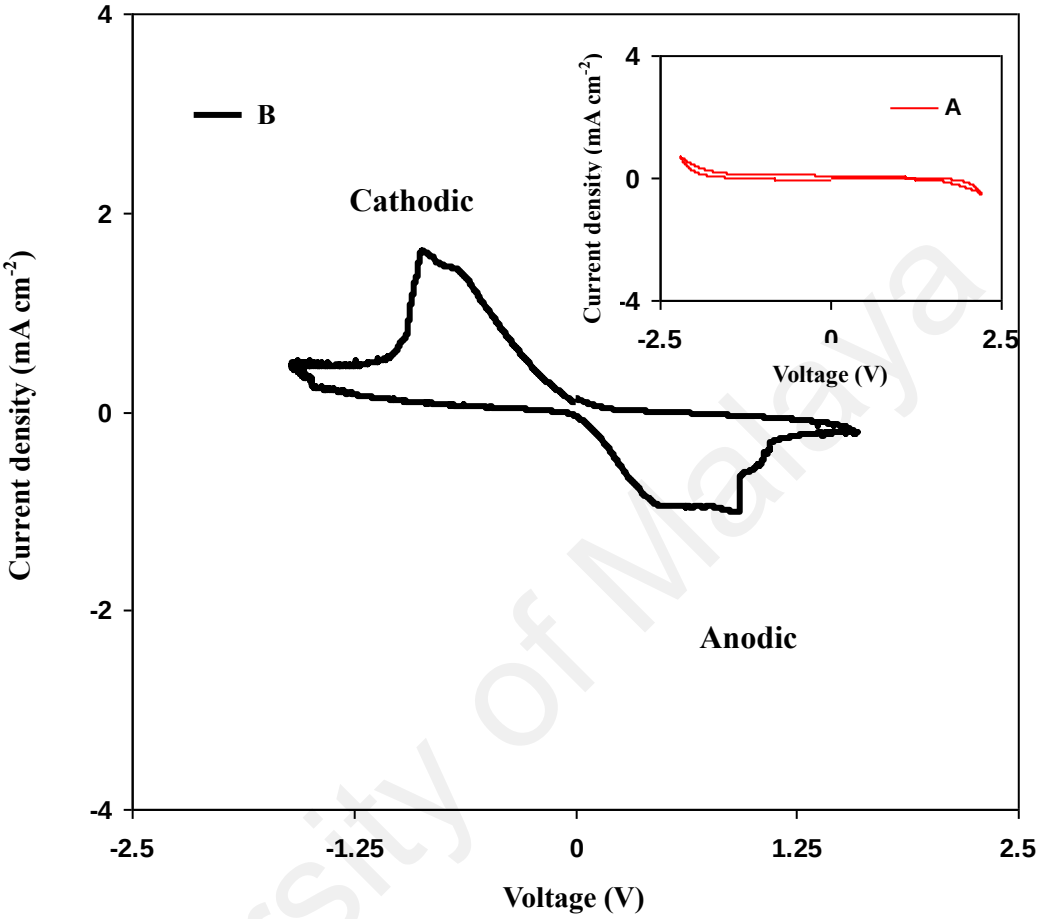

Figure 6.18: CV plot for C4 with different electrodes.

Figure 6.18 shows the CV plot for cell A and cell B. Neither anodic peak nor cathodic peak is observed in the CV plot of cell A. Meanwhile the CV plot for cell B consists of anodic and cathodic peaks. The presence of cathodic and anodic peaks are attributed to highly reversible H^+ plating/stripping at the interface between electrolyte and Zn + $ZnSO_4 \cdot 7H_2O$ electrodes. The large current signifies the protonic oxidation and reduction process at the interfaces between electrodes and electrolyte (Sellam & Hashmi, 2012). This result further proves the occurrence of protonic conduction in the electrolyte.

6.7 Dielectric Behavior

Dielectric analysis is the one of the ways to verify the pattern of conductivity for salted and plasticized electrolytes at room and high temperature. ε_r and ε_i are the charge stored in an electrolyte and energy dissipates to migrate ions during rapid electric reversal, respectively (Radivojevic, Rupcic, Srnovic & Bensic, 2018). Dielectric behavior of a material can be studied from the following equations:

$$\varepsilon_r = \frac{Z_i}{\omega C_o \left(Z_r^2 + Z_i^2\right)} \tag{6.17}$$

$$\varepsilon_i = \frac{Z_r}{\omega C_o \left(Z_r^2 + Z_i^2\right)} \tag{6.18}$$

where C_o and ω are the indicators for vacuum capacitance and radial frequency, respectively.

The influence of NH_4NO_3 content of the values of ε_r and ε_i are plotted in Figure 6.19(a) and 6.19(b), respectively. It is noticeable that the values of ε_r and ε_i maximized when the concentration of NH_4NO_3 reaches 30 wt.%. As the salt concentration increases, the formation of free charge carriers also increases which in turn enhance the conductivity value. The values of ε_r and ε_i start to reduce as 35 wt.% and 40 wt.% NH_4NO_3 are included. This is due to the process of ions recombination at high salt concentration (Sengwa, Dhatarwal & Choudhary, 2015). Khiar and Arof (2010) reported that the trend of conductivity is similar with the pattern of ε_r and ε_i for starch-NH_4NO_3 system. From Figure 6.19, it can be observed that the dielectric is higher at 5

kHz compared to 50 kHz. Iqbal and Rafiuddin (2016) stated that the development of charge accumulation happens at low frequency.

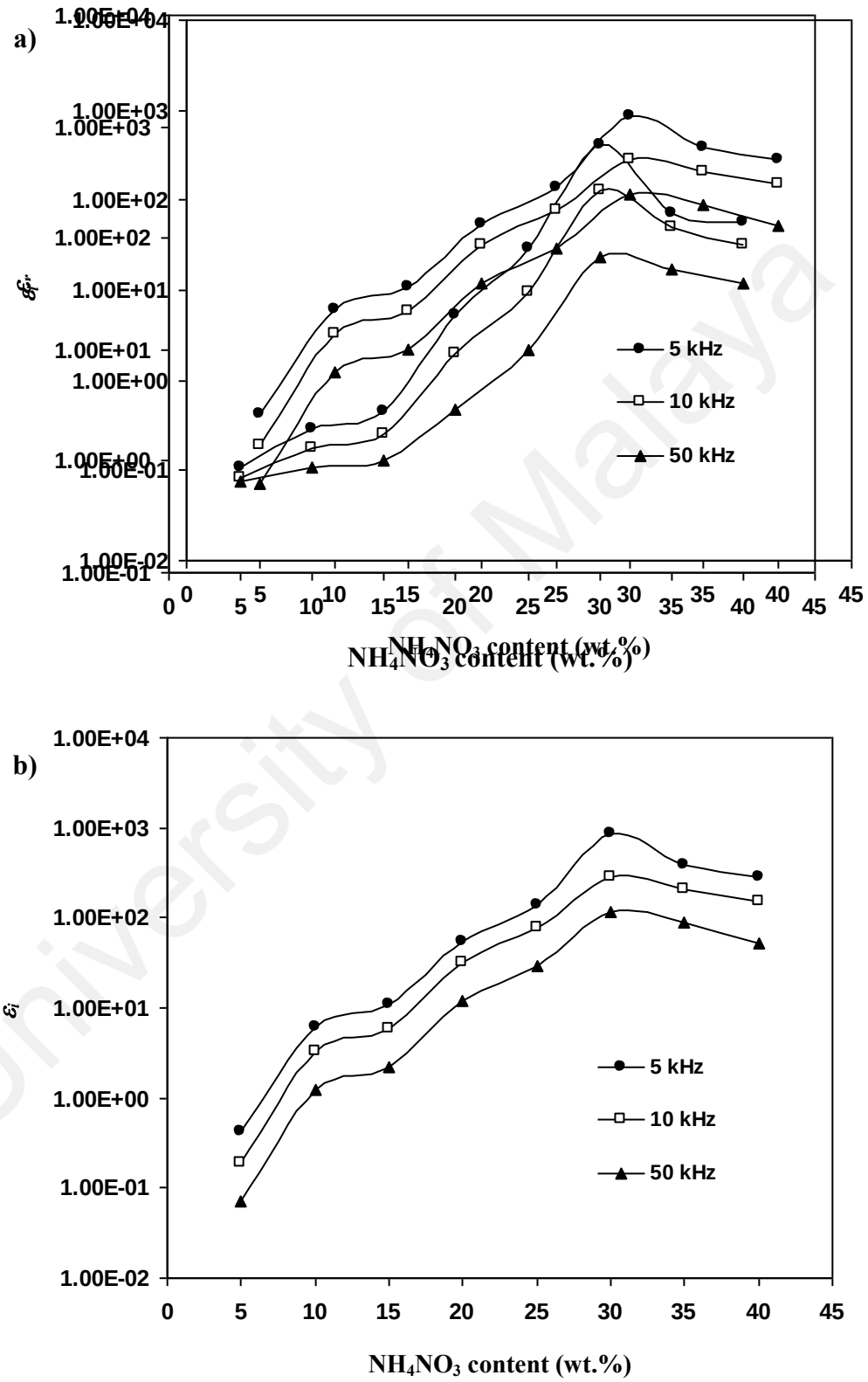

Figure 6.19: Room temperature a) dielectric constant, ε_r and b) dielectric loss, ε_i for salted electrolyte.

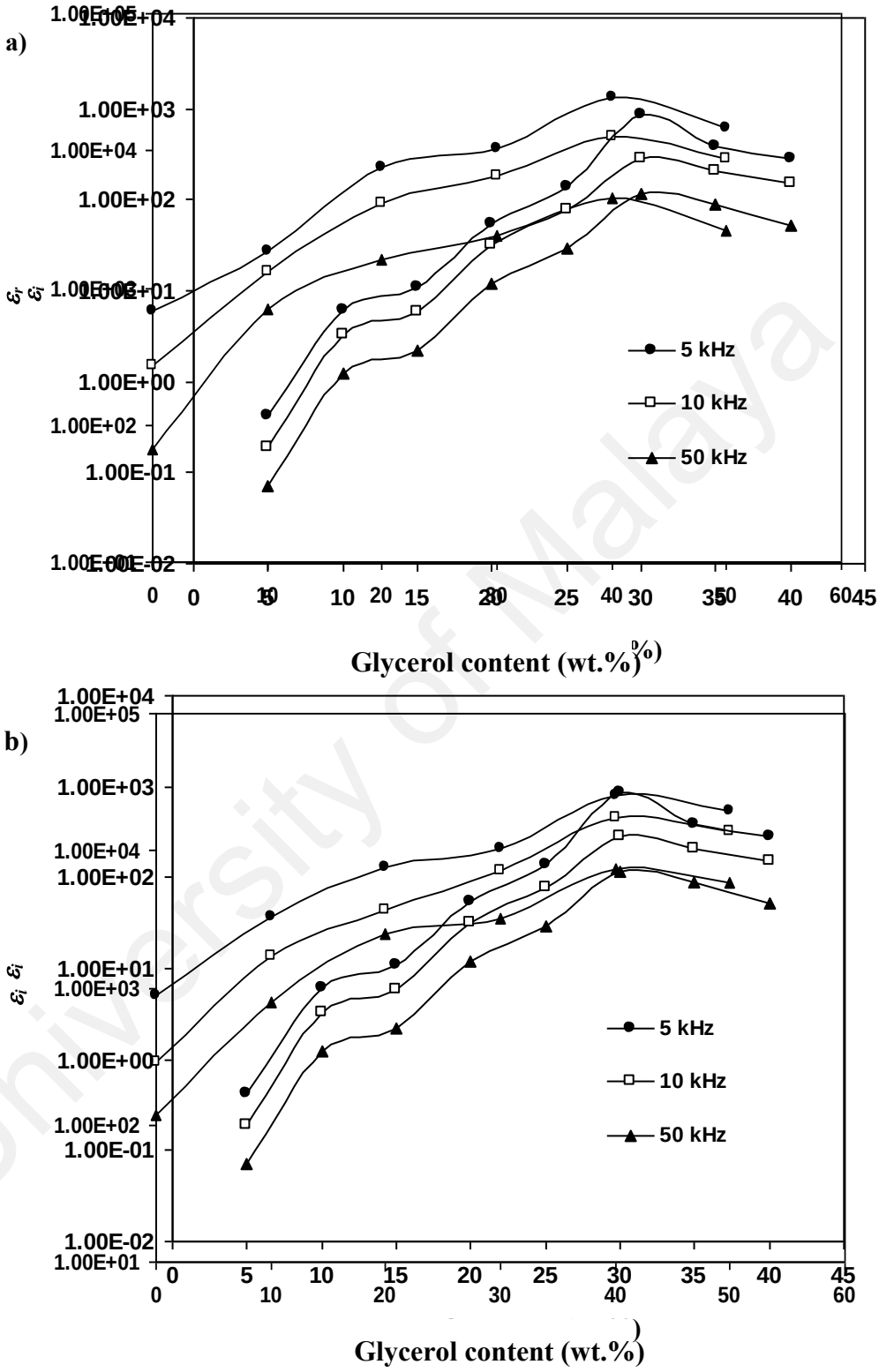

Figure 6.20: Room temperature a) dielectric constant, ε_r and b) dielectric loss, ε_i for plasticized electrolyte.

The changes of ε_r and ε_i values with the inclusion of glycerol are depicted in Figure 6.20. When 40 wt.% glycerol is added, ε_r and ε_i are at maximum. Ion dissociation improves with the presence of plasticizer. However, the values of ε_r and ε_i reduce at 50 wt.% glycerol. Excess amount of plasticizer promotes recrystalization or recombination of salt which in turn will reduce charge carriers number (Buraidah et al., 2009). These results are consistent with the result from conductivity and transport analysis where the conductivity value and ionic number density are maximum when 40 wt.% glycerol is added.

The influence of temperature on the values of ε_r and ε_i for B6 and C4 are shown in Figures 6.21 and 6.22, respectively. Both ε_r and ε_i are dependent on temperature for all frequencies. At high temperature, more free ions are dissociated in the polymeric network thus increase the value of dielectric constant. Chandra (2013) reported that more mobile ions are available at high temperature and produce high dielectric value for PEO/PVP-$NaNO_3$ system. By referring to Figure 6.14, values of ionic number density and mobility are both temperature dependence. Hence, results in Figures 6.21 and 6.22 are consistent with transport analysis and conductivity at high temperature.

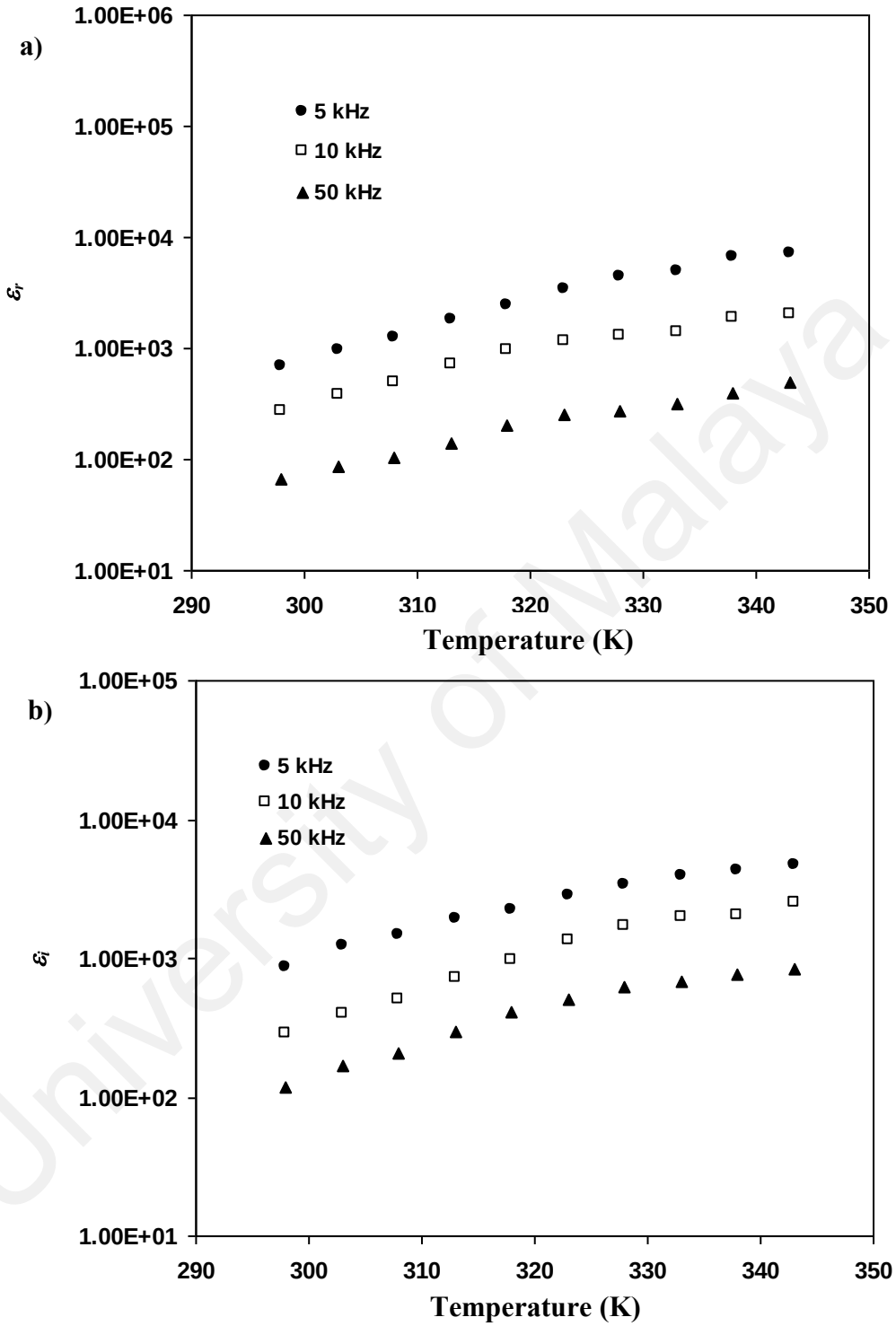

Figure 6.21: The changes of a) ε_r and b) ε_i values for B6 electrolyte with various temperatures at selected frequencies.

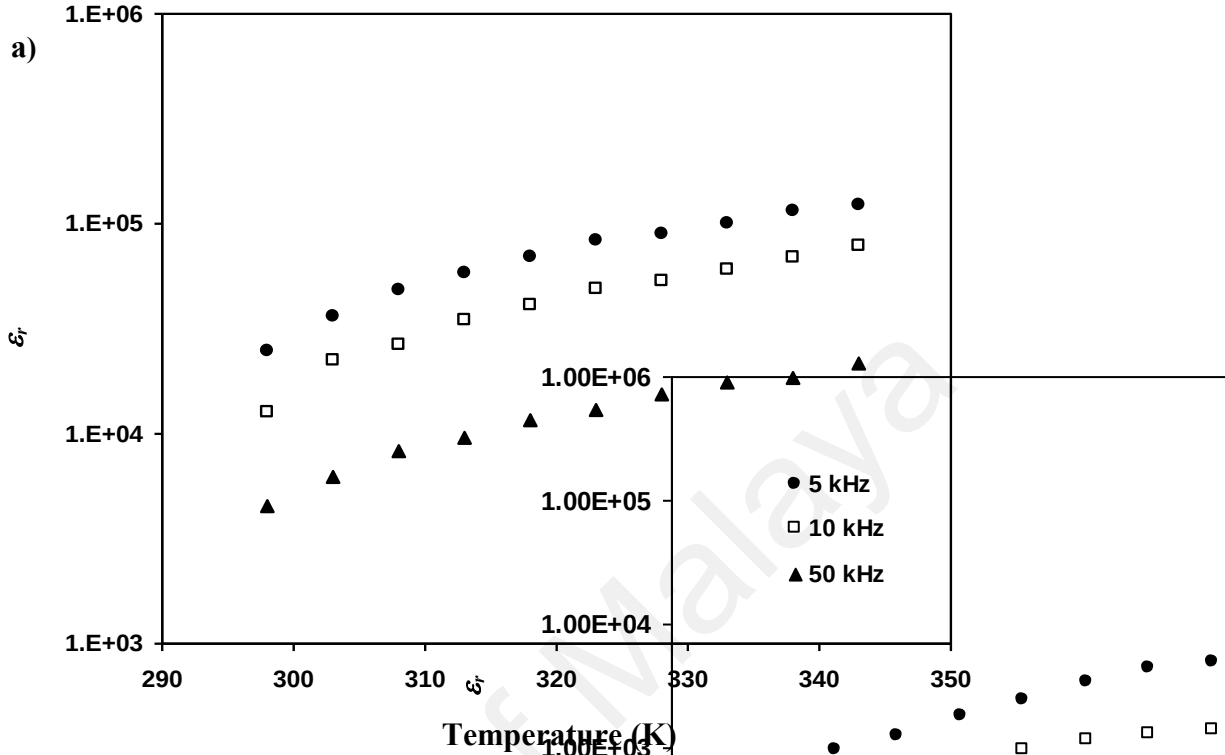

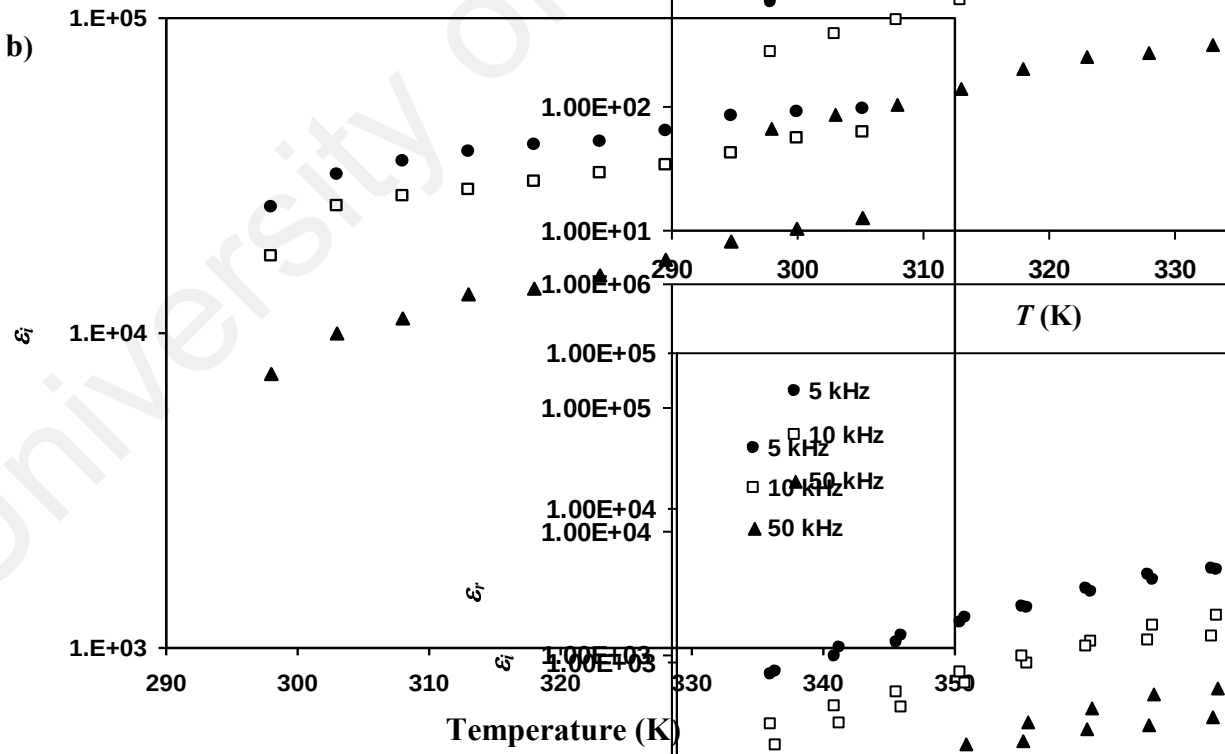

Figure 6.22: The changes of a) ε_r and b) ε_i values for C4 electrolyte with various temperatures at selected frequencies.

6.8 Electrical Modulus

Electrical modulus can also be used to monitor the dielectric behavior of a polymeric material. Electrical modulus is the inverse of complex relative permittivity which suppresses the polarization of electrode (Tian & Ohki, 2014). The real and imaginary parts of modulus are denoted as M_r and M_i, respectively, which can be expressed as:

$$M_r = \frac{\varepsilon_r}{\varepsilon_r^2 + \varepsilon_i^2} \tag{6.19}$$

$$M_i = \frac{\varepsilon_i}{\varepsilon_r^2 + \varepsilon_i^2} \tag{6.20}$$

Figures 6.23 and 6.24 show the influence of NH_4NO_3 and glycerol, respectively, on M_r at room temperature.

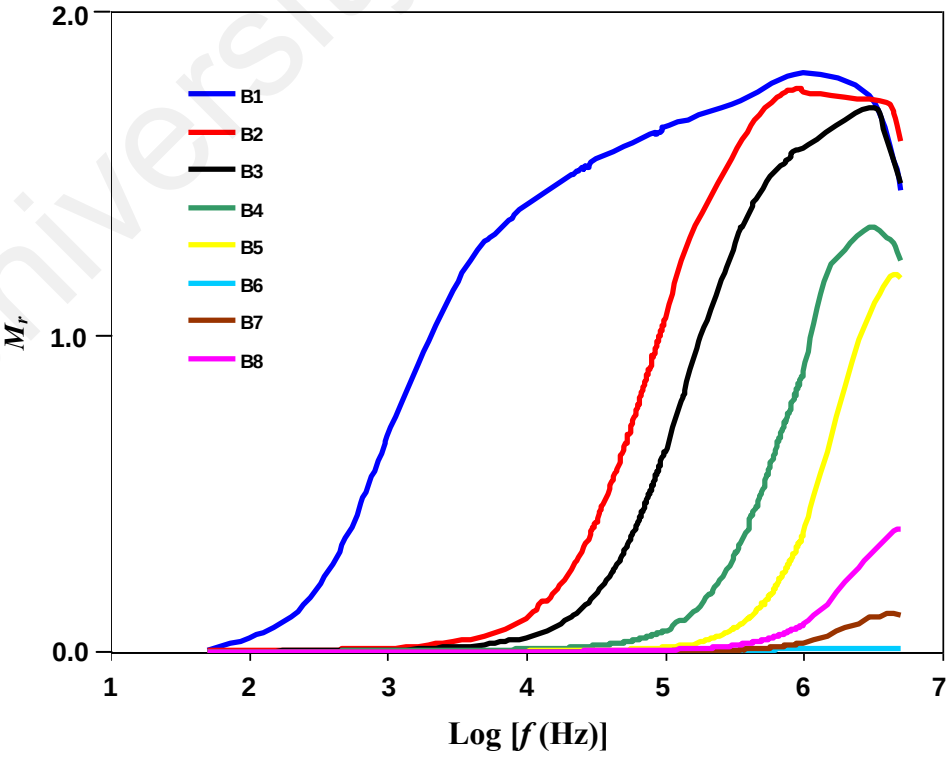

Figure 6.23: Room temperature M_r for salted electrolytes.

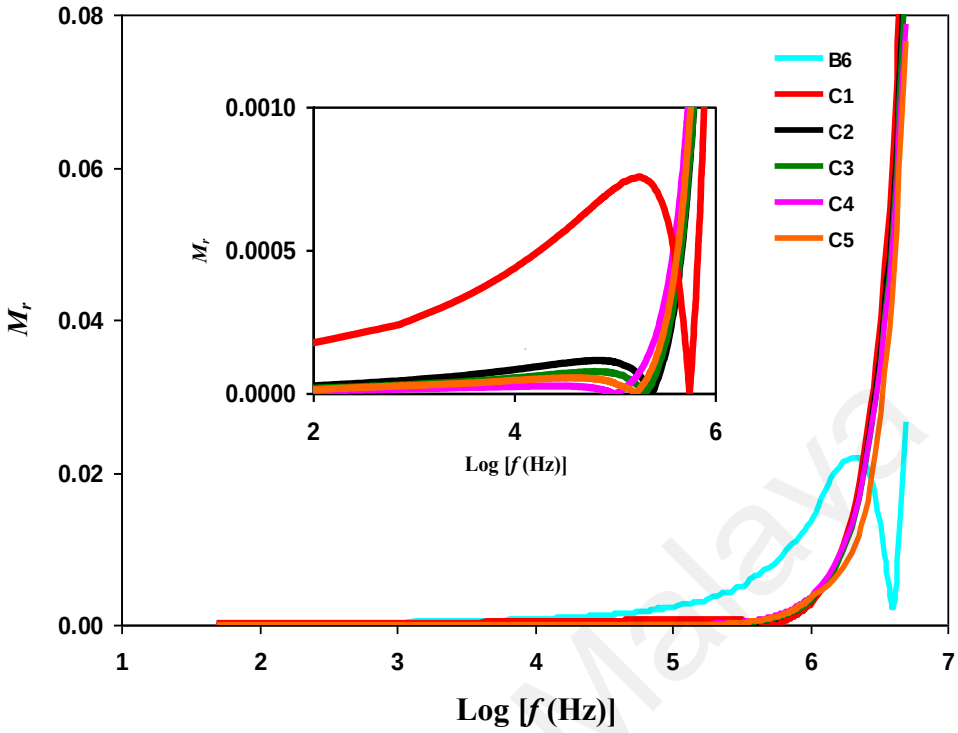

Figure 6.24: Room temperature M_r for plasticized electrolytes.

As observed in Figures 6.23 and 6.24, M_r value is almost zero with no dispersion at low frequency part. Gurusiddappa, Madhuri, Suvarna and Dasan (2016) stated that M_r is almost zero because of the domination of polarization effect at low frequency part. As more salt is added, the peak is observed to shift towards higher frequency. The peaks in Figures 6.23 and 6.24 correspond to the relaxation process of ionic conduction. High conducting electrolyte possesses the lowest M_r value which is due to high number of charge carriers (Pradhan, Choudhary & Samantaray, 2009).

Figures 6.25 and 6.26 depict the M_r plot for B6 and C4 electrolytes, respectively, at various temperatures.

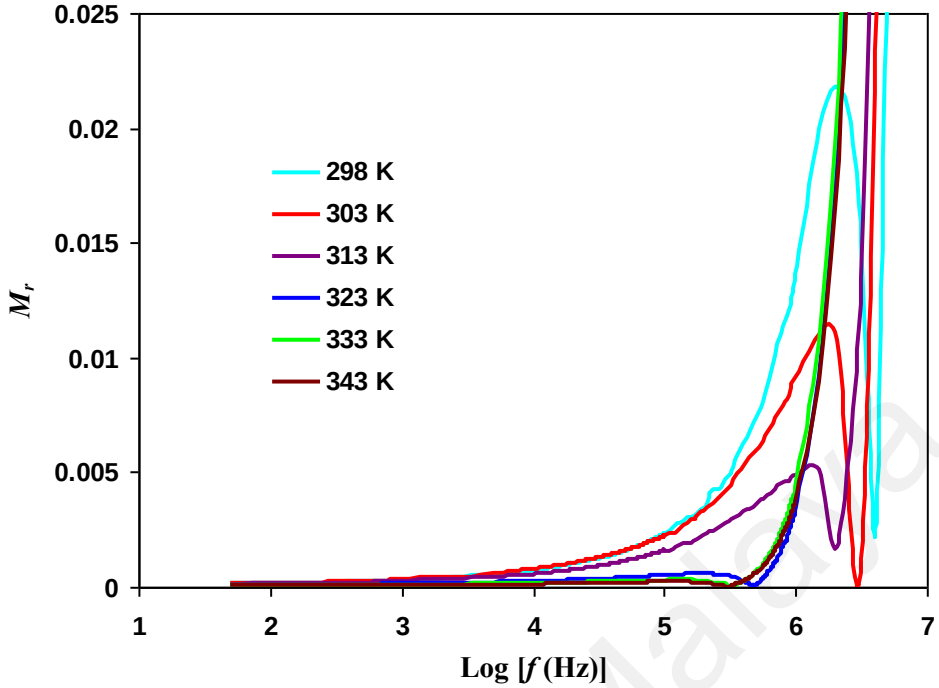

Figure 6.25: M_r plot for B6 at various temperatures.

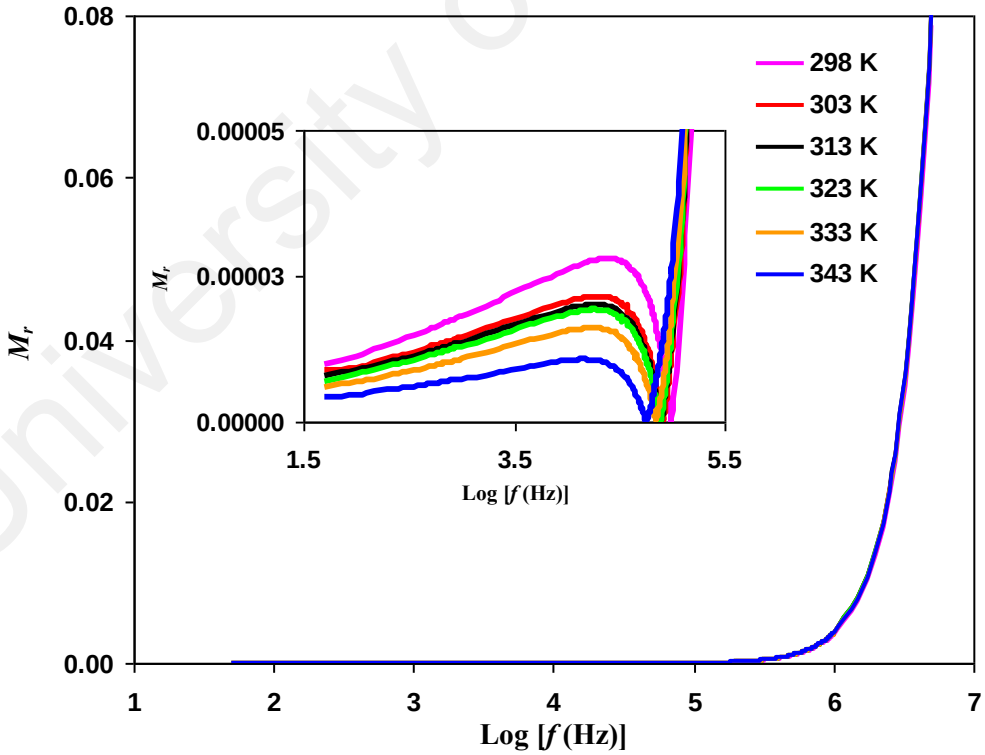

Figure 6.26: M_r plot for C4 at various temperatures.

From Figures 6.25 and 6.26, M_r is started to reduce as the temperature increases. More mobile ions are provided in the polymer matrix resulting in the increment of ionic mobility at high temperature which leads to decrement in M_r value (Ramesh & Arof, 2001). The maximum point indicates that MC-PS-NH_4NO_3 and MC-PS-NH_4NO_3-glycerol are ionic conductors. The tail near zero value at low frequency part is attributed to high capacitance at the electrode (Khiar, Puteh & Arof, 2006; Bin-Dahman et al., 2017).

The effects of NH_4NO_3 and glycerol addition on M_i values at room temperature are shown in Figures 6.27 and 6.28, respectively. Based on Figure 6.27, M_i is divided into high and low frequency regions by a maximum point. As stated in a report by Fuzlin et al. (2018), high and low frequency regions indicate the relaxation phenomenon and conduction process, respectively.

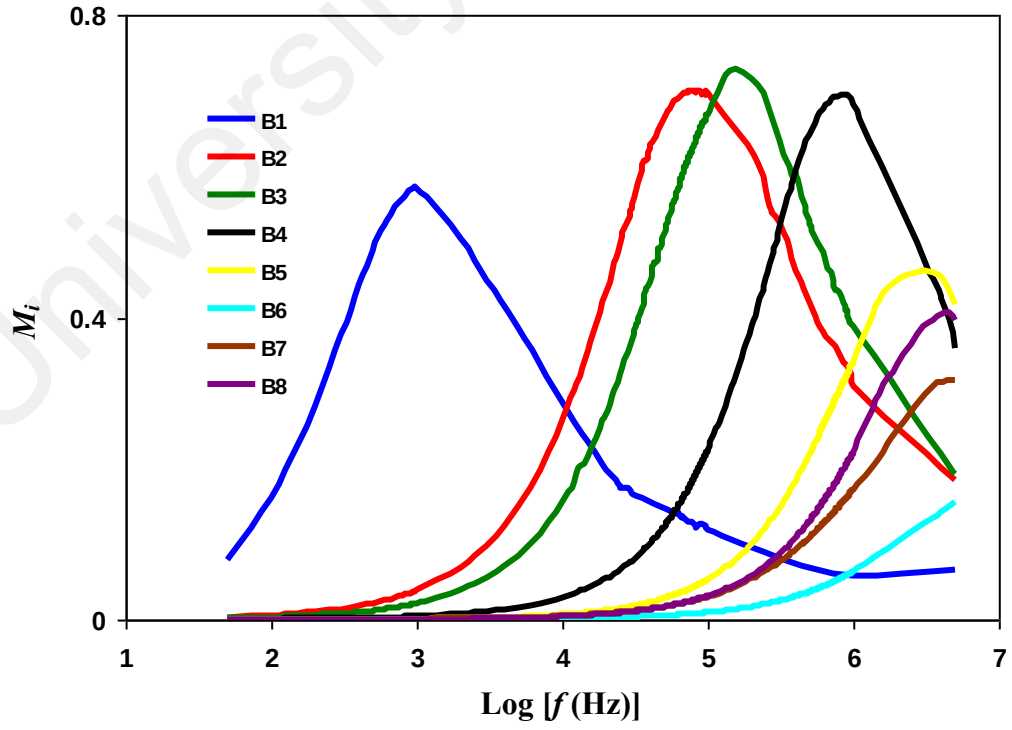

Figure 6.27: Room temperature M_r for salted electrolytes.

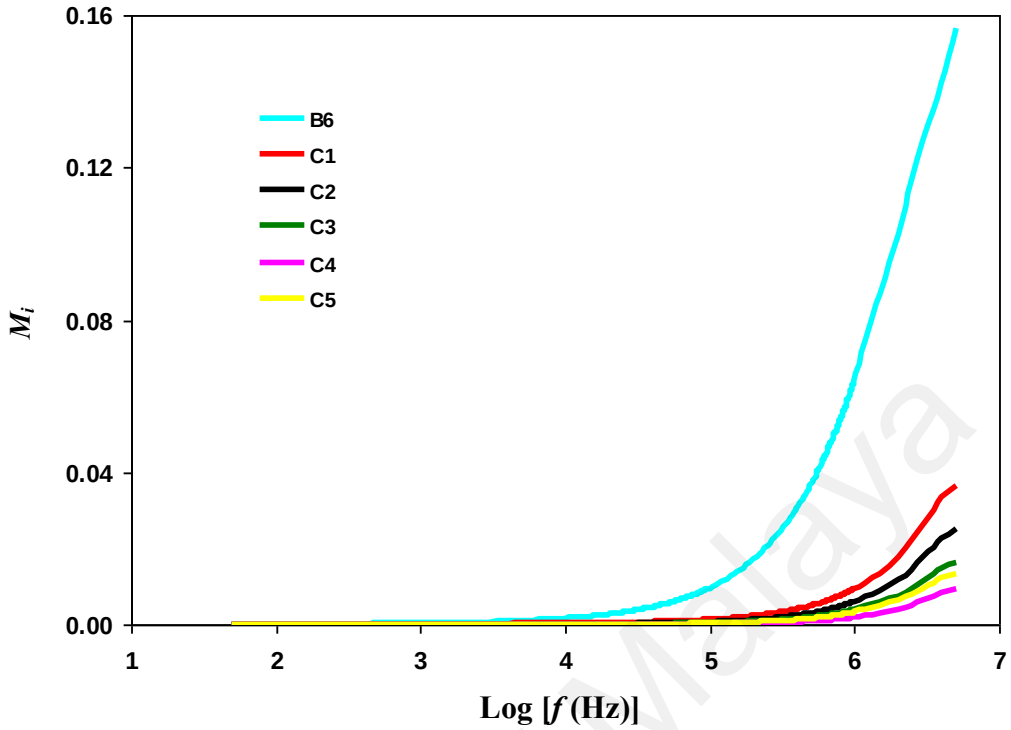

Figure 6.28: Room temperature M_i for plasticized electrolytes.

The asymmetry broadening of the peaks in Figure 6.27 portrays the spread of relaxation times with various time constants which follows non-Debye theory (Kobayashi, Noguchi & Miyayama, 2005; Das & Ghosh, 2015). The disappearance of peaks in Figure 6.28 is attributed to limited range of frequency in this current study. The relaxation time (t_{Mi}) of M_i can be extracted from the following equation:

$$t_{Mi} = \frac{1}{\omega_{peak}} \tag{6.21}$$

here ω_{peak} corresponds to the relaxation peak's radial frequency.

Table 6.10: Relaxation time for selected salted electrolyte at room temperature.

Electrolyte	t_{Mi} (s)
B1	1.59×10^{-4}
B2	2.27×10^{-6}
B3	1.14×10^{-6}
B4	2.18×10^{-7}
B5	5.30×10^{-8}
B8	3.98×10^{-8}

As observe in table 6.10, only several electrolytes can be used to calculate the value of t_{Mi} due to absence of peaks and frequency limitation. B1 possesses t_{Mi} of 1.59×10^{-4} s which reduces to 5.30×10^{-8} s as 25 wt.% NH_4NO_3 is added. As the conductivity increases, the peak shifts to higher frequency and possesses shorter relaxation time. This is due to correlation between conductivity and relaxation mechanism (Tang et al., 2015).

Figures 6.29 and 6.30 represent the dependence of M_i on temperature for B6 and C4 electrolyte, respectively. The value of M_i for B6 and C4 started to reduce as the temperature elevates. Temperature has a great influence on ionic mobility and segmental motion of polymeric network. Furthermore, ions and molecular dipoles can create a good orientation at high temperature (Aziz, Abidin & Arof, 2010; Wang & Alexandridis, 2016).

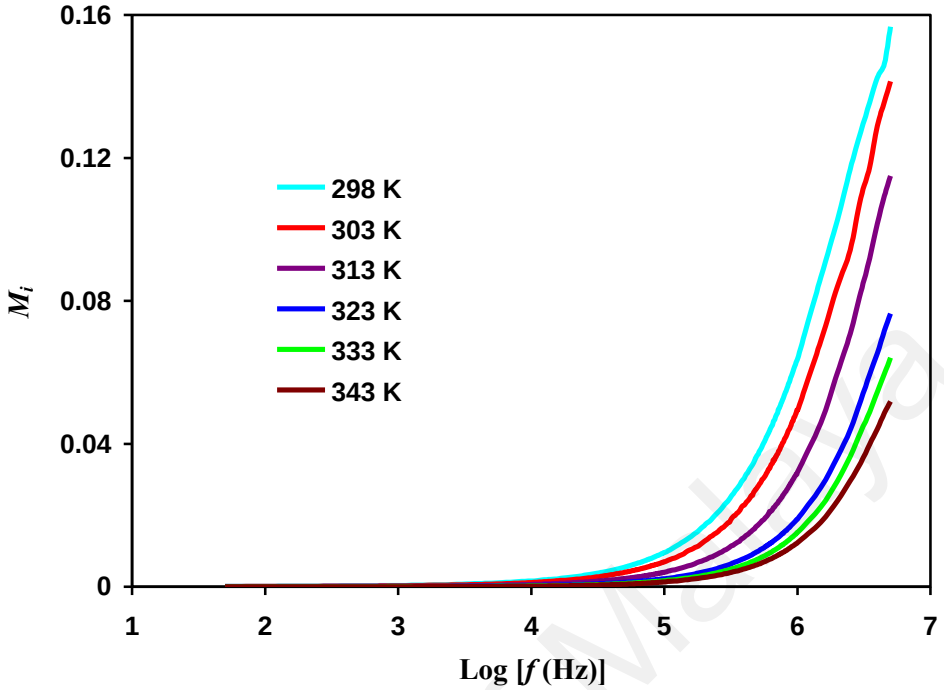

Figure 6.29: M_i Plot for B6 at various temperatures.

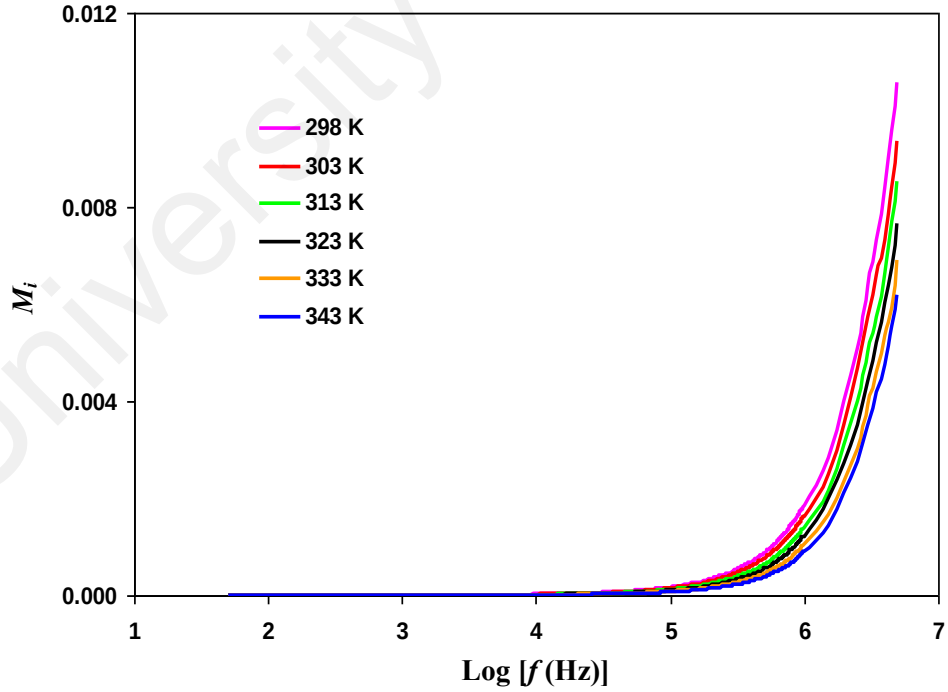

Figure 6.30: M_i plot for C4 at various temperatures.

6.9 Summary

The maximum room temperature conductivity of $(4.35 \pm 0.16) \times 10^{-5}$ S cm^{-1} and $(1.26 \pm 0.1) \times 10^{-3}$ S cm^{-1} have been achieved with 30 wt.% NH_4NO_3 (B6) and 40 wt.% glycerol (C4), respectively. Salted electrolytes obey Arrhenius theory while the addition of glycerol has altered the conduction of electrolyte to Vogel-Fulcher-Tammann theory. The transport analysis has been studied using A-N impedance method. The conductivity is discovered to be affected with ionic mobility, diffusivity and number density. Transference number proves that ions are the main charge carriers. The value of cation transference number is calculated via Watanabe method and found as 0.40. The redox peaks were observed in comparative cyclic voltammetry study proves the protonic conduction in MC-PS-NH_4NO_3-glycerol. Results from dielectric and modulus analysis are consistent with the conductivity pattern and verify that the electrolyte obeys non-Debye behavior.

CHAPTER 7: THERMAL PROPERTIES AND MORPHOLOGY STUDIES OF THE POLYMER ELECTROLYTE

7.1 Introduction

In this chapter, results from thermogravimetric analysis (TGA) for salted and plasticized electrolytes will be presented. The influence of NH_4NO_3 and glycerol on the decomposition temperature of methylcellulose (MC)-potato starch (PS) blend will be discussed. Differential scanning calorimetry (DSC) is employed to observe the changes of glass transition temperature (T_g) as NH_4NO_3 and glycerol are added to the polymer blend. From field emission scanning electron miscroscopy (FESEM), the changes of the surface of the electrolyte with the inclusion of NH_4NO_3 and glycerol will be studied. FESEM and DSC provide insights into the results from FTIR and impedance analysis in Chapters 5 and 6, respectively.

7.2 TGA Studies

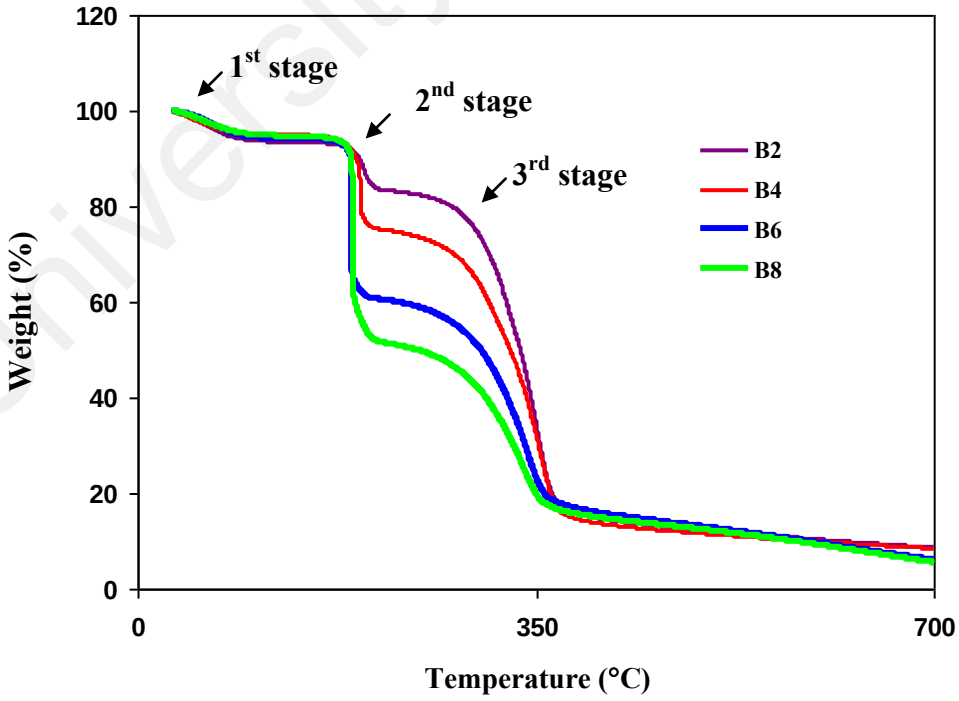

Figure 7.1: TGA curves of selected salted electrolytes.

TGA analysis is employed to examine the thermal stability of polymer electrolytes as NH_4NO_3 and glycerol are added into MC-PS blend (A6) film. Figure 7.1 shows the TGA curve for the selected salted electrolytes from 25°C to 700 °C. As observed in Figure 7.1, the TGA curves of B2, B4, B6 and B8 possess three stages of degradation. The first stage for each electrolyte appears at ~ less than 120 °C. Rahman et al. (2019) stated that the first degradation stage is due to unbound water weight loss. The second degradation stage occurs in between from 170 to 180 °C. This degradation corresponds to the degradation of NH_4NO_3. The result obtained for NH_4NO_3 is comparable to the reports by Gunawan and Zhang (2009) and Shuhaimi (2011). It is also noticeable that the weight losses for B2, B4, B6 and B8 at this stage are 10, 20, 30 and 40 %, respectively. As more salt is added, more weight loss is observed. This result is almost similar with MC-NH_4NO_3 system by Shuhaimi (2011). From Figure 4.9, MC-PS blend decomposed at 280 °C. Hence, the third degradation stage in each electrolyte is due to MC-PS blend. Figure 7.2 shows the TGA curves for selected plasticized electrolytes.

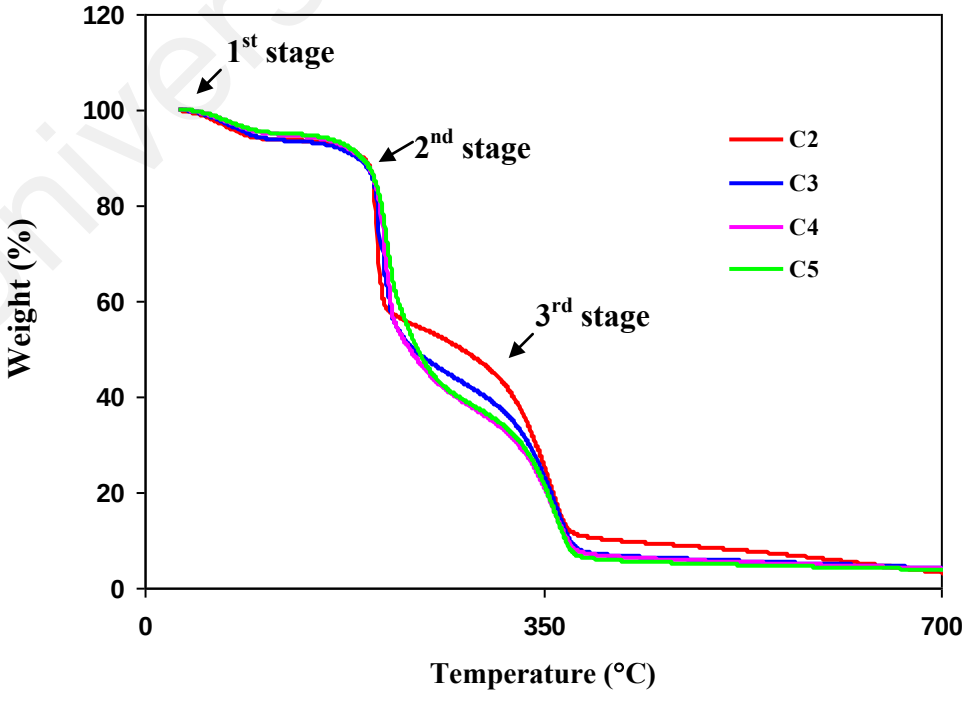

Figure 7.2: TGA curves of selected plasticized electrolytes.

Three degradation stages can be seen in the Figure 7.2. The first stage in each electrolyte corresponds to the weight loss of water (Rajendran et al., 2004; Rahman et al., 2019). The second degradation for C2 appears at 163 °C and 160 °C for C3. As 40 and 50 wt.% glycerol are added, the decomposition occurs at 153 and 150 °C, respectively. Hydrogen bonding of the polymeric network is disrupted by the addition of plasticizer (Sanyang et al., 2015). Mattos et al. (2012) reported that the decrease in decomposition temperature is due to the formation of chitosan-glycerol hydrogen bonding. As referred to Figure 5.14, the formation of hydrogen bond between glycerol and MC-PS blend has been verified via FTIR analysis. The third degradation stage in each electrolyte between 280 °C to 300 °C is due to the decomposition of MC-PS blend.

7.3 DSC Studies

Glass transition temperature (T_g) of the electrolytes is examine through DSC analysis. T_g is important to be determine due to its relation with segmental motion of the polymer chain. Furthermore, mobility of ions depends on the segmental motion in the amorphous regions of the polymer (Choudhary & Sengwa, 2016). From Figure 4.10, A6 blend film possesses T_g value at 132.7 °C. Figure 7.3 shows the DSC plot for selected salted electrolytes.

In Figure 7.3, the T_g decreases to 110.7 °C as 10 wt.% NH_4NO_3 is impregnated to the electrolyte. Further addition of salt up to 30 wt.% results in further decrease in T_g, where the T_g for B4 and B6 appear at 56.7 °C and 20.5 °C, respectively. Du, Bai, Chu and Qiao (2010) reported that the inclusion of 10 wt.% ammonium acetate ($NH_4CH_3CO_2$) decreased the T_g of pure chitosan film from 160 °C to 117 °C.

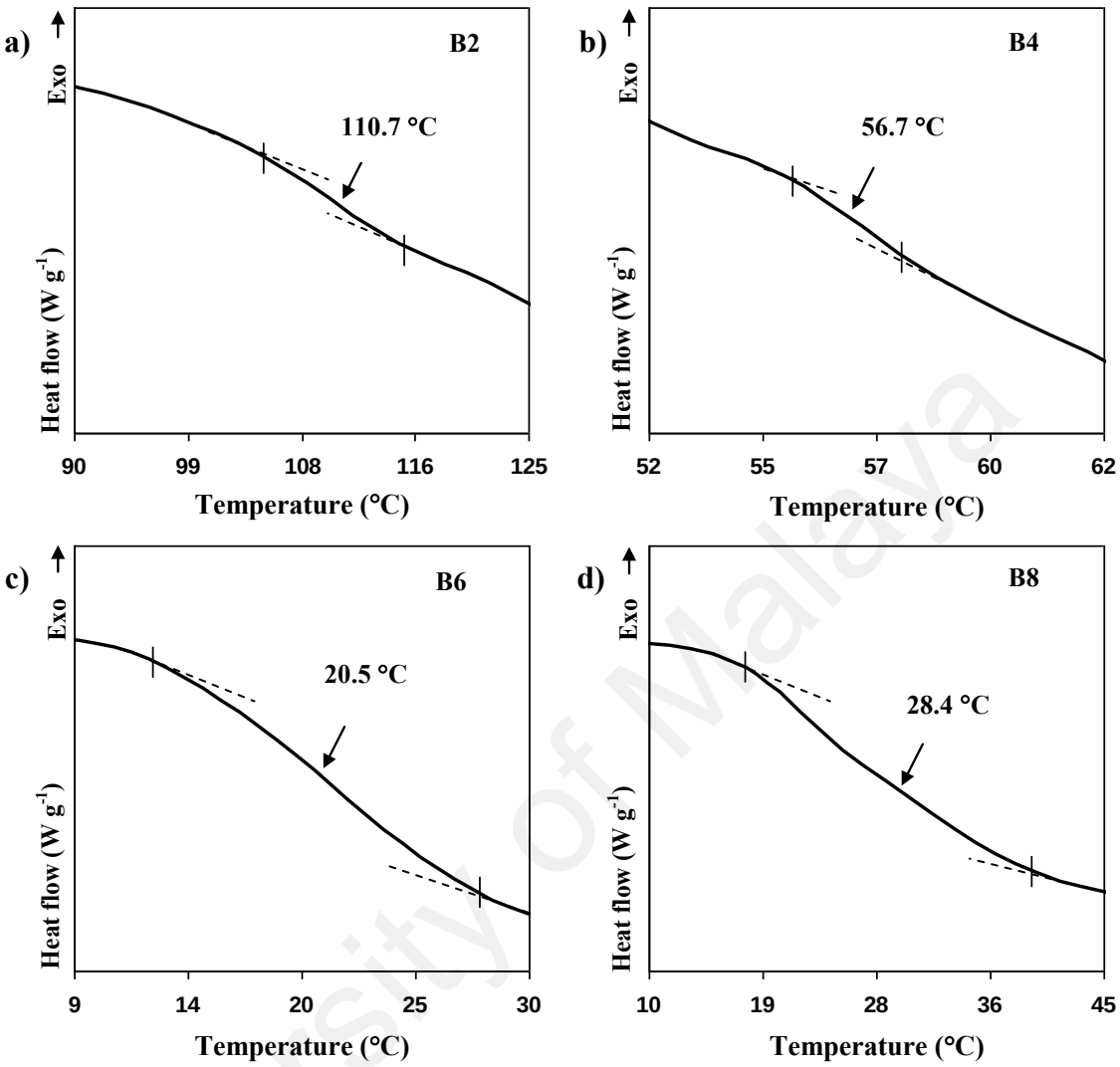

Figure 7.3 : DSC thermograms of selected salted electrolytes.

The decrease in T_g signifies the softening of polymer chains which is advantageous for the conduction of ions (Latha & Venkatachalam, 2016). When salt is added to the electrolyte, the dipole-dipole interaction in the polymer matrix is weakened, thus enhancing the flexibility of the polymer chain (Naimi et al., 2018). As the concentration of NH_4NO_3 exceeds 30 wt.%, the T_g is observed to increase to 28.4 °C. The flexibility of polymer reduces at high concentration of salt due to the development of salt aggregates, thus decrease the T_g (Karthikeyan et al., 2016).

Figure 7.4 illustrates the DSC thermograms for selected plasticized electrolytes

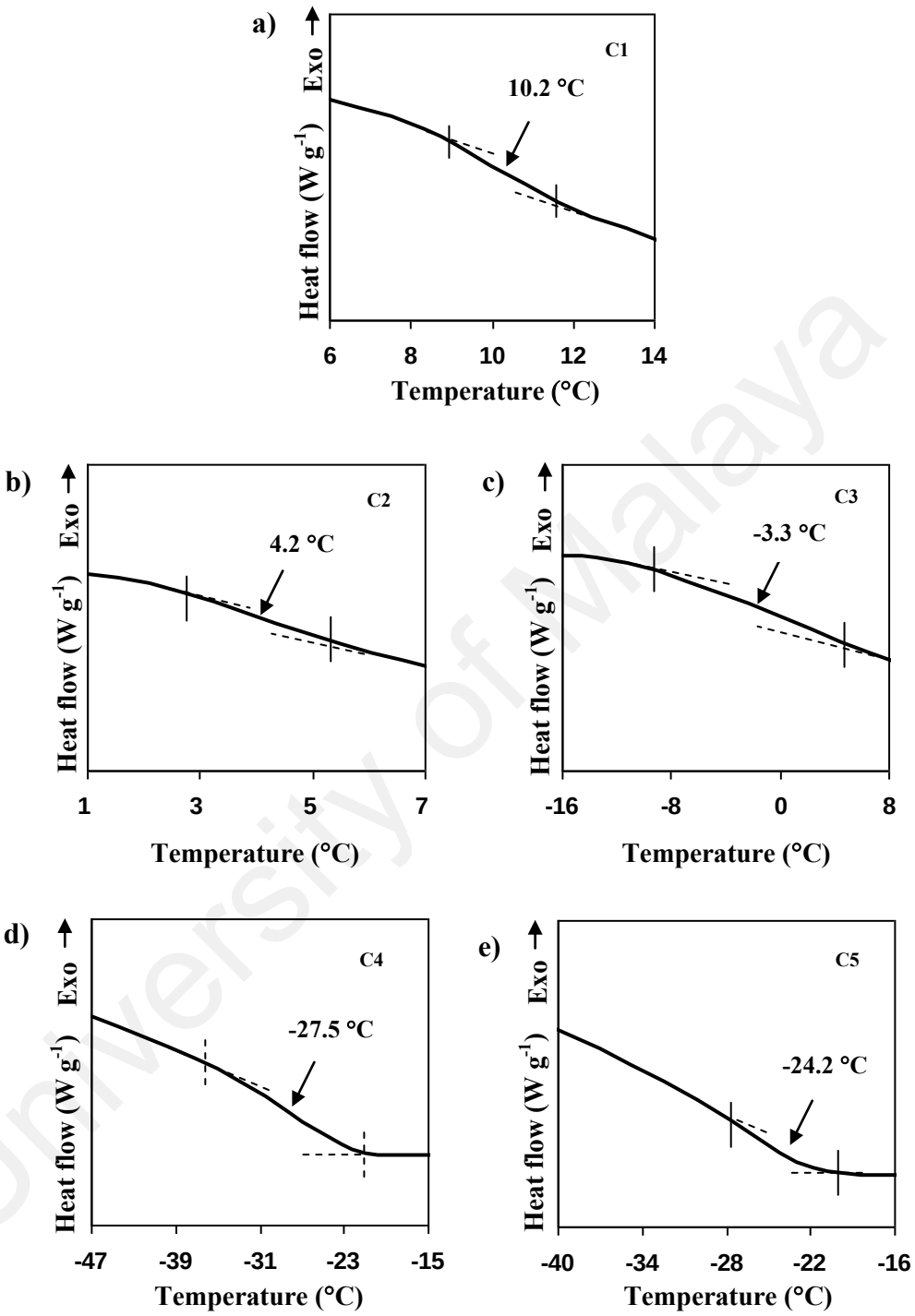

Figure 7.4: DSC thermograms for plasticized electrolytes.

. The T_g is observed at 10.2 °C as 10 wt.% glycerol is added to B6 electrolyte. The addition of more glycerol has further decreased the T_g as shown in Figure 7.4(a) to (e).

Mattos, Raphael, Majid, Arof and Pawlicka (2012) stated that the decrement of T_g is due to formation of hydrogen bonding between glycerol and polysaccharides. Glycerol improves the flexibility of the polymer chain which resulting in decrement of T_g and enhancement of conductivity value (Kumar & Sekhon, 2002; Sanyang, Sapuan, Jawaid, Ishak & Sahari, 2015). As 50 wt.% of glycerol is added the polymer chain has become less flexible as the T_g value is observed to increase back to −24.2 °C. The excess plasticizer can cause recrystallization of salt that obstruct the ion migration and segmental motion which reduce the ionic conductivity (Liew, Ramesh & Arof, 2014).

7.4 FESEM Studies

Further verification of conductivity trend and XRD patterns is conducted via FESEM analysis. The main objective is to examine the changes of electrolyte's surface with the presence of NH_4NO_3 and glycerol. The crystallinity or amorphousness of an electrolyte can be explained by XRD analysis where it can be verified by observing the surface of the electrolyte.

Based on Figure 4.8, the surface of A6 blend possesses small spherical structures which act as room for salt to fill in for ionic migration. Figure 7.5 shows the surface image for B2 electrolyte where the surface possesses a uniform complex formation. The complex formation is considered as ion particles or traps in the polymeric network that involve in the process of ionic conduction (Kadir, 2010).

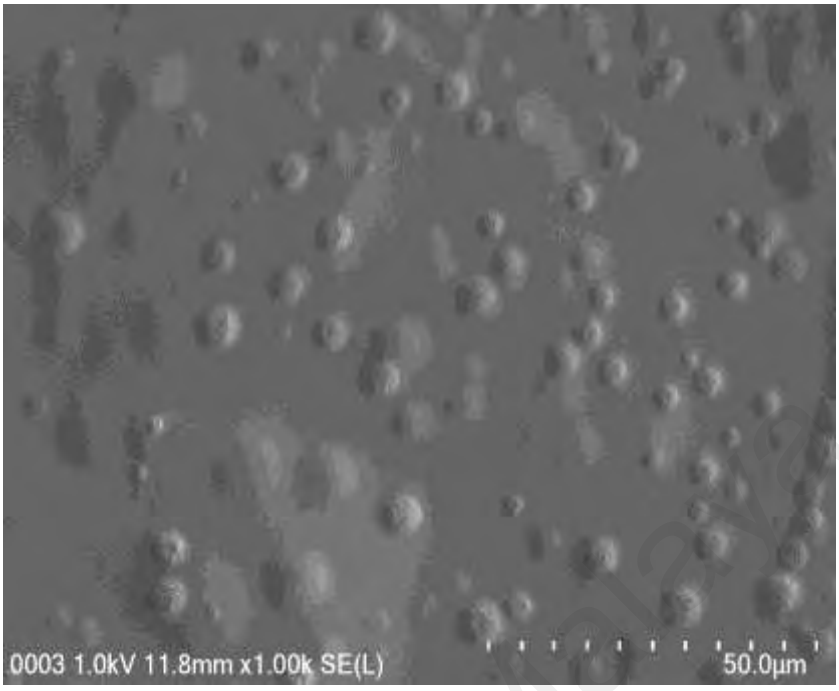

Figure 7.5: Surface image for B2.

Figure 7.6 reveals the surface image for B3. As 15 wt.% of NH_4NO_3 is added into the polymer blend, more ion traps can be seen in the electrolyte. These ion traps provide a channel for conduction of ion (Bhad & Sangawar, 2013).

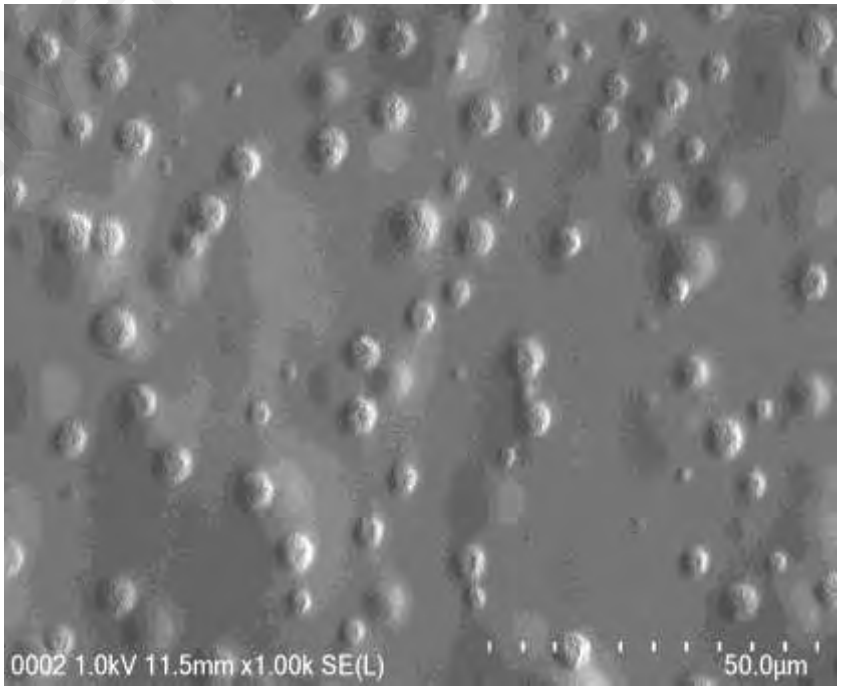

Figure 7.6: Surface image for B3.

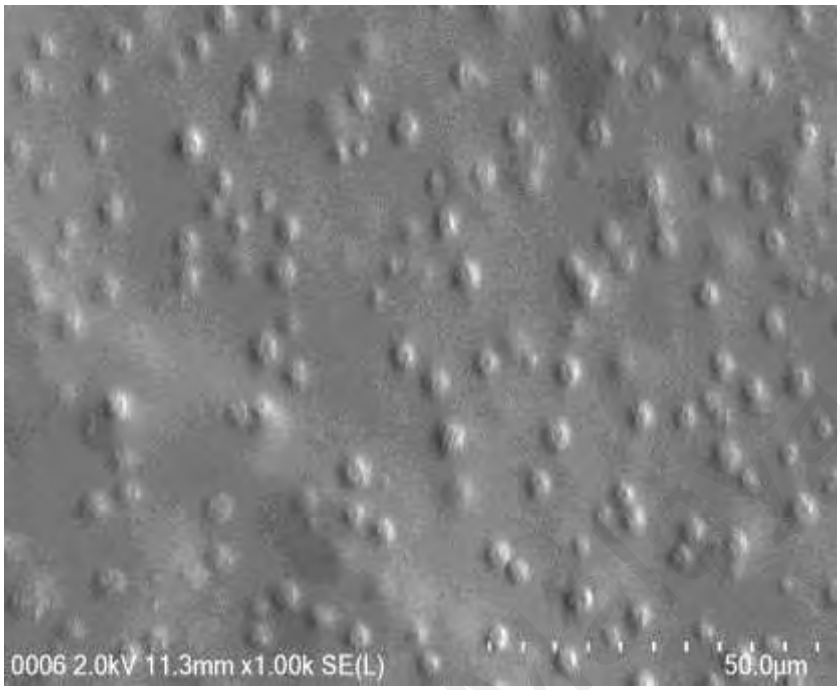

Figure 7.7: Surface image for B6.

The image of B6 surface can be observed in Figure 7.7. With 30 wt.% NH_4NO_3, the surface consists of more complex formation. This indicates that salt has utilized the space developed at the surface of A6 polymer blend (Figure 4.8). Furthermore, the ion traps are well dispersed at the surface of B6. This result is harmonized with conductivity result where B6 possesses the highest conductivity and lower activation energy value for salted electrolyte.

Figure 7.8 shows that as the concentration of NH_4NO_3 exceeded 30 wt.%, the surface is dramatically altered where sharp crystal like structure is protruded out of the surface. More crystal like objects are observed at the surface of B8 as illustrated in Figure 7.9. This signifies the recrystallization of salt which reduce the ionic conductivity. Results from Figures 7.8 and 7.9 are harmonized with the XRD patterns in Figure 5.1 where B7 and B8 possess crystalline peaks of NH_4NO_3.

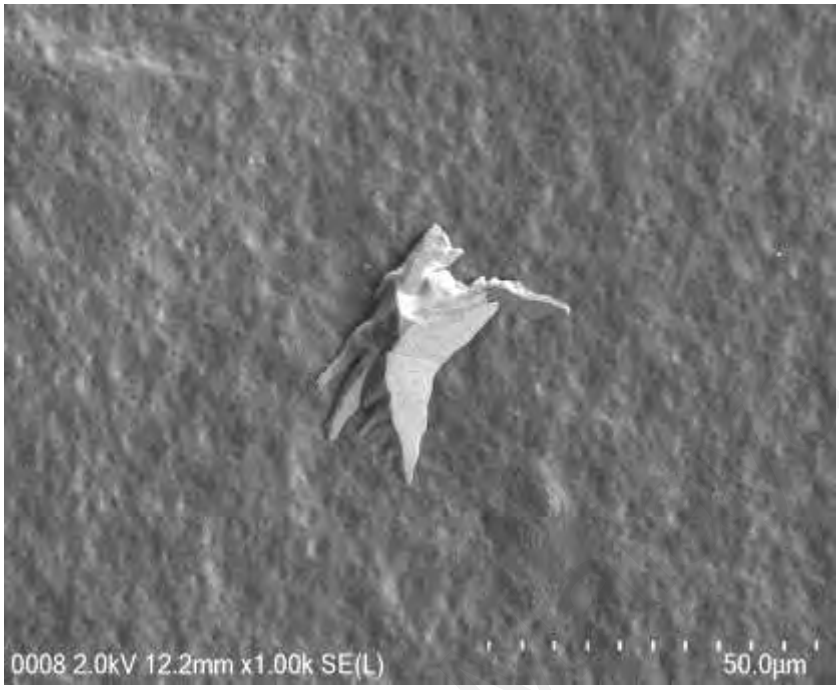

Figure 7.8: Surface image for B7.

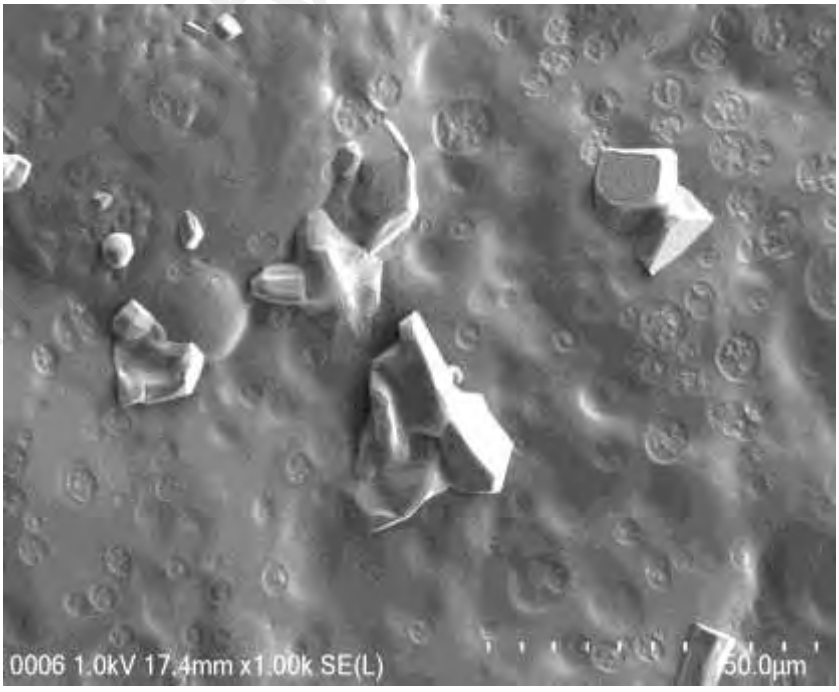

Figure 7.9: Surface image for B8.

Figures 7.10 and 7.11 depict the surface images of C1 and C2, respectively.

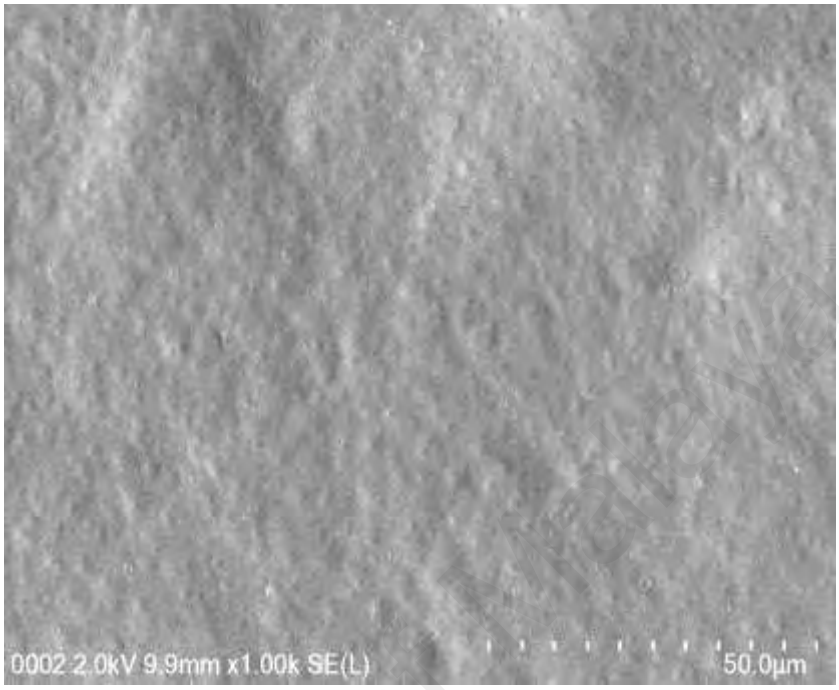

Figure 7.10: Surface image for C1.

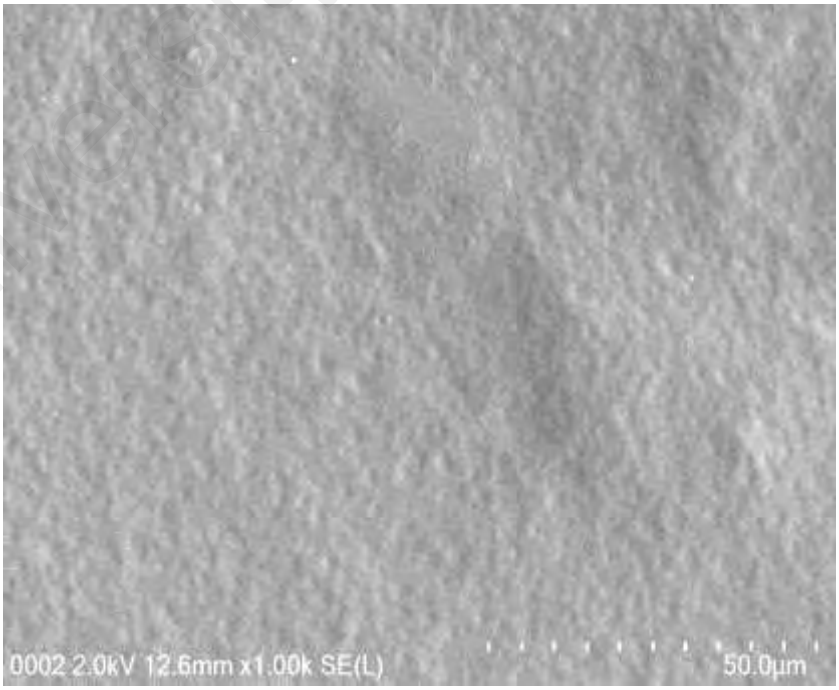

Figure 7.11: Surface image for C2.

Based on Figures 7.10 and 7.11, the inclusion of glycerol has transformed the surface of B6 to become more clear and amorphous where the ion traps in Figure 7.7 have been disappeared. The surface image for C4 can be seen in Figure 7.12. The surface of the electrolyte have turned to a denser structure with the inclusion of 40 wt.% glycerol. High dielectric constant of glycerol eliminates the process of ions recombination thus aid in the increment of ionic conductivity (Mattos et al., 2012). This phenomenon tallies with the result from Figure 6.13 where the inclusion of glycerol has increased the ionic number density. Results from Figures 7.10, 7.11 and 7.12 are consistent with the degree of crystallinity is in Table 5.2. The presence of glycerol has increased the amorphousness of the electrolyte.

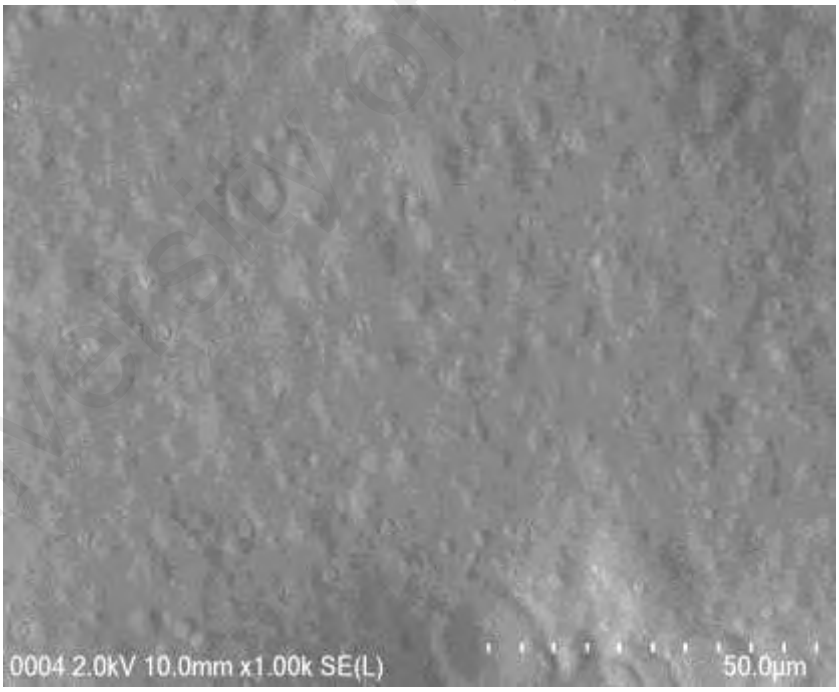

Figure 7.12: Surface image for C4.

Figure 7.13 illustrates the FESEM image for C5. It is noticeable that the surface undergoes a drastic alteration with the addition of 50 wt.% glycerol where large craters can be observed.

Figure 7.13: Surface image for C5.

The existence of craters signifies that the amorphousness of C5 has been reduced. Latif & Aziz (2013) reported that the craters block the free ions in its vicinity which obstruct the migration of ions. The authors also stated that these craters increase the energy barrier as well as activation energy that leads to decrement of conductivity value. According to Latif, Aziz, Ali & Yahya (2009), sample with craters possess lower conductivity compared to sample without craters. As referred in Table 6.5 in Chapter 6, the value of activation energy increases with 50 wt.% glycerol. Hence, the pattern of ionic conductivity for plasticized electrolyte is further verified via FESEM results.

7.5 Summary

It is discovered from TGA studies that the addition of NH_4NO_3 has reduced the decomposition temperature of the electrolyte. The decomposition temperature of the electrolyte is further decreased with the presence of glycerol. From FESEM analysis, it

is noticeable that addition of NH_4NO_3 provides a surface with well dispersed complex formation that aids in ionic conduction. Results from FESEM analysis also identify C4 to possess the most amorphous surface. As more than 40 wt.% glycerol is added, large craters can be seen which blocks the conduction of ions. The outcomes of FESEM for both salted and plasticized electrolytes are harmonized with the XRD results in Chapter 5. Furthermore results from FESEM are harmonized with the result from conductivity analysis in Chapter 6. Due to high conductivity value and amorphousness, C4 has been chosen to be employed in the construction and characterization of supercapacitor and protonic cell which will be discussed in Chapter 8.

CHAPTER 8: CHARACTERIZATIONS OF ENERGY DEVICES

8.1 Introduction

Based on the results obtained in the previous chapters, it is identified that methylcellulose (MC)-potato starch (PS)-NH_4NO_3 system with 40 wt.% glycerol (C4) has the maximum room temperature conductivity of $(1.26 \pm 0.1) \times 10^{-3}$ S cm^{-1}. Chandra, Chandra and Thakur (2016) stated that an energy storage device must consist of an electrolyte with conductivity of $\geq 10^{-4}$ S cm^{-1} in order to perform well. Hence, C4 electrolyte has passed this crucial requirement.

In this chapter, the potential stability of C4 will be tested using linear sweep voltammetry (LSV). C4 has been used as a separator in the protonic cell and supercapacitor fabrications. Results on various characterizations including charge-discharge characteristic of both devices are presented. The fabricated supercapacitor is also tested using cyclic voltammetry.

8.2 Potential Stability

Apart from having conductivity of at least ~ 10^{-4} S cm^{-1}, electrochemical stability of electrolyte is also an imperative characteristic in the application of electrochemical energy storage devices (Zhong, Yida, Hu & Zhang, 2015). Using LSV technique, the electrochemical stability as well as the maximum working voltage of an electrolyte can be identified. Figure 8.1 shows the LSV plot for C4 at different temperatures at 1 mV s^{-1} scan rate.

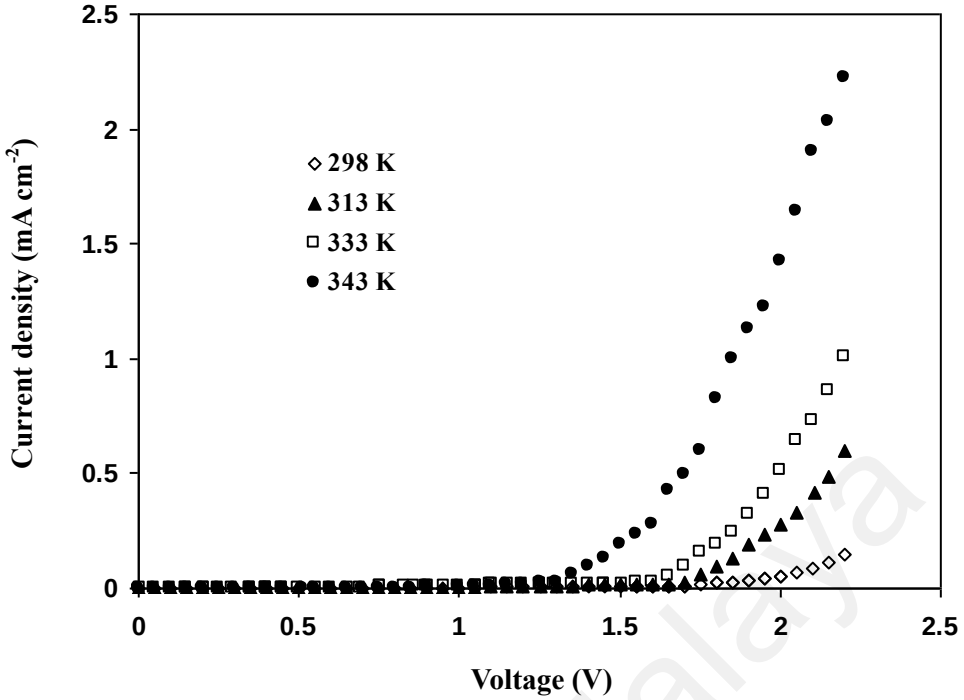

Figure 8.1: LSV plot for C4 at various temperatures.

It is noticeable that at each temperature, the current is stable initially before experiencing a drastic increase when reach a certain voltage. The increase in current signifies the decomposition of the electrolyte (Asmara et al., 2011). The current onset at 298 K is observed at 1.88 V. Ng and Mohamad (2008) reported that chitosan-NH_4NO_3-EC system with conductivity and electrochemical stability of ~10^{-3} S cm^{-1} and 1.80 V, respectively. Based on the work by Kadir and Arof (2011), electrochemical stability of 1.70 V is achieved with biopolymer blend electrolyte infused with NH_4NO_3. These results are comparable with result in this study. As the temperature increase to 313 K, the current onset decreases to 1.65 V and further decreases to 1.50 V at 343 K. Other studies also reported that increasing temperature has resulted in a decrease in the decomposition voltage (Ng & Mohamad, 2008; Lee et al., 2015; Cao et al., 2016; Lee et al., 2017). Even though the decomposition voltage is decreasing with increasing temperature, it is still considered good enough for application in energy devices at high temperature. Hence, C4 is found to be suitable for both devices application.

8.3 Characterization of Protonic Cell

The protonic cell was fabricated by sandwiching C4 in between manganese (IV) oxide (MnO_2) based cathode and zinc based anode. The characteristics of the protonic cell i.e. charge-discharge, open circuit potential (V_{oc}), *I-V* and *J-P* characteristic have been monitored.

8.3.1 Discharge Characteristic of the Protonic Cell

Figure 8.2 illustrates the V_{oc} for the protonic cells at 298 K, 313 K, 333 K and 343 K. It can be observed that there is a slight voltage decrement at initial hours for all temperature before constant V_{oc} is achieved. The decrease in voltage could be due to the oxidation of zinc at the anode (Samsudin et al., 2014).

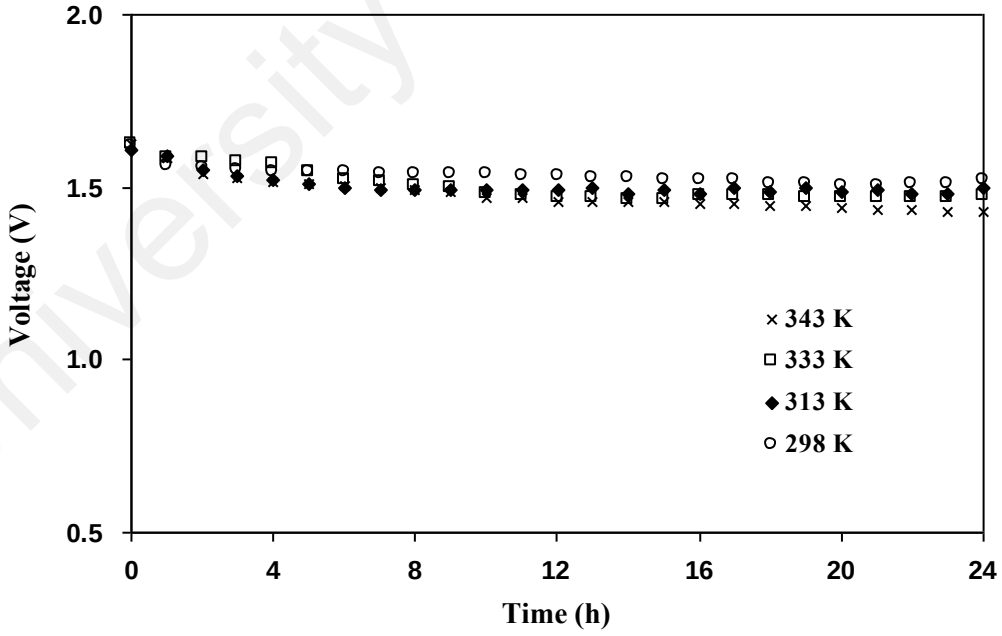

Figure 8.2: V_{oc} of the protonic cells at different temperatures.

At 298 K, the value of V_{oc} is observed to be constant at 1.52 V. Table 8.1 lists the value of room temperature V_{oc} reported by other ammonium salt-based protonic cells.

As the temperature increases to 343 K, the V_{oc} reduces to 1.46 V. This indicates that the electrode's components possess catalytic properties at low temperature (Ng & Mohamad, 2008). This result harmonized with LSV result.

Table 8.1: Comparison of V_{oc} with current system.

Electrolyte	V_{oc} (V)	Time (h)	References
Starch-chitosan-NH_4I-glycerol	1.31	24	Yusof, 2017
Carboxymethyl cellulose-NH_4Br	1.36	24	Samsudin et al., 2014
Cellulose acetate - NH_4NO_3	1.39	8	Monisha et al., 2014
(PVdF-HFP)-(PMMA)-NH_4SCN-EC-PC	1.45	24	Mishra, Hashmi & Rai, 2014
MC-PS-NH_4NO_3-glycerol	1.52	24	This work

Hydrated zinc sulphate provides H^+ during discharge process of the protonic cell while zinc undergoes oxidation which creates Zn^{2+} and electrons. These electrons provided flow in the internal circuit while Zn^{2+} is left at the anode. Thus chemical reactions at the anode are expressed as (Vanysek, 2011):

$$Zn \rightarrow Zn^{2+} + 2e^- \qquad E^o = 0.76 \text{ V} \tag{8.1}$$

$$ZnSO_4.7H_2O \rightarrow ZnSO_4 + 7H^+ + 7OH^- \qquad E^o = -0.82 \text{ V} \tag{8.2}$$

While chemical reaction at the cathode is expressed as:

$$MnO_2 + 2e^- + 4H^+ \rightarrow Mn^{2+} + 2H_2O \qquad E^o = 1.22 \text{ V} \tag{8.3}$$

Thus the overall reaction in the cell with $E^o = 1.28$ V is obtained as:

$$Zn + ZnSO_4.7H_2O + MnO_2 + 4H^+ \rightarrow Zn2^+ + ZnSO_4 + 7H^+ + 7OH^- + Mn^{2+} + 2H_2O \quad (8.4)$$

The difference between the experimental and theoretical V_{oc} is about 15.78 %. Botte and Muthuvel (2012) stated that the variation of E^o value is affected by several aspects including the ionic concentrations and transportation. Figure 8.3 reveals the discharge characteristic of the protonic cells at room temperature. The discharge capacity (Q) of the protonic cell can be expressed as:

$$Q = it_{plateau} \quad (8.5)$$

here $t_{plateau}$ is the time at the plateau region and i is the applied current.

Based on Figure 8.3, for all constant currents, there is a sudden decrease in potential after reaching ~1.0 V. As stated in Equations (8.1) and (8.3), MnO_2 and zinc are reduced and oxidized, respectively, during the discharge process. The development of Mn_2O_3-ZnO particles occur during discharge process. Mn_2O_3-ZnO particle is considered as semiconductor particle (McComsey, 2001; Rahman et al., 2013). Wang et al. (2005) stated that these particles increase the charge transfer resistance which decreases the potential significantly.

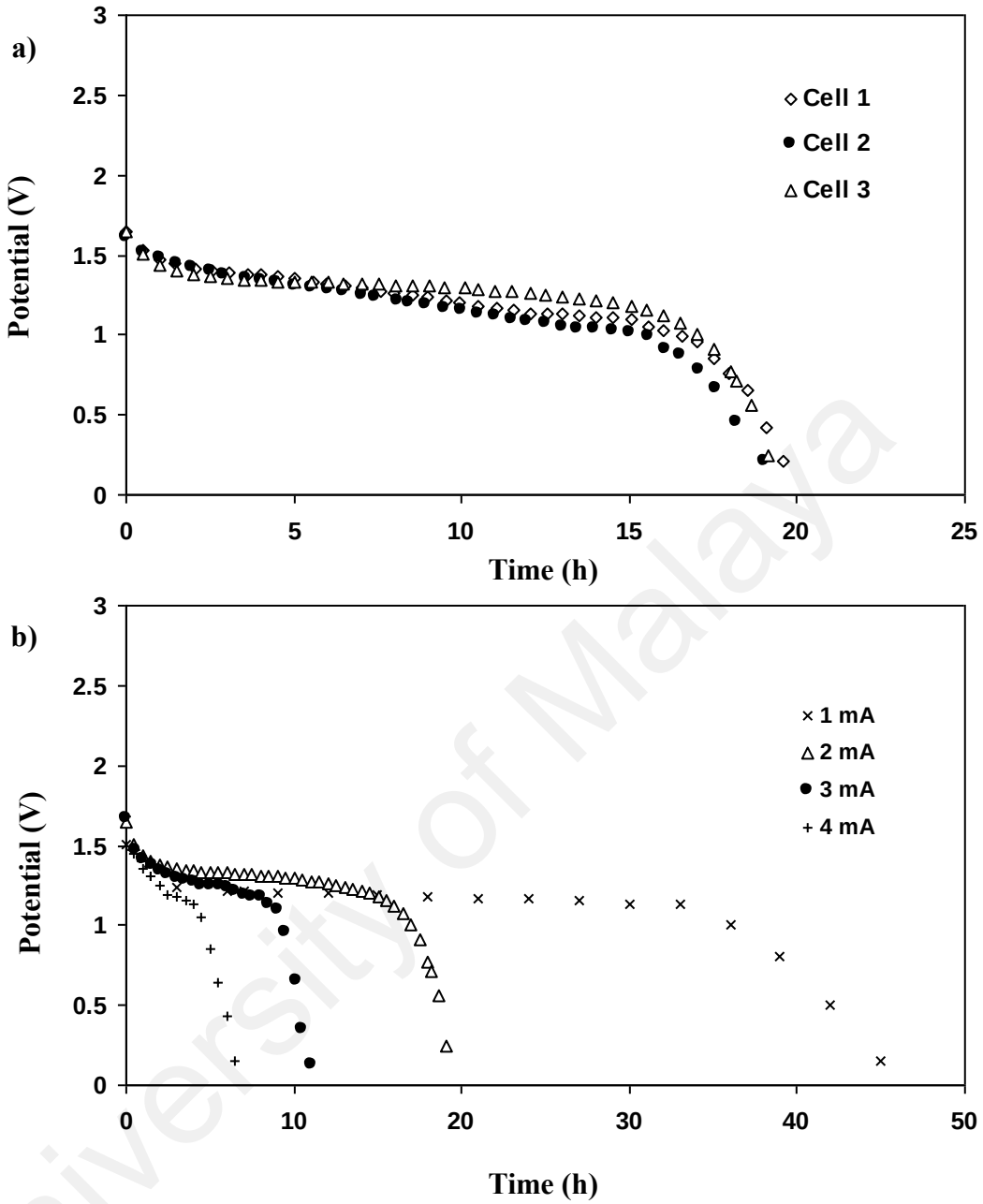

Figure 8.3: Discharge characteristics of the protonic cell at a) 2 mA and b) various constant currents.

As observed in Figure 8.3(a), the protonic cells were discharged for several times with 2 mA constant current in order to achieve the accurate value of *Q*. The plateau region is turn out to be shorter with larger constant current as observed in Figure 8.3(b). Table 8.2 lists the calculated values of *Q*.

Table 8.2: The influence of constant current on the value of discharge capacity.

Constant discharge current (mA)	Discharge capacity (mA h)
1	33.0
2	29.8
3	27.0
4	18

The discharge process at 2 mA is lasted after 14.9 hours where Q = 29.8 mA h. It is found that larger constant current gives lower value of Q. At 4 mA, Q is 18 mA h which is smaller than 2 and 3 mA. At higher constant current, the migration and intercalation process of H^+ is non-uniform. This phenomenon increases the difference in ionic concentration along the electrode's pores which resulting in the decrement of Q (Roscher, Bohlen & Vetter, 2011; Choudhury et al., 2019).

Discharge characteristics of the protonic cell at high temperature were performed at a constant current of 3 mA as illustrated in Figure 8.4. As observed in Figure 8.4, there is a small potential drop before approaching plateau. This is because the electrode's electrochemical reaction rate is processed by inactive electrode kinetics (Broadhead & Kuo 2001; Brownson et al., 2017). As the temperature increases to 343 K, the discharge time increases from 9 hours to 14 hours. Based on Table 8.3, the value of Q also increases from 27 mA h to 42 mA h as the temperature increases to 343 K. More free ions are created at high temperature as shown in Figure 6.16. This phenomenon increases the conductivity since more ions can contribute to intercalation process resulting in higher Q value.

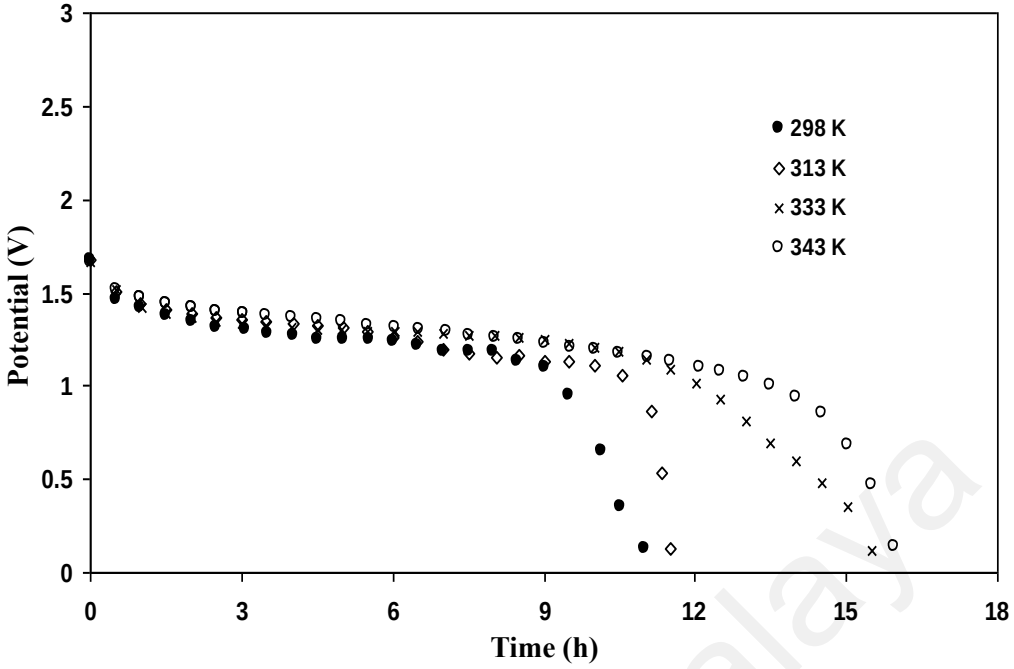

Figure 8.4: Discharge characteristic of the protonic cell at high temperature.

Table 8.3: The influence of temperature on the value of discharge capacity

Temperature (K)	Discharge capacity (mA h)
298	27.0
313	31.5
333	34.5
343	42.0

The influence of temperature on current-voltage (*I–V*) and current density-power density (*J–P*) characteristics are shown in Figure 8.5(a) and 8.5(b), respectively.

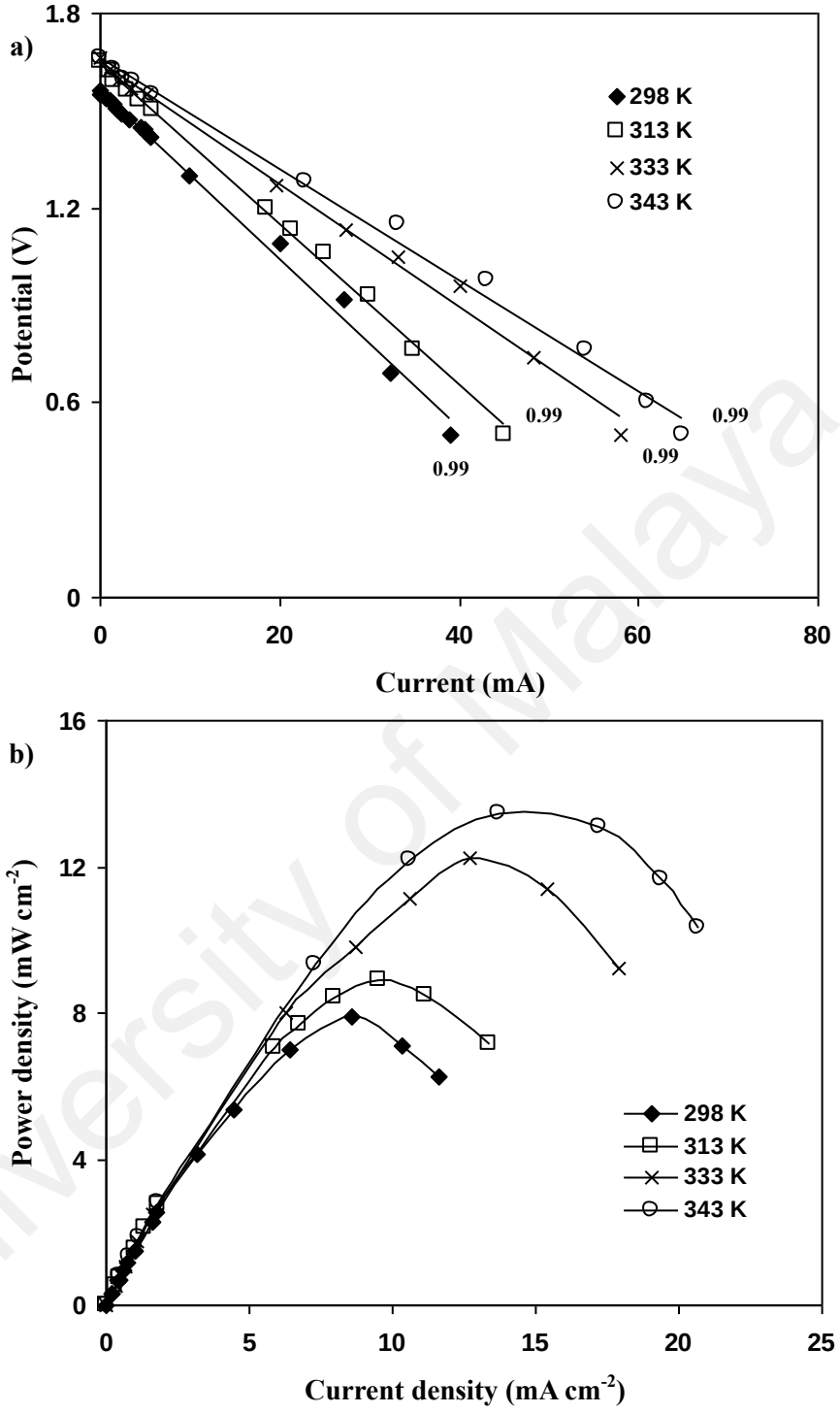

Figure 8.5: The influence of temperature on a) *I-V* and b) *J-P* characteristic.

The electrode polarization is dominated by ohmic indicated by the linear I-V plot (Yap & Mohamad, 2007; Swain et al., 2019). The *I-V* and *J-P* curves can be understood via equations:

$$V = V_{oc} - Ir \tag{8.6}$$

$$P = (IV) \times A^{-1} \tag{8.7}$$

here r corresponds to the internal resistance and A is the contact area.

The value of r and maximum power density (P_{max}) have been calculated and tabulated in Table 8.4. The value of r at 298 K and 343 K is 26 Ω and 17 Ω, respectively. Low internal resistance indicates the good electrode/electrolyte contact. The trend of r is consistent with the pattern of Q in Table 8.2. Yusof (2017) reported r value of 62.30 Ω at 298 K for chitosan-starch-NH_4I-glycerol system. A protonic cell with NH_4NO_3 as the proton provider with r of 33 Ω is reported by Kadir et al. (2010).

Table 8.4: The influence of temperature on internal resistance and power density.

Temperature (K)	Internal resistance (Ω)	Power density (mW cm^{-2})
298	26.0	7.91
313	25.5	8.88
333	19.2	12.2
343	17.0	13.5

Table 8.4 shows that the value P_{max} increases from 7.91 to 13.5 mW cm^{-2} as the temperature is increasing to 343 K. The value of P_{max} in this study is higher compared to other studies. Jamaludin and Mohamad (2010) reported that the protonic cell with NH_4NO_3 possessed P_{max} of 3.67 mW cm^{-2}. A chitosan acetate-NH_4CH_3COO-EC based

protonic cell with P_{max} of 1.83 mW cm^{-2} is reported by Alias et al. (2017). The short circuit of the protonic cell in this work is 39 mA at 298 K which is comparable to other works (Kadir, 2010; Shukur, 2015).

8.3.2 Rechargeability Test for the Protonic Cell

The plot of rechargeability test for the protonic cell is depicted in Figure 8.6.

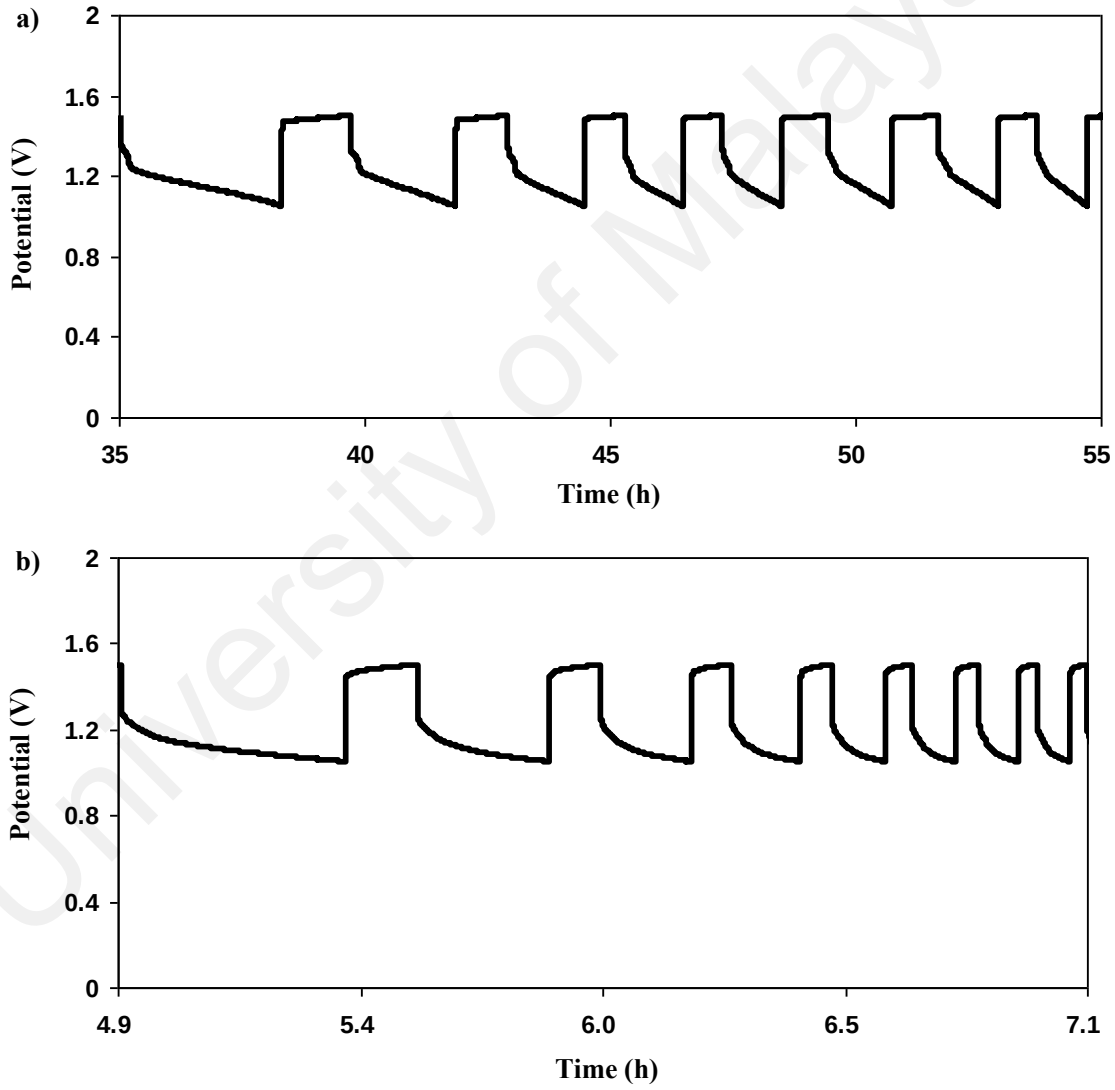

Figure 8.6: Rechargeability test for the protonic cell at a) 1 mA and b) 4 mA.

The rechargeability of the protonic cell is tested for 15 cycles at various constant currents. The cell is charged to 1.5 V and discharged to 1.0 V. The protonic cell is identified to experience faster process of charge/discharge at higher constant current. The protonic cell is lasted for 60 hours and 8 hours for 1 mA and 4 mA, respectively.

Figure 8.7 illustrates the specific capacity (Q_{spe}) versus the number of charge-discharge cycle at 1 mA and 4 mA constant current.

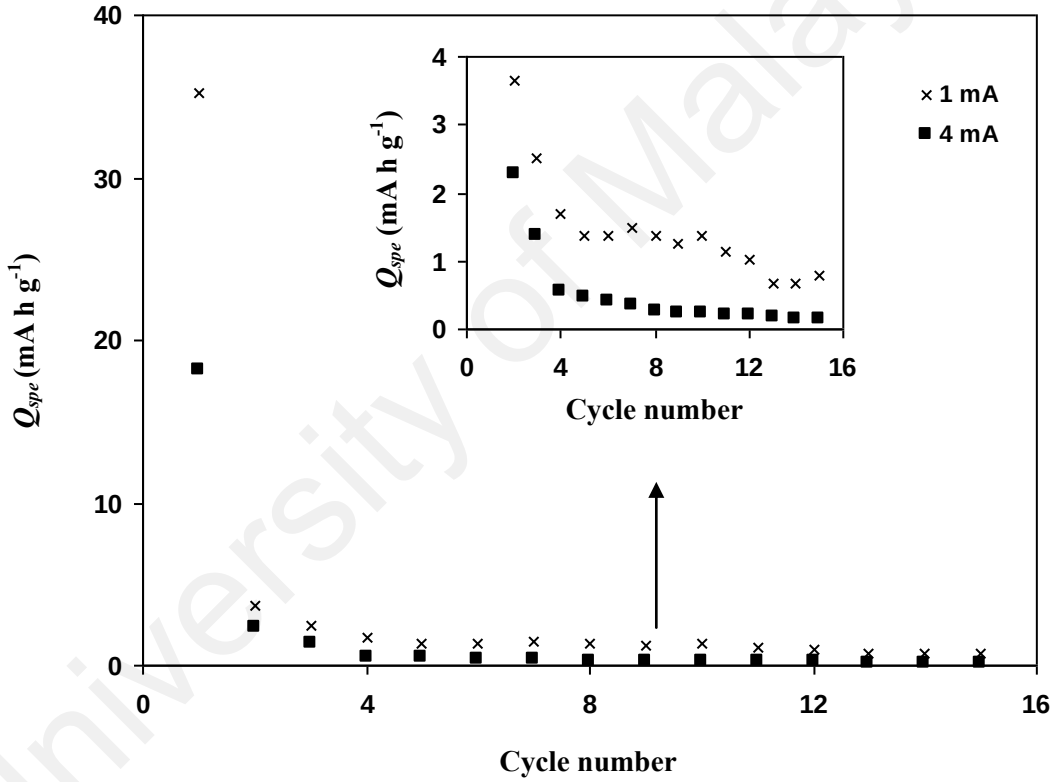

Figure 8.7: The influence of constant current on the specific capacity of the protonic cell.

The weight of MnO_2 is used to calculate the value of Q_{spe}. At 1 mA, the Q_{spe} drop from 35.2 mAh g^{-1} to 3.6 mAh g^{-1} after 2 charge-discharge cycles. The value of Q_{spe} is then stabilized at 1.2 mAh g^{-1} until 12th cycle which signifies a stable

electrode/electrolyte contact. Beyond 12th cycle the value of Q_{spe} reduces and maintain at 0.8 mAh g^{-1} until 15th cycle.

The value of Q_{spe} at 4 mA reduces from 18.2 mAh g^{-1} to 2.3 mAh g^{-1} after two cycles. The stabilization is achieved at ~ 0.27 mAh g^{-1} up to 15th cycle. The reversibility of cathode is the most crucial parameters for a rechargeable protonic cell. Mishra et al. (2013) stated that the reduction of capacity throughout charge/discharge process is due to the growth of interfacial resistance between electrode and electrolyte thus affecting stability. This phenomenon is similar to the work by Mishra et al. (2014) where the capacity reduces drastically after one cycle.

8.4 Characterization of Supercapacitor

An electrochemical double-layer capacitor (EDLC) is fabricated using two identical activated carbon based electrodes with C4 electrolyte as the separator. The fabricated EDLC is tested using cyclic voltammetry (CV). Several parameters are gained from charge-discharge characteristics of the EDLC e.g. efficiency, equivalent series resistance (ESR), power density and energy density.

8.4.1 CV for Supercapacitor

Figure 8.8 shows the CV plots for fabricated EDLC at scan rates of 2, 5, 10 and 20 mV s^{-1}. Shuhaimi (2011) reported that the EDLC with MC-NH_4NO_3-PEG as separator can be charged up to 0.85 V and even though the decomposition voltage of the electrolyte is 2.4 V. With polymer electrolyte that has decomposition voltage of 2.42 V, Asmara et al. (2011) applied 0.85 V to the EDLC.

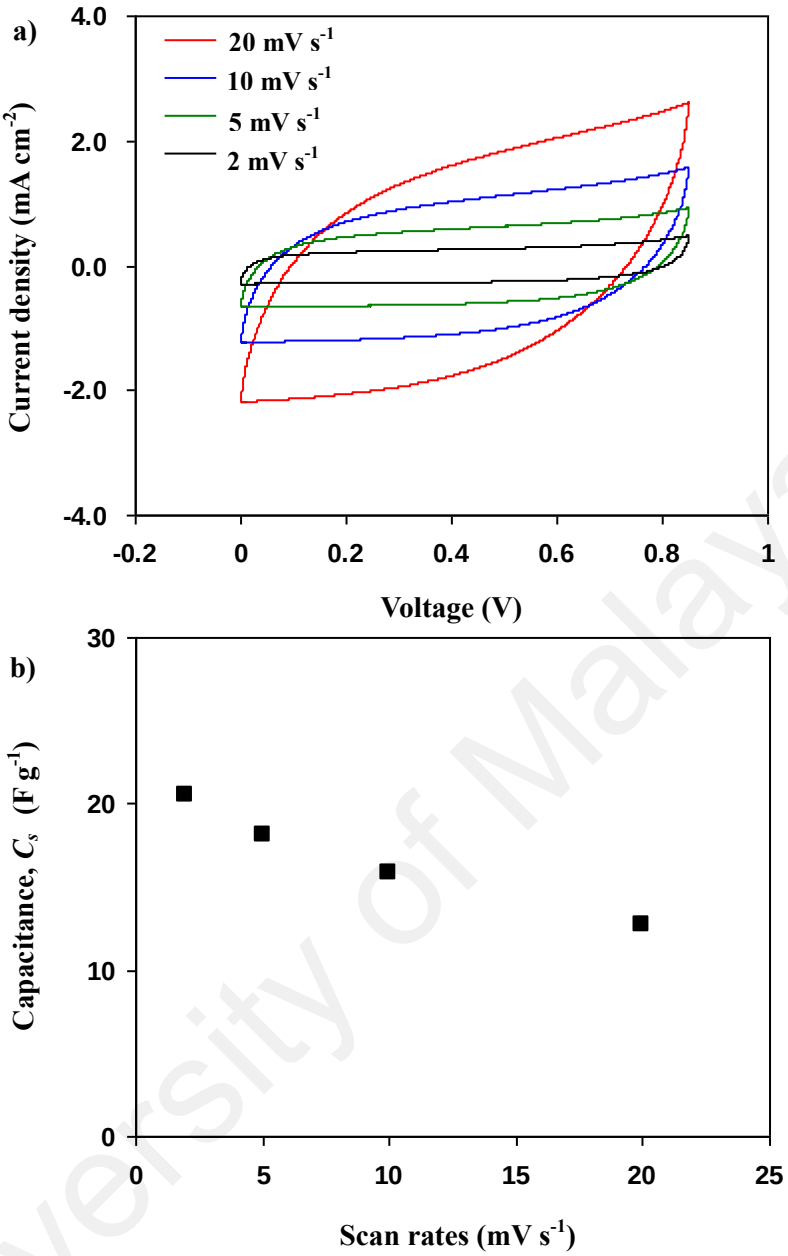

Figure 8.8: The a) CV plot for the EDLC and b) effect of scan rate on capacitance.

As observed in Figure 8.8(a), there is no peak appears in the range between 0 V to 0.85 V which indicates that redox reaction does not occur. The absence of redox peaks portrays the existence of double-layer in the EDLC (Liew & Ramesh, 2015). The CV plots turn to almost rectangular shape as the scan rate decreases. Applying high scan rate obtains CV plot of leaf like shape due to porosity of carbon and internal resistance

which creates current dependence of voltage (Liu et al., 2019). Specific capacitance (C_s) of the EDLC can be calculated via the following equation:

$$C_S = \int_{V_1}^{V_2} \frac{I(V)dV}{2(V_2 - V_1)mv} \tag{8.8}$$

here (V_2-V_1) is the potential, v is the applied scan rate, $I(V)$ stands for the current dependent potential where m is the mass of activated carbon used. Figure 8.8(b) shows the influence of scan rate on the C_s. The C_s obtained at scan rate of 2 mV s^{-1} is 20.48 F g^{-1}. The value of C_s is higher at lower scan rate. Teoh, Liew & Ramesh, (2014) stated that at low scan rate, charge carriers have enough time to vacant more sites at the surface of the electrodes, thus producing higher value of C_s.

8.4.2 Charge-Discharge Behavior of Supercapacitor

Figure 8.9 demonstrates the charge-discharge plot of the EDLC at 250th, 400th, 500th and 1000th cycle. The EDLC is charged up to 0.85 V and discharged to 0 V at a current density of 0.2 mA cm^{-2}. The presence of capacitive properties is shown as the slope of discharge curve is linear (Adam et al., 2019). The value of C_s can be obtained by substituting the value of the slope of discharge (s_{dis}) curve in the following equation:

$$C_S = \left(i/m\right) \times s_{dis}{}^{-1} \tag{8.9}$$

where i stands for current in ampere and m is the mass of activated carbon, which is the active material in the electrode.

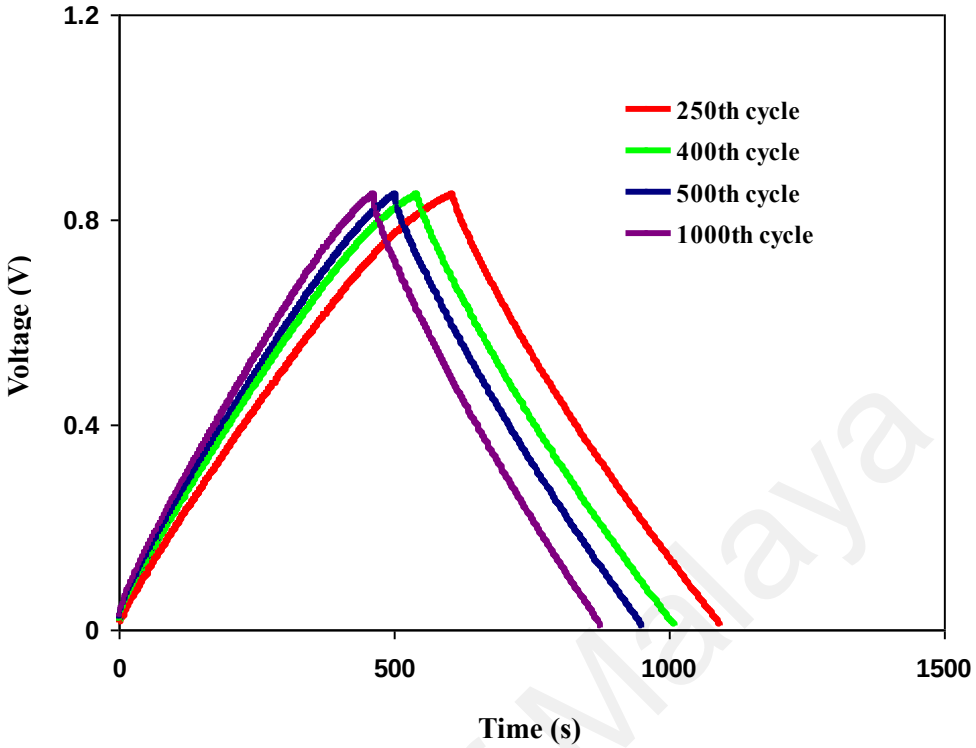

Figure 8.9: Charge-discharge plot of the EDLC at various cycles.

The plot of C_s versus cycle number is shown in Figure 8.10. The 1st cycle of the EDLC possesses C_s of 31 F g^{-1}. As the cycle number increases to 200, the value of C_s decreases to 24 F g^{-1}. The value of C_s then experiences stabilization at ~ 21 to 22 F g^{-1} until 1000th cycle. From Figure 8.8, the value of C_s obtained from CV is 20.48 F g^{-1} which is quite close to this result. Hence the value of C_s obtained from charge-discharge study is reliable. Table 8.5 shows the comparison between EDLC in this work with other protonic based EDLC with activated carbon electrodes at the 1st cycle.

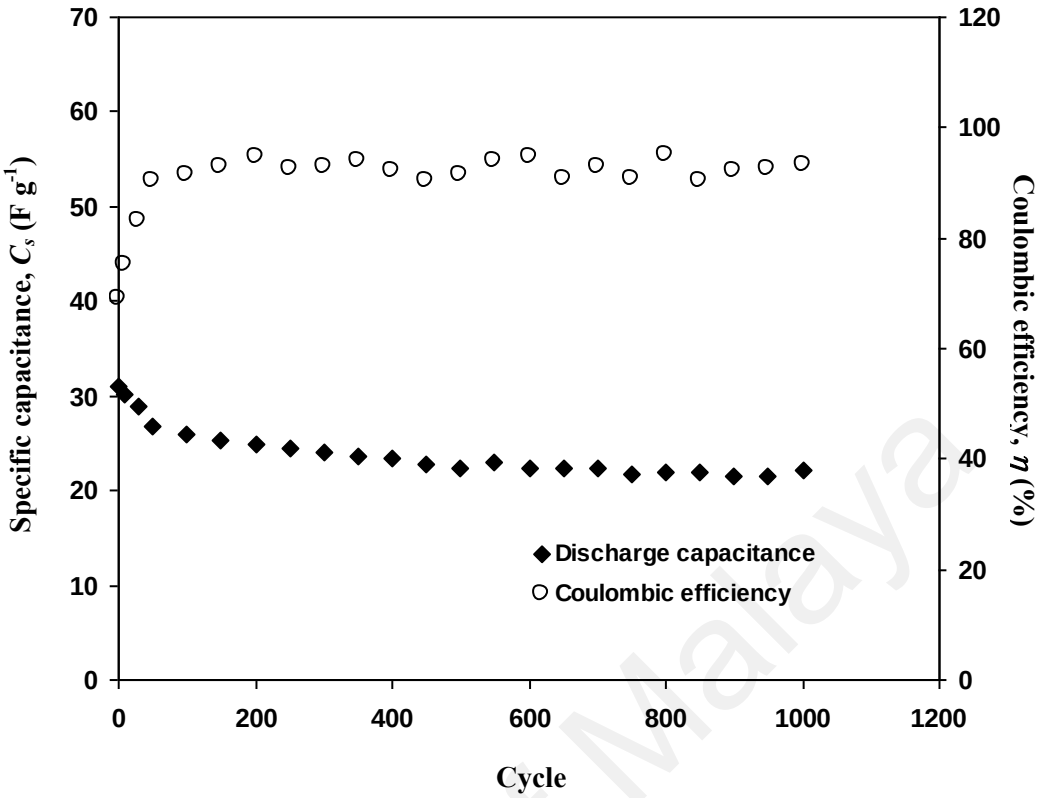

Figure 8.10: Coulombic efficiency and specific capacitance of the EDLC versus cycle number.

Table 8.5: Example of protonic based EDLC with activated carbon electrodes.

Electrolytes	Cycle number	C_s (F g^{-1}) at 1st cycle	Reference
Chitosan-κ-carrageenan-NH_4NO_3	20	18.5	Shuhaimi, Alias, Majid & Arof, 2008
MC-NH_4NO_3-poly (ethylene glycol) (PEG)	Not stated	25	Shuhaimi et al., 2012
Chitosan-PVA-NH_4NO_3-EC	100	27.1	Kadir, 2010
Chitosan-carrageenan-H_3PO_4-PEG	30	35	Arof et al., 2010
MC-PS-NH_4NO_3-glycerol	1000	31	This work

Coulombic efficiency (η) is one of the significant parameters for EDLC where it can portray the cycling stability of the EDLC. η can be calculated using the following equation:

$$\eta = \left(t_d \times t_{ch}^{-1}\right) \times 100\% \tag{8.10}$$

where time of discharge and charge are denoted as t_d and t_{ch}, respectively. The plot of η throughout the 1000 cycles is shown in Figure 8.10. It is noticeable that the value of η enhances from 69% to 90% towards the 50th cycle. η is observed to achieve stabilization at 90 to 94% up to 1000th cycle. Lim, Teoh, Liew and Ramesh (2014) stated that high value of η can be the indicator of a good electrode/electrolyte contact. A stable η values verifies that the EDLC possesses excellent cycle stability for 1000 cycles.

In Figure 8.9, it can be observed that there is a small voltage drop (V_{drop}) before discharging process. The occurrence of V_{drop} is attributed to the internal resistance of the EDLC. The value of V_{drop} for the EDLC in this work is in the range of 0.01 to 0.02 V. Small V_{drop} signifies that only small amount of energy is loss throughout the process of charge and discharge. EDLC's internal resistance is known as equivalent series resistance or ESR which can be expressed as:

$$ESR = \frac{V_{drop}}{i} \tag{8.11}$$

According to Arof et al. (2012), the existence of ESR in the capacitor is due to current collectors, electrolytes and the gap between current collectors with electrolyte.

The calculated value of ESR for the EDLC is shown in Figure 8.11. In this work, the ESR is in the range from 24 to 64 Ω. Small value of ESR indicates good contact between electrolyte and electrodes where charge carriers can migrate easily towards the electrodes (Mudila et al., 2019). An EDLC with κ-carrageenan/chitosan-NH_4NO_3 electrolyte and activated carbon based electrodes possesses ESR of 29 to 64 Ω (Shuhaimi et al., 2011). The increase in ESR or V_{drop} during charge-discharge process is due to degradation of electrolyte in the EDLC (Kumar & Bhat, 2009).

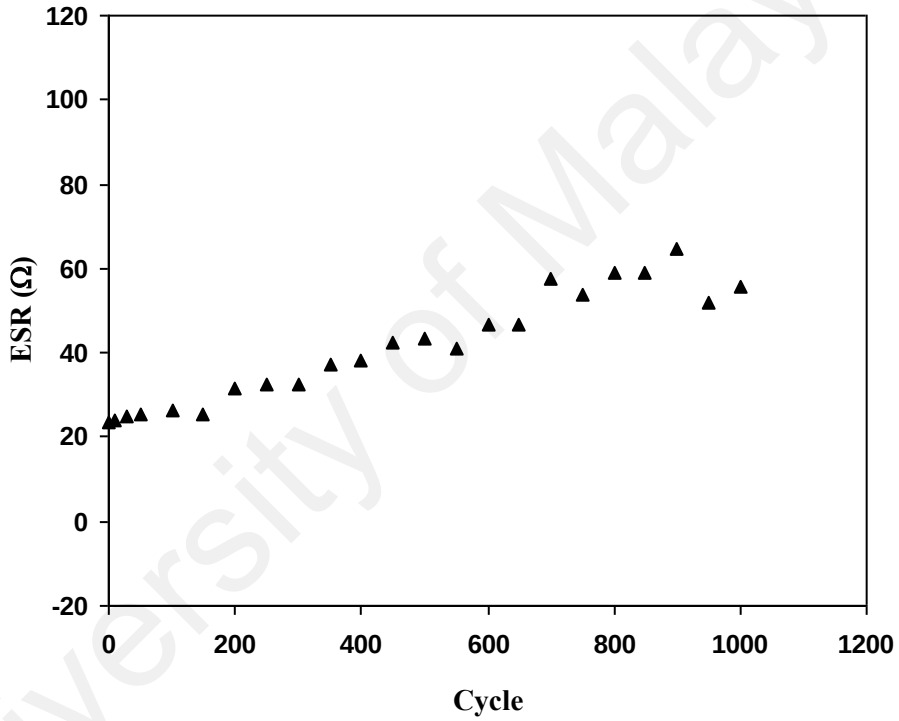

Figure 8.11: The equivalent series resistance of the EDLC.

Other crucial parameters are energy density (E) and power density (P) which can be explained via the following equation:

$$E = \frac{C_s V^2}{2} \tag{8.12}$$

$$P = \frac{V^2}{4mESR} \tag{8.13}$$

Figure 8.12 shows the energy and power density for the EDLC against the cycle number.

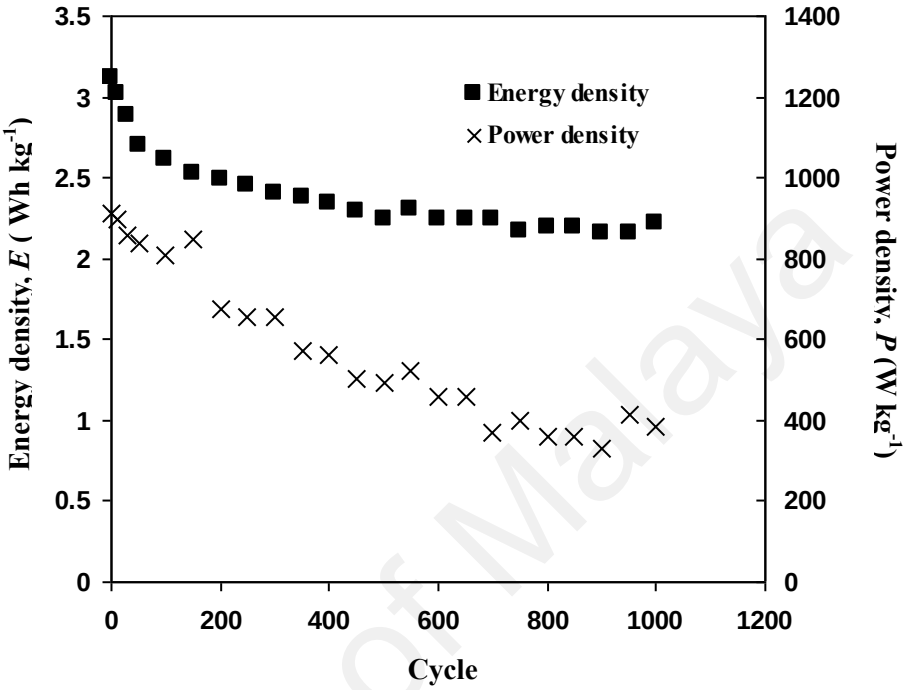

Figure 8.12: Energy and power density of the EDLC against cycle number.

From Figure 8.12 it can be observed that 1st cycle of the EDLC possesses *E* of 3.1 Wh kg^{-1}. The value of *E* starts to become constant from 350th to 1000th cycle in the range of 2.2 to 2.3 Wh kg^{-1}. Stable value of *E* indicates that the charge carriers go through almost the same energy barrier during migrations toward the electrode's surface at 350th to 1000th cycle. Taer et al. (2017) reported an activated carbon-based EDLC with energy density from 0.33 to 0.63 Wh kg^{-1}. The existence of internal resistance results in energy loss during charge-discharge process which explains the reduction of *E* value (Wei, Fang, Iwasa & Kumagai, 2005; Kadir & Arof, 2011).

The EDLC experiences a decrease in power density from 910 to 385 W kg^{-1}. Shukur, Ithnin and Kadir (2014) also reported a drop in *P* value throughout 1000 cycles for an

EDLC with starch based polymer electrolyte. The authors also stated that the depletion of electrolyte cause the reduction in the value of capacitance, energy density and power density. Various carbon-based EDLC have been reported with power density of 569 W kg^{-1} (Biswal et al., 2013), 400 W kg^{-1} (Hedge et al., 2015) and 263 W kg^{-1} (Fan & Shen, 2016). As reported by Liew et al. (2016), the aggregation of ions formed throughout the charge-discharge cycles will obstruct the ionic migration towards the carbon electrodes. Hence, less adsorption of ions occurs at the electrode-electrolyte interface.

8.5 Summary

From LSV analysis, it is found that C4 electrolyte possesses electrochemical stability up to 1.88 V. The protonic cell has open circuit voltage (V_{oc}) of 1.52 V at 298 K. The increase in temperature has reduced the value of V_{oc}. The highest capacity for the fabricated protonic cell at 298 K is 33 mA h. It has been identified that high temperature gives higher value of capacity. The short circuit current, power density and internal resistance of the protonic cell are 39 mA, 7.91 mW cm^{-2} and 26 Ω, respectively, at 298 K. The charge-discharge profile of the protonic cell has been tested for 15 cycles with constant current of 1 and 4 mA. The fabricated EDLC is conducted at 0.2 mA cm^{-2} for 1000 cycles. The 1st cycle possessed the specific capacitance and equivalent resistance of 31 F g^{-1} and 24 Ω. The coulombic efficiency of the EDLC is stabilized at ~ 90 to 94 % with energy and power density of 3.1 Wh kg^{-1} and 910 W kg^{-1}, respectively, at the 1st cycle.

CHAPTER 9: DISCUSSION

Polymer electrolytes (PEs) are found to be an attractive alternative to liquid electrolyte for application in energy storage devices e.g. supercapacitors (Liew & Ramesh, 2015), protonic cells (Asmara et al., 2011), solar cells (Dzulkurnain et al., 2018), fuel cells (Shuhaimi et al., 2010) and sensors (Strzelczyk, Jasinski & Chachulski, 2016). This is because the current trend in electronic devices industries e.g. laptops, mobile phones, tablets and television demand a flexible, safer, cheaper, good efficiency, light weight and simple preparation energy storage devices. PEs possess several advantages for energy device applications such as excellent mechanical properties, low toxicity, high ionic conductivity, high operation temperature and less flammability (Tripathi & Singh, 2018).

As reported in the work by Haward (2018), the number of plastic wastes in the ocean varies from 4.8 to 12.7 million metric ton per year and keeps on increasing. This issue leads to the attention towards green technology. Most biopolymers are biodegradable which can naturally breakdown by microorganism or bacteria (Vroman & Tighzert, 2009). The employment of biopolymers is also to develop alternative materials due to high prices of petroleum sources (Bouchet et al., 2013). The suitability of biopolymers has been reported in several studies of electrical energy storage devices (Jamaludin & Mohamad, 2010; Shukur et al., 2014a; Liew & Ramesh, 2015).

In this work, a PE system of methylcellulose (MC)-potato starch (PS) as polymer host, NH_4NO_3 as ionic provider and glycerol as plasticizer has achieved the requirements to be used in protonic cells and supercapacitors. The requirements are (Mukoma, Jooste & Vosloo, 2004; Kadir, 2010):

- High ionic conductivity (10^{-3} S cm^{-1}).
- Flexible.
- Thermally stable. The highest conducting electrolyte is thermally stable up to 150 °C which is obtained via TGA analysis.
- Electrically stable. Potential stability of 1.88 V has been achieved at room temperature.
- Miscibility. MC and PS miscibility has been checked via DSC and FESEM analysis. Single value of glass transition temperature (T_g) has been detected as well as no phase separation in the cross-section of MC-PS blend host.
- Ease of fabrication. Solution cast method is one of the simplest methods to form an electrolyte film.
- Good proton transference number. The cation transference number of the highest conducting electrolyte has been obtained as 0.40 using Watanabe method.

It is crucial to explain the choice of MC and PS as the polymer host for the electrolyte. MC and PS have been chosen due to:

- Cellulose/starch host possesses high ionic transference number and mobility (Abd El-Kader & Ragab, 2013).
- MC-PS starch based blend achieves higher conductivity compared single polymer system (Khiar & Arof, 2010; Shuhaimi, 2011).
- Excellent mechanical strength of cellulose/starch based polymer blend (Babu et al., 2014).

- The two polymers are miscible to one another (Miyamoto et al. 2009).

Due to reasons mentioned above, MC and PS have been selected to act as polymer host for the conduction of ions.

In this work, those materials were dissolved in 1% acetic acid solvent. It has been reported that using acetic acid based solvent can enhance the mechanical strength and functional properties of a polymer (Prokhorov et al., 2016). In this work, starch was dissolved at ~ 80 °C. It has been reported that 80 °C is the optimum temperature to activate the molecule of starch thus improving the rate of reaction by gelatinization (Diop, Li, Xie & Shi, 2011). As amylose and amylopectin of starch granule possess semi-crystalline structure which requires high energy to disrupt, it is crucial for the starch granules to experience the gelatinization (Wang, Li, Niu & Wang, 2015).

Salt is made up of positively and negatively charge ions which are held together by force of attraction or called as ionic bond. The strength of this bond can be estimated by knowing the lattice energy. It has been known that salt with low lattice energy requires less salvation (Husin & Tahir, 2018). Salt with smaller lattice energy provides higher conductivity value (Hema et al., 2009). Ammonium nitrate (NH_4NO_3) possesses low lattice energy of 648.9 kJ mol^{-1} compared to other ammonium salt e.g. for ammonium acetate ($NH_4CH_3CO_2$), ammonium sulfate ($(NH_4)_2SO_4$ and ammonium phosphate ($(NH_4)_3PO_4$) are 703.1, 1754.7, and 3334.0 kJ mol^{-1}, respectively (Kadir, 2010). Lattice energy for ammonium bromide (NH_4Br), ammonium chloride (NH_4Cl), ammonium fluoride (NH_4F) is 682.0, 708.0 and 834.0 kJ mol^{-1}, respectively (Jenkins & Morris, 1976). Low lattice energy salt provides more free ions to be used in the intercalation/deintercalation process at the electrode of protonic cell and polarization at

the electrode of supercapacitors. Hence, NH_4NO_3 has been selected to be doped in the polymer blend host for ionic conduction.

Confirmation on the best ratio for MC-PS blend has been done via several characterizations in Chapter 4. Raw data of XRD patterns has been deconvoluted to observe the changes in the crystalline and amorphous peaks position and intensity. Gaussian fitting was employed to separate these peaks. It is found that amorphous peak has suppressed the crystalline peaks for the blend of 60 wt.% MC and 40 wt.% PS (A6). This portrays the interaction and miscibility between PS and MC. A6 possesses the lowest degree of crystallinity (χ_{crys}) compared to other ratio showing that blending polymers creates more amorphous regions. FESEM shows that cross-section of A6 blend has no phase separation and higher structural integrity than pure PS film. This result confirms the miscibility and compatibility of this ratio. Surface of A6 is consisted of small spherical structure that acts as a room for ions of NH_4NO_3 to be filled and undergo ionic migration (Moura & Azeredo, 2012).

Based on TGA analysis, by blending PS and MC, the decomposition of the polymer blend (A6) is located at 280 °C. In Figure 4.9, PS experiences 35% weight loss while 80% for MC. By blending the polymers, the weight loss for A6 is ~ 53% which is lower than MC. These results strengthen the fact that the addition of MC to PS based film improves the thermal stability of PS film. From DSC analysis, the T_g for PS and MC are 164.8 °C and 118.0 °C, respectively. These results are comparable with other starch and MC studies (Gomez-Carracedo, Alvarez-Lorenzo, Gomez-Amoza & Concheiro, 2003; Graaf, Karman& Janssen, 2003). For A6 blend, the T_g is observed at 132.7 °C which located in between the T_g of single polymers. This signifies the combination of MC and PS characteristics in the polymer blend. The change in T_g is due to formation of

hydrogen bonding between the polymers which has been verified by FTIR analysis in Chapter 5. DSC thermogram of selected polymer blends consist only a single T_g. This result has confirmed the miscibility between MC and PS. The theoretical value of T_g was obtained using Fox equation. It is found that there is 0.3% percentage difference between theoretical and experimental T_g value which shows that the T_g is reliable. Hence, A6 is chosen as the polymeric network for ionic conduction.

Polysaccharides like MC and PS are composed of repetition units of monosaccharides which connected by glycosidic linkages (C-O-C) (Kamdev, 2015). MC possesses oxygen containing functional groups such as hydroxyl (OH), C-O-C and methoxy (OCH_3) while PS has oxygen of OH and C-O-C. These oxygen atoms serve lone pair electrons for cations from NH_4NO_3 to site (Biswal & Singh, 2004; Follain, Joly, Dole & Bliard, 2005). FTIR analysis in Chapter 5 shows that MC and PS has formed hydrogen bonding as the shape, position and intensity of peaks have been changed. As 30 wt.% NH_4NO_3 was added to MC-PS blend, the glycodisic linkages peak has shifted from 946 to 942 cm^{-1}. At the region between 3000 and 3600 cm^{-1}, three peaks have appeared as NH_4NO_3 was added. According to Kadir et al. (2011), this is due to overlapping between OH, asymmetry vibration ($v_{as}(NH_4^+)$) and symmetry vibration ($v_s(NH_4^+)$). Thus, in order to separate these peaks, deconvolution method was done. OH peak has shifted from 3428 to 3415 cm^{-1} as 30 wt.% NH_4NO_3 was doped. This verifies the complexation of NH_4^+ with polymer matrix through dative bond. Coordinate covalent bond or dative bond is when two electrons are derived from the same atom which in this case oxygen atoms (Le Tourneau, Birschm, Korbeck & Radkiewicz-Poutsm, 2005). No shifts or change in intensity are observed for OCH_3 portraying no or less interaction in these regions. The fact that addition of plasticizer

promotes more free ions can be observed as the peaks of OH, glycosidic linkages and ring's oxygen have shifted to lower wavenumber.

In Chapter 6, it is shown that the addition of 30 wt.% NH_4NO_3 has increased the conductivity of MC-PS based electrolyte from $1.04 \pm 0.19 \times 10^{-11}$ S cm^{-1} to $(4.35 \pm 0.16) \times 10^{-5}$ S cm^{-1}. It is well known that polymer blend provides more sites for salt coordination thus yield higher conductivity compared to single polymer (Yusof et al., 2014). The ionic conductivity of MC-PS-NH_4NO_3 in this work is higher than MC-NH_4NO_3 (Shuhaimi, 2011) and starch-NH_4NO_3 (Khiar & Arof, 2010). The conductivity has improved to $(1.26 \pm 0.1) \times 10^{-3}$ S cm^{-1} with the addition of 40 wt.% glycerol. The inclusion of salt and plasticizer provides positive and negative charge carriers for ionic conduction. From impedance analysis, capacitance of the electrolyte is observed to increase as NH_4NO_3 and glycerol are added. The electrode polarization has increased due to increase in ionic number density.

The impregnation of glycerol has changed the ionic conduction mechanism from Arrhenius to Vogel-Fulcher-Tammann type. Plasticizer promotes the polymeric network to become more flexible thus it is possible for ionic mechanism to change (Alves et al., 2016). The conductivity trend is further verified by transport analysis. This has been done using Arof-Noor impedance method (Arof et al., 2014). It was found that the addition of 30 wt.% NH_4NO_3 and 40 wt.% glycerol enhanced the ionic number density (n) to 1.17×10^{19} cm^{-3} and 2.15×10^{19} cm^{-3}, respectively. The maximum ionic mobility (μ) of the electrolyte is achieved at 3.24×10^{-4} cm^2 V^{-1} s^{-1} with 40 wt.% glycerol. The conductivity is strongly dependent on the changes in n and μ value where it can be explained via this equation:

$$\sigma = ne\mu \tag{9.1}$$

here e is the electronic charge. The drop in conductivity of both salted and plasticized electrolytes is consistent with the drop in the value of n and μ. Excess salt leads to the development of salt recrystallization while excess glycerol promotes self-linking among the plasticizer. Both conditions reduce the free ions in the PE, thus reducing the ionic number density and mobility (Andrade et al., 2009).

The conductivity and transport properties have increased with the increase in temperature. The polymer chains vibrate as the temperature increases. This phenomenon creates small spaces in the vicinity of the polymer structure which resulting in the increment of free volume. The free volume is utilized by ion pairs to form free ions for ion conduction process (Noor, 2016). Simultaneously, ions can easily migrate from one polymer chain to another and undergo transient interaction with the functional groups of the polymers host. This phenomenon enhances the segmental motion of the polymer chains thus assist the ions to hop to neighboring polymer chains (Koduru et al., 2017). High temperature also assists in breaking the ionic bond between anions and cations of the salt thus forming more free ions (Aziz et al., 2018). The ionic mobility and diffusivity improve as more ions are available for conduction process hence improving the ionic conductivity.

Dielectric studies show that addition of glycerol has increased the value of dielectric constant (ε). This is a verification of plasticization effect has occurred in the electrolytes. Glycerol has high ε of 42.5 thus providing more ionic dissociation which leads in ionic conductivity increment (Bibi, Villain, Guillaume, Sorli & Gontard, 2016). ε value of glycerol is higher than several other plasticizer e.g. dimethylacetamide (37.8)

and ethylene sulfite (39.6) (Kumar & Sekhon, 2012; Azli, Manan & Kadir, 2015). For acetonitrile, polyethylene glycol (PEG-200) and dimethyl carbonate, the values of ε are 36.0, 19.95 and 3.2, respectively (Shuhaimi, 2011; Daniels, Wang & Laird, 2017).

Plasticizer-polymers compatibility is a crucial parameter for an electrolyte. Glycerol has been reported to be compatible with MC and starch (Shukur, 2015; Amran et al., 2016; Salleh et al., 2016; Yusof, 2017). As pointed out by Speight & Speight (2002), glycerol possesses boiling and melting point at 290 °C and 18 °C, respectively. Low melting point and high boiling point avoid solidification, melting and boiling of glycerol in the temperature range of this work. Other than polymeric network, the structure of glycerol is rich in hydroxyl moiety thus provide different pathway for H^+ and NH_4^+ conduction (Gondaliya et al., 2013). From electrical modulus analysis the relaxation time (t_{Mi}) is determined. Relaxation time denotes as the time for ions to migrate from one site to another (Aziz et al., 2010). Hence, shorter t_{Mi} is preferable for fast ionic conduction. Hence, t_{Mi} is related to the ionic conductivity value (Suthanthiraraj, Kumar & Paul, 2011).

The ionic (t_i), electronic (t_e) and cation (t_c) transference numbers are crucial parameters for electrolyte studies. t_i is determined using DC polarization method where C4 is placed in between two stainless steel (SS) electrodes. An ionic conductor will portrays a drastic drop of current at the initial seconds due to ionic-blocking effect of SS (Wagner & Wagner, 1957). Only electron can pass through the SS electrodes. The values obtained for t_i and t_e are 0.98 and 0.02, respectively for C4 electrolyte. This signifies that ions are the primary charge carriers. It is important to monitor the contribution of proton (H^+) in the electrolyte because H^+ ion are the one responsible for the process of intercalation and deintercalation in a protonic cell. The value of t_c is

obtained by sandwiching C4 in between two manganese oxide electrodes via Watanabe method (Watanabe et al., 1988). The value of t_c for C4 is 0.40. This measurement gives an idea on the ionic transportation even though it could be affected by dissociation of ions.

The protonic conduction is further proven by conducting comparative cyclic voltammetry (CV) analysis. Most common anode materials used in protonic cells is a mixture of zinc and zinc sulphate (Samsudin et al., 2014; Shukur, 2015; Yusof, 2017; Alias et al., 2017). As referred to Equation (6.16), zinc sulphate will produces H^+ ions during discharge process of the protonic cell. Hence to make a comparison, C4 is placed in between two zinc + zinc sulphate and stainless steel electrodes. Cell with zinc + zinc sulphate electrodes shows the anodic and cathodic peaks in the CV plot which signifies the stripping and plating of H^+ ions at the electrode's surface (Sellam & Hashmi, 2012). No peaks are observed for the cell with SS electrodes. The conduction of proton is proven with the presence of anodic and cathodic peaks where these peaks are correlated to the process of oxidation and reduction at the interfaces (Kumar & Hashmi, 2010; Munichandraiah et al., 1995).

Decomposition temperature of the polymer blend is changed with the presence of salt and plasticizer which can be referred to TGA analysis of salted and plasticized electrolyte in Chapter 7. The first stage of degradation at less than 120 °C is usually due to unbound water (Andrade et al., 2009). Well known characteristic of polysaccharides is hydrophilic due to the existent of polar functional groups in the polymeric network (Kumar, Pandey, Raj & Kumar, 2017). The addition of NH_4NO_3 and glycerol has decreased the decomposition temperature to 180 °C and 150 °C, respectively. More weight loss is observed as more salt is added. More ions are available to form dative

bond with polymer matrix thus resulting in higher weight loss. The third degradation at ~ 280 to 300 °C is due to the decomposition of MC-PS blend as referred to Figure 4.9 in Chapter 4. As stated by Sanyang et al. (2015), salt and plasticizer interacted with the polymeric network which disturbs the hydrogen bonding between polymers thus the polymer chains become less rigid. Hence the decomposition temperature of the PE reduces as the polymer chain has become more flexible. DSC analysis showed that the value of T_g decreases to -27.5 °C indicating that the presence of glycerol provides more flexibility. These conditions have been verified using FTIR analysis in Chapter 5 where the interactions between molecules of NH_4NO_3 and glycerol with MC-PS blend have been detected through the shifting of OH, C-O-C and methoxy peaks. The result from TGA analysis proves that the highest conducting electrolyte (C4) is thermally stable for the electrical energy storage applications.

XRD and FESEM analysis are used to further check the compatibility of the electrolytes as demonstrated in Chapters 5 and 7, respectively. Raw XRD data has been deconvoluted due to the existent of overlapping peaks. The addition of NH_4NO_3 up to 30 wt.% has increased the amorphousness of the electrolyte where all crystalline peaks in the polymer blend have been suppressed. The highest conducting salted electrolyte (B6) holds the lowest degree of crystallinity (χ_{crys}) of 13.46. This is attributed to the increment of ions-polymer interaction due to enhancement of flexibility of the polymeric backbones which in turns improve the segmental motion. Rapid segmental motion assists the charge carriers to migrate thus increasing the ionic conductivity (Ahmad & Isa, 2015). This result is harmonized with FESEM images where uniform complex formation which can be considered as ion traps. These ion traps filled the room or space provided in the FESEM of A6 blend as shown in Figure 4.8 in Chapter 4. It is verified that more ions is available for ionic conduction as 30 wt.% NH_4NO_3 is added

where more formation of ion traps can be observed in Figure 7.7. As the concentration of NH_4NO_3 exceeded 30 wt.%, the XRD patterns show sharp and narrow peaks correspond to the peaks of pure NH_4NO_3 at 2θ = 28.8°, 32.9° and 39.9°. The space in the polymeric network is overcrowded at high concentration of salt which promotes the recrystallization of salt (Liu, Saikia, Ho, Chen & Kao, 2017). FESEM analysis provides the evidence of salt recrystallization where sharp solid structure is protruded out of the surface of the electrolyte as more than 30 wt.% NH_4NO_3 is included. Recrystallization of salt reduces the amount of free ions for ionic conductions process. This result is consistent with the result in Figure 6.12(b) where the ionic number density has been decreased beyond 30 wt.% NH_4NO_3. Thus leads to decrease in ionic conductivity. According to Aziz et al. (2017) the crystal solid on the electrolyte surface is due to formation of ion pairs and recrystallization of salt that reduces the conductivity value.

One crystalline peak disappears and other crystalline peaks have been surpressed with the presence of 40 wt.% glycerol (C4) as shown in Figure 5.4. This indicates that glycerol assists in improving the interaction between NH_4NO_3 and polymer blend (Amran et al., 2016). A drastic surface modification can be observed with the addition of glycerol where the ion traps have been disappeared. The surface also become denser with the presence of 40 wt.% glycerol. Furthermore, C4 has the lowest χ_{crys} value of 8.86. As mentioned earlier, glycerol has high dielectric constant (42.5) thus avoiding the recombination of ions which indirectly increases the ionic mobility and number of free ions (Mattos et al., 2012). This result tallies with the one in Figure 6.13(a) and (b), where addition of 40 wt.% glycerol has increased the ionic number density and mobility, respectively. The intensity of crystalline peaks has increased back as well as the value of χ_{crys} when the concentration of glycerol is beyond 40 wt.%. From Figure 7.15, it is found that there are formation of craters on the surface of the electrolyte as

50 wt.% glycerol is added. Sudhakar and Selvakumar (2013) stated that different size of crates results in different driving force which may decrease the ionic conductivity. These craters obstruct the migration of mobile ions in the electrolyte. During transportation process, ions have to overcome higher energy barrier with the existent of craters (Latif & Aziz, 2013). The phenomenon is consistent with the result from Table 6.5 in Chapter 6 where the activation energy increases as the concentration of glycerol surpassed 40 wt.%.

Lithium ions-based conductors are well known separator used in electrical energy storage devices due to its high energy density and conductivity (Xu, 2004). However, lithium-based energy devices industry has experienced several safety issues e.g. explosion of cell phones and aircraft energy backup system (Williard, He Hendricks & Pecht, 2013). Bouchet et al. (2013) reported that volatile solvent in lithium based electrolytes makes the price become expensive, occurrence of corrosion, leakage and harder to handle. Thus, PEs have been extensively used to overcome this kind of obstruction. Most common solvent and negative electrode used in commercial lithium ion cell is a mixture of ethylene carbonate (EC) with diethyl (DEC) or dimethyl carbonate (DMC) and carbon based electrodes, respectively. This solvent tends to form solid electrolyte interface (SEI) at the surface of carbon which increase the resistance of the cell and indirectly releases more heat. The electrolyte becomes very flammable with the presence of carbonate (Mauger & Julien, 2017). Alkaline cell is one of other options to replace lithium ion-based cells. Dell (2000) pointed out that during charge/discharge process of alkaline cell there is a development of intermediate particles which cause leakage and corrosion. This problem has attracted researchers and users to find other alternative.

Hydrogen ion (H^+) or protonic based ionic conductor is well known as other option to be employed in electrical energy storage devices (Jamaludin & Mohamad, 2010; Alias et al., 2017). The ionic radii of H^+ and Li^+ are 0.84×10^{-15} m and 0.90×10^{-10} m, respectively. Due to smaller ionic radius, H^+ ions can be intercalated easily into cathode's layer (Antognini et al., 2013). Typically Li^+ ion-based electrolyte has higher electrochemical stability (~ 4 V) than H^+ ion based electrolyte (~ 1 to 2 V) (Rani et al., 2016; Li et al., 2017). However, materials for protonic cell are less expensive than lithium cell. Common cathode material used for protonic cell is manganese (IV) oxide (MnO_2) (Bansod et al., 2007; Alias et al., 2017). MnO_2 is cheaper than lithium cobalt oxide ($LiCoO_2$), lithium manganese nickel oxide ($LiMn_3NiO_8$) and lithium manganese oxide ($LiMn_2O_4$). According to Belanger, Brousse and Long (2008), MnO_2-based cell possesses low toxicity compared to nickel oxide and cobalt oxide based cells.

Potential stability is a crucial parameter for an electrolyte which needed to be checked before the employment in electrical energy storage devices. LSV has been conducted to identify the potential window for the highest conducting electrolyte (C4). At 298 K, the current is observed to be stable up to 1.88 V indicating that C4 can be used in the construction of protonic cell and supercapacitors. The decomposition voltage has been reduced to 1.50 V at 343 K. Ng and Mohamad (2008) stated that decomposition voltage is dependent on the temperature. Despite the reduction at high temperature, C4 electrolyte still can be employed in the fabrication of energy devices because the minimum requirement for protonic based devices is ~ 1 V (Pratap et al., 2006).

The fabricated protonic cell is consisted of MnO_2 as cathode, C4 as the separator and mixture of zinc and zinc sulphate as anode. The open circuit potential (V_{oc}) of the

fabricated protonic cell has been tested for 24 hours at 298 K, 313 K, 333 K and 343 K. Typically the initial potential drops at initial hours is due to oxidation of zinc electrode (Samsudin et al., 2014). According to Nyuk and Isa (2017), the decrement of potential at initial time is attributed to the self-discharged of the protonic cell. The value of V_{oc} for 298 K is stabilized at 1.52 V until 24 hours. It is evidence that the components of electrode hold catalytic behavior at low temperature as the V_{oc} decreases to 1.46 V at 343 K (Ng & Mohamad, 2008). From theory the cell should have V_{oc} value of 1.28 V. The difference between theoretical and experimental V_{oc} is expected as several other parameters e.g. ionic transportation and concentration have been included (Botte & Muthuvel, 2012).

Various constant currents (2, 3 and 4 mA) have been used to test the protonic cell at room temperature. The protonic cells achieved stable discharge process at ~ 1.0 V and drastically dropped to ~ 0 V after a certain time. The extreme potential reduction is due to the growth of semiconductor particle from the electrode's materials (Mn_2O_3-ZnO). This semiconductor material is considered to increase the charge transfer resistance which leads to the decrement of potential (McComsey, 2001; Wang et al., 2005; Rahman et al., 2013). It is noticeable that the capacity (Q) of the protonic cell is higher at low constant current. A rapid reaction is needed if high constant current is applied. However, charge transfer cannot achieve the required rate which results in low H^+ ion diffusion rate. This condition may fail the electrical energy delivery (Roscher et al., 2011; Samsudin et al., 2014).

The protonic cell has been discharged at various working temperature from 298 K to 343 K with a constant current of 3 mA. The discharge time of the protonic cell at 298 K and 343 K are 9 hours and 14 hours, respectively. The value of Q is observed to

increase from 27 mA h to 42 mA h as the temperature elevates from 298 K to 343 K. At low temperature, fewer ions are available for the conduction process compared to high temperature thus delivers lower value of Q. As an evidence in Chapter 6 (Figure 6.16), the ionic number density (n) and mobility (m) increases at higher temperature. At high temperature, more ions can be conducted towards the cathode and undergo intercalation/deintercalation process thus produces a high value of Q.

Current-voltage (I–V) and current density-power density (J–P) characteristics illustrate that the protonic cell has the value of internal resistance (r) and maximum power density (P_{max}) of 26 Ω and 7.91 mW cm^{-2}, respectively. The short circuit of the protonic cell in this work is 39 mA at 298 K which is comparable to other works (Kadir, 2010; Shukur, 2015). As the temperature elevates to 343 K, the value of r drops to 17 Ω. An excellent electrode/electrolyte contact can be achieved with low value of r. Thus the value of r in this work is considered low if compared to other protonic cell studies (Subban & Arof, 1995; Kadir, 2010; Shukur, 2015; Yusof, 2017). The value of P_{max} is enhanced to 13.5 mW cm^{-2} at 343 K. Ng and Mohamad (2008) reported that the value of r and P_{max} increases with temperature. Hence it can be concluded that the cell performance can be improved when the temperature is elevated.

The circuit of a cell or battery is shown in Figure 9.1(a). Typically, all cell or batteries possess an internal resistance which could be due to the resistance of the electrolyte and electrolyte-electrode gap (Chen et al., 2016). The potential difference of a cell is known as terminal voltage which can be expressed as:

$$V_{xy} = emf - ir \tag{9.1}$$

here V_{xy} is the terminal voltage from point x to y as shown in Figure 9.1. *emf* or electromotive force is the energy per unit charge due to chemical reaction. i is the current and r is the internal resistance. Based on Equation (9.1), V_{xy} is equal to *emf* or V_{oc} when there is no current flow. If the cell is connected to an external circuit with load resistance (R_{load}) as shown in Figure 9.1(b), the value of V_{xy} will be decreased (Singal, 2013).

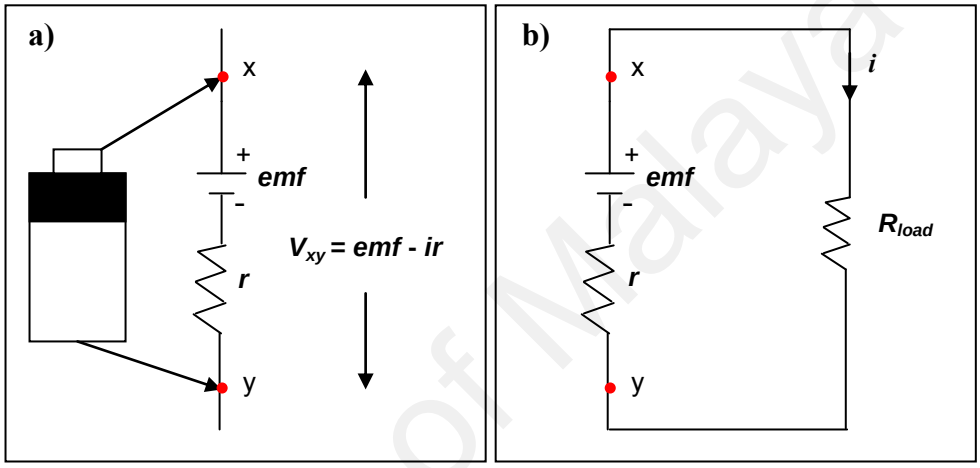

Figure 9.1: Illustration of the cell circuit a) without and b) with current flow.

The charge-discharge profile of the protonic cell has been conducted at two constant currents e.g. 1 mA and 4 mA for 15 complete cycles. These complete charge/discharge plot proves that H^+ ions from the electrolyte have been intercalated and deintercalated from the layer of MnO_2 electrode. The cell is discharged and charged to 1 V and 1.50 V, respectively. It takes 60 hours to complete 15 cycles with 1 mA current while 8 hours at 4 mA. The value of specific capacity (Q_{spe}) is calculated with respect to the weight of active material which is MnO_2. Q_{spe} value for both constant currents is observed to decrease at the 2nd cycle which could be due to the poor contact between electrode and electrolyte at the initial stage of charge-discharge (Mohamad et al., 2003). Cell with constant current of 1 mA achieved stabilization at 1.2 mAh g^{-1} up to 12th cycle and drop

to 0.8 mAh g^{-1} until 15th cycle. At 4 mA current, the Q_{spe} at the 1st cycle is 18.2 mAh g^{-1} which then drops to 2.3 mAh g^{-1} at the 2nd cycle. The cell is stabilized at 0.27 mAh g^{-1} up to cycle of 15. Shukur (2015) reported the same phenomenon for the protonic cell with chitosan-starch-NH_4Cl-glycerol system at 0.35 mA where the Q_{spe} drops from 6.13 mA h g^{-1} to 2.76 mA h g^{-1} at the 2nd cycle. It is noticeable that the Q_{spe} at the 1st cycle is lower than the one obtained in this work. This is could be to lower lattice energy of NH_4NO_3 (648.0 kJ mol^{-1}) compared to NH_4Cl (663.0 kJ mol^{-1}) (Buraidah & Arof, 2011). Lower lattice energy salt provides more ions for the intercalation/deintercalation process thus providing higher value of Q_{spe}. Vanadium pentoxide (V_2O_5)-based protonic cell reported by Mishra et al. (2014) possesses V_{oc} of 1.45 V which is lasted for 24 hours. The authors also stated a drastic capacity drops after the 1st cycle (240 μA h g^{-1}) and consistent up to 10 complete cycles at current of 10μA. The Q_{spe} and charge-discharge cycle number are lower compared to this study which is due to the use of V_2O_5 as the cathode instead of MnO_2. According to the work by Alias et al. (2017), MnO_2-based protonic cell possesses higher Q_{spe} and V_{oc} than the one with V_2O_5. Due to the mechanical stress during charge-discharge process, V_2O_5 experienced structural alteration which reduces the specific capacity (Fergus, 2010; Alias et al., 2017). Mohamad et al. (2003) stated that it is possible to achieved better electrode/electrolyte contact during charge-discharge process thus stabilization can be obtained at some cycles. The interfacial resistance between electrode and electrolyte is known to develop during the charge discharge process. This phenomenon could be the reason of reduction of Q_{spe} value (Selvasekarapandian et al., 2010).

C4 is placed in between two activated carbon electrodes for the construction of the EDLC. The capacitance and reliability of the EDLC are studied using CV analysis. Various scan rates have been applied during CV analysis from 2 to 20 mV s^{-1}. The CV

plot of the EDLC possesses no peak correspond to redox reaction process. This indicates the formation of double-layer in the EDLC (Liew & Ramesh, 2015). It is well known that the mechanism of charge storage for the EDLC is based on non-Faradaic process. In non-Faradaic process, ions from the PE are adsorbed onto the surface of the activated carbon electrodes (Iro, Subramani & Dash, 2016). The shape of the CV plot turns to almost rectangular shape at low scan rate. CV plot is altered to leaf shape as the scan rate is increased which is due to the void or porous in the carbon structure and internal resistance. This leads to current dependence of voltage (Kadir & Arof, 2011). It is found that the value of specific capacitance (C_s) is higher at low scan rate. Teoh et al. (2014) pointed out that ions can properly migrate and form double-layer or polarized at the surface of the carbon electrodes at low current density. Distribution of ions concentration at the electrodes is varied at fast rate for high scan rate thus reducing the value of C_s.

The rechargeability of the EDLC is analyzed from 0 V to 0.85 V at 0.2 mA cm^{-2}. The shape of charge-discharge plot in Figure 8.9 is almost a triangle shape with almost linear discharge slope. Sampathkumar et al. (2019) explained that the linearity of the discharge slope signifies the existent of capacitive characteristic in the EDLC. The value of C_s for the 1st cycle is 31 F g^{-1} which later drops to 24 F g^{-1} at 24th cycle. The EDLC achieves stabilization at 21 to 22 F g^{-1} until 1000th cycles. This value is almost the same with the one from CV analysis which is 20.48 F g^{-1}. Hence, the value of C_s for the fabricated EDLC in this work is reliable. Yusof (2017) reported a corn starch-chitosan-NH_4I-glycerol based EDLC at 0.04 mA cm^{-2} current density with C_s of 5.24 F g^{-1} at the 1st cycle and consistent at 1.82 F g^{-1} up to 50 cycles. In EDLC, cations are pulled towards negatively charge electrode while anions to positively charge electrode. Iodide (I^-) ion has ionic radius of 220 pm while nitrate (NO_3^-) ion is 179 pm (Jenkins &

Thakur, 1979). The mobility of an ion in a medium will decrease as the size increases (Shukur et al., 2013b). Hence, it is harder for I^- ion to migrate towards the electrode to form double-layer compared to NO_3^-. The EDLC experiences a constant coulombic efficiency (η) of ~ 90 to 94 % for 1000 cycles. High and stable coulombic efficiency portray good cycling stability and electrode/electrolyte contact (Stoller & Ruoff, 2010; Winie et al., 2018). A good EDLC must have a low equivalent series resistance (ESR) for better contact between electrode and electrolyte. The value of ESR for the EDLC is ranging from 24 Ω to 64 Ω. As referred in the work by Asmara et al., (2011), ions are expected to experience easier migration process towards the electrode if the ESR value is low. Shuhaimi (2011) reported a MC-NH_4NO_3-polyethylene glycol based EDLC with ESR of 109.1 Ω at 0.22 mA cm^{-2}. This result is higher compared to our result. As mentioned earlier, the dielectric constant of PEG-200 (19.95) is lower than glycerol (42.5) thus providing less free ion. Low number of free ions increases the bulk resistance of the electrolyte. This phenomenon has been verified from impedance and transport analysis in Chapter 6. Furthermore, Shuhaimi (2011) only used single polymer host (MC) instead of polymer blend host. Polymer blend possesses more complexation site for ionic migration. According to Arof et al. (2012), resistance of the electrolyte is one of the factors contributing in the ESR of the EDLC. Other important parameters of the EDLC are energy (E) and power density (P). The value of E for the 1st cycle is 3.1 Wh kg^{-1} and stabilized at ~ 2.2 to 2.3 Wh kg^{-1} up to 1000 cycles. The growth of internal resistance can be the reason of E reduction (Wei et al., 2005; Wang et al., 2016). The stable value of energy density explains that ions experience almost the same energy barrier during transportation to the surface of the electrodes. A reduction of P from 910 to 385 W kg^{-1} could be due to development of ionic aggregation which lessens the adsorption of ion at the surface of the carbon electrodes (Huo et al., 2019).

CHAPTER 10: CONCLUSIONS AND FUTURE IMPROVEMENTS

10.1 Conclusions

Through solution cast technique, three systems were successfully prepared. The systems include methylcellulose (MC)-potato starch (PS), MC-PS-NH_4NO_3 and MC-PS-NH_4NO_3-glycerol. The confirmation on polymer blend's composition was decided based on several characterization results including:

- Polymer blend with 60 wt.% MC and 40 wt.% PS (A6) was identified as the most amorphous blend from XRD analysis.
- Higher structural integrity and no phase separation were observed for the cross-section of A6 blend which portrayed the miscibility behavior between MC and PS.
- TGA results have showed that the weight loss of A6 is lower than pure MC and the decomposition temperature of A6 is higher than the pure PS. Thus it can be concluded that the thermal stability has been improved by blending MC and PS.
- Single T_g value of A6 and the value fall in between the T_g value of pure polymers confirmed the miscibility of MC and PS.
- Molecular level interactions e.g. hydrogen bonding between MC and PS have been revealed using FTIR analysis.

For salted electrolyte, the systems achieved the maximum conductivity of $(4.35 \pm 0.16) \times 10^{-5}$ S cm^{-1} with the incorporation of 30 wt.% NH_4NO_3 (B6) which can be explained from these several reasons:

- The amorphousness of the electrolyte has improved with addition of NH_4NO_3 thus provided higher conductivity where low value of T_g and degree of crystallinity were obtained.

- The inclusion of NH_4NO_3 has enhanced the ionic mobility, diffusion and number density which indirectly improved the conductivity value.

- Low value of lattice energy for NH_4NO_3 (648.9 kJ mol^{-1}) offered easier process of dissociation.

- Salted electrolytes were found to follow Arrhenius theory from high temperature conductivity study.

- Energy barrier in the electrolyte was found to decrease as the addition of NH_4NO_3 reduced the value of E_a.

The plasticization effect can be observed as the inclusion of 40 wt.% glycerol has optimized the conductivity value up to $(1.26 \pm 0.1) \times 10^{-3}$ S cm^{-1}. The conductivity enhancement could be due to several reasons such as:

- Alternative pathways for ions to conduct due to OH rich structure of glycerol.

- Efficient dissociation of salt due to high dielectric constant (42.5) of glycerol. Thus more ions are created and higher dielectric constant for the PE has been achieved.

- Transport analysis results have revealed that the addition of glycerol has increased the ionic number density, diffusion and mobility.

- The ionic conduction has been altered to Vogel-Fulcher-Tammann theory which portrayed the improvement of flexibility as the glycerol is added.

- The presence of glycerol has reduced the value of degree of crystallinity and T_g which resulted in higher amorphousness.

Furthermore, the ionic conductivity enhancement due to addition of NH_4NO_3 and glycerol has been evaluated using FTIR analysis. Interaction at OH and glycosidic linkages of the polymer blend is detected as the peak's shape, intensity and position have changed with addition of NH_4NO_3. The addition of glycerol has helped more ions to dissociate as the peak's position, shape and intensity of OH and glycosidic lingkages have changed. The ionic and cation transference number of C4 electrolyte were obtained as 0.98 and 0.40 from transference number study. Proton conduction has been further proved with the presence of anodic and cathodic peaks in the comparative CV analysis. LSV analysis result has exposed that the decomposition voltage for C4 electrolyte at 298 K was at 1.88 V.

The V_{oc} of the protonic cell was stable at ~ 1.52 V for 24 hours. The discharge capacity of the protonic cell was found to increase as the constant current decreased. The protonic cell achieved discharge capacity at 33 mA h for 1 mA. The capacity and V_{oc} were found to be dependent on temperature. At 298 K, the internal resistance, power density and short circuit current of the protonic cell were 26 Ω, 7.91 mW cm^{-2} and 39 mA, respectively. The rechargeability of the protonic cell has been analyzed with 1 mA and 4 mA for 15 cycles. The charge-discharged process took 60 and 8 hours for 1mA and 4 mA, respectively. The capacitance for the EDLC from CV was 20.48 F g^{-1} while from charge-discharge characteristic was found to stabilize at ~ 21 to 22 F g^{-1}.

The EDLC was stable for 1000 cycles with coulombic efficiency of ~ 90 to 94 %. The equivalent series resistance, power density and energy density for the EDLC at the 1st cycle were 24 Ω, 910 W kg^{-1} and 3.1 Wh kg^{-1}, respectively.

10.2 Thesis Contributions

The motivation of this thesis is to develop a polymer electrolyte (PE) using biodegradable polymers matrix as well as construction of compatible and reliable electrical energy storage devices. No work has been reported on MC-PS-NH_4NO_3-glycerol electrolyte based protonic cell and EDLC. Hence, this work contributes on the effort of improving the knowledge on bio electrical storage technologies. The characterizations of the electrolyte in this study may provide some guidelines or information for design of the electrical energy storage technologies in the future.

10.3 Future Improvements

Few methods can be applied to improve the electrical, thermal and chemical properties of the electrolyte in future including:

- Copolymers grafting is one of the method to increase the free volume that aids in the conduction of ions. It can be done by grafting low molecular weight polymer to the backbones of other polymers (Zhang et al., 2018).

- Applying gamma irradiation method to the PEs. This method helps in improvement of ionic dissociation thus provides more free charge carriers (Rahaman et al., 2014).

- Improving the ionic conductivity by method called dual-salt system. Two ionic sources are included to eliminate the aggregation of ion thus enhances the ionic number density (Li et al., 2018).

- The structure of the electrolyte can be altered to improve ionic conduction with the presence of inorganic filler. The filler complexes with oxygen atom of the polymer which reduces the T_g value (Maragani & Kumar, 2017). The filler includes zirconium dioxide (ZrO_2), titanium dioxide (TiO_2) and Silicon dioxide (SiO_2) (Sheng et al., 2017).

The performance of the EDLC and protonic cell can be improved in the future with several methods including:

- To improve cycle stability or capacitance of the EDLC, various modifications of carbon-based nanostructure electrodes can be built e.g. graphene, carbon fibers and carbon nanotube (Liu et al., 2017).

- Introducing the metal–organic frameworks (MOFs) to EDLC. This method is done by including the metal oxide in the electrodes to improve the surface area and capacitance (Jiao et al., 2017).

- Preparation of electrodes for the protonic cell by dissolving the electrode materials in a solvent and use coating technique instead of pellets.

- Using mixture of manganese (IV) oxide with other materials such as lead oxide (Chen et al., 2013), vanadium (IV) oxide (V_2O_5) (Wang et al., 2015) and vanadium (III) oxide (V_2O_3) (Morales et al., 2006) as the cathode for the protonic cell.

The highest conducting electrolyte can be employed in other electrochemical energy devices such as:

- Dye sensitized solar cells (DSSCs). Sugumaran et al. (2019) reported a DSSC with PE system based on carreegenan, NaI and 1-butyl-3-methylimidazolium iodide. Arof et al. (2017) fabricated a DSSC using PE consisted of double salt i.e. lithium iodide (LiI) and tetrapropyl ammonium iodide (TPAI).

- Polymer electrolyte membrane fuel cell (PEMFC). Shuhaimi et al. (2010) has assembled a fuel cell using MC-NH_4NO_3-polyethylene glycol systems. Fuel cell has been used in China to reduce air pollution as reported by Michaela (2018).

- Pseudocapacitors. Harankahawa, Weerasinghe, Vidanapathirana and Perera (2017) have fabricated a PAN-NaSCN-EC based pseudocapacitor.

REFERENCES

Abd El-Kader, M. F. H., & Ragab, H. S. (2013). DC conductivity and dielectric properties of maize starch/methylcellulose blend films. *Ionics, 19*(2), 361-369.

Abdelrazek, E. M., Hezma, A. M., El-khodary, A., & Elzayat, A. M. (2016). Spectroscopic studies and thermal properties of PCL/PMMA biopolymer blend. *Egyptian Journal of Basic and Applied Sciences, 3*(1), 10-15.

Abdullah, O. G., Aziz, S. B., & Rasheed, M. (2018). Incorporation of NH_4NO_3 into MC-PVA blend-based polymer to prepare proton-conducting polymer electrolyte films. *Ionics, 24*(3), 777-785.

Adam, K., Gonzalez, A. F., Mallows, J., Li, T., Thijssen, J. H. J., & Robertson, N. (2019). Facile synthesis and characterization of Bi13S18I2 films as a stable supercapacitor electrode material. *Journal of Material Chemistry A, 7*, 1638-1646.

Adams, K., Mallows, J., Li, T., Kampouris, D., Thijssen, J. H. J., & Robertson, N. (2019). $Cs_3Bi_2I_9$ as high-performance electrode material achieving high capacitance and stability in an economical supercapacitor. *Journal of Physics: Energy, 1*, 034001-0034011.

Agmon, N. (1995). The Grotthuss mechanism. *Chemical Physics Letters, 244*(5-6), 456-462.

Ahmad, N. H., & Isa, M. I. N. (2015). Proton conducting solid polymer electrolytes based carboxymethyl cellulose doped ammonium chloride: ionic conductivity and transport studies. *International Journal of Plastics Technology, 19*, 47-55.

Ahmad, N. H., & Isa, M. I. N. (2015). structural and ionic conductivity studies of cmc based polymer electrolyte doped with NH_4Cl. *Advanced Materials Research, 1107*, 247-252.

Ahmed, H. T., & Abdullah, O. G. (2019). Preparation and composition optimization of PEO:MC polymer blend films to enhance electrical conductivity. *Polymers, 11*(5), 1-18.

Ahmed, H. T., Jalal, V. J., Tahir, D. A., Mohamad, A. H., & Abdullah, O. G. (2019). Effect of PEG as a plasticizer on the electrical and optical properties of polymer blend electrolyte MC-CH-$LiBF_4$ based films. *Results in Physics, 15*, 102735-1-102735-7.

Aid, S., Eddhahak, A., Ortega, Z., Froelich, D., & Tcharkhtchi, A. (2017). Experimental study of the miscibility of ABS/PC polymer blends and investigation of the processing effect. *Journal of Applied Polymer Science, 134*(25), 1-9.

Alghunaim, N. S. (2016). Optimization and spectroscopic studies on carbon nanotubes/PVA nanocomposites. *Results in Physics, 6*, 456-460.

Alias, S. S., Chee, S. M., & Mohamad, A. A. (2017). Chitosan–ammonium acetate–ethylene carbonate membrane for proton batteries. *Arabian Journal of Chemistry, 10,* S3687- S3698.

Altayan, M. M., Darouich, T. M., & Karabet, F. (2017). On the Plasticization Process of Potato Starch: Preparation and Characterization. *Food Biophysics, 12*(4), 397-403.

Alves, R., & Silva, M. M. (2014). The influence of glycerol and formaldehyde in gelatin-based polymer electrolyte. *Molecular Crystal Liquid Crystal, 591*, 64-73.

Alves, R., Sentanin, F., Sabadini, R. C., Pawlicka, A., & Silva, M. M. (2016). Influence of cerium triflate and glycerol on electrochemical performance of chitosan electrolytes for electrochromic devices. *Electrochimica Acta, 217*, 108-116.

Amran, N. N. A., Manan, N. S. A, & Kadir, M. F. Z. (2016). The effect of $LiCF_3SO_3$ on the complexation with potato starch-chitosan blend polymer electrolytes. *Ionics, 22*(9), 1647-1658.

Andrade, J., Raphael, E., & Pawlicka, A. (2009). Plasticized pectin-based gel electrolytes. *Electrochimica Acta, 54*, 6479-6483.

Andres, B., Dahlstrom, C., Blomquist, N., Norgen, M., & Olin, H. (2018). Cellulose binders for electric double-layer capacitor electrodes: The influence of cellulose quality on electrical properties. *Material & Design, 141*, 342-349.

Antognini, A., Nez, F., Schuhmann, K., Amaro, F. D., Biraben, F., Cardoso, J. M. R., … Pohl, R. (2013). Proton structure from the measurement of 2S-2P transition frequencies of muonic hydrogen. *Science, 339*, 417-420.

Anuar, N. K., Subban, R. H. Y., & Mohamed, N. S. (2012). Properties of PEMA-$NH_4CF_3SO_3$ Added to BMATSFI Ionic Liquid. *Materials, 5*, 2609-2620.

Anuar, N. K., Zainal, N., Mohamed, N. S., & Subban, R. H. Y. (2012). Studies of poly(ethyl methacrylate) complexed with ammonium trifluoromethanesulfonate. *Advanced Materials Research, 501*, 19-23.

Armand, M. (1994). The history of polymer electrolytes. *Solid State Ionics, 69*, 309-319.

Armand, M. B., Chabagno, & J. M., Duclot, M. (1979). P. Vashista, J.N. Mundy, G.K. Shenoy Eds. Fast Ion Transport in Solids. *Elsevier*, 131.

Arof, A. K., Amirudin, S., Yusof, S. Z., & Noor, I. M. (2014). A method based on impedance spectroscopy to determine transport properties of polymer electrolytes. *Physical Chemistry Chemical Physics, 16*, 1856-1867.

Arof, A. K., Kufian, M. Z., Syukur, M. F., Aziz, M. F., Abdelrahman, A. E., & Majid, S. R. (2012). Electrical double layer capacitor using poly(methyl methacrylate)–C_4BO_8Li gel polymer electrolyte and carbonaceous material from shells of mata kucing (Dimocarpus longan) fruit. *Electrochimica Acta, 74*, 39-45.

Arof, A. K., Noor, I. M., Buraidah, M. H., Bandara, T. M. W. J., Careem, M. A., Albinsson, I., & Mellander, B. E. (2017). Polyacrylonitrile gel polymer electrolyte based dye sensitized solar cells for a prototype solar panel. *Electrochimica Acta, 251*, 223-234.

Arof, A. K., Shuhaimi, N. E. A., Alias, N. A., Kufian, M. Z., & Majid, S. R. (2010). Application of chitosan/iota-carrageenan polymer electrolytes in electrical double layer capacitor (EDLC). *Journal of Solid State Electrochemistry, 14*, 2145-2152

Arunkumar, R., Ravi, S. B., Usha Rani, M., & Kalainathan, S. (2017). Effect of PBMA on PVC-based polymer blend electrolytes. *Journal of Applied Polymer Science, 134*, 1-12.

Arya, A., & Sharma, A. L. (2018). Optimization of salt concentration and explanation of two peak percolation in blend solid polymer nanocomposite films*, Journal of Solid State Electrochemistry, 22*, 2725-2745.

Ashori, A., & Bahrami, R. (2014). Modification of physico-mechanical properties of chitosan-tapioca starch blend films using nano graphene. *Polymer-Plastics Technology and Engineering, 53*, 312-318.

Asmara, S. N., Kufian, M. Z., Majid, S. R., & Arof, A. K. (2011). Preparation and characterization of magnesium ion gel polymer electrolytes for application in electrical double layer capacitors. *Electrochimica Acta, 57*, 91-97.

Ashworth, C. R., Matthews, R. P., Welton, T., & Hunt, P. A. (2016). Doubly ionic hydrogen bond interactions within the choline chloride–urea deep eutectic solvent. *Physical Chemistry Chemical Physics, 18*(27), 18145-18160.

Azli, A. A., Manan, N. S. A., & Kadir, M. F. Z. (2017). The development of Li+ conducting polymer electrolyte based on potato starch/graphene oxide blend. *Ionics, 23*(2), 411-425.

Aziz, S. B., & Abidin, Z. H. Z. (2015). Innovative method to avoid the reduction of silver ions to silver nanoparticles ($Ag^{+} \rightarrow Ag^{o}$) in silver ion conducting based polymer electrolytes. *Physica Scripta, 90*, 1-9.

Aziz, S. B., Abidin, Z. H. Z., & Arof, A. K. (2010) Influence of silver ion reduction on electrical modulus parameters of solid polymer electrolyte based on chitosan silver triflate electrolyte membrane. *Express Polymer Letters, 4*, 300-310.

Aziz, S. B., Abdullah, O. G., Rasheed, M. A., & Ahmed, H. M. (2017). Effect of high salt concentration on structural, morphological, and electrical characteristics of chitosan based solid polymer electrolytes. *Polymers, 9*(6), 1-19.

Aziz, S. B., Karim, W. O., Qadir, K. W., & Zafar, Q. (2018). Proton ion conducting solid polymer electrolytes based on chitosan incorporated with various amounts of barium titanate ($BaTiO_3$). *International Journal of Electrochemical Science, 13*, 6112-6125.

Aziz, S. B., Woo, T. J., Kadir, M. F. Z., & Ahmed, H. M. (2018). A conceptual review on polymer electrolytes and ion transport models. *Journal of Science: Advanced Materials and Devices, 3*, 1-17.

Azli, A., Manan, N., & Kadir, M. F. Z. (2015). Conductivity and dielectric studies of lithium trifluoromethanesulfonate doped polyethylene oxide-graphene oxide blend based electrolytes. *Advances in Materials Science and Engineering, 2015*, 1-10.

Azmeera, V., Adhikary, P., & Krishnamoorthi, S. (2012). Synthesis and Characterization of Graft Copolymer of Dextran and 2-Acrylamido-2-methylpropane Sulphonic Acid. *International Journal of Carbohydrate Chemistry, 2012*, 1-7.

Babu, K., Bera, A., Kumari, K., Mandal, A., & Saxena, V. K. (2014). Characterization and application of methylcellulose and potato starch blended films in controlled release of urea. *Journal of Polymer Engineering, 35,* 79-88.

Balakrishna, P., Gopi, S., Sreekala, M. S., & Thomas, S. (2018). UV resistant transparent bionanocomposite films based onpotato starch/cellulose for sustainable packaging. *Starch/Stärke, 70*, 1700139.

Bansod, S. M., Bhoga, S. S., Singh, K., & Tiwari , R. U. (2007). The role of electrolyte in governing the performance of protonic solid state battery. *Ionics, 13*, 329-332.

Balqis, A. M., Khaizura, M. A. R., Russly, A. R., & Hanani, Z. A. (2017). International Journal of Biological Macromolecules. *International Journal of Biological Macromolecules, 103*, 721-732.

Basha, S. K. S., & Rao, M. C. (2018). Spectroscopic and electrochemical properties of (1−x)[PVA/PVP]:x[$MgCl_2\{_6H_2O\}$] blend polymer electrolyte films. *International Journal of Polymer Science, 2018*, 1-11.

Belanger, D., Brousse, T., & Long, J. W. (2008). Manganese Oxides: Battery Materials Make the Leap to Electrochemical Capacitors. *Electrochemical Society Interface, 17*(1), 49-52.

Berthier, C., Gorecki, W., Minier, M., Armand, M. B., Chabagno J. M., & Rigaud, P. (1983). Microscopic investigation of ionic conductivity in alkali metal salts-poly(ethylene oxide) adducts. *Solid State Ionics*, *11*, 91-95.

Bhad, S. N., & Sangawar, V. S. (2013). Optical study of PVA based gel electrolyte. *International Journal of Scientific & Engineering Research, 4*, 1719-1722.

Bibi, F., Villain, M., Guillaume, C., Sorli, B., & Gontard, N. (2016). A review: Origins of the dielectric properties of proteins and potential development as bio-sensors. *Sensors, 16*, 1-22.

Bin-Dahman, O. A., Rahaman, M., Khastgir, D., & Al-Harthi, A. (2017). Electrical and dielectric properties of poly(vinyl alcohol)/starch/ graphene nanocomposites. *The Canadian Journal of Chemical Engineering, 9999*, 1-9.

Bingbing, W., Hongming, L., Hongli, X., Junpeng, Z., Qiujun, W., Qiao, S., & Yonghong, D. (2018). High voltage, solvent-free solid polymer electrolyte based on a star-comb PDLLA–PEG copolymer for lithium ion batteries. *RSC Advances, 8*, 6373-6380.

Biswal, D. R., & Singh, R. P. (2004). Characterisation of carboxymethyl cellulose and polyacrylamide graft copolymer. *Carbohydrate Polymers, 57*, 379-387.

Biswal, M., Banerjee, A., Deo, & M., Ogale, S. (2013). From dead leaves to high energy density supercapacitors. *Energy and Environmental Science, 6*, 1249-1259.

Biswas, A., Willet, J. L., Gordon, S. H., Finkenstadt, V. L., & Cheng, H. N. (2006). Complexation and blending of starch, poly(acrylic acid), and poly(N-vinyl pyrrolidone). *Carbohydrate Polymers, 65*, 397–403.

Bokobza, L. (2018). Spectroscopic Techniques for the Characterization of Polymer Nanocomposites: A Review. *Polymers, 10*(7), 1-21.

Botte, G. G., & Muthuvel, M. (2012). Electrochemical energy storage: Applications, processes, and trends. In J.A. Kent (Ed.), *Handbook of industrial chemistry and biotechnology* (pp 1497-1539). Florida: Springer.

Bouchet, R., Maria, S., Meziane, R., Aboulaich, A., Lienafa, L., Bonnet, J.-P., ... Armand, M. (2013). Single-ion BAB triblock copolymers as highly efficient electrolytes for lithium metal batteries. *Nature materials, 12*(5), 452-457.

Bourtoom, T., & Chinnan, M. S. (2008). Preparation and properties of rice starch–chitosan blend biodegradable film. *LWT-Food Science and Technology, 41*(9), 1633-1641.

Braun, P., Uhlmann, C., Weiss, M., Weber, A., & Ivers-Tiffée, E. (2018). Assessment of all-solid-state lithium-ion batteries. *Journal of Power Sources, 393*, 119-127.

Broadhead, J., & Kuo, H. C. (2001). Electrochemical Principles and Reactions. In D. Linden, T.B. Reddy (Eds.), *Handbook of Batteries, Third edition* (pp 2.10-2.37). New York: McGraw-Hill.

Brownson, D. A. C., Smith, G. C., & Banks, C. E. (2017). Graphene oxide electrochemistry: the electrochemistry of graphene oxide modified electrodes reveals coverage dependent beneficial electrocatalysis. *Royal Society Open Science, 4*(11), 1-15.

Bruce, P. G., & Vincent, C. A. (1993). Polymer electrolytes. *Journal of the Chemical Society, Faraday Transactions, 89*(17), 3187-3203.

Buraidah, M. H., & Arof, A. K. (2011). Characterization of Chitosan/PVA Blended Electrolyte Doped With NH_4I. *Journal of Non-Crystalline Solids, 357*, 3261-3266.

Buraidah, M. H., Teo, L. P., Majid, S. R., & Arof, A. K. (2009). Ionic conductivity by correlated barrier hopping in NH_4I doped chitosan solid electrolyte. *Physica B, 404*, 1373-1379.

Cao, X., He, X., Wang, J., Liu, H., Roser, S., Rad, B. R., … Cekic-Laskovic, I. (2016). High Voltage $LiNi_{0.5}Mn_{1.5}O_4/Li_4Ti_5O_{12}$ Lithium Ion Cells at Elevated Temperatures: Carbonate versus Ionic Liquid-Based Electrolytes. *ACS Applied Materials, 8*, 25971-25978.

Chai, M. N., & Isa, M. I. N. (2016). Novel proton conducting solid biopolymer electrolytes based on carboxymethyl cellulose doped with oleic acid and plasticized with glycerol. *Scientific Reports, 6*, 1-7.

Chandra, A. (2013). Synthesis and dielectric studies of PEO-PVP blended solid polymer. *Indian journal of Pure and Applied Physics, 51*, 788-791.

Chandra, A., Chandra, A., & Thakur, K. (2016). Synthesis and ion conduction mechanism on hot-pressed sodium ion conducting nano composite polymer electrolytes. *Arabian Journal of Chemistry, 9*(3), 400-407.

Chartterjee, B., Kulshrestha, N., & Gupta, P. N. (2015). Electrical properties of starch-PVA biodegradable polymer blend. *Physica Scripta, 90*, 025805-025814.

Chen, T., Ma, H., & Kong, D. (2013). Discharge performance of nanostructured PbO_2 microspheres as the positive active material. *Material Letter 90,* 103-106.

Chen, R., Qu, W., Guo, X., Li, L., & Wu, F. (2016). The pursuit of solid-state electrolytes for lithium batteries: from comprehensive insight to emerging horizons. *Materials Horizons, 3*, 487-516.

Cheng, J., Jeong, E. Y., & Dou, E. (2016). Samsung to permanently discontinue Galaxy Note 7 smartphone. *The Wall Street Journal.*

Chiou, C. W., Lin, Y. C., Wang, L., Hirano, C., Suzuki, Y., Hayakawa, T., & Kuo, S. W. (2014). Strong screening effect of polyhedral oligomeric silsesquioxanes (POSS) nanoparticles on hydrogen bonded polymer blends. *Polymers, 6*, 926-948.

Choi, B. N., Yang, J. H., Kim, Y. S., & Chung, C. H. (2019). Effect of morphological change of copper-oxide fillers on the performance of solid polymer electrolytes for lithium-metal polymer batteries. *RSC Advances, 9*, 21760-21770.

Choudhary, S., & Sengwa, R. J. (2016). Structural dynamics and ionic conductivity of amorphous type plasticized solid polymer electrolytes. *Indian Journal of Pure & Applied Physics, 54*, 159-169.

Choudhury, S., Stalin, S., Vu, D., Warren, A., Deng, Y., Biswal. P., & Archer, L. A. (2019). Solid-state polymer electrolytes for highperformance lithium metal batteries. *Nature Communication, 10*, 1-8.

Chuan-Pei, L., Chun-Ting, L., & Kuo-Chuan, H. (2017). Use of organic materials in dye-sensitized solar cells. *Materials Today, 20*, 267-283.

Coates, J. (2006). Interpretation of Infrared Spectra, A Practical Approach. In *Encyclopedia of Analytical Chemistry* (pp. 1-23). Newtown, USA, NA: Encyclopedia of Analytical Chemistry.

Dai, Z., Peng, C., Chae, J. H. Ng, K. C., & Chen, G. Z. (2015). Cell voltage versus electrode potential range in aqueous supercapacitors. *Scientific Reports, 5*, 1-8.

Daniels, I. N., Wang, Z., & Laird, B. B. (2017). Dielectric properties of organic solvents in an electric field. *The Journal of Physical Chemistry, 121*, 1025-1031.

Danielle, M., Yukyung, J., Alexandra, L. H., Michael, A. W., Geoffrey, W. C. & Nitash, B. (2016). Effect of monomer structure on ionic conductivity in a systematic set of polyester electrolytes. *Solid State Ionics, 289*, 118–124.

Das, S., & Ghosh, A. (2015). Ion conduction and relaxation in PEO-LiTFSI-Al_2O_3 polymer nanocomposite electrolytes. *Journal of Applied Physics, 117*(17), 174103-1-174103-7.

Dell, R. (2000). Batteries: fifty years of materials development. *Solid State Ionics, 134*(1), 139-158.

Deraman, S. K., Mohamed, N. S., & Subban, R. H. Y. (2013). Conductivity and Electrochemical Studies on Polymer Electrolytes Based on Poly Vinyl (chloride) - Ammonium Triflate-Ionic Liquid for Proton Battery. *International Journal of Electrochemical Science, 8*, 1459-1468.

Desbrières J., Hirrien M., & Ross-Murphy S. B. (2000). Thermogelation of methylcellulose: Rheological considerations, *Polymer, 41*, 2451-2461.

Devi, G. N., Chitra, S., Selvasekarapandian, S., Premalatha, M., Monisha, S., & Saranya, J. (2017). Synthesis and characterization of dextrin-based polymer electrolytes for potential applications in energy storage devices. *Ionics, 23*(12), 3377-3388.

Diederichsen, K. M., Buss, H. G., & McCloskey, B. D. (2017). The compensation effect in the vogel–tammann–fulcher (vtf) equation for polymer-based electrolytes. *Macromolecules, 50*(10), 3831-3840.

Diop, C. I. K., Li, H. L., Xie, B. J., & Shi, J. (2011). Effects of acetic acid/acetic anhydride ratios on the properties of corn starch acetates. *Food chemistry, 126*(4), 1662-1669.

Donatell, P., Barbara, B., Romano, L., Cristian, R., & Alessandro, S. (2003). Starch–methylcellulose based edible films: rheological properties of film-forming dispersions. *Journal of Food Engineering, 59*, 25-32.

Dose, W. M., & Donne, S. W. (2014). Optimising heat treatment environment and atmosphere of electrolytic manganese dioxide for primary Li/MnO_2 batteries. *Journal of Power Sources,* 247, 852-857.

Du, J. F., Bai, Y., Chu, W.Y., & Qiao, L. J. (2010). The structure and electric characters of proton-conducting chitosan membranes with various ammonium salts as complexant, *Journal of Polymer Science part B: Polymer Physics, 48*, 880-885.

Du, B. W., Hu, S. Y., Singh, R., Tsai, T. T., Lin C. C., & Ko, F. U. (2017). Eco-Friendly and Biodegradable Biopolymer Chitosan/Y_2O_3 Composite Materials in Flexible Organic Thin-Film Transistors. *Materials, 10*, 1026-1-1026-9.

Dyartanti, E. R., Purwanto, A., Widiasa, I. N., & Susanto, H. (2018). Ionic conductivity and cycling stability improvement of pvdf/nano-clay using pvp as polymer electrolyte membranes for $LiFePO_4$ batteries. *Membranes, 8*, 1-15.

Dzulkurnain, N. A., Rani, M. S. A., Ahmad, A., & Mohamed, N. S. (2018). Effect of lithium salt on physicochemical properties of P(MMA-co-EMA) based copolymer electrolytes for dye-sensitized solar cell application. *Ionics, 24*, 269-276.

El-Hadi, A. M. (2019). Miscibility of crystalline/amorphous/crystalline biopolymer blends from PLLA/PDLLA/PHB with additives. *Polymer-Plastics Technology and Materials, 58*(1), 31-39.

Fadzallah, I. A., Noor, I. M., Careem, M. A., & Arof, A. K. (2016). Investigation of transport properties of chitosan-based electrolytes utilizing impedance spectroscopy. *Ionics, 22*(9), 1635-1645.

Fan, H., & Shen, W. (2016). Gelatin-Based Microporous Carbon Nanosheets as High Performance Supercapacitor Electrodes. *ACS Sustainable Chemistry and Engineering, 4*, 1328–1337.

Farghali, J., & Ahmad, A. H. (2015). Fourier transform infrared spectroscopy and electrical characterization of methylcellulose based solid polymer electrolyte doped with sodium iodide. *Jurnal Teknologi, 76*, 41-45.

Feng, N. N., He, P., & Zhou, H. S. (2016). Critical challenges in rechargeable aprotic Li–O_2 batteries. *Advanced Energy Materials, 6*, 1-24.

Fergus, J. W. (2010). Recent developments in cathode materials for lithium ion batteries. *Journal of Power Sources, 195*, 939-954.

Filho, G. R., de Assuncao, R. M. N., Viera, J. G., Meireles, C. Da, S., Cerqueira, D. A., … Messaddeq, Y. (2007). Characterization of methylcellulose produced from sugar cane bagasse cellulose: crystallinity and thermal properties. *Polymer Degradation and Stability 92,* 205-210.

Follain , N., Joly, C., Dole P., & Bliard, C. (2005). Properties of starch based blends. Part 2. Influence of poly vinyl alcohol addition and photocrosslinking on starch based materials mechanical properties. *Carbohydrate Polymers, 60*, 185-192.

Fong, F. K., Self, J., Diederichsen, K. M., Wood, B. M., McCloskey, B. D., & Persson, K. A. (2019). Ion transport and the true transference number in nonaqueous polyelectrolyte solutions for lithium ion batteries. *ACS Central Science, 5*(7), 1250-1260.

French, A. D. (2014). Idealized powder diffraction patterns for cellulose polymorphs. *Cellulose, 21*(2) 885-896.

Frinkenstadt, V. L. (2005). Natural polysaccharides as electroactive polymers, *Applied Microbiology and Biotechnology, 67*(6), 735-745.

Fuzlin, A. F., Rasali, N. M. J., & Samsudin, A. S. (2018). Effect on ammonium bromide in dielectric behavior based alginate solid biopolymer electrolytes. *Materials Science and Engineering, 342*, 012080-1-012080-8.

Gao, H., & Lian, K. (2014). Proton-conducting polymer electrolytes and their applications in solid supercapacitors: a review. *Royal Society of Chemistry, 4*, 33091-33113.

Gobel, K., & Kanchan, D. K. (2016). Ionic transport studies in PVdF-HFP-PMMA-(PC+DEC)-$LiClO_4$ gel polymer electrolyte. *AIP Conference Proceedings, 1832*, 140047-1-140047-3.

Gohel, K., & Kanchan, D. K. (2018). Ionic conductivity and relaxation studies in PVDF-HFP:PMMA-based gel polymer blend electrolyte with $LiClO_4$ salt. *Journal of Advanced Dielectrics, 8*(1), 1-13.

Gómez-Carracedo, A., Alvarez-Lorenzo, C., Gómez-Amoza, J. L., & Concheiro, A. (2003). Chemical structure and glass transition temperature of non-ionic cellulose ethers DSC, TMDSC. *Journal of Thermal Analysis Calorimetry, 73*, 587-596.

Gondaliya, N., Kanchan, D. K., & Sharma, P. (2013). Effect of a plasticizer on a solid polymer electrolyte. *Society of Plastics Engineers, 4,* 2-4.

Graaf, R. A., Karman, A. P., & Janssen, P. B. M. (2003). Material properties and glass transition temperatures of different thermoplastic starches after extrusion processing. *Starch/Stärke, 55*, 80-86.

Gunawan, R., & Zhang, D. (2009). Thermal stability and kinetiks of decomposition of ammonium nitrate in the presence of pyrite. *Journal of Hazard Material, 165*, 751-758.

Gurusiddappa, J., Madhuri,W., Suvarna ,R. P., & Dasan, K. P. (2016). Conductivity and Dielectric behavior of polyethylene oxide-lithium perchlorate solid polymer electrolyte films. *Indian journal of Advance in Chemistry Science, 4*, 14-19.

Halal, S. L. M. E., Colussi, R., Deon, V. G., Pinto, V. Z., Villanova, F. A., Carreno, N. L. V., ... Zavareze, E. R. (2015). Films based on oxidized starch and cellulose from barley. *Carbohydrate Polymers, 133,* 644-653.

Hashmi, S. A., Kumar, A., Maurya, K. K., & Chandra, S. (1990). Proton-conducting polymer electrolyte I. The polyethylene oxide NH_4ClO_4 system. *Journal of Physics D: Applied Physics, 23*, 1307-1314.

Hana, C. C., Shia, W., & Jin, J. (2013). Morphology and Crystallization of Crystalline/Amorphous Polymer Blends. *Encyclopedia of Polymers and Composites, 52*(30), 10198-10205.

Harankahawa, N., Weerasinghe, S., Vidanapathirana, K., & Perera, K. (2017). Investigation of a Pseudo Capacitor with Polyacrylonitrile based Gel Polymer Electrolyte. *Journal of Electrochemical Science and Technology, 8*(2), 107-114.

Haward, M. (2018). Plastic pollution of the world's seas and oceans as a contemporary challenge in ocean governance. *Nature Communications, 9*, 1-3.

Hegde, G., Abdul Manaf, S. A., Kumar, A., Ali, G. A. M., Chong, K. F., Ngaini, Z., & Sharma, K. V. (2015). Biowaste Sago Bark Based Catalyst Free Carbon Nanospheres: Waste to Wealth Approach. *ACS Sustainable Chemistry and Engineering, 3*, 2247-2253.

Hema, M., Selvasekerapandian, S., Hirankumar, G., Sakunthala, A., Arunkumar, D., & Nithya, H. (2009). Structural and thermal studies of PVA: NH_4I. *Journal of Physics and Chemistry of Solids, 70*, 1098-1103.

Hemalatha, R., Alagar, M., Selvasekarapandian, S., Sundaresan, B., & Moniha, V. (2019). Studies of proton conducting polymer electrolyte based on PVA, amino acid proline and NH_4SCN. *Journal of Science: Advanced Materials and Devices, 4*(1), 101-110.

Huo, P., Ni, S., Hou, P., Xun, Z., Liu, Y., & Gu, J. (2019). A crosslinked soybean protein isolate gel polymer electrolyte based on neutral aqueous electrolyte for a high-energy-density supercapacitor. *Polymers, 11*, 863-1-863-13.

Husin, M. A., & Tahir, S. M. (2018). Effect of Metal Salts on Ionic Conductivity of Waste Cooking Oil Based Polyurethane Solid Polymer Electrolyte. *Journal of Physics, 1083,* 012052-1-012052-8.

Isahak, W. N. R. W., Ismail, M., Yarmo, M. A., Jahim, J. M., & Salimon, J. (2010). Purification of crude glycerol from transesterification RBD palm oil over homogeneous catalysts for the biolubricant preparation. *Journal of Applied Sciences, 10*, 2590-2595.

Ismail, H., Irani, M., & Ahmad, Z. (2013). Starch-Based Hydrogels: Present Status and Applications. *International Journal of Polymeric Materials and Polymeric Biomaterials, 62*, 411-420.

Iqbal, M. Z., & Rafiuddin, S. (2016). Structural, electrical conductivity and dielectric behavior of Na_2SO_4–LDT composite solid electrolyte. *Journal of Advance Research, 7*, 135-141.

Iro, Z., Subramani, C., & Dash, S. S. (2016). A Brief Review on Electrode Materials for Supercapacitor. *International Journal of Electrochemical Science, 11*, 10628-10643.

Jamaludin, A., & Mohamad, A. A. (2010). Application of liquid gel polymer electrolyte based on chitosan-NH_4NO_3 for proton batteries. *Journal of Applied Polymer Science, 118*, 1240-1243.

Jansky, S. & Fajardo, D. (2016). Amylose content decreases during tuber development in potato. *Journal of the Science of Food and Agriculture, 96*(13), 4560-4564.

Jenkins, H. D. B., & Morris, D. F. C. (1976). A new estimation of the lattice energies of the ammonium halides and the proton affinity of gaseous ammonia. *Molecular Physics, 32*(1), 231-236.

Jenkins, H. D. B., & Thakur, K. P. (1979). Reappraisal of thermochemical radii for complex ions. *Journal of Chemical Education, 56*(9), 576-1-576-2.

Jesintha, L. R. M., Radha, K. P., & Hemalatha, R. (2017). Effect of NH_4NO_3 on Conductivity of biopolymer electrolyte based on potato starch. *International Journal of Multidisciplinary Education and Research, 2*(2), 47-49.

Jiang, Y., Yan, X., Ma, Z., Mei, P., Xiao, W., You, Q., & Zhang, Y. (2018). Development of the PEO based solid polymer electrolytes for all-solid state lithium ion batteries. *Polymers, 10*, 1237-1-1237-13.

Jiao, Y., Pei, J., Chen, D., Yan, C., Hu, Y., Zhanf, Q., & Chen, G. (2017). Mixed-metallic MOF based electrode materials for high performance hybrid supercapacitors. *Journal of Materials Chemistry A, 5*, 1094-1102.

Johan, M. R., & Ting, L. M. (2011). Structural, thermal and electrical properties of Nano manganese-composite polymer electrolytes. *International Journal Electrochemical Science, 6,* 4737-4748.

Jung, Y. C., Park, M. S., Kim, D. H., Ue, M., Eftekhari, A., & Kim, D. W. (2017). Room-temperature performance of poly(ethylene ether carbonate)-based solid polymer electrolytes for all-solid-state lithium batteries. *Scientiific Reports, 7*, 17482-1-17482-11.

Kadir, M. F. Z. (2010). *Characteristics of proton conducting PVA-chitosan polymer blend electrolytes*. (Doctoral thesis, Univeristy of Malaya, Kuala Lumpur, Malaysia). Retrieved from http://studentsrepo.um.edu.my/2744/

Kadir, M. F. Z., Abdul, L. P., Teo, Majid, S. R., & Arof, A. K. (2009). Conductivity studies on plasticised PEO/chitosan proton conducting polymer electrolyte. *Materials Research Innovations, 13*, 259-262.

Kadir, M. F. Z., Aspanut, Z., Majid, S. R., & Arof, A. K. (2011). FTIR studies of plasticized poly(vinyl alcohol)–chitosan blend doped with NH_4NO_3 polymer electrolyte membrane. *Spectrochimica Acta Part A, 78*, 1068-1074.

Kadir, M. F. Z., & Arof, A. K. (2011). Application of PVA–chitosan blend polymer electrolyte membrane in electrical double layer capacitor. *Materials Research Innovation, 15*, S2-217-S2-220.

Kadir, M.F.Z., Majid, S.R., & Arof, A.K. (2010). Plasticized chitosan–PVA blend polymer electrolyte based proton battery. *Electrochimica Acta, 55*, 1475-1482.

Kamdev, S., Mishra, S. K., Mohanty, P. P., Agarawal, J., Meher, P., Satapathy, D., ... Nayak, S. M. (2015). An overview of non starch polysaccharide. *Journal of Animal Nutrition and Physiology, 1*, 17-22.

Kampeerapappun, P., Aht-ong, D., Pentrakoon, D., & Srikulkit, K. (2007). Preparation of cassava starch/montmorillonite composite film. *Carbohydrate Polymers, 67*(2), 155-163.

Kartha, S. A. (2013). *A Preparation of B_2O_3-Li_2O-MO (M=Pb, Zn) glass thin films and study of thin properties.* (Dissertation, Mahatma Gandhi University, India). Retrieved from http://shodhganga.inflibnet.ac.in/handle/10603/6510

Karthikeyan, S., Sikkanthar, S., Selvasekarapandian, S., Arunkumar, D., Nithya, H., & Kawamura, J. (2016). Structural, electrical and electrochemical properties of polyacrylonitrile-ammonium hexaflurophosphate polymer electrolyte system. *Journal of Polymer Research, 23*, 51-1-51-10.

Kathe, K., & Kathpalia, H. (2017). Film forming systems for topical and transdermal drug delivery. *Asian Journal of Pharmaceutical Sciences, 12*(6), 487-497.

Kento, S., Hiroki, M., & Atsumi, M. (2016). Effects of amino acids on solid-state phase transition of ammonium nitrate. *Journal of Thermal Analysis and Calorimetry, 127*, 851-856.

Khiar, A. S. A., & Arof, A. K. (2010). Conductivity studies of starch-based polymer electrolytes. *Ionics, 16*(2), 123-129.

Khiar, A. S. A., Arof, A. K. (2011). Electrical properties of starch/chitosan-NH_4NO_3 polymer electrolyte. *International Journal of Mathematical, Computational, Physical, Electrical and Computer Engineering, 5*, 1662-1666.

Khiar, A. S. A., Puteh, R., & Arof, A. K. (2006). Conductivity studies of a chitosan-based polymer electrolyte. *Physica B, 373*, 23-27.

Kizil, R., Irudayaraj, J., & Seetharaman, K. (2002). Characterization of Irradiated Starches by Using FT-Raman and FTIR Spectroscopy. *Journal of Agricultural and Food Chemistry, 50*(14), 3912-3918.

Kobayashi, T., Noguchi, Y., & Miyayama, M. (2005). Enhanced spontaneous polarization in super lattice structure $Bi_4Ti_3O_{12}$−$BaBi_4Ti_4O_{15}$ single crystal. *Applied Physics Letters, 86*, 01290.

Koduru, H. K., Marino, L., Scarpelli, F., Petrov, A. G., Marinov, Y. G., … Scaramuzza, N. (2017). Structural and dielectric properties of $NaIO_4$ - Complexed PEO/PVP blended solid polymer electrolytes. *Current Applied Physics, 17*, 1518-1531.

Kotz, R., Carlen, M., & Carlen, R. M. (2000). Principles and applications of electrochemical capacitors. *Electrochimica Acta, 45*, 2483-2498.

Krishnan, K., Jayaraman, P., Balasubramanian, S., & Mani, U. (2018). Nanoionic transport and electric double layer formation at the electrode/polymer interface for high performance supercapacitors. *Journal of Materials Chemistry A, 6*, 23650-23658.

Kufian, M. Z., Aziz, M. F., Shukur, M. F., Rahim, A. S., Ariffin, N. E., … Arof A. K. (2012). PMMA LiBOB gel electrolyte for application in lithium ion batteries. *Solid State Ionics, 208*, 36-42.

Kumar, M. S., & Rao, M. C. (2019). Effect of Al_2O_3 on structural and dielectric properties of PVP-CH_3COONa based solid polymer electrolyte films for energy storage devices. *Heliyon, 5*, 1-10.

Kumar, M. S., & Bhat, D. K. (2009). Polyvinyl alcohol-polystyrene sulphonic acid blend electrolyte for supercapacitor application. *Physica B, 404*, 1143-1145.

Kumar, D., & Hashmi, S. A. (2010). Ion transport and ion–filler-polymer interaction in poly(methyl methacrylate)-based, sodium ion conducting, gel polymer electrolytes dispersed with silica nanoparticles. *Journal of Power Sources, 195*, 5101-5108.

Kumar, D., Pandey, J., Raj, V., & Kumar, P. (2017). A review on the modification of polysaccharide through graft copolymerization for various potential applications. *The Open Medicinal Chemistry Journal, 11*, 109-126.

Kumar, M., & Sekhon, S. S. (2002). Role of plasticizer's dielectric constant on conductivity modification of PEO–NH_4F polymer electrolytes. *European Polymer Journal, 38*, 1297-1304.

Kumar, R., Sharma, S., Dhiman, N. & Pathak, D. (2016). Study of Proton Conducting PVdF based Plasticized Polymer Electrolytes Containing Ammonium Fluoride. *Material Science Research India, 13*, 21-27.

Kuo, S. W. (2008). Hydrogen-bonding in polymer blends. *Journal of Polymer Research, 15*, 459-486.

Kuo, C. W., Huang, C. W., Chen, B. K., Li, W. B., Chen, P. R., Ho, T.H., … Wu, T. Y. (2013). Enhanced Ionic Conductivity in PAN–PEGME-$LiClO_4$-PC Composite Polymer Electrolytes. *International Journal of Electrochemical Science, 8*, 3834-3850.

Latha, C., & Venkatachalam, K. (2016). Synthesis and characterization of PVP: PVC: CH_3COONH_4. *International Journal of Trend in Research and Development, 3*(5), 4-7.

Latif, F., & Aziz, M. (2013). The anti-plasticization effects of dimethyl carbonate plasticizer in poly (methyl metacrylate) electrolyte containing rubber. *Materials Sciences and Application, 4*(11), 663-666.

Latif, F., Aziz, M., Ali, A. M. M., & Yahya, M. Z. A. (2009). The coagulation impact of 50% epoxidised natural rubber chain in ethylene carbonate-plasticized solid electrolytes. *Macromolecular Symposia, 277*, 62-68.

Lau, C., & Mi, Y. (2002). A study of blending and complexation of poly (acrylic acid)/poly (vinyl pyrrolidone). Polymer, 43(3), 823-829.

Lee, J. H., Lee, A. S., Lee, J. C., Hong, M., Hwang, S. S., & Koo, C. M. (2015). Hybrid ionogel electrolytes for high temperature lithium batteries. *Journal of Materials Chemistry A, 3*, 2226-2233.

Lee, H., Kim, J., Lim, T., Sung, Y. E., Kim, H. J., Lee, H. N., ... Cho, Y. H. (2017). A facile synthetic strategy for iron, aniline-based non-precious metal catalysts for polymer electrolyte membrane fuel cell. *Scientific Reports, 7*, 5396-1-5396-8.

Lee, H., Yanilmaz, M., Toprakci, O., Fu, K., & Zhang, X. (2014). A review of recent developments in membrane separators for rechargeable lithium-ion batteries. *Energy Environmental Science, 7*, 3857-3886.

Le Tourneau, H. A., Birschm R. E., Korbeck, G., & Radkiewicz-Poutsm, J. L. (2005). Study of the dative bond in 2-aminoethoxydiphenyl borate at various levels of theory: another poor performance of the B_3LYP Method for B-N dative bonds. *Journal of Physical Chemistry A, 109*, 12014-12019.

Li, S., Chen, Y. M., Liang, W., Shao, Y., Liu, K., Nikolov, Z., & Zhu, Y. (2018). A Superionic Conductive, Electrochemically Stable Dual-Salt Polymer Electrolyte. *Joule, 2*(9), 1838-1856.

Li, W., Pang, Y., Liu, J., Liu, G., Wang, Y., & Xia, Y. (2017). A PEO-based gel polymer electrolyte for lithium ion batteries. *RSC Advances, 7*, 23494-23501.

Li, M. X., Wang, X., Yang, Y. Q., & Holze, R. (2015). A dense cellulosebased membrane as a renewable host for gel polymer electrolyte of lithium ion batteries. *Journal of Membrane Science, 476*, 112-118.

Li, Y., Wong, K. W., Dou, Q., Zhang, W., & Ng, K. M. (2018). Improvement of lithium-ion battery performance at low temperature by adopting ionic liquid-decorated PMMA nanoparticles as electrolyte component. *ACS Applied Energy Materials, 1*(6), 2664-2670.

Liebeck, B. M., Hidalgo, N., Roth, G., Popescu, C., & Boker, A. (2017). Synthesis and characterization of methyl cellulose/keratin hydrolysate composite membranes. *Polymers, 9*, 91-1-91-13.

Liew, C. W. (2015). *High conducting poly(vinyl alcohol)–ionic liquid based electrolytes for electric double layer capacitors (EDLCS) application* (Master's thesis, University of Malaya, Kuala Lumpur, Malaysia). Retrieved from http://studentsrepo.um.edu.my/6496/

Liew, CW., & Ramesh, S. (2015). Electrical, structural, thermal and electrochemical properties of corn starch-based biopolymer electrolytes. *Carbohydrate Polymers, 124*, 222-228.

Liew, C. W., Ramesh, S., Arof, A. K. (2014). Good prospect of ionic liquid based-poly(vinylalcohol) polymer electrolytes for supercapacitors with excellent

electrical, electrochemical and thermal properties. *International Journal of Hydrogen Energy, 39*, 2952-2963.

Liew, C. W., Ramesh, S., & Arof, A. K. (2016). Enhanced capacitance of EDLCs (electrical double layer capacitors) based on ionic liquid-added polymer electrolytes. *Energy, 109*, 546-556.

Lim, C. S., Teoh, K. H., Ng, H. M., Liew, C. W., & Ramesh, S. (2017). Ionic conductivity enhancement studies of composite polymer electrolyte based on poly (vinyl alcohol)-lithium perchlorate-titanium oxide. *Advance Materials Letters, 8*(4), 465-471.

Lim, C. S., Teoh, K. H., Liew, C. W., & Ramesh, S. (2014). Capacitive behavior studies on electrical double layer capacitor using poly (vinyl alcohol)-lithium perchlorate based polymer electrolyte incorporated with TiO_2. *Materials Chemistry and Physics, 143*, 661-667.

Lim, D. W., Sadakiyo, M., & Kitagawa, H. (2019). Proton transfer in hydrogen-bonded degenerate systems of water and ammonia in metal–organic frameworks. *Chemical Science, 10*, 16-33.

Lin, Y. C., Ito, K., & Yokohama, H. (2018). Solid polymer electrolyte based on crosslinked polyrotaxane. *Polymer, 136*, 121-127.

Liu, D., Zhong, T., Chang, P. R., Li, K., & Wu, Q. (2010). Starch composites reinforced by bamboo cellulosic crystals. *Bioresource Technology, 101*(7), 2529-2536.

Liu, H., Hu, Z., Su, Y., Ruan, H., Hu, R., & Zhang, L. (2017). MnO_2 nanorods/3D-rGO composite as high performance anode materials for Li-ion batteries. *Applied Surface Science, 392*, 777-784.

Liu, H., Yu, L., Xie, F., & Chen, L. (2006). Gelatinization of cornstarch with different amylose/amylopectin content. *Carbohydrate Polymers, 65*, 257-363.

Liu, J., Ren, X., Kang, X., He, X., Wei, P., Wen, Y., & Li, X. (2019). Fabrication of nitrogen-rich three-dimensional porous carbon composites with nanosheets and hollow spheres for efficient supercapacitors. *Inorganic Chemistry Frontiers, 6*, 2082-2089.

Liu, T. M., Saikia, D., Ho, S. Y., Chen, M. C. & Kao, H. M. (2017). High ion-conducting solid polymer electrolytes based on blending hybrids derived from monoamine and diamine polyethers for lithium solid-state batteries. *RSC Advances, 7*, 20373-20383.

Lu, D. R., Xiao, C. M., & Xu, S. J. (2009). Starch-based completely biodegradable polymer materials. *eXPRESS Polymer Letters, 3*(6), 366-375.

Lufrano, F., Staili, V. B. P., Arico, A. S., & Antonucci, V. (2008). Polymer electrolytes based on sulfonated polysulfone for direct methanol fuel cells. *Journal of Power Sources, 179*(1), 34-41.

Ma, X., Zuo, X., Wu, J., Deng, X., Xiao, X., Liu, J., & Nan, J. (2018). Polyethylene-supported ultra-thin polyvinylidene fluoride/hydroxyethyl cellulose blended polymer electrolyte for 5 V high voltage lithium ion batteries. *Journal of Materials Chemistry A, 6*(4), 1496-1503.

Mahalakshmi, N., Selvanayagam, S., Selvasekarapandian, S., Moniha, V., Manjuladevi, R., & Sangeetha, P. (2019). Characterization of biopolymer electrolytes based on cellulose acetate with magnesium perchlorate ($Mg(ClO_4)_2$) for energy storage devices. *Journal of Science: Advanced Materials and Devices, 4*(2), 276-284.

Mainar, A. R., Iruin, E., Colmenares, L. C., Kvasha, A., Meatza, I., Bengoechea, M., ... Blazquez, J. A. (2018). An overview of progress in electrolytes for secondary zinc-air batteries and other storage systems based on zinc. *Journal of Energy Storage, 15*, 304-328.

Maitz, M. F. (2015). Applications of synthetic polymers in clinical medicine. *Biosurface and Biotribology, 1,* 161-176.

Majid, S. R., & Arof, A. K. (2005). Proton-conducting polymer electrolyte films based on chitosan acetate complexed with NH_4NO_3 salt. Physica *B: Condensed Matter, 355*, 78-82.

Manaresi, P., Bignozzi, M. C., Pilati, F., Munari, A., Mastragostino, M., Meneghello, L., & Chiolle, A. (1993). Polymer electrolytes based on polyesters of thiodipropionic acid: 1. Synthesis, characterization and ionic conductivity measurements. *Polymer, 34*(11), 2422-2426.

Maragani, N., & Kumar, K. V. (2017). Ion-conducting gel polymer electrolyte based on poly (acrylonitrile) complexed with (naf + zro2): application as an electrochemical cell. *RASAYAN Journal of Chemistry, 10*(4), 1128-1136.

Masashi, K., Shufeng, S., Rika, T., Shunichi, Y., & Li, L. (2017). Improvement of Li ion conductivity of $Li_5La_3Ta_2O_{12}$ solid electrolyte by substitution of Ge for Ta. *Journal of Power Sources, 349*, 105-110.

Mason, R. N., Hu, L., Glatzhofer, D. T., & Frech, R. (2010). Infrared spectroscopic and conductivity studies of poly(N-methylpropylenimine)/ lithium triflate electrolytes. *Solid State Ionics, 180*, 1626-1632.

Mathew, S., & Abraham, T. E. (2008). Characterisation of ferulic acid incorporated starch-chitosan blend films. *Food hydrocolloids, 22*(5), 826-835.

Mathew, S., & Abraham, T. E. (2008). Characterisation of ferulic acid incorporated starch-chitosan blend films. *Food Hydrocolloids, 22*, 826-835.

Matthew, C. M., Karthika, B., Ulaganathan, M., & Rajendran, S. (2015). Electrochemical analysis on poly(ethyl methacrylate)-based electrolyte membranes. *Bulletin of Materials Science, 38*(1), 151-156.

Mattos, R. I., Raphael, E., Majid, S. R., Arof, A. K., & Pawlicka, A. (2012). Enhancement of electrical conductivity in plasticized chitosan based membranes. *Molecular Crystal Liquid Crystal, 554*, 150-159.

Mauger, A., & Julien, C. M. (2017). Critical review on lithium-ion batteries: are they safe? Sustainable?. *Ionics, 23*(8), 1933-1947.

McComsey, D. W. (2001). Zinc-carbon batteries (Leclanche and zinc chloride cell systems). In D. Linden & T.B. Reddy (Eds.), *Handbook of batteries, Third edition* (pp 8.1-8.45). New York: McGraw-Hill Professional.

Mendes, J. P., Esperanca, J. M. S. S., Medeiros, M. J., Pawlicka, A., & Silva, M. M. (2017). Structural, morphological, ionic conductivity, and thermal properties of pectin-based polymer electrolytes. *Molecular Crystals and Liquid Crystals, 643*, 266-273.

Mendes, J F., Paschoalin, R., Carmona, V. B., Sena Neto, A., Marques, A. C. P., Marconcini, J.M., ... Oliveira, J. E. (2016). Biodegradable polymer blends based on corn starch and thermoplastic chitosan processed by extrusion. *Carbohydrate Polymers, 137*, 452-458.

Michaela, K. (2018). Fuel cell development for New Energy Vehicles (NEVs) and clean air in China. *Progress in Natural Science: Materials International, 28*, 113-120.

Mishra, K., & Rai, D. K. (2013). Studies of a plasticized PEO + NH_4PF_6 proton-conducting polymer electrolyte system and its application in a proton battery. *Journal of the Korean Physical Society, 62*(2), 311-319.

Mishra, K., Pundir, S. S., & Rai, D. K. (2014). All-solid-state proton battery using gel polymer electrolyte. *AIP Conference Proceedings, 1591*, 633-635.

Mishra, K., Hashmi, S. A., & Rai, D. K. (2013). Nanocomposite blend gel polymer electrolyte for proton battery application. *Journal of Solid State Electrochemistry, 17*(3), 785-793.

Mishra, K., Hashmi, S. A., & Rai, D. K. (2014). Protic ionic liquid-based gel polymer electrolyte: structural and ion transport studies and its application in proton battery. *Journal of Solid State Electrochemistry, 18*, 2255-2266.

Mishra, K., Hashmi, S. A., & Rai, D. K. (2014). Studies on a proton battery using gel polymer electrolyte. *High Performance Polymers, 26*, 672-676.

Miyamoto, H., Yamane, C., Seguchi, M., & Okajima, K. (2009). Structure and properties of cellulose-ctarch blend films regenerated from aqueous sodium hydroxide solution. *Food Science and Technology Research, 15*, 403-412.

Mobarak, N. N., Ramli, N., Ahmad, A., & Rahman, M. Y. A. (2013). Chemical interaction and conductivity of carboxymethyl κ-carrageenan based green polymer electrolyte. *Solid State Ionics*, *224*, 51-57.

Mohamad, A. A. (2005). Degradation in polymer Ni-MH battery. *Ionics, 11*(3-4), 294-300.

Mohamad, A. A., Mohamed, N. S., Yahya, M. Z. A., Othman, R., Ramesh, S., Alias, Y., & Arof, A. K. (2003). Ionic conductivity studies of poly (vinyl alcohol) alkaline

solid polymer electrolyte and its use in nickel–zinc cells. *Solid State Ionics, 156*(1), 171-177.

Mohamed, N. S., Subban, R. H. Y., & Arof, A. K. (1995). Polymer batteries fabricated from lithium complexed acetylated chitosan. *Journal of Power Sources, 56*, 153-156.

Monisha, S., Mathavana, T., Selvasekarapandian, S., Milton, T., Franklin, B., Aristatil, G., … Vinoth, D. (2017). Investigation of bio polymer electrolyte based on cellulose acetate-ammonium nitrate for potential use in electrochemical devices. *Carbohydrate Polymers, 157*, 38-47.

Morales, J., Petkova, G., Cruz, M., & Caballero, A. (2006). Synthesis and characterization of lead dioxide active material for lead-acid batteries. *Journal of Power Sources, 158*(2), 831-836.

Mostafa, N. A., Farag, A. A., Abo-dief, H. M., & Tayeb, A. M. (2018). Production of biodegradable plastic from agricultural wastes. *Arabian Journal of Chemistry, 11*(4), 546-553.

Moura, M. R., & Azeredo, H. M. C. (2012). Microfluidizer technique for improving microfiber properties incorporated into edible and biodegradable films. In R. Kelly (Eds.), *Advances in Microfluidics* (pp. 200-240).

Mudila, H., Praksher, P., Kumar, M., Kumar, A., Zaidi, M. G. H., & Kumar, A. (2019). Critical analysis of polyindole and its composites in supercapacitor application. *Materials for Renewable and Sustainable Energy, 8*(9), 1-19.

Mujaheddin, Jagadish, R. L., Sheshappa, R. K., & Guru, G. S. (2012). Miscibility Studies of Agar-Agar/Starch blends using Various Techniques. *International Journal of Research in Pharmacy and Chemistry, 2*, 2231-2781.

Mukoma, P., Jooste, B. R., & Vosloo, H. C. M., (2004). Synthesis and characterization of crosslinked chitosan membranes for application as alternative proton exchange membrane materials in fuel cells. *Journal of Power Sources, 136*, 16-23.

Muldoon, J., Bucur, C. B, Boaretto, N., Gregory, Th., & Di Noto, V. (2015) Polymers: opening doors to future batteries. *Polymer Reviews, 55*, 208-246.

Muscat, D., Adhikari, B., Adhikari, R., & Chaudhary, D. (2012). Comparative study of film forming behaviour of low and high amylose starches using glycerol and xylitol as plasticizers. *Journal of Food Engineering, 109*(2), 189-201.

Muthuvinayagam, M., & Gopinathan, C. (2015). Characterization of proton conducting polymer blend electrolytes based on PVdF-PVA. *Polymer, 68*, 122-130.

Muthukrishnan, M., Shanthi, C., Selvasekarapandian, S., Manjuladev, R., Perumal, P., & Chrishtopher Selvin, P. (2018). Synthesis and characterization of pectin-based biopolymer electrolyte for electrochemical applications. *Ionics, 25*(4), 1-12.

Munichandraiah, N., Scanlon, L. G., Marsh, R. A., Kumar, B., & Sircar, A. K. (1995). Influence of zeolite on electrochemical and physicochemical properties of polyethylene oxide solid electrolyte. *Journal of Applied Electrochemistry, 25*, 857-863.

Na, W., Wei, W., Yu, W., & Taohai, L. (2017). Studies on the Effect of Nano-Sized MgO in Magnesium-Ion Conducting Gel Polymer Electrolyte for Rechargeable Magnesium Batteries. *Energies, 10*, 1215-1225.

Nafchi, A. M., Alias, A. K., Mahmud, S., & Robal, M. (2012). Antimicrobial, rheological, and physicochemical properties of sago starch films filled with nanorod-rich zinc oxide. *Journal of Food Engineering, 113*, 511-519.

Nagraj, P., Sasidharan, A., David, V., & Sambandam, A. (2017). Effect of cross-linking on the performances of starch-based biopolymer as gel electrolyte for dye-sensitized solar cell applications. *Polymers, 9*, 667-1-667-13.

Naimi, T. S. R., Aung, M. M., Ahmad, A., Rayung, M., Su'ait, M. S., Yusof, N. A., & Lae, K. Z. W. (2018). Enhancement of plasticizing effect on bio-based polyurethane acrylate solid polymer electrolyte and its properties. *Polymers, 10*, 1142-1-1142-18.

Nemazifard, M., Kavoosi, G., Marzban, Z., & Ezedi, N. (2017). Physical, mechanical, water binding, and antioxidant properties of cellulose dispersions and cellulose film incorporated with pomegranate seed extract. *International Journal of Food Properties, 20*(S2), S1501-S1514.

Ng, L. S., & Mohamad, A. A. (2008). Effect of temperature on the performance of proton batteries based on chitosan–NH_4NO_3–EC membrane. *Journal of Membrane Science, 325,* 653-657.

Ng, B. C., Wong, H. Y., Chew, K. W., & Osman, Z. (2011). Development and characterization of poly-ε-caprolactone based polymer electrolyte for lithium rechargeable battery. *International Journal of Electrochemical Science, 6*, 4355-4364.

Nik Aziz, N. A., Idris, N. K., & Isa, M. I. N. (2010). Proton conducting polymer electrolytes of methylcellulose doped ammonium fluoride: Conductivity and ionic transport studies. *International Journal of the Physical Sciences, 5*, 748-752.

Nishida, R., & Takahashi, M. (2008). Self-assembled orientation of polymer chains in methylcellulose gel during drying process. *Polymer Journal, 40*, 148-153.

Noor, I. M. (2016). Characterization and transport properties of PVA–LiBOB based polymer electrolytes with application in dye sensitized solar cells (Doctoral thesis, University of Malaya, Kuala Lumpur, Malaysia). Retrieved from http://studentsrepo.um.edu.my/7017/

Noor, S. A. M., Ahmad, A., Rahman, M. Y. A., & Talib, I. A. (2010). Solid polymeric electrolyte of poly(ethylene)oxide-50% epoxidized natural rubber-lithium triflate (PEO-ENR50-$LiCF_3SO_3$). *Natural Science, 2*, 190-196.

Noor, I. S., Majid, S. R., & Arof, A. K. (2013). Poly(vinyl alcohol)-LiBOB complexes for lithium-air cells. *Electrochimica Acta, 102*, 149-160.

Noronha, C. M., de Carvalho, S. M., Lino, R. C. & Barreto, P. L. M. (2014). Characterization of antioxidant methylcellulose film incorporated with a-tocopherol nanocapsules. *Food Chemistry, 159*, 529-535.

Nurhaziqah, A. M. S., Afiqah, I. Q., Aziz, M. F. H., Aziz, N. A., & Hasiah, S. (2018). Optical, structural and electrical studies of biopolymer electrolytes based on methylcellulose doped with $Ca(NO_3)_2$. *IOP Conference Series: Materials Science and Engineering, 440*, 012034-1-012034-7.

Nuwamanya, E., Baguma, Y., Emmambux, N., & Rubaihayo, P. (2010). Crystalline and pasting properties of cassava starch are influenced by its molecular properties. *African Journal of Food Science, 4*, 8-15.

Nyamweya, N., & Hoag, S. W. (2000). Assessment of polymer-polymer gas chromatography, rheology, and spectroscopic techniques. *Pharmaceutical Research, 17,* 625-631.

Nyuk, C. M. N., & Isa, M. I. N. (2017). Solid biopolymer electrolytes based on carboxymethyl cellulose for use in coin cell proton batteries. *Journal of Sustainability Science and Management, 2017*(2), 42-48.

Oladunmoye, O. O., Aworh, O. C., Maziya-Dixon, B., Erukainure, O. L., & Elemo, G. N. (2014). Chemical and functional properties of cassava starch, durum wheat semolina flour, and their blends. *Food Science & Nutrition, 2*, 132-138.

Othman, S. H. (2014). Bio-nanocomposite materials for food packaging applications: types of biopolymer and nano-sized filler. *Agriculture and Agricultural Science Procedia, 2*, 296-303.

Osman, Z., Ghazali, M. I., & Othman, L., & Isa K. B. (2012). AC ionic conductivity and DC polarization method of lithium ion transport in PMMA–$LiBF_4$ gel polymer electrolytes. *Results in Physics, 2*, 1-4.

Pandey, M., Joshi, G. M., & Ghosh, N. N. (2017). Ionic conductivity and diffusion coefficient of barium-chloride-based polymer electrolyte with poly(vinyl alcohol)–poly(4-styrenesulphonic acid) polymer complex. *Bulletin of Materials Science, 40*(4), 655-666.

Park, M., Ibanez, A. N., & Shoemaker, C. F. (2007). Rice Starch Molecular Size and its Relationship with Amylose Content. *Starch-Starke, 59*, 69-77.

Park, S. B., Lih, E., Park, K. S., Joung, Y. K., & Han, D. K. (2017). Biopolymer-based functional composites for medical applications. *Progress in Polymer Science, 68*, 77-105.

Perďochová, D., Tomanová, K., Alexy, P., Bočkaj, J., Feranc, J., Plavec, R., ... Přikryl, R. (2017). The influence of additives on crystallization of blends based on polylactid acid. *Materials Science and Engineering, 266*, 012014-1-012014-10.

Polu, A. R., & Kumar, R. (2013). Preparation and characterization of PVA based solid polymer electrolytes for electrochemical cell applications. *Chinese Journal of Polymer Science, 31*, 641-648.

Pozyczka, K., Marzantowicz, M., Dygas, J. R., & Krok, F. (2017). Ionic conductivityand lithium transference number of poly (ethylene oxide):litfsi system. *Electrochimica Acta,* 227, 127-153.

Pradhan, D. K, Choudhary, R. N. P., & Samantaray, B. K. (2009). Studies of dielectric and electrical properties of plasticized polymer nanocomposite electrolytes. *Material Chemistry and Physics, 115*, 557-561.

Pradima, J., Kulkarni, M. R., & Archna, P. (2016). Review on enzymatic synthesis of value added products of glycerol, a by-product derived from biodiesel production. *Resource-Efficient Technologies, 3*(4), 394-405.

Prajapati, G. K., Roshan, R., & Gupta, P. N. (2010). Effect of plasticizer on ionic transport and dielectric properties of PVA–H_3PO_4 proton conducting polymeric electrolytes. *Journal of Physics and Chemistry of Solids, 71*, 1717-1723.

Pratap, R., Singh, B., & Chandra, S. (2006). Polymeric rechargeable solid state proton battery. *Journal of Power Sources, 161*, 702-706.

Premalatha, M., Vijaya, N., Selvalakshmi, S., & Monisha, S. (2015). Study of proton conducting blend polymer electrolyte based on PVA-PVP. *Indian Journal of Research, 4*(6), 189-192.

Prokhorov, E., Luna-Bárcenas, G., González-Campos, J., Kovalenko, Y., García, C. Z., & Mota-Morales, J. (2016). Proton conductivity and relaxation properties of chitosan-acetate films. *Electrochimica Acta, 215*, 600-608.

Qi, L., Juner, C., Lei, F., Xueqian., & Yingying, L. (2016). Progress in electrolytes for rechargeable Li-based batteries and beyond. *Green Energy & Environment, 1*, 18-42.

Qian, X., Gu, N., Cheng, Z., Yang, X., Wang, E., & Dong, S. (2001). Impedance study of $(PEO)_{10}LiClO_4$-Al2O_3 composite polymer electrolyte with blocking electrodes. *Electrochimica Acta, 46*, 1829-1836.

Radivojevic, V. M., Rupcic, S., Srnovic, M., & Bensic, G. (2018). Measuring the dielectric constant of paper using a parallel plate capacitor. *International Journal of Electrical and Computer Engineering Systems, 9*(1), 1-10.

Rahaman, M. H. A., Khandaker, M. U., Khan, Z. R., Kufian, M. Z., Noor, I. S. M., & Arof, A. K. (2014). Effect of gamma irradiation on poly(vinyledene difluoride)-lithium bis(oxalato)borate electrolyte. *Physical Chemistry Chemical Physics, 16*, 11527- 11537.

Rahman, M. M., Gruner, G., Al-Ghamdi, M. S., Daous, M. A., Khan, S. B., & Asiri, A. M. (2013). Chemo-sensors development based on low-dimensional codoped Mn_2O_3-ZnO nanoparticles using flat-silver electrodes. *Chemistry Central Journal, 7*, 60-1-60-12.

Rahman, N. A., Hanifah, S. A., Mobarak, N. N., Su'ait M. S., Ahmad, A., Shyuan, L. K., & Khoon, L. T. (2019). Synthesis and characterizations of onitrochitosan based biopolymer electrolyte for electrochemical devices. P*los ONE, 14*(2), 1-17.

Rajendran, S., Sivakumar, M., & Subadevi, R. (2004). Li-ion conduction of plasticized PVA solid polymer electrolytes complexed with various lithium salts. *Solid State Ionics, 167*(3-4), 335-339.

Ramesh, S., & Arof, A. K. (2001). Ionic conductivity studies of plasticized poly(vinyl chloride) polymer electrolytes. *Material Science Engineering B, 85*, 11-15.

Ramesh, S., & Liew, C. W. (2013). Dielectric and FTIR studies on blending of [xPMMA-(1 - x)PVC] with LiTFSI. *Measurement, 46*, 1650-1656.

Ramesh, S., Shanti, R., & Morris, E. (2012). Studies on the thermal behavior of CS:LiTFSI:[Amim] Cl polymer electrolytes exerted by different [Amim] Cl content. *Solid State Sciences, 14*(1), 182-186.

Ramly, K., Isa, M. I. N., & Khiar, A. S. A. (2011). Conductivity and dielectric behaviour studies of starch/PEO+x wt-% NH_4NO_3 polymer electrolyte. *Materials Research Innovations, 15*, S82-S85.

Rani, M. S. A., Ahmad, A., & Mohamed, N. S. (2017). A comprehensive investigation on electrical characterization and ionic transport properties of cellulose derivative from kenaf fibre-based biopolymer electrolytes. *Polymer Bulletin, 75*(11), 5061-5074.

Rani, S. A., Mohamed, N. S., & Isa, M. I. N. (2016). Characterization of proton conducting carboxymethyl cellulose/chitosan dual-blend based biopolymer electrolytes. *Materials Science Forum, 846*, 539-544.

Rasali, N. M. J., & Samsudin, A. S. (2018). Ionic transport properties of protonic conducting solid biopolymer electrolytes based on enhanced carboxymethyl cellulose-NH_4Br with glycerol. *Ionics, 24*(6), 1639-1650.

Rasali, N. M. J., Muzakir, S. K., & Samsudin, A. S. (2017). A study on dielectric properties of the cellulose derivative-NH_4Br-glycerol based the solid polymer electrolyte system. *Makara Journal of Technology, 21*(2), 65-69.

Ratner, M. A. (1987). Aspects of the theoretical treatments of polymer solid electrolytes: Transport theory and models. *In polymer electrolyte review, I*, 173-237.

Ravi, M., Kumar, K. K., Mohan, V. M., & Rao, V. V. R. N. (2014). Effect of nano TiO_2 filler on the structural and electrical properties of PVP based polymer electrolyte films, *Polymer Testing, 33*, 152-160.

Rebelo, R., Fernandes, M., & Fangueiro, R. (2017). Biopolymers in Medical Implants: A Brief Review. *Procedia Engineering, 200*, 236-243.

Rigo, E., Dong, Z., Park, J. H., Kennedy, E., Hokmabadi, M.,Garcia, L., ... Timp, G. (2019). Measurements of the size and correlations between ions using an electrolytic point contact. *Nature Communications, 10*, 2382-1-2382-13.

Rivas, B. L., Maureira, A., Guzmán, C., & Mondaca, M. A. (2009). Poly(2-acrylamido glycolic acid-co-2-acrylamido-2-methyl-1-propane sulfonic acid): synthesis, characterization, and retention properties for environmentally impacting metal ions. *Journal of Applied Polymer Science, 111*, 78-86.

Rodriguez, C. W., Flores, F. J., Martinez, F., Castillo, F., & Espinoza, F. J. (2015). Nanomechanical properties and thermal stability of recycled cellulose reinforced starch-gelatin polymer composite. *Journal of Applied Polymer Science, 132*(14), 41787-1-41787-7.

Rohan, R., Sun, Y., Cai, W., Zhang, Y., Pareek, K., Xu, G., & Cheng, H. (2014). Functionalized polystyrene based single ion conducting gel polymer electrolyte for lithium batteries. *Solid State Ionics, 268*, 294-299.

Roscher, M. A., Bohlen, O., & Vetter, J. (2011). OCV hysteresis in Li-ion batteries including two-phase transition materials. *International Journal of Electrochemistry, 2011*, 984320-1-984320-6.

Rubio, A. M., Flanagan, B. M., Gilbery, E. P., & Gidley, M. J. (2008). A novel approach for calculating starch crystallinity and its correlation with double helix content: a combined XRD and NMR study. *Biopolymers, 89*(9), 761-768.

Rudziah, S., Mohamed, N. S., & Ahmad, A. (2013). Conductivity and structural studies of poly(vinylidene fluoride co-hexafluoropropylene)/polyethyl methacrylate blend doped with ammonium triflate. *International Journal of Electrochemical Science, 8*(1), 421-434.

Sahli, N., & Ali, A. M. M. (2012). Effect of lithium triflate salt concentration in methyl cellulose-based Solid Polymer Electrolytes. *IEEE Colloquium on Humanities, Science & Engineering Research,* 739-742.

Salanne, M., Rotenberg, B., Naoi, K., Kaneko, K., Taberna, P. L., Grey, C. P., ... Simon, P. (2016). Efficient storage mechanisms for building better supercapacitors. *Nature Energy, 1*, 16070-1-16070-10.

Salleh, N. S., Aziz, S. B., Aspanut, Z., & Kadir M. F. Z. (2016). Electrical impedance and conduction mechanism analysis of biopolymer electrolytes based on methyl cellulose doped with ammonium iodide. *Ionics*, *22*, 2157-2167.

Salman, Y. A. K., Abdullah, O. G., Hanna, R. R., & Aziz, S. B. (2018). Conductivity and electrical properties of chitosan-methylcellulose blend biopolymer electrolyte incorporated with lithium tetrafluoroborate. *International Journal of Electrochemical Science, 13*, 3185-3199.

Sampathkumar, L., Selvin, P. C., Selvasekarapandian, S., Perumal, P., Chitra, R., & Muthukrishnan, M. (2019). Synthesis and characterization of biopolymer electrolyte based on tamarind seed polysaccharide, lithium perchlorate and ethylene carbonate for electrochemical applications. *Ionics, 25*, 1067-1082.

Samsudin, A. S., & Isa, M. I. N. (2015). Conductivity study on plasticized solid bioelectrolytes CMC-NH_4Br and application in solid-state proton batteries. *Jurnal Teknologi, 78*(6-5), 43-48.

Samsudin, A. S., Khairul, W. M., & Isa, M. I. N. (2012). Characterization on the potential of carboxy methylcellulose for application as proton conducting biopolymer electrolytes. *Journal of Non-Crystalline Solids, 358*, 1104-1112.

Samsudin, A. S., Lai, H. M, & Isa, M. I. N. (2014). Biopolymer materials based carboxymethyl cellulose as a proton conducting biopolymer electrolyte for application in rechargeable proton battery. *Electrochimica Acta, 129*, 1-13.

Sanyang, M., Sapuan, S. M., Jawaid, M., Ishak, M. R., & Sahari, J. (2015). Effect of plasticizer type and concentration on tensile, thermal and barrier properties of biodegradable films based on sugar palm (arenga pinnata) starch. *Polymers, 7*, 1106-1124.

Sechi, N. S., & Marques, P. T. (2017). Preparation and physicochemical, structural and morphological characterization of phosphorylated starch. *Materials Research, 20*(2), 174-180.

Sekhar, P. C., Kumar, P. N., & Sharma, A. K. (2012). Effect of plasticizer on conductivity and cell parameters of (PMMA+$NaClO_4$) polymer electrolyte system. *Journal of Applied Physics, 2,* 1-6.

Sellam, & Hashmi, S.A. (2012). Enhanced zinc ion transport in gel polymer electrolyte. *Journal of Solid State Electrochemistry, 16*(9), 3105-3114.

Sellam, & Hashmi, S. A. (2013). High rate performance of flexible pseudocapacitors fabricated using ionic-liquid-based proton conducting polymer electrolyte with poly(3, 4-ethylenedioxythiophene):poly(styrene sulfonate) and its hydrous ruthenium oxide composite electrodes. *ACS Applied Materials Interfaces, 5*(9), 3875-3883.

Selvasekarapandian, S., Baskaran, R., & Hema, M. (2005). Complex AC impedance, transference number and vibrational spectroscopy studies of proton conducting PVAc–NH_4SCN polymer electrolytes. *Physica B*, 357, 412-419.

Selvasekarapandian, S., Hema, M., Kawamura, J., Kamishima, O., & Baskaran, R. (2010). Characterization of PVA-NH_4NO_3 polymer electrolyte and its application in rechargeable proton battery. *Journal of Physic Society Japan, 79*, 163-168.

Sengwa, R. J., Dhatarwal, P., & Choudhary, S. (2015). Effects of plasticizer and nanofiller on the dielectric dispersion and relaxation behaviour of polymer blend based solid polymer electrolytes. *Current Applied Physics, 15,* 135-143.

Senna, M. M., El-Shahat, H. A., & El-Naggar, A. W. (2011). Characterization of gamma irradiated plasticized starch/poly (vinyl alcohol) (PLST/PVA) blends and their application as protected edible materials. *Journal of Polymer Research*, *18*, 763-771.

Shamsuddin, L., Noor, L. M., Albinsson, I., Mellander, B. E., & Arof, A. K. (2017). Perovskite solar cells using polymer electrolytes. *Molecular Crystal Liquid Crystal, 655*(1), 181-194.

Sheng, O., Jin, C., Luo, J., Yuan, H., Fang, C., Huang, H., ... Tao, X. (2017). Ionic conductivity promotion of polymer electrolyte with ionic liquid grafted oxides for all-solid-state lithium–sulfur batteries. *Journal of Materials Chemistry A, 5*, 12934-12942.

Shuhaimi, N. E. A. (2011*). Ionic conductivity and related studies in methyl cellulose based polymer electrolytes and application in supercapacitors.* (Master's thesis, Univeristy of Malaya, Kuala Lumpur, Malaysia). Retrieved from http://studentsrepo.um.edu.my/1978/

Shuhaimi, N. E. A., Alias, N. A., Kufian, M. Z., Majid, S. R., & Arof, A. K. (2010). Characteristics of methyl cellulose-NH_4NO_3-PEG electrolyte and application in fuel cells. *Journal of Solid State Electrochemistry, 14*, 2153-2159.

Shuhaimi, N. E. A., Alias, N. A., Majid, S. R., & Arof, A. K. (2008). Electrical double layer capacitor with proton conducting κ-carrageenan-chitosan electrolytes. *Functional Materials Letters, 1*, 195-201.

Shuhaimi, N. E. A., Majid, S. R., & Arof, A. K. (2010). On complexation between methyl cellulose and ammonium nitrate. *Materials Research Innovations, 13*(3), 239-242

Shuhaimi, N. E. A., Teo, L. P., Majid, S. R., & Arof, A. K. (2010). Transport studies of NH_4NO_3 doped methyl cellulose electrolyte. *Synthetic Metal, 160*, 1040-1044.

Shuhaimi, N. E. A., Teo, L. P., Woo, H. J., Majid, S. R., & Arof, A. K. (2012). Electrical double-layer capacitors with plasticized polymer electrolyte based on methyl cellulose. *Polymer Bulletin, 69*, 807-826.

Shukur, M. F. (2015). *Characterization of ion conducting solid biopolymer electrolytes based on starch-chitosan blend and application in electrochemical devices.* (Doctoral thesis, University of Malaya, Malaysia). Retrieved from http://studentsrepo.um.edu.my/5943/

Shukur, M. F., Azmi, M. S., Zawawi, S. M. M., Majid, N. A., Illias, H.A., & Kadir, M.F.Z. (2013a). Conductivity studies of biopolymer electrolytes based on chitosan incorporated with NH_4Br. *Physica Scripta, T157*, 014049-014054.

Shukur, M. F., Ithnin, R., & Kadir M. F. Z. (2014a). Electrical characterization of corn starch-LiOAc electrolytes and application in electrochemical double layer capacitor. *Electrochimica Acta,136*, 204-216.

Shukur, M. F., Ithnin, R., & Kadir, M. F. Z. (2014b). Electrical properties of proton conducting solid biopolymer electrolytes based on starch–chitosan blend. *Ionics, 20*, 977-999.

Shukur, M. F., Ithnin, R., & Kadir, M. F. Z. (2016). Ionic conductivity and dielectric properties of potato starch-magnesium acetate biopolymer electrolytes: the effect of glycerol and 1-butyl-3-methylimidazolium chloride. *Ionic, 22,* 1113-1123.

Shukur, M. F. & Kadir, M. F. Z. (2015). Electrical and transport properties of NH_4Br-doped cornstarch-based solid biopolymer electrolyte. *Ionics, 21*, 111-124.

Shukur, M. F., & Kadir, M. F. Z. (2015). Hydrogen ion conducting starch chitosan blend based electrolyte for application in electrochemical devices. *Electrochimica Acta, 158*, 152-165.

Shukur, M. F., Majid, N. A., Ithnin, R. & Kadir M. F. Z. (2013b). Effect of plasticization on the conductivity and dielectric properties of starch–chitosan blend biopolymer electrolytes infused with NH_4Br. *Physica Scripta, T157*, 014051-014057.

Sikkanthar, S., Karthikeyan, S., Selvasekarapandian, S., Pandi, D. V., Nithya, S., & Sanjeeviraja, C. (2014). Electrical conductivity characterization of polyacrylonitrile-ammonium bromide polymer electrolyte system. *Journal of Solid State Electrochemistry, 19*(4), 987-999.

Sim, L. N., Majid, S. R., & Arof, A. K. (2012). FTIR studies of PEMA/PVdFHFP blend polymer electrolyte system incorporated with $LiCF_3SO_3$ salt. *Vibrational Spectroscopy, 58*, 57-66.

Simari, C., Lufrano, E., Coppola, L., & Nicotera, I. (2018). Composite Gel Polymer Electrolytes Based on Organo-Modified Nanoclays: Investigation on Lithium-Ion Transport and Mechanical Properties. *Membranes, 8*, 69-84.

Simonetti, E., Carewsk, M., Maresca, G., De Francesco, M., & Appetecchi, G. B. (2017) Highly conductive, ionic liquid-based polymer electrolytes. *Journal of The Electrochemical Society, 164*, A6213-A6219.

Singal, A. K. (2013). The Internal Resistance of a Battery. *Physics Education, 33*, 1-7. Retrieved from https://arxiv.org/pdf/1308.4913.pdf

Singh, V., Ali, S. Z., Somashekar, R., & Mukherjee, P. S. (2006). Nature of crystallinity in native and acid modified starches. *International Journal of Food Properties, 9*(4), 845-854.

Singh, N., Singh, J., & Sodhi, N. S. (2002). Morphological, thermal, rheological and noodle-making properties of potato and corn starch. *Journal of Science of Food Agriculture. 82*, 1376-1383.

Singh, R., Polu, A. R., Bhattacharya, B., Rhee, H. W., Varlikli, C., & Singh, P. K. (2016). Perspectives for solid biopolymer electrolytes in dye sensitized solar cell and battery application. *Renewable and Sustainable Energy Reviews, 65*, 1098-1117.

Song, S., Wang. J., Tang. J., Muchakayala, R., & Ma, R. (2017). Preparation, properties, and Li-ion battery application of EC + PC-modified PVdF-HFP gel polymer electrolyte films. *Ionics, 23*(12), 3365-3375.

Speight, J. G., & Speight, J. (2002). *Chemical and process design handbook*: McGrawHill New York.

Srivastava, N., & Chandra, S. (2000). Studies on a new proton conducting polymer system:poly(ethylene succinate) + NH_4ClO_4. *European Polymer Journal, 36*, 421-433.

Stephan, A. M., Kumar, T. P., Kulandainathan, M. A., & Lakshmi, N. A. (2009). Chitin-incorporated poly (ethylene oxide)-based nanocomposite electrolytes for lithium batteries. *The Journal of Physical Chemical B, 113*, 1963-1971.

Stoller, M. D. & Ruoff, R. S. (2010). Best practice methods for determining an electrode material's performance for ultracapacitors. *Energy & Environmental Science, 3*, 1294-1301.

Strzelczyk, A., Jasinski, G., & Chachulski, B. (2016). Investigation of solid polymer electrolyte gas sensor with different electrochemical techniques. *IOP Conference Series: Materials Science and Engineering, 104*(1), 012029-1-012029-8.

Su'ait, M. S., Ahmad, A., Badri, K. H., Mohamed, N. S., Rahman, M. Y. A., Ricardo, C. L., & Scardi, P. (2014). The potential of polyurethane bio-based solid polymer electrolyte for photoelectrochemical cell application. *International Journal of Hydrogen Energy, 39*(6), 3005-3017.

Subban, R. H. Y., & Arof, A. K. (2004). Plasticiser interactions with polymer and salt in PVC-$LiCF_3SO_3$-DMF electrolytes. *European Polymer Journal, 40*, 1841-1847.

Subba Reddy, C. V., Jin, A. P., Zhu, Q. L., Mai, L. Q. X., & Chen, W. (2006). Preparation and characterization of (PVP + $NaClO_4$) electrolytes for battery applications. *The European Physical Journal E, 19*, 471-476.

Subramanian, V., Zhu, H., & Wei, B. (2008). Nanostructured manganese oxides and their composites with carbon nanotubes as electrode materials for energy storage devices. *Pure and Applied Chemistry, 80*, 2327-2343.

Sudhakar, Y. N., & Selvakumar, M. (2013). Ionic conductivity studies and dielectric studies of Poly(styrene sulphonic acid)/starch blend polymer electrolyte containing $LiClO_4$, *Journal of Applied Electrochemistry, 43*, 21-29.

Sugumaran, T., Silvaraj, D. S., Saidi, N. M., Farhana, N. K., Ramesh, K., & Ramesh, S. (2019). The conductivity and dielectric studies of polymer electrolytes based on iota-carrageenan with sodium iodide and 1-butyl-3-methylimidazolium iodide for the dye-sensitized solar cells. *Ionics, 25*(2), 763-771.

Sun, Y., Tang, J., Qin, F., Juan, J., Zhang, K., Jing, L., ... Cin, L. C. (2017). Hybrid lithium-ion capacitors with asymmetric graphene electrodes. *Journal of Materials Chemistry A, 5*, 13601-13609.

Suthanthiraraj, S. A., Kumar, R., & Paul, B. J. (2011). Dielectric relaxation studies in soft–matter like nanocomposite polymer electrolyte PPG_4–$AgCF_3SO_3$: MgO. *Transactions of the Indian Institute of Metals, 64*(1-2), 155-158.

Swain, A. B., Rath, M., Biswas, P. P., Rao, M. S., & Murugavel, P. (2019). Polarization controlled photovoltaic and self-powered photodetector characteristics in Pb-free ferroelectric thin film. *APL Materials, 7*(1), 011106-1-011106-7.

Synytsya, A., & Novak, M. (2014). Structural analysis of glucans. *Annals of Translational Medicine, 2*(2), 1-14.

Taer, E., Taslim, R., Aini, Z., Hartati, S. D., & Mustika, W. S. (2017). Activated carbon electrode from banana-peel waste for supercapacitor applications. *AIP Conference Proceedings, 1801*, 040004-1-040004-4.

Taghavikish, M., Subianto, S., Gu, Y., Sun, X., Zhao, X. S. & Roy Choudhury, N. (2018). A Poly(ionic liquid) Gel Electrolyte for Efficient all Solid Electrochemical Double-Layer Capacitor. *Scientific Reports, 8*, 10918-1-10918-10.

Tamilselvi, P., & Hema, M. (2014). Conductivity studies of $LiCF_3SO_3$ doped PVA: PVdF blend polymer electrolyte. *Physica B, 437*, 53-57.

Tan, C.H., Ahmad, A., & Anuar F.H. (2014). Synthesis and characterization of polylactide-poly(ethylene glycol) block copolymer as solid polymer electrolyte. *Asian Journal of Chemistry, 26*, S230-S236.

Tang, R., Jiang, C., Qian, W., Jian, J., Zhang, X., Wang, H., & Yang, H. (2015). Dielectric relaxation, resonance and scaling behaviors in $Sr_3Co_2Fe_{24}O_{41}$ hexaferrite. *Scientific Reports, 5*, 13645-1-13645-11.

Teoh, K.H. (2012). *Effect of doping fillers towards corn starch based green polymer electrolytes* (Master's thesis, University of Malaya, Kuala Lumpur, Malaysia). Retrieved from http://studentsrepo.um.edu.my/4175

Teoh, K. H., Liew, C. W., & Ramesh, S. (2014). Electric double layer capacitor based on activated carbon electrode and biodegradable composite polymer electrolyte. *Ionics, 20*, 251-258.

Teoh, K. H., Lim, C. S., Liew, C. S., Ramesh, S., & Ramesh, S. (2015). Electric double-layer capacitors with corn starch-based biopolymer electrolytes incorporating silica as filler. *Ionics, 21*(7), 2061-2068.

Teramoto, N., Motoyama, T., Mosomiya, R., & Shibata, M. (2003). Synthesis, thermal properties, and biodegradability of propyl-etherified starch. *European Polymer Journal, 39*, 255-261.

Terinte, N., Ibbett, R., & Schuster, K. C. (2011). Overview on native cellulose and microcrystalline cellulose structure studied by x-ray diffraction (waxd): comparison between measurement techniques. *Lenzinger Berichte, 89*, 118-131.

Tian, F., & Ohki, Y. (2014). Electric modulus powerful tool for analyzing dielectric behavior. *IEEE Transactions on Dielectrics and Electrical Insulation, 21*(3), 929-931.

Tiwari, T., Srivastava, N., & Srisvastava, P. C. (2013). Ion dynamics study of potato starch + sodium salts electrolyte system. *International Journal of Electrochemistry, 2013*, 1-8.

Tongdeesoon, W., Mauer, L.J., Wongruong, S., Sriburi, P., & Rachtanap, P. (2011). Effect of carboxymethyl cellulose concentration on physical properties of biodegradable cassava starch-based films. *Chemical Central Journal, 5*, 1-8.

Tora, R. O., Jimenez, A., Talens, P., & Chiralt, A. (2014). Properties of starch–hydroxypropyl methylcellulose based films obtained by compression molding. *Carbohydrate Polymers, 109*, 155-165.

Tran, C., & Kalra, V. (2013). Fabrication of porous carbon nanofibers with adjustable pore sizes as electrodes for supercapacitors. *Journal of Power Sources, 235*, 289-296.

Tripathi, A. K., & Singh, R. K. (2018). Lithium salt assisted enhanced performance of supercapacitor based on quasi solid-state electrolyte. *Journal of Saudi Chemical Society, 22*, 838-845.

Tripathi, M., & Kumar, A. (2018). Electrochemical studies of EDLC Cells fabricated using drum stick (DS) activated charcoal. *Material Today: Proceedings, 5*(7), 15458-15465.

Tuan, T. S. R., Aung, M. M., Ahmad, A., Rayung, M., Su'ait, M. S., Yusof, N. A., & Lee, K. Z. W. (2018). Enhancement of plasticizing effect on bio-based polyurethane acrylate solid polymer electrolyte and its properties. *Polymers, 10*, 1-18.

Vani, G. N. S., Raja, V., Sharma, A. K., & Rao, V. V. R. (2013). Development of PVP based polymer electrolytes for solid state battery applications. T International *Journal of Research in Engineering and Advanced Technology, 1*(3), 1-10.

Vanysek, P. (2011). Electrochemical series. In W.M. Haynes (Ed.), *Handbook of Chemistry and Physics 92nd Edition* (pp. 5-80). Boca Raton: CRC Press.

Vieira, J. G., Filho, G. R., Meireles, C. S., Faria, F. A. C., Gomide, D. D., Pasquini, D., ... Motta, L. (2012). Synthesis and characterization of methylcellulose from cellulose extracted from mango seeds for use as a mortar additive. *Polimeros, 22*(1), 80-87.

Vijaya, N., Selvasekarapandian, S., Malathi, J., Iwai, Y., Nithya, H., & Kawamura, J. (2013). NMR study on PVP-NH_4Cl based- proton conducting polymer electrolyte. *Indian Journal of Applied Research, 3*, 506-510.

Vodrak, J., Kova, M. S., Velicka, J. Klapste, B., Novak, T., & Reiter, J. (2001). Gel polymer electrolytes based on PMMA. *Electrochimica Acta, 46*(13-14), 2047-2048.

Vroman, I., & Tighzert, L. (2009). Biodegradable polymers. *Materials (Basel), 2*(2), 307-344.

Wagner, J. B., & Wagner, C. B. (1957). Electrical conductivity measurements on cuprous halides. *Journal of Chemical Physics, 26*(6), 1597-1601.

Watanabe, M., Nagano, S., Sanui, K., & Ogata, N. (1988). Estimation of Li+ transport number in polymer electrolytes by the combination of complex impedance and potentiostatic polarization measurements. *Solid State Ionics, 28*, 911-917.

Wang, C.Y., Sun, J., Liu, H.K., Dou, S.X., MacFarlace, D., & Forsyth, M. (2005). Potential application of solid electrolyte P11OH in Ni/MH batteries. *Synthetic Metals, 152*, 57-60.

Wang, H., Bai, Y., Chen, S., Luo, X., Wu, C., Wu, V., & Lu, K. (2015). Amine, binder-free V_2O_5 cathode for greener rechargeable aluminum battery. *ACS Applied Material. Interfaces 7,* 80-84.

Wang, H., Lin, J., & Shen, Z. X. (2016). Polyaniline (PANi) based electrode materials for energy storage and conversion. *Journal of Science: Advanced Materials and Devices, 1*(3), 225-255.

Wang, S., Li., C., Niu, Q., & Wang, S. (2015). Starch retrogradation: A comprehensive review. *Comprehensive Reviews in Food Science and Food Safety, 14*, 568-585.

Wang, W., & Alexandridis, P. (2016). Composite polymer electrolytes: nanoparticles affect structure and properties. *Polymers, 8*(11), 387-1-387-36.

Wang, Y., Song, Y., & Xia, Y. (2016). Electrochemical capacitors: mechanism, materials, systems, characterization and applications. *Chemical Society Reviews, 45*, 5925-5950.

Wei, Y. Z., Fang, B., Iwasa, S., & Kumagai, M. (2005). A novel electrode material for electric double-layer capacitors. *Journal Power Source, 141*, 386-391.

Williard, N., He, W., Hendricks, C., & Pecht, M. (2013). Lessons learned from the 787 Dreamliner issue on lithium-ion battery reliability. *Energies, 6*(9), 4682-4695.

Winie, T., Jamal, A., Saaid, F. I., & Tseng, T. Y. (2018). Hexanoyl chitosan/ENR25 blend polymer electrolyte system for electrical double layer capacitor. *Polymers for Advanced Technologies, 30*(3), 726-735.

Winter, A., & Schubert, U. S. (2016). Synthesis and characterization of metallo-supramolecular polymers. *Chemical Society Reviews, 55*, 5311-5357.

Wongsaenmai, S., Ananta, S., & Yimnirun, R. (2012). Effect of Li addition on phase formation behavior and electrical properties of $(K_{0.5}Na_{0.5})NbO_3$ lead free ceramics. *Ceramics International, 38*, 147-152.

Woo, H. J., Majid, S. R., & Arof, A. K. (2011). Conduction and thermal properties of a proton conducting polymer electrolyte based on poly (ε-caprolactone). *Solid State Ionics, 199*, 14-20.

Woo, H. J., Majid, S. R., & Arof, A. K. (2013). Effect of ethylene carbonate on proton conducting polymer electrolyte based on poly(ε-caprolactone) (PCL). *Solid State Ionics, 252*, 102-108.

Woo, H. J., Liew, C. W., Majid, S. R., & Arof, A. K. (2014). Poly(ε-caprolactone)-based polymer electrolyte for electrical double-layer capacitors. High Performance Polymers, 26(6), 637-640.

Xu, K. (2004). Nonaqueous liquid electrolytes for lithium-based rechargeable batteries. *Chemical reviews, 104*(10), 4303-4418.

Xu, K. (2014). Electrolytes and Interphases in Li-Ion Batteries and Beyond. *Chemical Reviews, 114*(23), 11503-11618.

Xu, M., Li, D., Yan, Y., Guo, T., Pang, H., & Xue, H. (2017). Porous high specific surface area-activated carbon with co-doping N, S and P for high-performance supercapacitors. *RSC Advances, 7*, 43780-43788.

Yan, S., Zeng, S., Su, X., Yin, H., Xiong, Y., & Xu, W. (2011). H_3PO_4-doped 1,2,4-triazole-polysiloxane proton conducting membrane prepared by sol–gel method. *Solid State Ionics, 198*, 1-5.

Yang, I., Kim, S. G., Kwon, S. H., Lee, J. H., Kim, M. S., & Jung, J. C. (2016). Pore size-controlled carbon aerogels for EDLC electrodes in organic electrolytes. *Current Applied Physics, 16*(6), 665-672.

Yao, P., Yu, P., Ding, Z., Liu, Y., Lu, J., Lavorgna, M., ... Liu, X. (2019). Review on polymer-based composite electrolytes for lithium batteries. *Frontiers in Chemistry, 7*, 1-17.

Yap, K. S. (2012). *Characteristics of PMMA-grafted natural rubber polymer electrolytes*. (Doctoral thesis, University of Malaya, Kuala Lumpur, Malaysia). Retrieved from http://studentsrepo.um.edu.my/3815/

Yap, S. C., & Mohamad, A. A. (2007). Proton batteries with hydroponics gel as gel polymer electrolyte. *Electrochemical and Solid State Letters, 10*, A139-A141.

Younes, B. (2017). Classification, characterization, and the production processes of biopolymers used in the textiles industry. *The Journal of Textile Institute, 108*(5), 674-682.

Yulianti, E., Deswita, D., Sudaryanto, S., & Mashadi, S. (2019). Yulianti, E., Study of solid polymer electrolyte based on biodegradable polymer polycaprolactone. *Malaysian Journal of Fundamental and Applied Sciences, 15*(5), 467-471.

Yusof, Y. M. (2017). *Characteristics of corn starch/chitosan blend green polymer electrolytes complexed with ammonium iodide and its application in energy devices.* (Doctoral thesis, University of Malaya, Malaysia). Retrieved from http://studentsrepo.um.edu.my/7494/

Yusof, Y. M., & Kadir, M. F. Z. (2016). Electrochemical characterizations and the effect of glycerol in biopolymer electrolytes based on methylcellulose-potato starch blend. *Molecular Crystal Liquid Crystal, 627*(1), 220-233.

Yusof, Y. M., Majid, N. A., Kasmani, R. M., Illias, H. A., & Kadir, M. F. Z. (2014). The effect of plasticization on conductivity and other properties of starch/chitosan blend biopolymer electrolyte incorporated with ammonium iodide. *Molecular Crystals and Liquid Crystals, 603*(1), 73-88.

Yusof, Y. M., Shukur, M. F., Illias, H. A., & Kadir, M. F. Z. (2014). Conductivity and electrical properties of corn starch–chitosan blend biopolymer electrolyte incorporated with ammonium iodide. *Physica Scripta, 89*, 035701-035711.

Yu, X., Xiong, C., You, Y., Dong, L., & Yao, J. (2008). Aromatic azo-polyamide electrolyte with liquid crystal structure and photoelectrical properties. *Synthetic Metals, 158*(8-9), 375-378.

Yuan, X., & Quesnel, D. J. (2016). Synthesis and electrochemical study of sodium ion transport polymer gel electrolytes. *RSC Advances, 6*, 7504-7510.

Zainol, N. H., Osman, Z., Othman, L., & Isa, K. B. (2013). Transport and morphological properties of gel polymer electrolytes containing $Mg(CF_3SO_3)_2$. *Material Research, 686*, 137-144.

Zhang, J., Li., X., Li., Y., Wang, H., Ma, C., Wang, Y., ... Wei, W. (2018). Cross-linked nanohybrid polymer electrolytes with POSS cross-linker for solid-state lithium ion batteries. *Frontiers in Chemistry, 6*, 186-1-186-10.

Zhang, R., Xu, Y., Harrison, D., Fyson, & Southee, D. (2016). A Study of the Electrochemical Performance of Strip Supercapacitors under Bending Conditions. *International Journal of Electrochemical Science, 11*, 7922-7933.

Zhao, X. Andersson, M., & Andersson, R. (2018). Resistant starch and other dietary fiber components in tubers from a high-amylose potato. *Food Chemistry, 251*, 58-63.

Zhao, X. Y., Wu, Y., Cao, J. P., Zhuang, Q. Q., Wan, X., He, S., & Wei, X. Y. (2018). Preparation and characterization of activated carbons from oxygen-rich lignite for electric double-layer capacitor. *International Journal of Electrochemical Science, 13*, 2800-2816.

Zhong, C., Yida, D., Hu, W., & Zhang, J. (2015). A review of electrolyte materials and compositions for electrochemical supercapacitors. *Chemical Society Reviews, 4*4(21), 7431-7920.

LIST OF PUBLICATIONS AND PAPER PRESENTED

Thesis related publications:

Hamsan, **M. H.,** Aziz, S.B., Shukur, M. F., & Kadir, M. F. Z. (2019). Protonic cell performance employing electrolytes based on plasticized methylcellulose-potato starch-NH_4NO_3. *Ionics, 25*(2), 559-572.

Hamsan, **M. H.,** Shukur, M. F., & Kadir, M. F. Z. (2017). NH_4NO_3 as charge carrier contributor in glycerolized potato starch-methyl cellulose blend-based polymer electrolyte and the application in electrochemical double-layer capacitor. *Ionics, 23*(12), 3429-3453.

Hamsan, **M. H.,** Shukur, M. F., & Kadir, M. F. Z. (2017). The effect of NH_4NO_3 towards the conductivity enhancement and electrical behavior in methyl cellulose-starch blend based ionic conductors. *Ionics, 23*(5), 1137–1154.

Other publications:

Aziz, S. B., **Hamsan, M. H.,** Kadir, M. F. Z., & Woo, H. J. (2020). Design of Polymer Blends Based on Chitosan:POZ with Improved Dielectric Constant for Application in Polymer Electrolytes and Flexible Electronics. *Advances in Polymer Technology,* Manuscript Accepted.

Aziz, S. B., Barza, M. A., Mishra, K., **Hamsan, M. H.,** Karim, W. O., Abdullah, R. M., ... Abdulwahid, R. (2020). Fabrication of High Performance Energy Storage EDLC Device from Proton Conducting Methylcellulose: Dextran Polymer Blend Electrolytes. *Journal of Materials Research and Technology,* Manuscript Accepted.

Aziz, S. B., Marif, R. B., Brza, M. A., **Hamsan, M. H.,** & Kadir, M. F. Z. (2019). Employing of Trukhan model to estimate ion transport parameters in PVA based solid polymer electrolyte. *Polymer, 11*, 1694.

Hamsan, M. H., Aziz, S. B., Azha, M. A. S., Azli, A. A., Shukur, M. F., Yusof, Y. M., ... Kadir, M. F. Z. (2019). Solid-state double layer capacitors and protonic cell fabricated with dextran from *Leuconostoc mesenteroides* based green polymer electrolyte. *Materials Chemistry and Physics, 241*, 122290.

Aziz, S. B., Abdulwahid, R., **Hamsan, M. H.,** Brza, M. A., Abdullah, R., Kadir, M. F. Z., & Muzakir, S. K. (2019). Structural, impedance, and EDLC characteristics of proton conducting chitosan based polymer blend electrolytes with high electrochemical stability. *Molecules, 24*, 3508.

Aziz, S. B., Kadir, M. F. Z., **Hamsan, M. H.,** Woo, H. J., & Brza, M. A. (2019). Development of polymer blends based on PVA:POZ with low dielectric constant for microelectronic applications. *Scientific Reports, 9*, 13163.

Hamsan, M. H., Shukur, M. F., Aziz, S. B., Yusof, Y. M., & Kadir, M. F. Z. (2019). Influence of NH_4Br as ionic source on the structural/electrical properties of

dextran based biopolymer electrolytes and EDLC application. *Bulletin of Materials Science,* Manuscript Accepted.

Aziz, S. B., **Hamsan, M. H.,** Brza, M. A., Kadir, M. F. Z., Abdulwahid, R. T., Ghareeb, H. O., & Woo, H. J., (2019). Fabrication of energy storage EDLC device based on cs:peo polymer blend electrolytes with high Li^+ ion transference number. *Results in Physics, 15*, 102584.

Aziz, S. B., **Hamsan, M. H.,** Kadir, M. F. Z., Karim, W., & Abdullah, R. (2019). Development of polymer blend electrolyte membranes based on chitosan:dextran with high ion transport properties for EDLC application. *International Journal of Molecular Sciences, 20*, 3369.

Aziz, S. B., **Hamsan, M. H.,** Abdullah, R., & Kadir, M. F. Z. (2019). A promising polymer blend electrolytes based on chitosan: methyl cellulose for EDLC application with high specific capacitance and energy density. *Molecules, 24*, 2503.

Aziz, S. B., **Hamsan, M. H.,** Karim, W., Kadir, M. F. Z., Brza, M. A., & Abdullah, O. G. (2019). High proton conducting polymer blend electrolytes based on chitosan:dextran with constant specific capacitance and energy density. *Biomolecules, 9*, 267.

Yusof, Y. M., Shukur, M. F., **Hamsan, M. H.,** Jumbri, K., & Kadir, M. F. Z. (2019). Plasticized solid polymer electrolyte based on natural polymer blend incorporated with lithium perchlorate for electrical double-layer capacitor fabrication. *Ionics, 25*, 5733-5484.

Aziz, S. B., Brza, M. A., Woo, H. J., Mohammed, P., Kadir, M. F. Z., **Hamsan, M. H.,** & Abdulwahid, R. (2019). Increase of metallic silver nanoparticles in chitosan:agnt based polymer electrolytes incorporated with alumina filler. *Results in Physics, 12*, 102326.

Aziz, S. B., Brza, M. A., Kadir, M. F. Z., **Hamsan, M. H.,** Abidin, Z. H. Z., Tahir, D. A., & Abdullah, O. G. (2019). Investigation on degradation and viscoelastic relaxation of li ion in chitosan based solid electrolyte. *International Journal of Electrochemical Science*, *14*, 5521-5534.

Shukur, M. F., **Hamsan, M. H.,** & Kadir, M. F. Z. (2019). Investigation of plasticized ionic conductor based on chitosan and ammonium bromide for EDLC application. *Materials Today: Proceedings, 17*, 490-498.

Hamsan, M. H., Shukur, M. F., Aziz, S. B., & Kadir, M. F. Z. (2019). Dextran from *leuconostoc mesenteroides* doped ammonium salt based green polymer electrolyte. *Bulletin of materials science, 42*, 57.

Shukur, M. F., **Hamsan, M. H.,** & Kadir, M. F. Z. (2018). Plasticized and plasticizer free lithium acetate doped polyvinyl alcohol−chitosan blend biopolymer electrolytes: comparative studies. *Journal of Physics: Conference Series, 1123*, 012001.

Kadir, M. F. Z., Salleh, N. S., **Hamsan, M. H**., Aspanut, Z. Majid, N.A., & Shukur, M. F. (2018). Biopolymeric electrolyte based on glycerolized methyl cellulose with NH_4Br as proton source and potential application in EDLC. *Ionics, 24*, 1651-1662.

Kadir, M.F.Z., & **Hamsan, M. H.** (2018). Green electrolytes based on dextran-chitosan blend and the effect of NH_4SCN as proton provider on the electrical response studies. *Ionics, 24*, 2379-2398.

Conferences:

Hamsan, M. H., Aziz, S. B., Azha, M. A. S., Azli, A. A., Shukur, M. F., Yusof, Y. M., ... Kadir, M. F. Z. "Solid-state double layer capacitors and protonic cell fabricated with dextran from *Leuconostoc mesenteroides* based green polymer electrolyte" American Society on Campus (ACS), Kuala Lumpur, Malaysia (October 2019).

Hamsan, **M. H.,** Shukur, M. F., & Kadir, M. F. Z. "Characterization of starch-methyl cellulose blend based proton conductor and application in energy device" 15th International Symposium on Polymer Electrolytes (ISPE), Uppsala, Sweden (August 2016).